WEDDELL SEA EXPEDITION 2019

Cruise Scientific Report

8 March 2019

Edited by
J.A. Dowdeswell (Expedition Chief Scientist)

Contents

1. Introduction to the Cruise and its Scientific Aims

Julian Dowdeswell and John Shears

1.1 Introduction and scientific aims

The Weddell Sea Expedition 2019 (WSE) was conceived with dual aims: (i) the undertaking of a comprehensive inter-disciplinary programme of science centred in the waters around the Larsen C Ice Shelf; and (ii) to search for, survey and image the wreck of Sir Ernest Shackleton's *Endurance*, which sank in the Weddell Sea in 1915.

The expedition, funded in full by the Flotilla Foundation, a Netherlands-based charity, was to last about six weeks, and required the use of a substantial ice-strengthened vessel given the very difficult sea-ice conditions habitually encountered in the Weddell Sea, and especially in its central and western areas. The South African ship SA *Agulhas II* was chartered for both its Polar Class 5 icebreaking capability and its design as a scientific research vessel. The expedition was also equipped with state-of-the-art Autonomous Underwater Vehicles (AUVs) and a Remotely Operated Vehicle (ROV) which were capable of deployment to waters more than 3,000 m deep, thus making both the Larsen C continental shelf and slope, and the *Endurance* wreck site, accessible.

The underlying rationale for the science of the WSE was the importance of floating ice shelves and their stability or otherwise on the timescale of decades to centuries. Ice shelves are floating tongues of ice that extend seaward from grounded glaciers and ice sheets on land. They are dynamically part of the ice sheet and are fed by ice from up-glacier. Ice shelves make up about 75% of Antarctica's coastline and together cover about 1.5 M km^2 (about 12% of the total area of Antarctica). They are typically a few hundred metres thick and the ocean-water cavities beneath them are often of similar depth. These sub-ice shelf cavities are among the most inaccessible places on our planet. Ice shelves gain mass by ice-flow from adjacent ice sheets, by snow accumulation on their surface, and by freezing-on of seawater at their floating base. They lose mass by basal melting and the production of icebergs. Ice-shelf change can be driven by shifting atmospheric and ocean conditions, but calving events can also be parts of the natural growth and decay cycle of an ice shelf.

Ice shelves are important not just locally, but more generally because they affect (i) the mass-balance and stability of the Antarctic Ice Sheet and (ii) ocean-current circulation. Changes to ice shelves therefore have environmental implications that are of considerable significance globally (IPCC, 2013). Ice shelves act to buttress or restrain ice flow from the huge interior of the Antarctic Ice Sheet. If ice shelves thin, break up to produce icebergs and retreat as the atmosphere and ocean waters warm, then ice flow from the interior accelerates and more mass is lost, contributing to global sea-level rise. A velocity increase of eight times was linked to recent ice-shelf collapse on the eastern Antarctic Peninsula. Melting at the base of ice shelves

and calved icebergs releases fresh water which can inhibit the generation of very dense Antarctic Bottom Water; one of the major drivers of the thermohaline circulation of the oceans (IPCC, 2013).

The Weddell Sea sector of Antarctica, through which Shackleton's *Endurance* drifted and sank, is surrounded by a number of major ice sheet-ice shelf systems. Several of these ice shelves are changing rapidly, making investigations here very timely. The Larsen A and B ice shelves collapsed in a matter of days in 1995 and 2002, respectively (Rott *et al*., 1996; Rack and Rott, 2005), and one of the biggest iceberg calving events ever recorded took place from Larsen C Ice Shelf in July 2017 (Hogg and Gudmundsson, 2017); iceberg A68 had an area of 5,800 km^2 or about four times the size of Greater London.

The WSE's key scientific objectives were:

- To use upward-looking multibeam echo-sounding from AUVs to investigate the underwater shape of ice-shelf and sea-ice bases.
- To use drone-deployed radar and field measurements of snow thickness and stratigraphy of sea ice to calibrate ICESat-II and CryoSat-2 satellite-altimetric observations of sea-ice freeboard and thickness.
- To use downward-looking multibeam echo-sounding and sub-bottom profiling from AUVs to investigate the detailed morphology and shallow stratigraphy of the seafloor beneath and adjacent to floating ice shelves, providing key information on past ice-shelf dynamics and stability.
- To image and map the seafloor, extract sediment cores from areas of the seafloor recently made accessible to icebreaking vessels through iceberg calving, allowing the dating of past ice-shelf changes using radiocarbon.
- To investigate the marine biology of the seafloor in a set of locations with different histories of recent coverage by floating ice shelves, to assess ecological variability and ecosystem change in such environments.
- To obtain a series of measurements of the salinity and temperature of the water column adjacent to and beneath a floating ice shelf to assess the modern oceanographic setting and melt rate of these ice shelves.
- To make field measurements of sea-ice thickness and mechanical properties to better understand the stresses affecting the hulls of icebreakers.

In addition to these scientific objectives, the expedition aimed to reach the ice-infested waters in which Shackleton's *Endurance* sank and to locate, image and photograph the wreck and the surrounding sea floor using high-resolution AUV- and ROV-deployed instruments.

1.2 Cruise Narrative

The Weddell Sea Expedition 2019 aboard the Antarctic logistics and research vessel SA *Agulhas II* took place between 1 January and 22 February 2019. The science and technical teams were flown in from Cape Town to Wolf's Fang blue-ice runway in three flights of White Desert's Gulfstream aircraft. Transport from Wolf's Fang to Penguin Bukta at the edge of the

Fimbul Ice Shelf was by Basler aircraft and some expedition members were then helicoptered aboard while others were taken to the ice-shelf edge by tractor and caboose and then onto the ship by crane and basket.

The cruise started and finished in Penguin Bukta, on the East Antarctic coast 158 km from the South African's SANAE Base. The ship first took a week-long passage to the area of the Weddell Sea east of the Antarctic Peninsula between Larsen C Ice Shelf and Iceberg A68, largely skirting north of the sea ice of the Weddell Sea and using relatively open water immediately east of the Peninsula to access the northern Larsen Sea area.

A total of 16 days was spent in the western Weddell Sea undertaking a combination of scientific observations and testing of two autonomous underwater vehicles (AUVs 7 and 9 from Ocean Infinity) and a remotely operated vehicle (ROV from Eclipse). The scientific investigations are described in detail in Sections 3-10 of this Cruise Report. During this initial part of the expedition there was also a four-day period during which AUV9 was first lost and then recovered from beneath a large sea-ice floe.

The ship then took passage to the search box in which the wreck of Shackleton's *Endurance*, which sank in about 3,000 m of water in November 1915, was located according to Captain Frank Worsley's original sextant observations. After a four-day passage towards the wreck site the pressure housing on the ROV failed during a sea trial and the ship then proceeded to King George Island in the South Shetland Islands to obtain spares and to fly out a number of the science team (this was to alleviate any delays in flying out of Wolf's Fang at the end of the expedition, reducing the number of outward flights from three to two).

Almost five days were spent waiting for a weather window to receive the ROV spares at King George Island before it was decided to proceed to the wreck search box without them. Passage to the wreck site skirted most of the pack ice of the western Weddell Sea over a four-day period before penetrating the thick multi-year ice into the *Endurance* search box.

Sea-ice conditions in the search box were difficult, but AUV7 was launched on a 40 hour dive to image the sea floor and, hopefully, the wreck of *Endurance*. After 7 of the 11 under-water legs were completed contact was lost with AUV7 and, despite a major search operation by the *Agulhas II*, AUV7 was not located and was considered lost. The ship then proceeded out of the thick pack ice of the search box and completed the cruise with a 6-day passage back to Penguin Bukta followed by the demobilisation of the remaining scientists and technical expedition members in two flights from Wolf's Fang to Cape Town. The expedition finished on 22 February 2019.

2. Timeline and Ship Tracks

Julian Dowdeswell and Christine Batchelor

2.1 Expedition Timeline

S 30 Dec	First White Desert flight to Wolf's Fang and then Penguin Bukta
M 31 Dec	Second White Desert flight to Wolf's Fang and then to Penguin Bukta
T 1 Jan	Begin charter of *Agulhas II*, Penguin Bukta
W 2 Jan	Third White Desert flight to Wolf's Fang
T 3 Jan	Third flight from Wolf's Fang to Penguin Bukta, board *Agulhas II*
F 4 Jan	Passage to Larsen C
S 5 Jan	Passage to Larsen C
S 6 Jan	Passage to Larsen C
M 7 Jan	Passage to Larsen C, 3 CTD/ 1 Core
T 8 Jan	Passage to Larsen C
W 9 Jan	Passage to Larsen C, passing Seymour Island
T 10 Jan	Passage to Larsen C, down eastern AP, arrival at Larsen C
F 11 Jan	2 CTD/Cores; Trials of ROV
S 12 Jan	AUV Trails (unsuccessful); 3 CTD/3 Cores
S 13 Jan	AUV Trials (unsuccessful)
M 14 Jan	ROV Biology Transect B; 1 CTD/1 Core
T 15 Jan	AUV9 lost off Cape Framnes
W16 Jan	Search for AUV9; Sea Ice/Drone; Sea Ice Eng
T 17 Jan	Search for AUV9; Sea Ice/Drone; Sea Ice Eng
F 18 Jan	Search for AUV9
S 19 Jan	AUV9 recovered; Bulk ice samples; CTD/1 Core
S 20 Jan	ROV Biology Transect D; 4 CTD/4 Cores
M 21 Jan	ROV Biology Transect Ci; CTD, AUV7 Trials; 2 CTD/3 Cores
T 22 Jan	ROV Biology Transect Cii; 2 CTD/2 Cores; AUV 4 Trials
W 23 Jan	CTD/Core; ROV Biology
T 24 Jan	AUV9 Sea Ice; Sea Ice/Drone; CTD/Core
F 25 Jan	AUV7 at Larsen Inlet - GZWs
S 26 Jan	AUV9 Snow Hill – Sea Ice/Drone
S 27 Jan	Leave Larsen for wreck site
M 28 Jan	Passage to wreck site
T 29 Jan	Passage to wreck site; deep-water CTD
W30 Jan	Passage to wreck site; course change to KGI about noon
T 31 Jan	Passage to KGI

F 1 Feb	KGI (science team departs)
S 2 Feb	KGI
S 3 Feb	KGI
M 4 Feb	KGI
T 5 Feb	Depart KGI
W 6 Feb	Transit to wreck site
T 7 Feb	Transit to wreck site
F 8 Feb	Transit to wreck site
S 9 Feb	Transit to wreck site in pack
S 10 Feb	Arrive at *Endurance* sinking site. AUV 7 Search Dive 1 begins
M 11 Feb	AUV7 Search Dive 1
T 12 Feb	AUV7 missing
W 13 Feb	AUV missing, search abandoned. Sea Ice work.
T 14 Feb	Exit wreck area; CTD/Core, Sea Ice work
F 15 Feb	Begin passage to Penguin Bukta
S 16 Feb	Passage to Penguin Bukta
S 17 Feb	Passage to Penguin Bukta
M 18 Feb	Passage to Penguin Bukta
T 19 Feb	Passage to Penguin Bukta
W 20 Feb	Arrive at Penguin Bukta
T 21 Feb	White Desert flight to Cape Town
F 22 Feb	White Desert flight to Cape Town. End Charter of *Agulhas II*

2.2 Ship tracks of *SA Agulhas II* in the Weddell Sea

The SA *Agulhas II* departed Penguin Bukta, Fimbul Ice Shelf on 3 January 2019. The ~3500 km-long voyage to the Larsen C science location east of the Antarctic Peninsula took 8 days at an average speed of ~10 knots (Figure 2.1). The ship travelled north of the main sea-ice pack in the central Weddell Sea and encountered multi-year sea ice between 6 and 9 January. The Larsen C science location was accessed via relatively open water east of the Antarctic Peninsula, with the ship arriving in the evening of 10 January. On 24 January, after 14 days at the Larsen C science location, the ship travelled north along the eastern Antarctic Peninsula before heading into the central Weddell Sea and entering the *Endurance* wreck search phase of the Expedition (Figure 2.1). The ship reached the *Endurance* sinking location on 10 February 2019. The search for the wreck proved unsuccessful and AUV7 was lost. The ship then returned to Penguin Bukta for demobilisation of the expedition and finished on 22 February 2019.

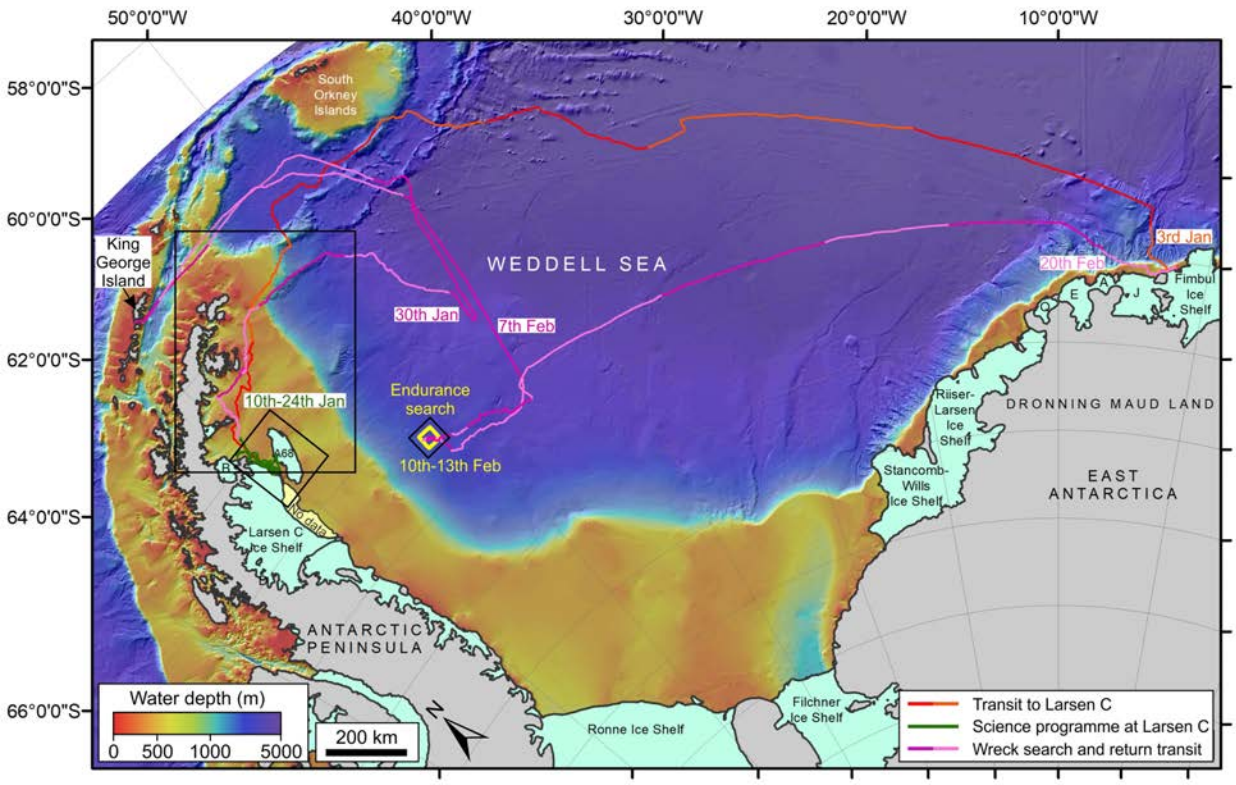

Figure 2.1. *Map of the ship tracks of the SA Agulhas II during the Weddell Sea Expedition 2019, coloured by Expedition phase. Black boxes show locations of Figures 2.2-2.6. Background is from International Bathymetric Chart of the Southern Ocean (IBCSO; Arndt et al., 2013), with 500 m contours. A = Atka Ice Shelf; B = Larsen B Ice Shelf; D = Larsen D Ice Shelf; E = Ekström Ice Shelf; J = Jelbart Ice Shelf; Q = Quar Ice Shelf.*

2.2.1 Eastern Antarctic Peninsula

The SA *Agulhas II* approached and departed the Larsen C science location via the eastern Antarctic Peninsula (Figure 2.2). During the approach, three CTDs and one gravity core were acquired on the upper slope and outer shelf of the north-east Antarctic Peninsula on 9 January. Data were also acquired during the ship's return voyage along the eastern Antarctic Peninsula: one CTD/ gravity core/ multi-core site (R1) was acquired in the inner shelf of Robertson Trough during 24/25 January; a downwards-looking survey of Larsen Inlet was performing using AUV7 on 25 January; an upwards-looking survey of an ice floe off Snow Hill Island was performed using AUV9 on 26 January; and associated sea ice fieldwork was carried out on the ice floe on 26 January.

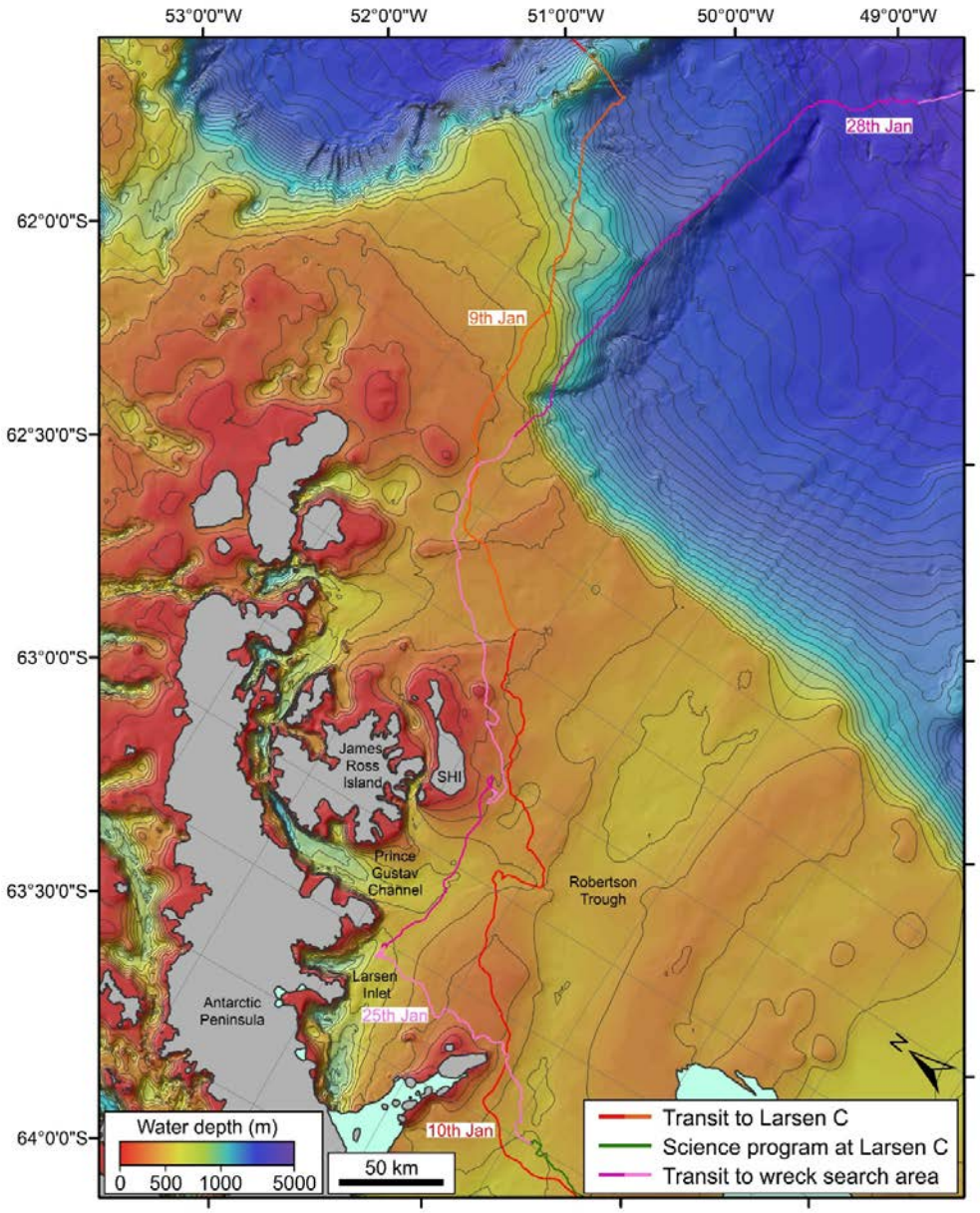

***Figure 2.2**. Map of the ship tracks of the SA Agulhas II along the eastern Antarctic Peninsula, coloured by Expedition phase. Background is from International Bathymetric Chart of the Southern Ocean (IBCSO; Arndt et al., 2013), with 100 m contours. SHI = Snow Hill Island.*

2.2.2 Northern Larsen C

The region beyond the northern Larsen C Ice Shelf (Figure 2.3) was the main science location during the Weddell Sea Expedition. The ship was in this location between 10 and 24 January (Figure 2.3). Sea ice conditions, notably the absence of a suitable lead along the front of the central Larsen C Ice Shelf, precluded scientific activity in the area south of Bawden Ice Rise that was formerly covered by the ice shelf prior to the calving of iceberg A68 in 2017 (Figure 2.3).

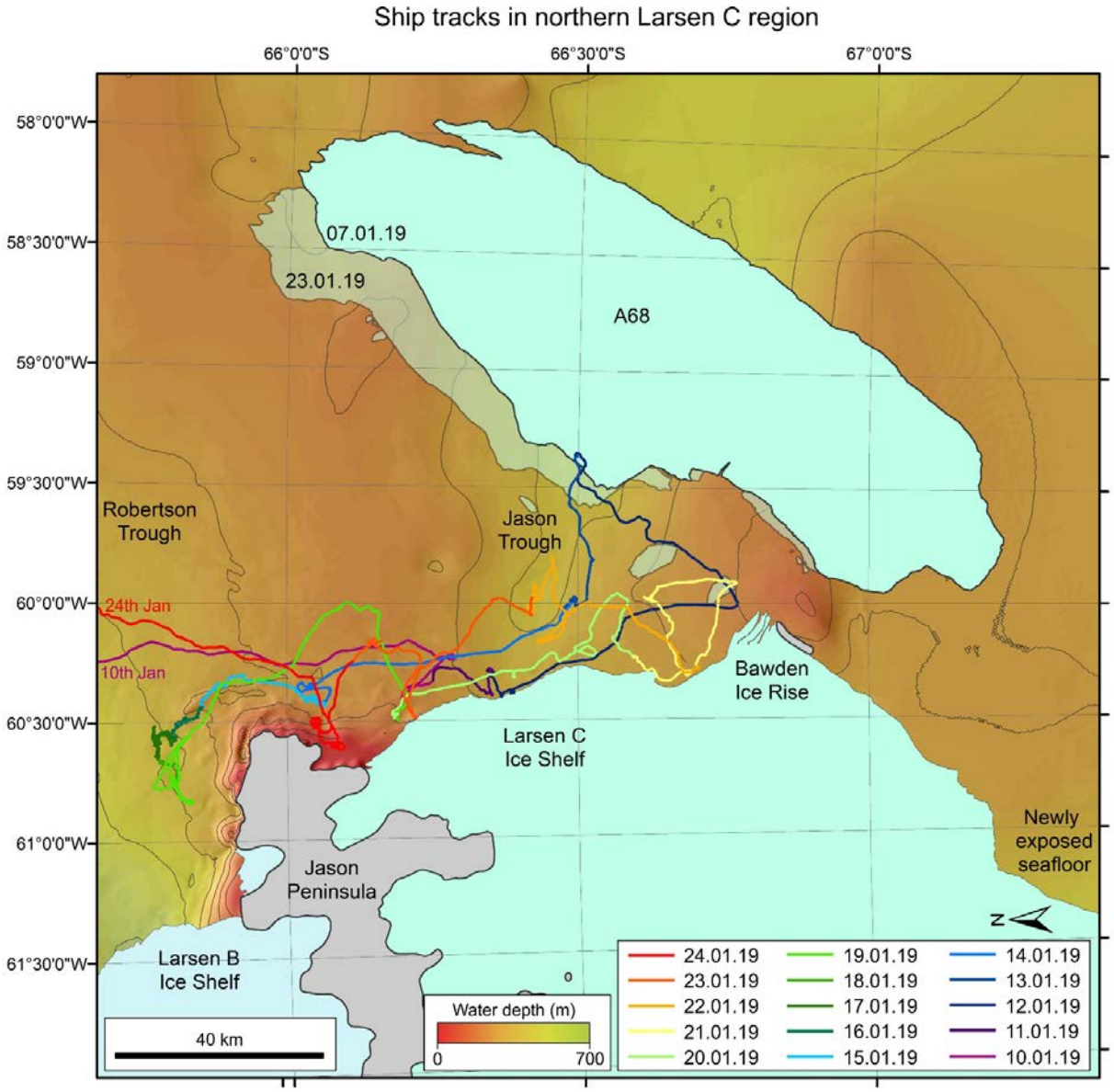

Figure 2.3. *Ship tracks of the SA Agulhas II in the northern Larsen C region, between 10 and 24 January 2019. Note the changing position of iceberg A68 during this time. Background is from International Bathymetric Chart of the Southern Ocean (IBCSO; Arndt et al., 2013), with 100 m contours.*

During the main scientific phase of the Expedition, the SA *Agulhas II* collected geophysical, geological, oceanographic and biological data from close to the front of Larsen C Ice Shelf, from close to Iceberg A68 (which shifted its position throughout this time), from the central axis of Jason Trough, and from close to Jason Peninsula (Figure 2.3). Between 15 and 19 January, AUV operations took the ship north of Jason Peninsula into the vicinity of Larsen B Ice Shelf. Seafloor surveys and ice-floe measurements were also made at Larsen Inlet (covered until 1998 by Larsen A Ice Shelf) and offshore of Snow Hill on the way northwards from the Larsen C area to begin passage to the *Endurance* wreck site (Figures 2.2 and 2.4). The locations

of data collection sites in the northern Larsen C area, between the ice shelf and Iceberg A68, are shown in Figure 2.5.

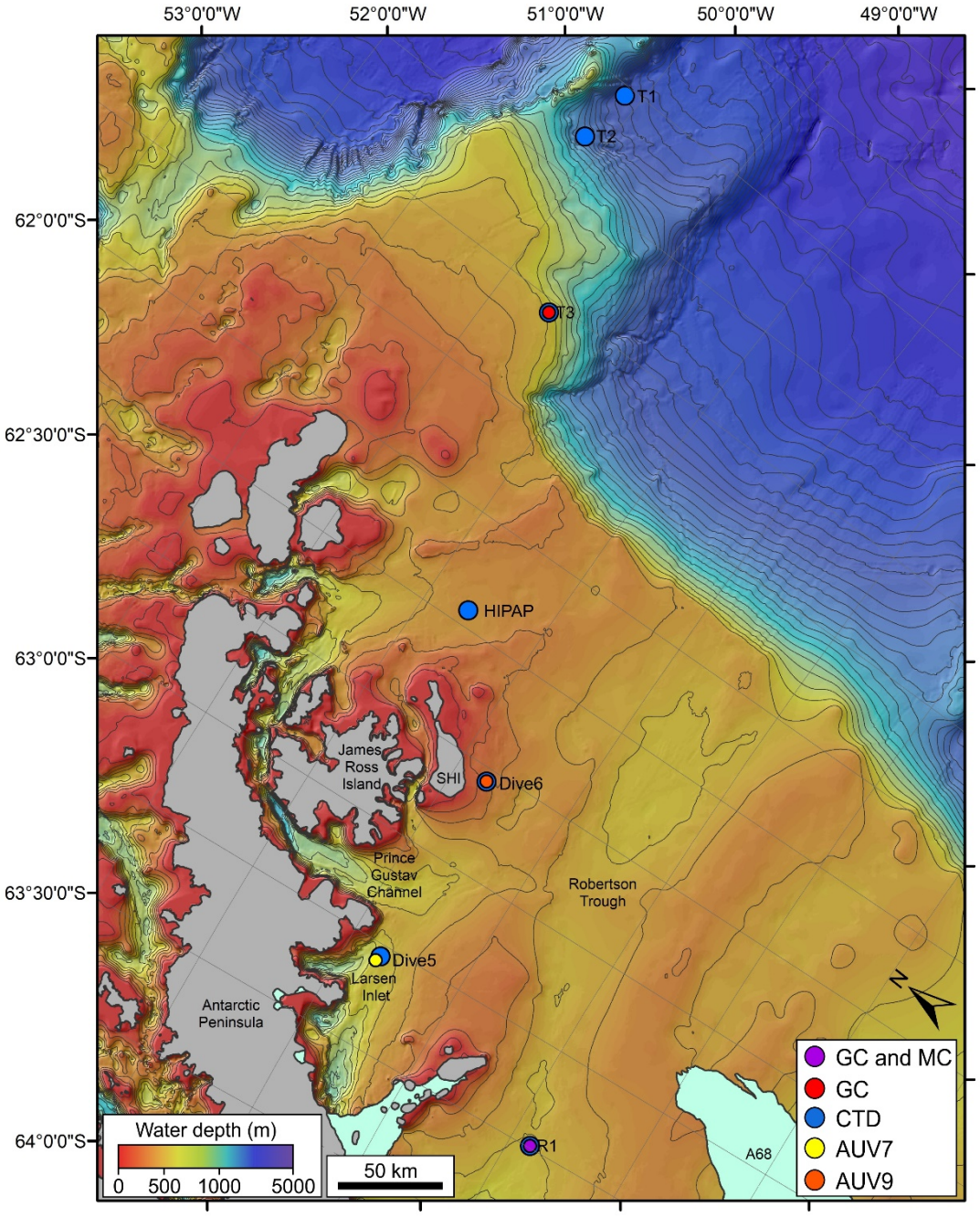

***Figure 2.4**. Map of the data collected along the eastern Antarctic Peninsula during the Expedition. Background is from International Bathymetric Chart of the Southern Ocean (IBCSO; Arndt et al., 2013), with 100 m contours. SHI = Snow Hill Island.*

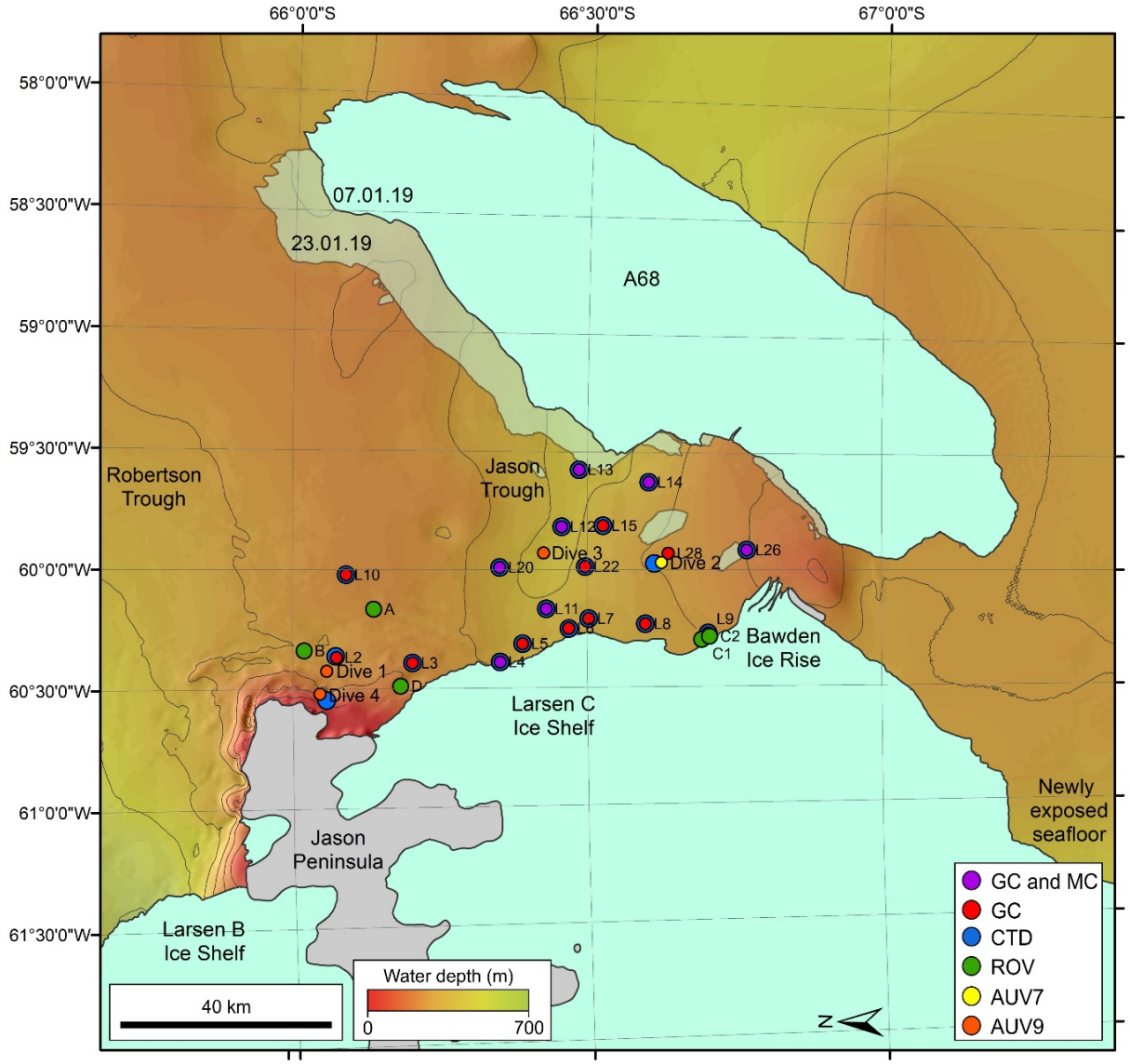

***Figure 2.5**. Map of the data collected in the northern Larsen C region during the Expedition. Background is from International Bathymetric Chart of the Southern Ocean (IBCSO; Arndt et al., 2013), with 100 m contours.*

2.2.3 Wreck site search box

The ship tracks between the principal area of scientific investigations near the eastern Peninsula areas and the search box around the last known position of Shackleton's *Endurance* are shown in Figure 2.1. This includes the deviation to King George Island to offload ten scientists and an attempt to obtain ROV spares. The pack ice around the wreck site was eventually entered from the southeast and the ship tracks in and around the search box for the *Endurance* are shown in Figure 2.6.

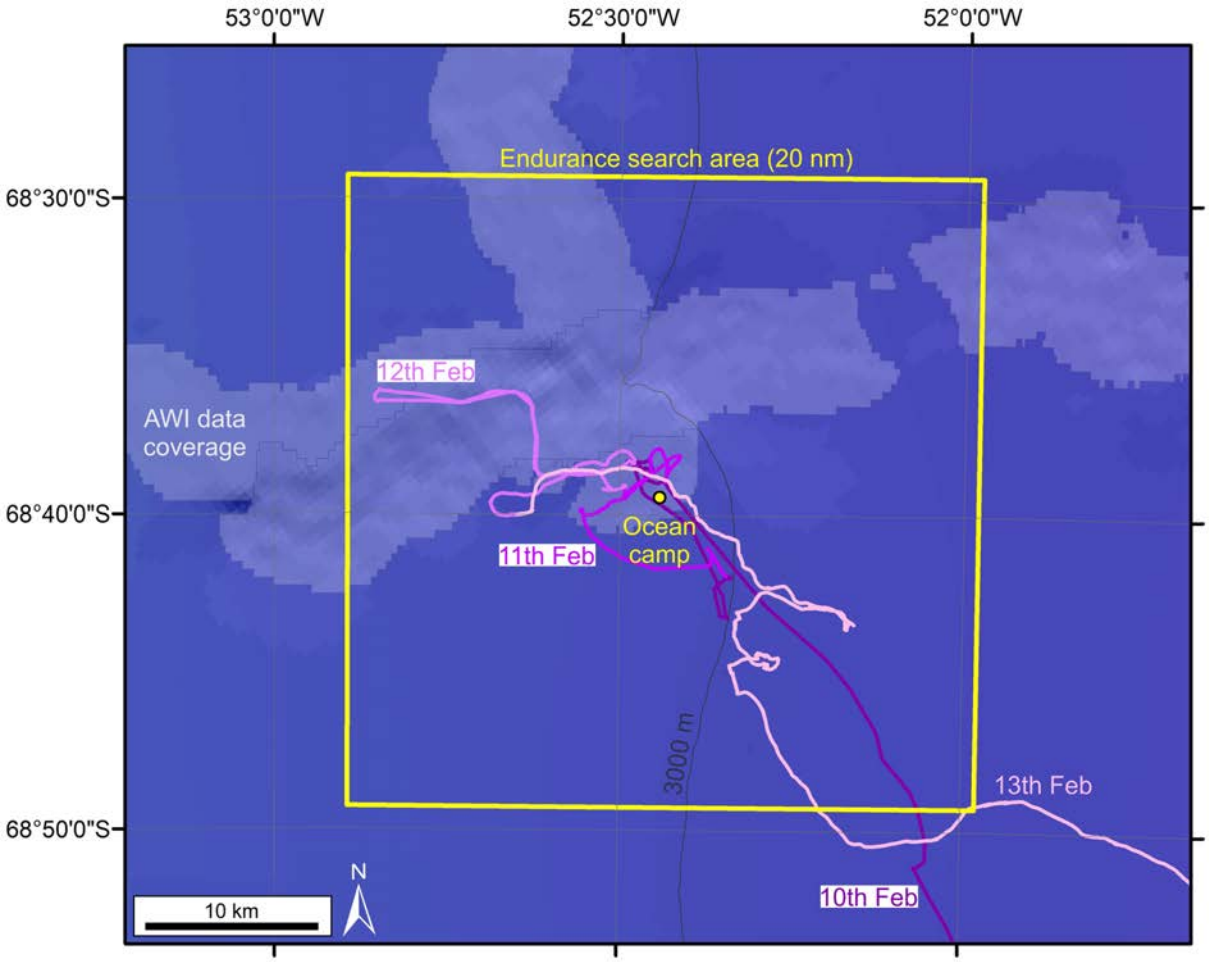

***Figure 2.6**. Map of the ship tracks in the search box for the wreck of Shackleton's Endurance. Background is from International Bathymetric Chart of the Southern Ocean (IBCSO; Arndt et al., 2013), with 100 m contours. AWI multibeam echo-sounder coverage is also shown along with Shackleton's 'Ocean Camp'.*

2.3 Personnel Aboard the *Agulhas II*

2.3.1 Expedition Members

Expedition Leadership Team

Dr John Shears (Expedition Leader, Shears Polar Ltd)

Professor Julian Dowdeswell (Chief Scientist and Director of the Scott Polar Research Institute, University of Cambridge)

Dr Mensun Bound (Director of Exploration)

Members of the Expedition Team

Reisna Audh (Oceanography MSc student, University of Cape Town)

Dr Christine Batchelor (Geophysicist, Scott Polar Research Institute, University of Cambridge and NTNU Norway)

Paul Bealing (Drone operator and technician, University of Canterbury NZ)

Professor Anriëtte Bekker (Mechanical Engineer, Sound and Vibration Research Group, Stellenbosch University)

Chad Bonin (AUV technician, Ocean Infinity)

Dr Tommy Bornman (Marine biologist, South African Environmental Observation Network/ Nelson Mandela University)

Jessica Burger (Oceanography PhD student, University of Cape Town)

Dr Frazer Christie (Glaciologist and remote sensing analyst, Scott Polar Research Institute, University of Cambridge)

Ray Darville (ROV technician, Eclipse)

Evelyn Dowdeswell (Geologist, Scott Polar Research Institute, University of Cambridge)

Dr Jeff Evans (Geologist, University of Loughborough)

Holly Ewart (Project Manager, Ocean Infinity and representative of the Flotilla Foundation)

Professor Sarah Fawcett (Oceanographer and Chief South African Scientist, University of Cape Town)

Raquel Flynn (Oceanography MSc student, University of Cape Town)

Betina Frinault (Marine biology PhD researcher, Nekton Foundation/University of Oxford)

Dr Claire Grogan (Medical Doctor)

Tahlia Henry (CTD operator, Iwandle)

Tim Huseyin (IT technician, Ocean Infinity)

James Howard (AUV technician, Ocean Infinity)

Dr Katherine Hutchinson (Oceanographer, University of Cape Town)

Devon James (AUV technician, Ocean Infinity)

Olive King (Location Director, Atlantic Productions)

Liangliang Lu (Naval Architect, Marine and Arctic Technology Research Group, Aalto University, Finland)

Kobus Loubser (Assistant Cameraman, Atlantic Productions)

Harry Luyt (Oceanography PhD student, University of Cape Town)

Pierre Le Gall (Survey analyst, Deep Ocean Search)

Steven March (ROV pilot, Eclipse)

James-John Mattee (Mechanical engineering graduate, Sound and Vibration Research Group, Stellenbosch University)

Sasha Montelli (Glacial Geology PhD researcher, Scott Polar Research Institute, University of Cambridge)

Dave O'Hara (ROV pilot, Eclipse)

Dr Dag Ottesen (Norwegian Geological Survey)

Todd Oxner (AUV technician, Ocean Infinity)

Professor Wolfgang Rack (Glaciologist, University of Canterbury NZ)

Steve Saint Amour (ROV manager, Eclipse)

Claire Samuel (Offshore Manager, Deep Ocean Search)

Shantelle Smith (Oceanography MSc student, University of Cape Town)

Kurt Spence (Oceanography MSc student, University of Cape Town)

Espen Stange (Senior AUV techncian, Kongsberg Marine)

Tamara Stubbs (Sound technician and drone operator, Atlantic Productions)

Dr Michelle Taylor (Marine biologist, University of Essex)

Channing Thomas (Senior AUV technician, Ocean Infinity)

Julien Trincali (Survey Data Analyst, Deep Ocean Search)

Christof van Zijl (M.Eng student, Sound and Vibration Research Group, Stellenbosch University)

Paul Williams (Cameraman, Atlantic Productions)

Dr Lucy Woodall (Senior marine biologist, Nekton Foundation/University of Oxford)

Leon Wuis (Sediment coring technician, Netherlands Institute of Oceanographic Research)

2.3.2 Other Scientists and Passengers

Dr Colin de la Harpe (Marine technician, South African Council for Industrial and Scientific Research)

Thapi Magabutlane (Meteorologist, South African weather service)

2.3.3 Ship's Captain and Ice Pilot

Captain Knowledge Bengu, Master

Captain Freddie Ligthelm, Ice Pilot

2.4 References

Arndt, J.E. and 15 others, 2013. The International Bathymetric Chart of the Southern Ocean (IBCSO) Version 1.0 – A new bathymetric compilation covering circum-Antarctic waters. *Geophysical Research Letters*, 40, 3111-3117.

Hogg, A.E. and Gunmundsson, H., 2017. Impacts of the Larsen-C Ice Shelf calving event. *Nature Climate Change*, **7**, 540-542.

Intergovernmental Panel on Climate Change (IPCC), 2013. The IPCC Fifth Assessment Report, *Climate Change 2013.*

Rack, W. and Rott, H., 2004. Pattern of retreat and disintegration of the Larsen B ice shelf, Antarctic Peninsula. *Annals of Glaciology*, **39**, 505-510.

Rott, H., Skvarca, P. and Nagler, T., 1996. Rapid collapse of Northern Larsen Ice Shelf, Antarctica. *Science,* **271**, 788-792.

3. Satellite Remote Sensing of Ice

Frazer Christie and Wolfgang Rack

This section outlines the satellite remote sensing carried out during the expedition, to enable safe vessel navigation, AUV mission planning, and the detection and tracking of icebergs and floes of scientific interest.

3.1 Sensors and datasets

A suite of passive and active remote-sensing data was used in support of the expedition, in terms of both ice navigation and scientific investigations. The details of these satellites and sensors are summarized in Table 3.1.

***Table 3.1**. Satellite sensors and data products used in support of the expedition*

Satellite	Sensor Type	Product Type	Spatial Resolution (m)	Orbital Repeat Pass Time (Days)	Source
Landsat 8	Panchromatic/ Multispectral	Full resolution	15/30	16	NASA[2]/USGS[3], processed by SPRI
MODIS Aqua	Multispectral	Full Resolution	c. 250	1	NASA[2], processed by SPRI
MODIS Terra	Multispectral	Full Resolution	c. 250	1	NASA[2], processed by SPRI
Sentinel-1a/b	SAR[1]	Scaled Amplitude	20	2-3	ESA[3]/Copernicus, via Drift & Noise, ICEPAD.
Sentinel-2a/b	Multispectral	Full resolution	10	6	ESA[3]/Copernicus, processed by SPRI
TerraSAR-X	SAR[1]	Quicklook Amplitude	10 - 60 m	1-2	DLR[4]
Suomi-NPP VIIRS	Multispectral	Full Resolution	c. 250	1	NASA[2], processed by SPRI

[1]Synthetic Aperture Radar, [2]National Aeronautics and Space Administration, [3]United States Geological Survey
[4]German Aerospace Center (Deutsches Zentrum für Luft – und Raumfahrt)

3.2 Ice Navigation and AUV mission planning

3.2.1 Synthetic Aperture Radar (SAR)

SAR amplitude image data were utilized as the primary data source for ice navigation and AUV mission planning due to their all-weather (cloud independent) imaging capabilities and dense spatial-temporal coverage at high latitudes. Sentinel-1a/b data were acquired free-of-charge from the European Space Agency (ESA) and staged in scaled amplitude georeferenced format (Table 4.1) to the vessel via the Drift & Noise 'ICEPAD' software. Compressed, ungeoreferenced JPEG format images were also provided to the vessel via daily email for the rapid assessment of sea-ice conditions outwith the GIS working environment.

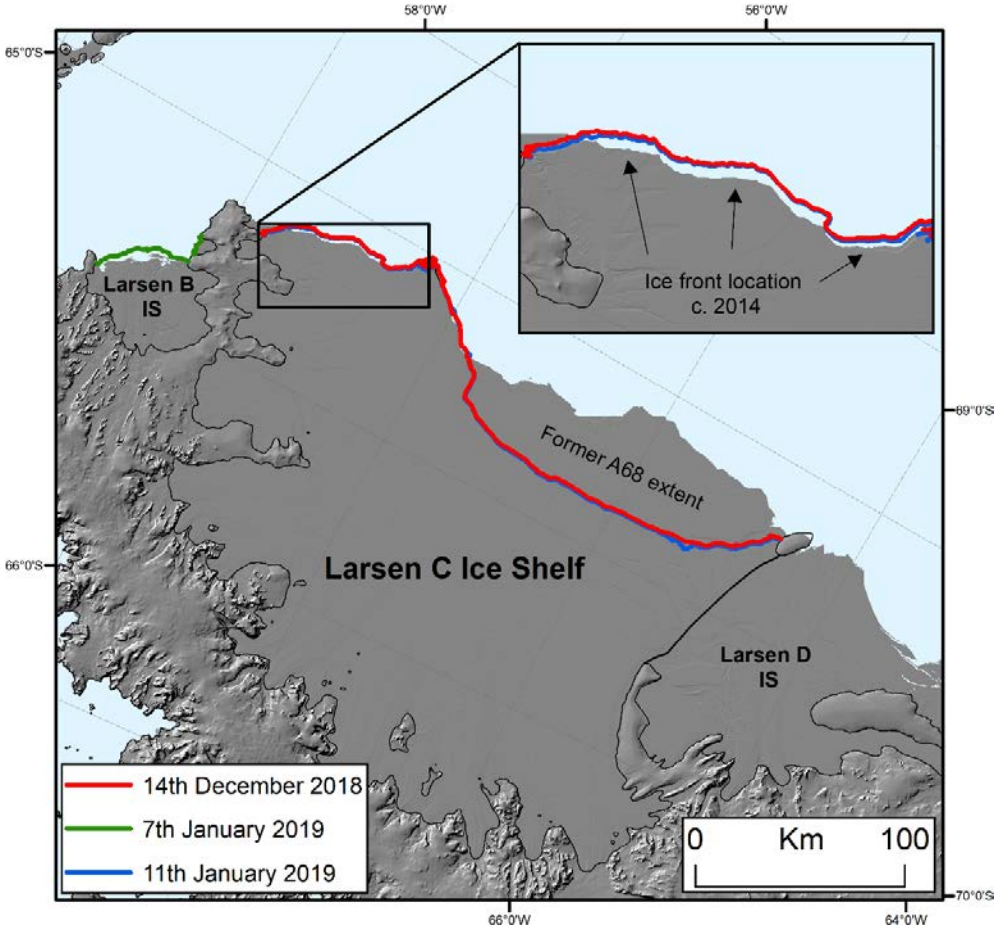

Figure 3.1. *Example ice fronts across the width of Larsen C Ice Shelf, as constrained from Sentinel-1a/b imagery acquired immediately prior to (red) and during the expedition (blue). The contemporary ice front of the remnant Larsen B Ice Shelf (green) was also ascertained during the expedition. Data are superimposed over the Reference Elevation Map of Antarctica (Howat et al., 2018). Thin black line = grounding line (Depoorter et al., 2013); thick black line, Larsen C and D Ice Shelf marginal limits (Mouginot et al., 2017). Projection: EPSG:3031.*

In addition to Drift & Noise Sentinel-1a/b imagery, full-resolution products and daily notifications of upcoming satellite overpasses were made available to the expedition via the 'PolarView' web-based data archive (polarview.org/). Quicklook amplitude TerraSAR-X

imagery in various acquisition modes (widescansar, scansar, stripmap, spotlight; Table 3.1) and ground resolutions was acquired in compressed format from DLR following dedicated orbital tasking over specific areas of interest (AoIs), as decided by the expedition remote sensing team in conjunction with the Chief Scientist, the Voyage Leader and the Captain and Ice Pilot of S.A. *Agulhas II*. Full resolution TerraSAR-X data corresponding to these acquisitions will become available for scientific analysis post-expedition.

The all-weather imaging capabilities and high geometric accuracy of Sentinel-1a/b and TerraSAR-X data enabled the accurate delineation of Larsen C's ice-shelf front during the expedition; an important parameter for safe and effective vessel operations and AUV/ROV launch and recovery. An example mapped ice fronts across the width of Larsen C Ice Shelf, as constrained from Sentinel-1a/b imagery acquired immediately prior to and during the expedition, is shown in Figure 3.1.

3.2.2 Multispectral Data

To characterise the transient nature of sea-ice conditions across the Weddell Sea Sector, for use in both vessel navigation and AUV mission planning, daily MODIS/VIIRS multispectral composite image updates were also generated by SPRI and staged to the vessel (Table 3.1). With coarser spatial resolution but superior swath coverage than that of SAR imagery (Table 3.1), this permitted examination of domain-wide sea ice characteristics where cloud cover permitted. An example image is shown in Figure 3.2.

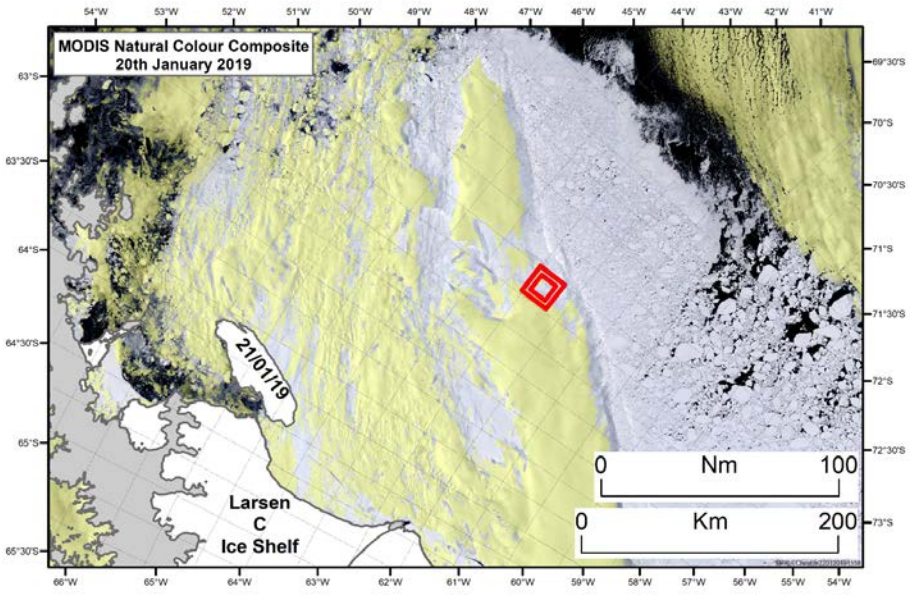

Figure 3.2. *MODIS multispectral composite image of the Weddell Sea Sector, 20 January 2019. Yellow masking denotes persistent cloud cover in both MODIS Aqua and Terra image acquisitions, as determined by the SPRI image processing chain. Red boxes = 20 NM and 12 NM Endurance wreck site locations. Grey hatching denotes grounded ice (Depoorter et al., 2013); white, ice shelf extents and the position of iceberg A68 on 21st January 2019. Projection: EPSG:3031.*

3.3 Ice floe and iceberg tracking

For expedition navigation and AUV mission planning (Section 4), a range of temporally successive SAR and multispectral datasets were used to examine and track the position several sea-ice floes in the Larsen C Ice Shelf region, as well as iceberg A68. Ice floes were predominantly tracked to ascertain the surface properties and geographical origin of these masses through time, as well as to examine the potential for their tracks to intercept upcoming IceSat-2 and CryoSat-2 overpasses.

3.3.1 Ice floe detection and tracking

The tracked position of an ice floe proximal to Larsen C Ice Shelf during the expedition is shown in Figure 3.3, superimposed over a TerraSAR-X amplitude image of the surrounding region. The figure also highlights the differences in the floe's surface properties depending on the satellite sensor utilised (Table 3.1); multispectral data (e.g. Sentinel-2, Landsat 8) primarily yields information on floe extent, crack locations and approximate ice thickness/stage of development, and SAR data yields information about the extent, surface 'roughness' and development stage of the floe (e.g. Sentinel-1, and TerraSAR-X; Table 3.1).

In SAR amplitude imagery, surface 'roughness' and snow morphology were qualitatively assessed by the spatial distribution of speckle returns corresponding to changes in the rheology of the firn-to-ice boundary layer, whereby spatially-uniform amplitude returns were indicative of smoother floe surfaces, and more chaotic, 'salt and pepper-like' returns were indicative of rougher terrain. In general, smoother and lower brightness returns in any given scene were attributed as younger, less-developed ice floes. However, it should be noted that variations in backscattering were also observed on the ice shelf and iceberg A68 as a result of short-lived surface melting events. Similar effects can therefore also be expected on the sea ice of the Weddell Sea.

Surface roughness and inferred thickness/stage of development information from SAR data were subsequently used to identify the three ice floes chosen for *in-situ* scientific study during the expedition, where on-floe, unmanned aerial vehicle (UAV) and sub-sea ice AUV measurements were carried out (Section 6).

3.3.2 Iceberg detection and tracking

As per pre-expedition planning, updates on the position of iceberg A68 were generated by Toby Benham in SPRI to ensure safe navigation and scientific operations in the Larsen C Ice Shelf region. These iceberg outlines were derived from full-resolution Landsat 8, Sentinel-2a/b (where cloud cover permitted) and Sentinel-1a/b data at SPRI, and were staged to the vessel on a daily basis in JPEG 'overview' and ESRI .shp format. An example of these data contemporaneous with the expedition is shown in Figure 3.4.

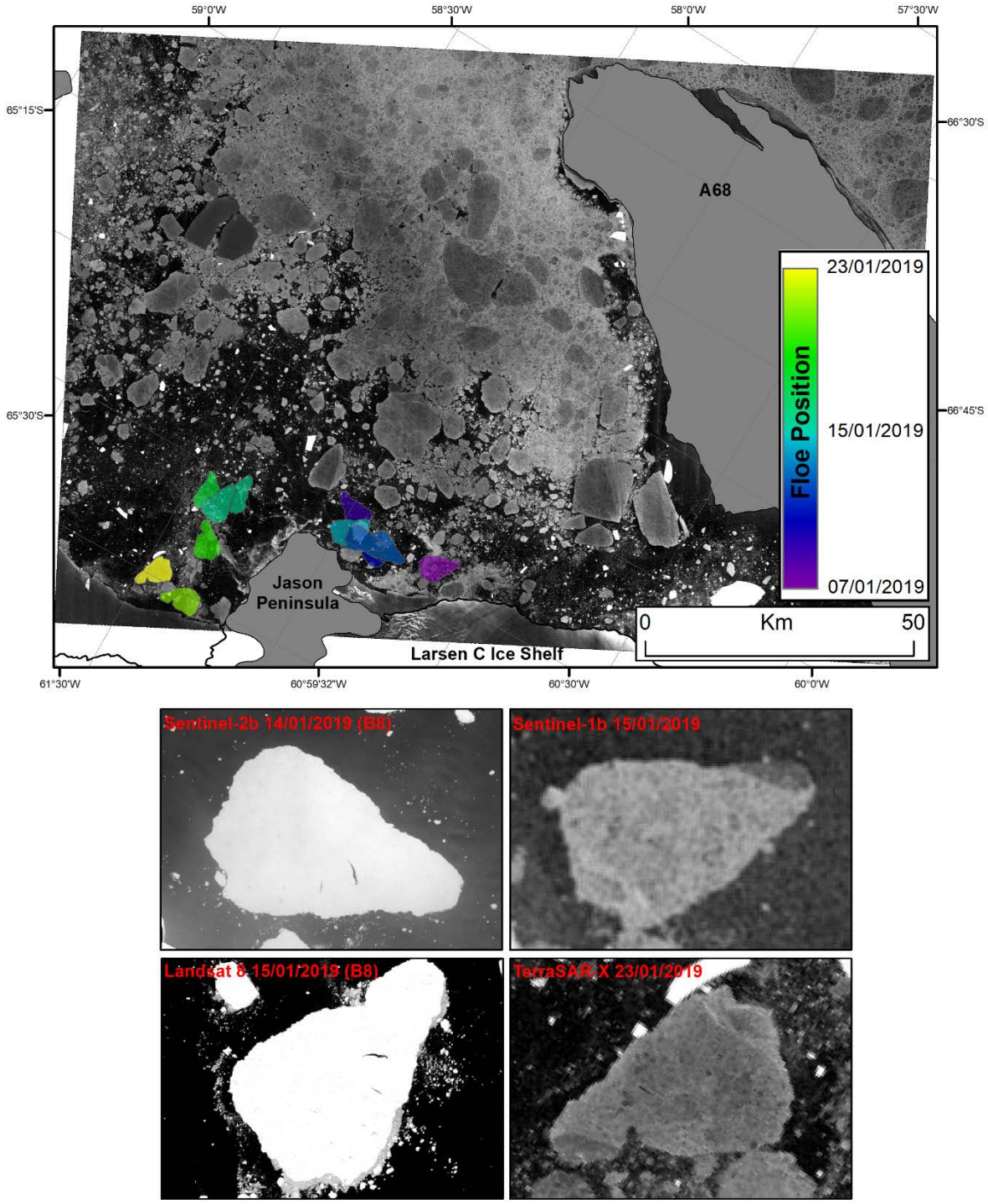

Figure 3.3. *(Main panel) TerraSAR-X amplitude image acquired on the 23rd January 2019 in the region of Larsen C Ice Shelf and iceberg A68. The different brightness and speckle returns broadly correspond to ##differences in the stage and development of sea-ice floes across the domain (see text). Also shown is the tracked position of ice floe #1 ('FloeTilla') where on-floe and sub-sea ice measurements were acquired. (Bottom panels) Surface characteristics of FloeTilla as observed from a range of satellite sensors used during the tracking process. The 'salt and pepper-like' speckle returns visible in the Sentinel-1b and TerraSAR-X images reveal the surface of this floe to be relatively rough. The darker corner of the flow (upper right in Sentinel-1b image; bottom left in TerraSAR-X image) was observed to be a smoother band of ice congealed to the floe, possibly of different sea ice genesis). Projection: EPSG:3031.*

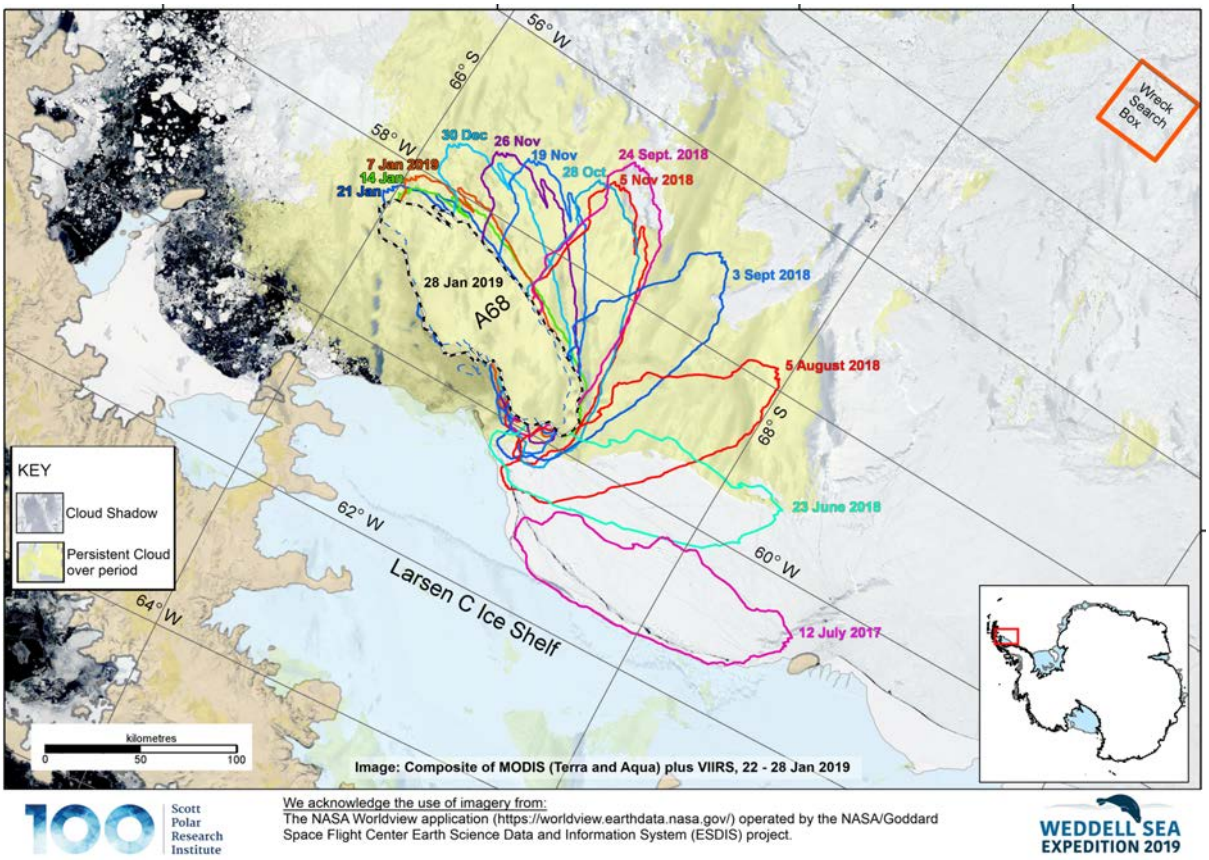

Figure 3.4. *Location of iceberg A68, updated to reflect its location contemporaneous with expedition timings. Data are superimposed over a MODIS/VIIRS image composite. Yellow masking denotes persistent cloud cover. Brown hatching denotes grounded ice; blue, ice shelf extent (Depoorter et al., 2013). Projection: EPSG:3031.*

3.4 References

Depoorter, M.A., Bamber, J.L., Griggs, J.A., Lenaerts, J.T.M., Ligtenberg, S.R.M., van den Broeke, M.R. and Moholdt, G., 2013. Calving fluxes and basal melt rates of Antarctic ice shelves. *Nature*, 502, 89-92, doi:10.1038/nature12567.

Howat, I., Morin, P., Porter, C. and Noh, M-J., 2018. *The Reference Elevation Model of Antarctica*. https://doi.org/10.7910/DVN/SAIK8B, *Harvard Dataverse*, V1].

Mouginot, J., Rignot, E. and Scheuchl, B., 2017. *MEaSURES Antarctic Boundaries for IPY 2007-2009 from Satellite Radar, Version 1*, digital media, NASA National Snow and Ice Data Center Distributed Active Archive Center, Boulder, Colorado, USA, doi:10.5067/AXE4121732AD.

4. AUV Investigations of Submarine Glacial Landforms

Christine Batchelor and Sasha Montelli

4.1 Introduction

The identification and interpretation of glacial landforms on mid- and high-latitude continental margins can provide information about the past dimensions and dynamic behaviour of ice sheets, as well as the processes by which sediment is eroded, transported and deposited by ice sheets (e.g. Shipp et al., 1999; Evans et al., 2005; Dowdeswell et al., 2008, 2016). Our understanding of past ice-sheet behaviour is presently limited by poor data coverage in some high-latitude regions, where data collection has historically been hampered by sea ice. In addition, there is a need to collect higher-resolution data of the seafloor and the subsurface to capture the complexity in the past behaviour of ice sheets and in the processes and patterns of glacier-influenced sedimentation.

In this Expedition, data about the seafloor and the subsurface of the western Weddell Sea, including the continental shelf beyond Larsen C Ice Shelf, were acquired by a ship-mounted single-beam echo-sounder and by Autonomous Underwater Vehicles (AUVs). Extensive sea ice cover, even during the austral summer, had previously restricted the collection of geophysical data from this region of the Antarctic Peninsula. As a result, little is known about the depth and characteristics of the seafloor in this area.

4.2. Hull-mounted sonar

4.2.1 Single-beam echo-sounding

SA *Agulhas II* is fitted with a Simrad EA600 single-beam echo-sounder that acquires data about the depth of the seafloor directly beneath the vessel, using a frequency of 18 kHz. While onboard, the seafloor depth was recorded every 60 seconds by the ship's ECDIS system. All data were provided at the end of the charter. On this Expedition, the single-beam echo-sounder data that were acquired by the ship provide valuable information about the depth of the seafloor in a remote area of the world that is rarely accessed by ships.

4.2.2 Sub-bottom profiler

SA *Agulhas II* is fitted with a hull-mounted Kongsberg TOPAS 3.5 kHz sub-bottom profiler (SBP). At the start of the Expedition, it was discovered that the TOPAS system had a hardware fault that was unable to be fixed even after intervention from Kongsberg staff. No hull-mounted SBP data were therefore recorded during the Expedition. It is thought that the TOPAS system may need inspection during the next dry-docking of the ship.

4.3. Marine-geophysical investigations using AUV7

The use of AUVs to collect geophysical data about the seafloor and subsurface has gained widespread application in the field of marine archaeology, as well as in search efforts for planes, boats and submarines (e.g. Ødegård et al., 2018). However, few AUV missions have investigated the glacial-geological record of high-latitude margins (Graham et al., 2013) or the sub-ice morphology of floating ice shelves and sea ice (Williams et al., 2014). The main advantage of collecting geophysical data from AUVs is the high resolution of the data that can be acquired when the vehicle operates close to the seafloor or to the base of a floating ice mass.

On this Expedition, AUVs were used to collect geophysical data about seafloor, subsurface and sub-sea ice morphology in the western Weddell Sea. Two AUVs, the downward-looking AUV7 and the upward- and downward-looking AUV9, were used to perform six geophysical surveys between 14 and 26 January 2019 (Figure 4.1).

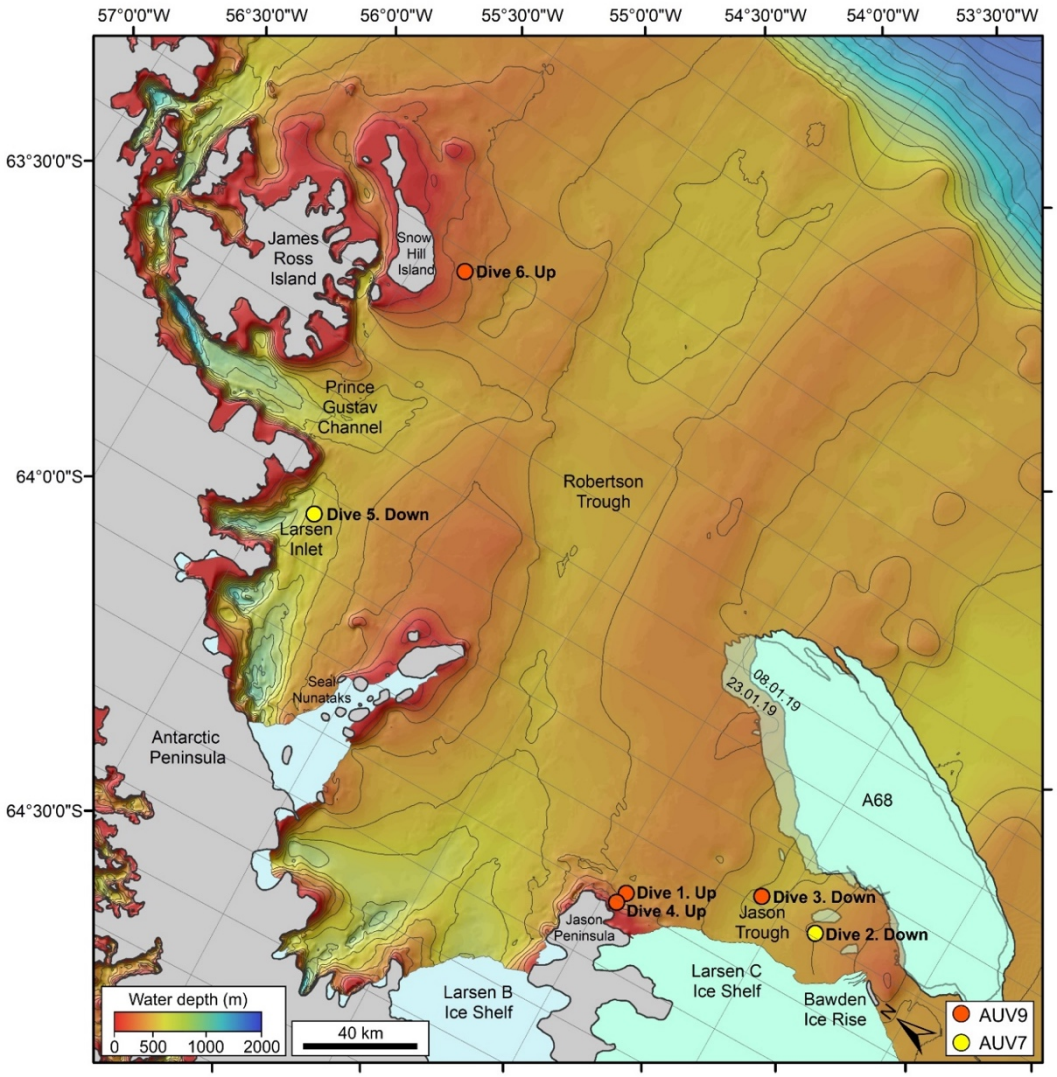

***Figure 4.1**. Map showing the locations of AUV upward-looking and downward-looking survey dives in the western Weddell Sea.*

4.3.1 AUV7 specifications

AUV7 is a Kongsberg Maritime HUGIN 6000 AUV, which operates in downward-looking mode only. AUV7 is equipped with a multi-beam echo sounder (MBES), side-scan sonar (SSS) and SBP (Table 1). The MBES, which is an EM2040 system, operates with a frequency of 200 or 400 kHz, depending on the required resolution and coverage. Higher-resolution MBES data can be acquired by lowering the separation height between the AUV and the seafloor. The SSS has three frequency modes, ranging from low (75 kHz) to high (400 kHz). The SBP operates at a frequency between 2 and 16 kHz, depending on the separation height between the vehicle and the seafloor. AUV7 has a bottom-tracking function, which can be used when the vehicle has a separation distance of 70 m or less from the seafloor.

Data	Abbreviation	System	Mode	Frequency
Multi-beam echo sounder	MBES	Kongsberg EM2040	Downwards	200 and 400 kHz
Side-scan sonar	SSS	EdgeTech 2205	Downwards	High: 400 kHz Mid: 230 kHz Low: 75 kHz
Sub-bottom profiler	SBP	EdgeTech	Downwards	2 – 16 kHz

Table 4.1*. Details of the sonar equipment on AUV7.*

4.3.2 AUV7 survey dives

AUV7 performed two downward-looking surveys in the western Weddell Sea - one trial at the southern margin of Jason Trough, and one science mission in Larsen Inlet (Figure 4.1; Tables 4.2 and 4.3). High-density beam spacing (400 beams) was used for both MBES surveys and the beam angle was set to 60° for each of the port and starboard sides of the vehicle. AUV7 was used in its bottom-tracking mode for both surveys and the SBP operated at 11 kHz. Onboard data processing by Deep Ocean Search (DOS) involved applying navigation and tidal corrections and a low-pass filter to remove erroneous soundings. The MBES data were adjusted for tidal variations relative to the WGS Ellipsoid.

During the trial dive at the southern margin of Jason Trough, geophysical data were collected during three surveys of the same region of the seafloor: first, with a separation height of 60 m and the MBES operating at 200 kHz; secondly, with a separation height of 60 m and the MBES operating at 400 kHz; and thirdly, with a separation height of 10 m and the MBES operating at 400 kHz (high-resolution MBES survey) (Table 4.2). SBP and SSS data were also collected during this mission. The speed of the AUV during data collection was 3.2 knots (with a margin of ~0.3 knots).

Dive	Mission	Date	Approximate location	Data	Format	Approximate survey size*
2	Downwards trial	21.01.19		MBES High-res MBES SBP (11 kHz) SSS BS	.xyz, .all .xyz, .all .xtf, .seg, .tif .xtf, .tif .tif	0.65 km² 0.075 km² 4.1 line-km 6.1 km² 1.6 km²
5	Downwards survey Larsen Inlet	25.01.19		MBES SBP (11 kHz) SSS BS	.xyz, .all .xtf, .seg, .tif .xtf, .tif .xtf, .tif	8.6 km² 64 line-km 80 km² 16 km²

***Table 4.2**. Details of downward-looking surveys by AUV7. *Includes overlapping images*

An example of the variety of geophysical data collected by AUV7 is shown in Figure 4.2. The horizontal resolution of the MBES data, which ranges from around 50 cm for the MBES data collected with a seafloor separation height of 60 m to around 20 cm for the higher-resolution MBES data collected from 10 m above the seafloor, facilitates the identification and interpretation of subdued glacial landforms. Individual clasts can be identified from the high-resolution MBES data (Fig. 4.2). The horizontal and vertical resolution of the SBP data, which is around 50 cm and 10 cm, respectively, enables a number of subsurface horizons to be identified and interpreted.

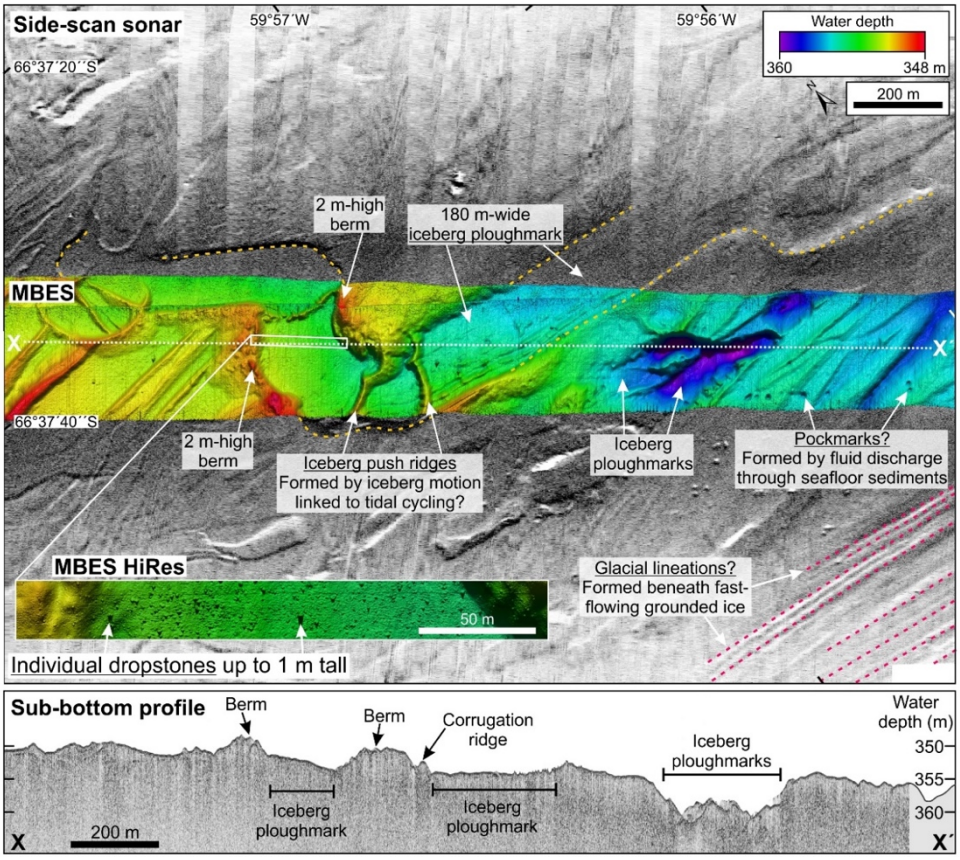

***Figure 4.2**. Example of geophysical data, including seafloor imagery and sub-bottom profiles, collected by AUV7 during its trial survey at the southern margin of Jason Trough (Dive 2).*

Dive 2: 21st Jan 2019

Sea Trial Downward Looking AUV 7 *AUV7 Sequence 1*	
Depth Control Mode	**Trajectory**
Altitude (m)	**60**
Speed (knts)	**3.2**
DVL	**Down Looking**
Ping Rate (Hz)	1
MBES	**YES**
Ping rate (Hz)	10
Angle	60° Port / 60° Stbd (Primary)
Swath (m)	200 Port / 200 Stbd (Secondary)
Min Height (m)	1
Max Height (m)	500
Angular Coverage	Auto
Ping Trigger	Internal
Beam Spacing	High density (400 beams)
Frequency (kHz)	200 + 400
Detection Mode	Tracking
Pulse Mode	CW Pulse
Master Ping Rate (Hz)	**2.4**
SSL (75KHz)	**YES**
trigger	**External**
divisor	**2**
pulse width	**20**
predicted range (m)	**600**
SSH (230KHz)	**NO**
SSX (410KHz)	**NO**
SBP	**YES**
Trigger	**Coupled to SSL**
divisor	**1**
pulse type	**1-11 @ 20ms**
power	**100%**
Magnetometer	**NO**
CathX	**NO**

Dive 2 High-Res: 21st Jan 2019

Sea Trial Downward Looking AUV 7 Hi-res *AUV7 Sequence 2*	
Depth Control Mode	**Trajectory**
Altitude (m)	**10**
Speed (knts)	**3.2**
DVL	**Down Looking**
Ping Rate (Hz)	1
MBES	**YES**
Ping rate (Hz)	10
Angle	60° Port / 60° Stbd (Primary)
Swath (m)	15 Port / 15 Stbd (Secondary)
Min Height (m)	1
Max Height (m)	500
Angular Coverage	Auto
Ping Trigger	Internal
Beam Spacing	High density (400 beams)
Frequency (kHz)	400
Detection Mode	Tracking
Pulse Mode	FM Pulse
Master Ping Rate (Hz)	
SSL (75KHz)	**NO**
SSH (230KHz)	**NO**
SSX (410KHz)	**NO**
SBP	**NO**
Magnetometer	**NO**
CathX	**YES**

Dive 5: 25th Jan 2019

Downward Looking AUV 7	
Depth Control Mode	**Trajectory**
Altitude (m)	**70**
Speed (knts)	**3.6**
DVL	**Down**
Ping Rate (Hz)	1
MBES	**Yes**
Ping rate (Hz)	10
Angle	60° Port / 60° Stbd (Primary)
Swath (m)	200 Port / 200 Stbd (Secondary)
Min Height (m)	1
Max Height (m)	500
Angular Coverage	Auto
Ping Trigger	Internal
Beam Spacing	High density (400 beams)
Frequency (kHz)	400
Detection Mode	Tracking
Pulse Mode	CW Pulse
Master Ping Rate (Hz)	**1**
SSL (75KHz)	**Yes**
trigger	**Coupled to SBP**
divisor	**1**
pulse width	**30**
predicted range (m)	**700**
SSH (230KHz)	**No**
SSX (410KHz)	**No**
SBP	**Yes**
Trigger	**External**
divisor	**1**
pulse type	**1-11 @ 20ms**
power	**100%**
Magnetometer	**No**
CathX	**No**

***Table 4.3**. Tables of detailed parameters used for the downward-looking surveys performed by AUV7. Dive 2 (test survey) was performed on 21.01.19 at the southern margin of Jason Trough. Three lines were run: 1) Altitude of 60 m, MBES operating at 200 kHz; 2) Altitude of 60 m, MBES operating at 400 kHz; and 3) Altitude of 10 m, MBES operating at 400 kHz. Dive 5 (survey in Larsen Inlet) was performed on 25.01.19 with an altitude of 70 m and the MBES operating at 400 kHz.*

AUV7 was used to perform a targeted geophysical survey of a former grounding-zone position of the Antarctic Peninsula Ice Sheet in Larsen Inlet (Dive 5 in Figure 4.1 and Table 4.2). The location of the former grounding-zone position was known from existing bathymetric data (Evans et al., 2005; Evans and Hogan, 2016). During this survey, a separation height of 70 m between the vehicle and the seafloor was used, the MBES operated at 400 kHz and the AUV speed was 3.6 knots (Table 4.3). SBP and SSS data were also collected during the 12 hour mission in Larsen Inlet.

4.4 Marine-geophysical and sea-ice investigations using AUV9

4.4.1 AUV9 specifications

AUV9 is a Kongsberg Maritime HUGIN 6000 AUV that has been modified to operate in upward- as well as downward-looking mode. The AUV must be onboard the vessel to change between modes. AUV9 is equipped with an upward-looking MBES, downward-looking high-resolution synthetic aperture sonar (HISAS), and a downwards-looking SBP (Table 4.4). The MBES EM2040 system operates with a frequency of 200 to 400 kHz, depending on the required resolution and coverage. The SBP operates at frequencies between 2 and 16 kHz, depending on the separation height between the vehicle and the seafloor. The SBP can be used in downward-looking mode at the same time that the MBES is used in upward-looking mode. The HISAS operates with a frequency of 60-120 kHz (Table 4.4). Bathymetric maps can be generated from HISAS images of the seafloor.

Data	Abbreviation	System	Mode	Frequency
Multi-beam echo sounder	SMBES	Kongsberg EM2040	Upwards	200-400 kHz
High-resolution synthetic aperture sonar	HISAS	HISAS 1030	Downwards	60-120 kHz
Sub-bottom profiler	SBP	EdgeTech 216	Downwards	2 – 16 kHz

Table 4.4*. Details of the sonar equipment on AUV9.*

4.4.2 AUV9 survey dives

AUV9 performed one downward-looking trial survey (Dive 3 in the centre of Jason Trough) and three upward-looking surveys beneath ice floes (Dives 1, 4 and 6) (Figure 4.1; Table 4.5). In all four dives, high-density beam spacing (400 beams) was used for the MBES, with a beam angle of 60° for each of the port and starboard sides. The SBP operated at 11 kHz. All dives were collected with an AUV speed of 3.2 knots. To aid navigation, AUV9 was used in bottom-tracking mode for its upward- and downward-looking missions, which limited the maximum separation height between the vehicle and the underlying seafloor to around 200 m. Ice floes in less than around 300 m water depth were therefore targeted for upward-looking surveys (assuming a separation distance of around 100 m between the AUV and the base of the ice floe). Onboard data processing by DOS involved applying navigation and tidal corrections and a low-pass filter to remove erroneous soundings.

HISAS images and SBP data were acquired during the trial dive of AUV9 in downward-looking mode in the centre of Jason Trough (Dive 3 in Figure 4.1 and Table 4.5). Bathymetric data were generated from the HISAS data.

AUV9 acquired upward-looking MBES and downward-looking SBP data during its trial survey beneath ice floe 'FloeTilla' on 14 January (Table 4.5). A separation distance of around 110 m between the AUV and the base of the sea ice was used (Table 4.6). Upwards-looking MBES data were collected beneath a further two ice floes on 24 and 26 January (Fig. 4.1 and Table 4.5), with a separation distance of 50 m and 110 m, respectively, between the AUV and the base of the ice floes (Table 4.7). Further details about the upward-looking surveys performed by AUV9 are provided in Section 6.2 on AUV operations under sea ice.

Dive	Mission	Date	Approximate location	Data	Format	Approximate survey size*
1	Upward survey 1 'FloeTilla'	14.01.19		Upward MBES SBP (11 kHz)	.xyz, .all .seg, .tif	0.6 km² 1.9 line-km
3	Downward trial in Jason Trough	22.01.19		Bathymetry from HiSAS SBP (11 kHz) HiSAS images	.xyz, .all .seg, .tif .tif	4 km² 13 line-km 4 km²
4	Upward survey 2 'FloeExpectations'	24.01.19		Upward MBES	.xyz, .all	0.6 km²
6	Upward survey 3 'FloeRida'	26.01.19		Upward MBES	.xyz, .all	1.1 km²

Table 4.5*. Details of the downward- and upward-looking surveys performed by AUV9. *Includes overlapping images*

Dive 3: 22nd Jan 2019

Sea Trial Downward looking AUV 9 HISAS	
Depth Control Mode	**Trajectory**
Altitude (m)	**25**
Speed (knts)	**3.2**
DVL	**Down Looking**
Ping Rate (Hz)	1
MBES	**NO**
SBP	**YES**
Trigger	**External**
divisor	**1**
pulse type	**1-11 @ 20ms**
power	**100%**
HISAS	**YES**
Power Level	High
Ping overlap	4
Custom mode	Deep
In Mission SAS	ON
Synchronized trigger	Distance
CathX	**NO**

Sea Trial Downward looking AUV 9 HISAS	
Depth Control Mode	**Trajectory**
Altitude (m)	**10**
Speed (knts)	**3.2**
DVL	**Down Looking**
Ping Rate (Hz)	1
MBES	**NO**
SBP	**NO**
HISAS	**YES**
Power Level	High
Ping overlap	4
Custom mode	Deep
In Mission SAS	ON
Synchronized trigger	Distance
CathX	**YES**

Table 4.6*. Tables of parameters used for the one downward-looking dive of AUV9 in the centre of Jason Trough on 22.01.19 (Dive 3).*

Dive 1: 15th Jan 2019

Upward looking AUV 9	
Depth Control Mode	**Trajectory**
Depth below Ice-shelf (m)	**110**
Speed (knts)	**3.2**
DVL	**Down+Up Looking**
Ping Rate (Hz)	1
MBES	**YES**
Ping rate (Hz)	10
Angle	60° Port / 60° Stbd (Primary)
Swath (m)	350 Port / 350 Stbd (Secondary)
Min Height (m)	1
Max Height (m)	500
Angular Coverage	Auto
Ping Trigger	Internal
Beam Spacing	High density (400 beams)
Frequency (kHz)	400
Detection Mode	Tracking
Pulse Mode	FM Pulse

Dive 4: 24th Jan 2019

Upward looking AUV 9	
Depth Control Mode	**Trajectory**
Depth below Ice-shelf (m)	**50**
Speed (knts)	**3.2**
DVL	**Up Looking**
Ping Rate (Hz)	1
MBES	**YES**
Ping rate (Hz)	10
Angle	60° Port / 60° Stbd (Primary)
Swath (m)	200 Port / 200 Stbd (Secondary)
Min Height (m)	1
Max Height (m)	500
Angular Coverage	Auto
Ping Trigger	Internal
Beam Spacing	High density (400 beams)
Frequency (kHz)	400
Detection Mode	Tracking
Pulse Mode	FM Pulse
HISAS	**NO**
Magnetometer	**NO**
CathX	**NO**

Dive 6: 26th Jan 2019

Upward looking AUV 9	
Depth Control Mode	**Trajectory**
Depth below Ice-shelf (m)	**110**
Speed (knts)	**3.2**
DVL	**Down+Up Looking**
Ping Rate (Hz)	1
MBES	**YES**
Ping rate (Hz)	10
Angle	60° Port / 60° Stbd (Primary)
Swath (m)	350 Port / 350 Stbd (Secondary)
Min Height (m)	1
Max Height (m)	500
Angular Coverage	Auto
Ping Trigger	Internal
Beam Spacing	High density (400 beams)
Frequency (kHz)	400
Detection Mode	Tracking
Pulse Mode	FM Pulse
HISAS	**NO**
Magnetometer	**NO**
CathX	**NO**

Figure 4.7*. Tables of parameters used for the three upward-looking AUV9 missions beneath sea ice. Dive 1 (test survey) was performed on 14.01.19 beneath ice floe 'Floe Tilla', close to Jason Peninsula. Dive 4 was performed on 24.01.19 beneath a second ice floe, close to Jason Peninsula. Dive 6 was performed on 26.01.19 beneath a third ice floe, off Snow Hill Island.*

4.5 Conclusions

The AUV and single-beam echo-sounder data that were acquired from the Weddell Sea, including from the continental shelf beyond Larsen C Ice Shelf, provide useful information about the depth of the seafloor in this remote region. These depth soundings will be incorporated into future charts and to the IBCSO compilation of Arndt et al. (2013), where they will aid ship navigation and future scientific expeditions in the Weddell Sea.

The high-resolution of the geophysical data collected by the AUVs will facilitate in-depth studies of the seafloor and the subsurface and the reconstruction of past glacial activity in the region. The assemblages of glacial landforms that are identified in these data provide insights into complexities in ice-sheet behaviour, including the past form and motion of ice sheets, ice shelves and icebergs (e.g. Dowdeswell et al., 2016). The geophysical data collected by the AUVs also reveal the form and internal structure of glacial landforms in unprecedented detail, which will further our understanding of the processes that are involved in their formation.

4.6 References

Arndt, J.E. and 15 others, 2013. The International Bathymetric Chart of the Southern Ocean (IBCSO) Version 1.0 – A new bathymetric compilation covering circum-Antarctic waters. *Geophysical Research Letters*, 40, 3111-3117.

Dowdeswell, J.A., Evans, J., Mugford, R., Griffiths, G., McPhail, S., Millard, N., Stevenson, P., Brandon, M.A., Banks, C., Heywood, K.J., Price, M.R., Dodd, P.A., Jenkins, A., Nicholls, K.W., Hayes, D., Abrahamsen, E.P., Tyler, P., Bett, B., Jones, D., Wadhams, P., Wilkinson, J.P., Stansfield, K. and Ackley, S., 2008. Autonomous underwater vehicles (AUVs) and investigations of the ice-ocean interface in Antarctic and Arctic waters. *Journal of Glaciology*, 54, 661-672.

Dowdeswell, J.A., Canals, M., Jakobsson, M., Todd, B.J., Dowdeswell, E.K. and Hogan K.A., (eds), 2016. Atlas of Submarine Glacial Landforms: Modern, Quaternary and Ancient. *Geological Society, London, Memoirs*, 46, 618 pp.

Evans, J., Pudsey, C.J., Ó Cofaigh, C., Morris, P.W. and Domack, E.W., 2005. Late Quaternary glacial history, dynamics and sedimentation of the eastern margin of the Antarctic Peninsula Ice Sheet. *Quaternary Science Reviews*, 24, 741-774.

Evans, J. and Hogan, K.A., 2016. Grounding-zone wedges on the northern Larsen shelf, Antarctic Peninsula. *In* Dowdeswell, J.A., Canals, M., Jakobsson, M., Todd, B.J., Dowdeswell, E.K. and Hogan K.A., (eds), *Atlas of Submarine Glacial Landforms: Modern, Quaternary and Ancient. Geological Society, London, Memoirs*, 46, 237-238.

Graham, A.G.C., Dutrieux, P., Vaughan, D.G., Nitsche, F.O., Gyllencreutz, R., Greenwood, S.L., Larter, R.D. and Jenkins, A., 2013. Seabed corrugations beneath an Antarctic ice shelf revealed by autonomous underwater vehicle survey: origin and implications for the history of Pine Island Glacier. *Journal of Geophysical Research*, 118, 1356-1366.

Shipp, S.S., Anderson, J.B. and Domack, E.W., 1999, Late Pleistocene-Holocene retreat of the West Antarctic Ice-Sheet system in the Ross Sea: Part 1 – Geophysical results. *Geological Society of America Bulletin*, 111, 1486-1516.

Williams, G., Maksym, T., Wilkinson, J., Kunz, C., Murphy, C., Kimball, P. and Singh, H., 2014. Thick and deformed Antarctic sea ice mapped with autonomous underwater vehicles. *Nature Geoscience*, 8, 61-67.

5. Sediment Coring

Jeff Evans, Evelyn Dowdeswell and Dag Ottesen

5.1 Introduction and background

Sediment cores recovered from the continental shelf of the north-western Weddell Sea provide an important record of Late Quaternary environmental change. The sedimentary record reveals key insights into the glacial processes, history, flow and dynamics of the Antarctic Ice Sheet and associated nature and mechanisms of environmental change during the last glaciation, deglaciation and the Holocene in the Antarctic Peninsula (Evans et al., 2002, 2005; Bentley et al., 2009; Reinardy et al., 2009, 2011; Davies et al., 2012; Ó Cofaigh et al., 2014). Marine sediment core records also constrain the relative stability of fringing ice shelves over multi-millennial timescales corresponding to the present interglacial period or Holocene (e.g. Pudsey and Evans, 2001; Gilbert and Domack, 2003; Domack et al., 2005; Pudsey et al., 2006).

Existing marine sedimentary records reveal a consistent stratigraphic sequence across much of the northern Larsen continental shelf representing the period from the last glacial maximum to the present-day (Evans et al., 2002, 2005; Gilbert et al., 2003; Domack et al., 2005): (i) a lowermost sediment unit comprising an upper soft diamicton and a lower stiff diamicton representing traction tills deposited beneath an expanded ice sheet; (ii) an overlying coarse-grained glacimarine unit deposited in the cavity of an ice shelf proximal to the grounding line; and (iii) an uppermost fine-grained facies deposited distal to the grounding line beneath an ice shelf and in an open marine environment beyond the ice shelf calving margin. The Antarctic Peninsula Ice Sheet (APIS) extended across the continental shelf of the NW Weddell Sea during the last glaciation depositing the traction tills. The soft traction till indicates that this ice sheet was characterised by fast-flowing ice streams that transferred ice from interior drainage basins of the Antarctic Peninsula through Greenpeace and Robertson troughs and Prince Gustav Channel to the shelf edge south of James Ross Island (Fig. 5.1) (Evans et al., 2005), and through Vega Trough north of James Ross Island (Camerlenghi et al., 2001). The subsequent deglaciation of the ice sheet is marked across the region by a transition from grounded ice to ice shelf with deposition of a coarse-grained glacimarine unit proximal to the grounding line. The transition from grounded ice to ice shelf was completed sometime before 11 cal kyr BP on the outer- and mid-continental shelf south of Prince Gustav Channel and by 10.7-10.6 cal kyr BP in the inner Greenpeace Trough in the Larsen A area (Brachfeld et al., 2003; Evans et al., 2005; Heroy and Anderson 2005, 2007; Ó Cofaigh et al., 2014). The recent disintegration of ice shelves is documented in sediment cores as a recent influx of coarse-grained particles related to ice-rafting during ice-shelf collapse preceded by a coarsening upward of grain size that reaches 40% sand at the sea-floor and a doubling to quadrupling in the rates of accumulation of sediment related to the release of fine sorted sediment in periodic draining of small lakes and crevasses on the ice shelf before their collapse (Gilbert and Domack 2003).

Sediment cores have revealed that ice shelves established in the Larsen A and Larsen B regions and in Prince Gustav Channel responded differently to Holocene natural climate variability (Pudsey and Evans, 2001; Domack et al., 2005; Pudsey et al., 2006; Balco et al., 2013). Prince Gustav Ice Shelf, located between James Ross Island and the Antarctic Peninsula, has not only disappeared since the 1980s but was also absent between 2 kyr and 6 kyr coinciding with the mid-Holocene Hypsithermal. This indicates that Prince Gustav Ice Shelf has undergone cycles of formation, stabilisation and break-up related to natural climate variability (Pudsey and Evans, 2001; Pudsey et al., 2006; Sterken et al., 2012). The Larsen A Ice Shelf is also thought to have been largely absent during part of the Holocene in addition to its break-up in the 1990s (Domack et al., 2005). In contrast, the Larsen B Ice Shelf was present throughout the Holocene and its collapse in 2002 was unprecedented during the current interglacial period (Domack et al., 2005). The diversity of ice shelf history over recent decades and during the Holocene implies that recent environmental change has resulted in more spatially extensive ice shelf collapse and has reached higher latitudes than was the case during the Holocene.

The glacial and ice-shelf history and glacial sedimentary processes of the western Weddell Sea are unconstrained and unstudied compared to the NW Weddell Sea. The extent, timing, dynamics and history of the Antarctic Peninsula Ice Sheet along a large extent of the central eastern Antarctic Peninsula during the last glaciation, deglaciation and Holocene is unknown. Reconstructing the glacial history in this region is required in order to provide the regional geological constraints for models of the last glacial Antarctic Ice Sheet that are used to investigate ice sheet dynamics and how ice sheets respond to warming. Similarly, the history of the Larsen C Ice Shelf and corresponding climatic and oceanic environmental change during the Holocene has not been investigated, thus limiting our ability to assess the temporal stability of the largest ice shelf in the Antarctic Peninsula, and fourth largest in Antarctica, and the associated environmental drivers forcing any change during the past 11,000 years. Establishing records of environmental change (e.g. climate and ocean) from sediment-core proxies alongside records of ice shelf stability will enable identification of the drivers of any ice shelf change that might have taken place and will provide a useful long-term context for the drivers of contemporary ice shelf collapse. Constraining the relative stability of this ice shelf during the Holocene will also help determine whether ice shelf disappearance in the NW Weddell Sea over recent decades is unprecedented in terms of its spatial and latitudinal extent. Marine sediment cores recovered during the Weddell Sea Expedition will be used to address the uncertainties highlighted above and coring activities will be concentrated in the only accessible region of the inner Jason Trough and shallower banks of the inner continental shelf adjacent to the northern Larsen C Ice Shelf.

5.2 Methods

The sediment coring operations in the Weddell Sea began on 1 January 2019 with a series of three test cores in Penguin Bukta, western Fimbul Ice Shelf, while awaiting the arrival of the remaining scientific and AUV/ROV team (Fig. 2.1). The remaining 19 core sites were concentrated primarily in the northern Larsen C area (Fig. 5.1a). The majority of sites were located along the present Larsen C Ice Shelf margin and in the Jason Trough. Exact core site locations

between the ice shelf and tabular iceberg A68 was dependent upon sea-ice conditions and the safety of the ship. In addition, one core was collected on the outer shelf during transit to the Larsen C and another was taken from the Robertson Trough, near Cape Framnes (Fig. 5.1b).

.

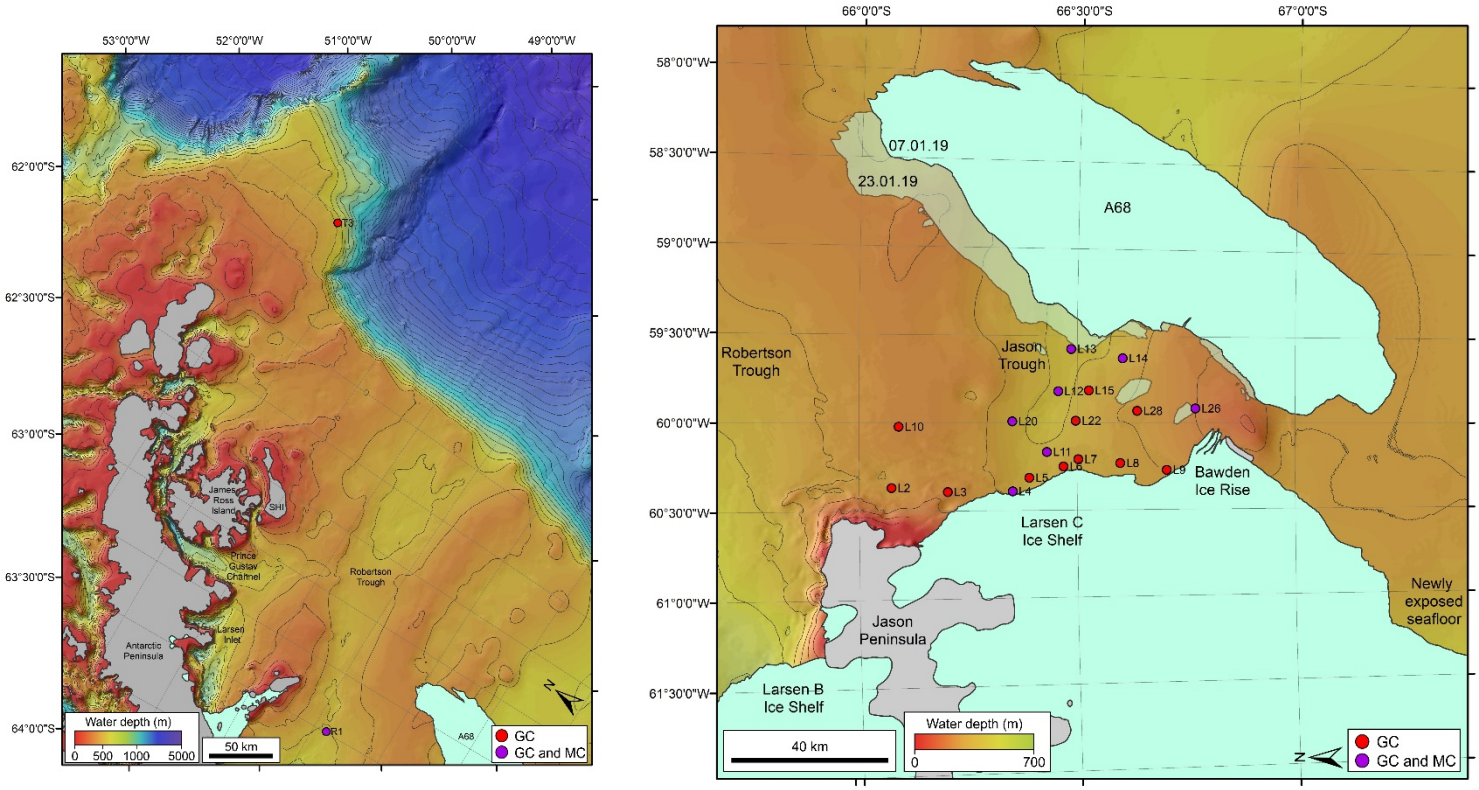

Figure 5.1. *Locations of the gravity core and multi-core site: A. northern Larsen C area; B. outer shelf and Robertson Trough. See Table 5.1 for core numbers and ship stations.*

Gravity cores were taken using a NIOZ gravity corer with either a 3 m or 6 m barrel depending upon the expected substrate, which was estimated from IBSCO bathymetric data (Arendt, 2013; Fig. 5.2). The intention was to evaluate core sites using sub-bottom profile data from the onboard TOPAS system, but equipment failure prevented this. The core liner diameter was 100 mm internally and 110 mm externally.

Multi-cores were also collected at the nine sites with mud-rich substrates as shown by the recovered gravity core. The multi-corer (Craib-type) held 12 tubes: 8 smaller tubes (6.7 diameter, 61.5 cm long) and 4 larger tubes (10 cm diameter, 60 cm long) (Fig. 5.3). The multi-core samples were distributed between the biologists and geologists on board, with two of the large core barrels being collected for sediment analysis from the majority of the sites where multi-cores were taken wherever possible.

The gravity cores and multi-cores were deployed by manually connecting a cable to the corers. This was then lifted over the back of the of the SA *Agulhas II* by a winch system (Figs. 5.2, 5.3). This system proved satisfactory in most cases. The cable twisted around the core barrel at one site requiring lowering the core barrel to the seafloor and raising it again, possibly affecting recovery. In addition, there were occasions where the entire core barrel went into the substrate as shown by a muddy core barrel and weight, and yet this was not reflected by the recovery. These occurrences are considered part of the normal difficulties in retrieving core material via gravity cores in an area with relatively hard substrate, such as subglacial till. Similarly, the multi-corer failed to retrieve core material in areas with surface stones, such as ice-rafted detritus.

Figure 5.2. *The gravity core is seen here with a 6 m core barrel being winched over the back of the SA Agulhas II.*

***Figure 5.3**. The multi-corer being deployed by winch over the stern of the SA Agulhas II.*

***Figure 5.4**. Cores were cut into 1 m lengths, labelled and placed in cold storage on board. Splitting and analysis will take place at BOSCORF, UK.*

5.3 Results

The sediment core collection sites, water depth and core recovery data are given in Tables 1 and 2 for the gravity cores and the multi-cores, respectively. In addition to the gravity core recovery lengths given in Table 1, the majority of sediment cores also had core catcher and core cutter sample bags (boxed in Figure 5.4). Although the cores were not split and analysed at the time of collection, some general characteristics could be ascertained from the core tops and core cutter/catcher samples:

- The majority of sediment cores terminated in over-consolidated diamicton which was the limiting factor in core length as it was too hard to penetrate. The sediment in the core cutter often consisted of a very hard, dry, dark grey mud with varying amounts of sand, gravel and pebbles. In one case, the entire core cutter was enclosed by a large stone.
- The sediment at the top of the cores often consisted of an olive-brown mud layer, with some sand, gravel and pebbles of varying sizes, although the pebbles appeared to be fewer in number and smaller in size than those in the basal unit. In some cases, this upper brown layer was thin, being only a few centimetres thick.
- One core contained a grain-supported gravel layer at the base. This may be the result of winnowing by currents.

However, these generalities need to be substantiated during core analysis.

Table 5.1. *Gravity Core locations and basic information.*

Core ID	Map Site	*SA Agulhas II* Station	Date	General Location	Latitude (S)	Longitude (W)	Water depth (m)	Recovery (cm)
GC001	-	-	01/01/2019	Penguin Bukta	-70° 09.860'	-02° 08.422'	147	0
GC002	-	-	02/01/2019	Penguin Bukta (	-70° 09.860'	-02° 08.422'	147	0
GC003	-	-	03/01/2019	Penguin Bukta	-70° 14.734	-02°41.464	295	0
GC004	3	AM000974	09/01/2019	Outer shelf, taken during transit	-63° 44.305	-53° 06.657'	526	22
GC005	3	AM000975	10/01/2019	Northern Larsen C	-66° 12.234'	-60° 23.568'	334	2 spl bags
GC006	4	AM000976	11/01/2019	Northern Larsen C	-66° 21.148'	-60° 23.453	445	183.5
GC009	14	AM000978	12/01/2019	Northern Larsen C	-66° 36.297'	-59° 37.636'	446	339
GC011	13	AM000979	13/01/2019	Northern Larsen C	-66° 29.193'	-59° 34.561'	513	327
GC013	15	AM000980	13/01/2019	Northern Larsen C	-66° 31.644'	-59° 48.823'	472	293
GC014	22	AM000981	13/01/2019	Northern Larsen C	-66° 29.848'	-59° 59.282'	484	330
GC015	2	AM000982	14/01/2019	Northern Larsen C	-66.04.493'	-60° 22.088'	373	200
GC016	10	AM000983	19/01/2019	Northern Larsen C	-66 05.493'	-60° 01.329'	322	100
GC017	5	AM000984	20/01/2019	Northern Larsen C	-66° 23.458'	-60° 18.858'	472	37
GC018	6	AM000985	20/01/2019	Northern Larsen C	-66° 28.179'	-60° 15.065'	457	115
GC019	6	AM000985	20/01/2019	Northern Larsen C	-66° 28.163'	-60° 15.016'	458	151
GC020	7	AM000986	20/01/2019	Northern Larsen C	-66° 30.493'	-60° 12.873'	449	58
GC021	8	AM000987	21/01/2019	Northern Larsen C	-66° 35.978'	-60° 13.910'	427	135
GC022	28	AUV trial site	21/01/2019	Northern Larsen C	-66° 38.310'	-59° 55.880'	371	234
GC023	26	AM000988	21/01/2019	Northern Larsen C	-66° 46.319'	-59° 55.003'	323	136
GC025	9	AM000989	22/01/2019	Northern Larsen C	-66° 42.372'	-60° 16.362'	377	7
GC026	11	AM000990	22/01/2019	Northern Larsen C	-66° 25.881'	-60° 10.035'	512	380
GC028	12	AM000991	22/01/2019	Northern Larsen C	-66° 27.437'	-59° 49.132'	521	280
GC030	20	AM000992	23/01/2019	Northern Larsen C	-66° 21.129'	-59° 59.493'	479	105
GC032	R1	AM000993	25/01/2019	Nr Cape Framnes	-65° 35.410'	-59° 58.718'	529	57

***Table 5.2**. Multi-core locations and basic information.*

Core ID	Map Site	*SA Agulhas II* Station	Date	General Location	Latitude (S)	Longitude (W)	Water depth (m)	Recovery (cm)
MC007	4	AM000976	11/01/2019	Northern Larsen C	-66° 21.148'	-60° 23.453'	445	0
MC008	5	AM000976	12/01/2019	Northern Larsen C	-66° 21.148'	-60° 23.453'	445	6
MC010A	14	AM000978	12/01/2019	Northern Larsen C	-66° 36.297'	-59° 37.636'	446	47
MC010B	14	AM000978	12/01/2019	Northern Larsen C	-66° 36.297'	-59° 37.636'	446	47
MC012A	13	AM000979	13/01/2019	Northern Larsen C	-66° 29.193'	-59° 34.561'	513	34
MC012B	13	AM000979	13/01/2019	Northern Larsen C	-66° 29.193'	-59° 34.561'	513	34
MC024A	26	AM000988	21/01/2019	Northern Larsen C	66° 46.315'	-59° 55.002'	323	31
MC024A	26	AM000988	21/01/2019	Northern Larsen C	66° 46.315'	-59° 55.002'	323	35
MC027A	11	AM000990	22/01/2019	Northern Larsen C	-66° 25.881'	-60° 10.035'	512	38
MC027B	11	AM000990	22/01/2019	Northern Larsen C	-66° 25.881'	-60° 10.035'	512	37
MC029A	12	AM000991	22/01/2019	Northern Larsen C	-66° 27.454'	-59° 49.392'	521	26
MC029B	12	AM000991	22/01/2019	Northern Larsen C	-66° 27.454'	-59° 49.392'	521	28
MC031A	20	AM000992	23/01/2019	Northern Larsen C	-66° 21.129'	-59° 59.493'	479	28
MC031B	20	AM000994	23/01/2019	Northern Larsen C	-66° 21.129'	-59° 59.493'	479	13.5
MC033A	R1	AM000993	25/01/2019	Nr Cape Framnes	-65° 35.335'	-59° 58.975'	530	30
MC033B	R1	AM000993	25/01/2019	Nr Cape Framnes	-65° 35.335'	-59° 58.975'	530	30

5.6 Further Work

The sediment cores will be split at the BOSCORF in the National Oceanography Centre, Southampton, UK and each core will be logged and sampled. The logging of the cores will describe key sedimentological features. This will be complemented by undertaking x-radiography of the cores and then sedimentological logging of the x-radiographs. The concentration of ice-rafted debris down-core will be established by counting sediment particles >2 mm every 1 cm that are visible on the core x-radiographs. Core sediment samples will be analysed for water content, porosity, grain-size distribution, magnetic susceptibility, lithological/petrographic identification, microfossil identification and abundance, and XRD/XRF geochemistry. Subglacial and proximal sub-ice shelf sediments will be analysed using micromorphology complemented by the measurement of sediment shear strength and AMS-fabric to assess subglacial processes of till genesis, deposition, transport and sediment deformation history.

The biggest challenge will be establishing core and regional chronological control on sediments due to corrosive seawater on the Antarctic Peninsula continental shelf and poor preservation of calcium carbonate shells in sea-floor sediments. Chronology of sediments deposited in the last 200 – 300 years will be constrained by ^{210}Pb-dating and older sediments with radiocarbon ^{14}C dating. Major efforts will be made in identifying and sampling calcium carbonate foraminifera and/or coral shells within the coarse-grained fraction of sediment samples from each core for radiocarbon dating. If carbonate shells are not abundant or absent in cores, then acid-insoluble organic matter from bulk sediment will be used instead for radiocarbon dating. One approach is to subtract the multi-core surface age from downcore ages. In cases where a multi-core was not recovered or dated we will use either a local marine reservoir correction or the surface age from the gravity core to correct the downcore ages. Magnetic susceptibility profiles of each core will also help correlate between dated cores and non-dated cores.

Micropalaeontological analysis of core sediment will also be undertaken to provide additional oceanic environmental information.

The aim is to use the cores and the analyses performed on them to:

(1) reconstruct the extent, history and glacial sedimentary processes of the Antarctic Ice Sheet in the central eastern Antarctic Peninsula since the last glacial maximum using the core sedimentology;
(2) investigate and characterise subglacial processes of till genesis, transport and deposition, and their links to palaeo-ice stream dynamics and flow of the ice sheet in this region using micromorphology, shear strength and AMS-fabric analysis;
(3) establish a chronological framework for core sediments using a variety of dating methods;
(4) reconstruct the history of the Larsen C Ice Shelf during the Holocene by analysing the spatial and temporal patterns of proximal grounding-line sub-ice shelf sediment facies in cores combined with detailed provenance studies of ice-rafted debris and bulk sediments in cores and source geological outcrops in the ice-shelf catchment;
(5) develop a record of Holocene palaeoceanographic and environmental change using geochemical and micropalaeotological analyses of core sediments.

5.5 References

Balco, G. A., Schaefer, J. M., and LARISSA Group., 2013. Terrestrial exposure-age record of Holocene ice sheet and ice-shelf change in the northeast Antarctic Peninsula. *Quaternary Science Reviews*, 59, 101-111.

Bentley, M.J., Hodgson, D.A., Smith, J.A., Ó Cofaigh, C., Domack, E.W., Larter, R.D., Roberts, S.J., Brachfeld, S., Leventer, A., Hjort, C., Hillenbrand, C.-D., Evans, J., 2009. Mechanisms of Holocene palaeoenvironmental change in the Antarctic Peninsula region. *The Holocene*, 19, 51-69.

Brachfeld, S., Domack, E.W., Kissel, C., Laj, C., Leventer, A., Ishman, S. Gilbert, R., Camerlenghi, A., Eglinton, L.B., 2003. Holocene history of the Larsen-A Ice Shelf constrained by geomagnetic paleointensity dating. *Geology*, 31, 749-752.

Camerlenghi, A., Domack, E., Rebesco, M., Gilbert, R., Ishman, S., Leventer, A., Brachfeld, S. and Drake, A., 2001. Glacial morphology and post-glacial contourites in northern Prince Gustav Channel (NW Weddell Sea, Antarctica). *Marine Geophysical Research*, 22, 417-443.

Davies, B.J., Hambrey, M.J., Smellie, J.L., Carrivick, J.L. and Glasser, N.F., 2012. Antarctic Peninsula Ice Sheet evolution during the Cenozoic Era. *Quaternary Science Reviews*, 31, 30-66.

Domack, E., Duran, D., Leventer, A., Ishman, S., Doane, S., McCallum, S., Amblas, D., Ring, J., Gilbert, R., Prentice, M., 2005. Stability of the Larsen B ice shelf on the Antarctic Peninsula during the Holocene epoch. *Nature*, 436, 681-685.

Evans, J. and Pudsey, C.J., 2002. Sedimentation associated with Antarctic Peninsula ice shelves: implications for palaeoenvironmental reconstructions of glacimarine sediments. *Journal of the Geological Society, London,* 159, 233–238.

Evans, J., Pudsey, C.J., Ó Cofaigh, C., Morris, P.W. and Domack, E.W., 2005. Late Quaternary glacial history, dynamics and sedimentation of the eastern margin of the Antarctic Peninsula Ice Sheet. *Quaternary Science Reviews*, 24, 741-774.

Gilbert, R. and Domack, E.W., 2003. Sedimentary record of disintegrating ice shelves in a warming climate, Antarctic Peninsula. *Geochemistry Geophysics Geosystems*, 4, doi:10.1029/2002GC000441.

Gilbert, R., Domack, E.W. and Camerlenghi, A., 2003. Deglacial history of the Greenpeace Trough: ice sheet to ice shelf transition in the northern Weddell Sea. *In* Domack, E., Leventer, A., Burnett, A., Bindschadler, R., Convey, P., Kirby, M. (Eds.), *Antarctic Peninsula Climate Variability: Historical and Palaeoenvironmental Perspectives*, 79. Antarctic Research Series, AGU, Washington, DC, 195–204.

Heroy, D.C., and Anderson, J.B., 2005. Ice-sheet extent of the Antarctic Peninsula region during the Last Glacial Maximum (LGM) – Insights from glacial geomorphology. *Geological Society of America Bulletin*, 117, 1497-1512.

Heroy, D.C. and Anderson, J.B., 2007. Radiocarbon constraints on Antarctic Peninsula Ice Sheet retreat following the Last Glacial Maximum (LGM). *Quaternary Science Reviews*, 26, 3286-3297.

Ó Cofaigh, C., Davies, B., Livingstone, S., Smith, J., Johnson, J., Hocking, E., Hodgson, D., Anderson, J., Bentley, M., Canals, M., Domack, E., Dowdeswell, J.A., Evans, J., Glasser, N., Hillenbrand, C.-D., Larter, R., Roberts, S. and Simms, A., 2014. Reconstruction of ice-sheet changes in the Antarctic Peninsula since the Last Glacial Maximum. *Quaternary Science Reviews*, 100, 87-110.

Pudsey, C.J. and Evans, J., 2001. First survey of Antarctic sub-ice shelf sediments reveals Mid-Holocene ice shelf retreat. *Geology*, 29, 787-790.

Pudsey, C.J., Murray, J.W., Appleby, P., Evans, J., 2006. Ice shelf history from petrographic and foraminiferal evidence, northeast Antarctic Peninsula. *Quaternary Science Reviews*, 25, 2357-2379.

Reinardy, B.T.I., Pudsey, C.J., Hillenbrand, C.-D., Murray, T. and Evans, J., 2009. Contrasting sources for glacial and interglacial shelf sediments used to interpret changing ice flow directions in the Larsen Basin, Northern Antarctic Peninsula. *Marine Geology*, 266, 156-171.

Reinardy, B.T.I., Hiemstra, J., Murray, T., Hillenbrand, C-D. and Larter, R., 2011. Till genesis at the bed of an Antarctic Peninsula palaeo-ice stream as indicated by micromorphological analysis. *Boreas*, 40, 498-517.

Sterken, M., Roberts, S. J., Hodgson, D. A., Vyverman, W., Balbo, A. L., Sabbe, K., Moreton, S.G. and Verleyen, E., 2012. Holocene glacial and climate history of Prince Gustav Channel, northeastern Antarctic Peninsula. *Quaternary Science Reviews*, 31, 93-111.

6. Sea Ice

Wolfgand Rack, Evelyn Dowdeswell and Frazer Christie

6.1 Introduction

The western Weddell Sea is one of the few regions around Antarctica covered by perennial sea ice (Haas et al., 2008). Because of the general sea-ice conditions and the logistical difficulties these present, there have been few local sea-ice measurements in this area of the Southern Ocean (e.g. James, 1924; Gordon, 1993; Hellmer et al., 2008). Due to its age, the pack ice in this area is much thicker than in most other places of Antarctica (Renner and Lytle, 2007). Nevertheless, the deep snow cover frequently observed on sea ice from this region often depresses the ice surface below sea level (Haas et al., 2008).

The sea ice in the western Weddell Sea is frequently a mixture of fragments of deformed first-year and multi-year sea-ice which is consolidated in larger ice floes. Prevalent is also the occurrence of fragments of fast ice and, as our observations show, of bay ice, which has been either advected into this area or has a more local origin. Ice drift varies strongly with tides, ocean currents and wind. For the Weddell Sea, it was shown that the large-scale weather patterns influence significantly the annual and inter-annual drift variability (Heil et al., 2008; Hellmer et al., 2008).

A number of satellite-based products describing sea-ice characteristics, such as ice thickness, exist for this region, but little or no ground truth for the validation of these products has been collected. The verification of the amount of snow overlying the ice is important because the freeboard to thickness conversion, which is the basic principle used to derive ice thickness using remote sensing, is highly sensitive to the amount of surface snow. Ultimately our measurements will lead to a better understanding of the sea-ice mass balance, which is critical to quantifying the magnitude and change of deep-water production and ocean-atmosphere energy flux.

We have collected data enabling us to determine the three-dimensional shape of sea-ice floes in the form of point measurements from on-ice activities, airborne measurements and underwater bottom profiles. In addition, snow thickness data from radar was collected in a pilot study for a number of sea-ice floes during normal ship movement to assess the snow/ice interface on a variety of floe types.

Sea-ice morphology has been characterised using near-synchronous temporal and spatial measurements from (i) AUV with upward-looking multibeam sonars, (ii) drones equipped with cameras and radar sensors / lasers and (iii) manually-derived on-ice surveys and samples such as snow pits, snow-depth transects, drill holes and ice cores. We have also deployed ice-drifter buoys on several ice floes which will be used in conjunction with satellite imagery and altimetry (ICESat-2 and CryoSat-2) to provide floe drift and ice thickness information in the future.

Remote sensing and on-ice methods were used to determine the following geophysical properties of sea-ice:

A. Remote sensing: draft and underside roughness of sea-ice floes (AUV), surface roughness, topography and freeboard (drones and satellites).

B. On-ice validation: snow morphology (density; stratigraphy with ice layers from previous melting events), possibly sedimentary dust layers originating from storm events along the coast, the thickness and freeboard (both consolidated ice and snow) from drill holes, snow thickness profiles (using a GPS equipped Magna Probe), as well as ice-floe drift by leaving GPS buoys on ice.

6.2 AUV operations under sea ice

Three upward-looking AUV9 missions were carried out on 14, 24 and 26 January 2019 to examine ice thicknesses underneath three pre-selected ice floes (see Table 4.4 for specifications of instruments on AUV9; Figure 4.1 for locations). Following Sections 3 and 4 of this report, these floes were chosen for AUV operations to coincide with near-contemporaneous on-floe and unmanned aerial vehicle (UAV) measurements, and to comply with pre-defined AUV operating limitations. The AUV used for these measurements was configured with an upward-looking Kongsberg 200/400 kHz multibeam system (Table 4.4).

A brief summary of each mission and preliminary findings with respect to sea-ice thickness are presented in the following sections. Reference is made throughout to Table 6.1, which presents simple descriptive statistics associated with each mission (see also Table 4.5).

Table 6.1. *Details of upward-looking dives performed by AUV9.*

Dive	Floe Name	Area (km^2)	Mission Date	Starting location (WGS 84)	Approximate area surveyed (km^2)
1	"FloeTilla"	24.1	14.01.2019	-60.43, -66.04	0.62
2	"FloeExpectations"	1.3	24.01.2019	-60.52, -66.04	0.56
3	"FloeRida"	5.0	26.01.2019	-57.18, -64.70	1.07

6.2.1 Dive 1: Upward-looking survey at Floe #1: "FloeTilla"

Technical difficulties during this mission – a trial dive to test the upward-looking capabilities of AUV 9 in sea-ice conditions – resulted in a loss of originally planned spatial coverage underneath this ice floe, with a net result of ~0.62 km^2 surveyed by the AUV (Table 6.1). Nonetheless, the area surveyed by this mission partially overlapped near-contemporaneous

over-snow UAV operations, from which a high-resolution orthophoto and digital elevation model (DEM) were produced (Section 6.5).

A preliminary grid of AUV-derived ice thickness, together with the spatial distribution of the UAV-derived orthophoto, is presented in Figure 6.1. To generate this figure, each grid was orientated onto a common reference plane, corresponding to last known absolute position of the floe constrained from the closest TerraSAR-X image acquisition in time. Where possible, this allowed for the direct comparison/overlay of overlapping UAV and AUV data in geographical space, irrespective of ice floe displacement. A similar correction was applied to generate Figures 6.2 and 6.3.

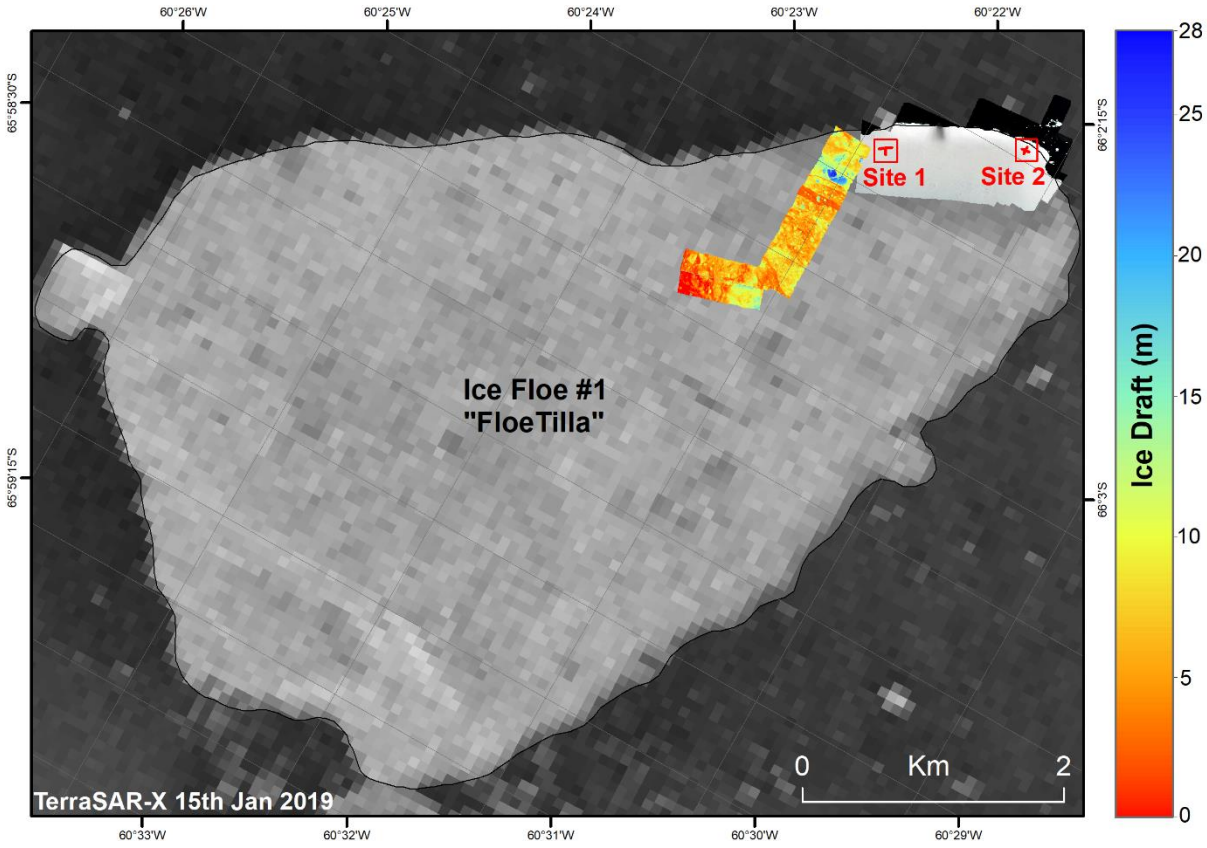

Figure 6.1. *Floe #1 AUV-derived ice draft (1 m posting) with respect to the WGS84 ellipsoid, superimposed on the location of the floe on 15 January 2019 as observed by TerraSAR-X. UAV-derived orthophoto (~0.1 x 0.3 m posting) and on-floe measurement (Sites 1 and 2) locations (cf. Section 6.3) are also shown. Note that all sites and grids have been orientated onto a common reference plane (TerraSAR- X image coordinates) to correct for the effects of ice-floe drift between AUV/UAV/on-floe science missions.*

6.2.2 Dive 2: Upward-looking survey at Floe #2: "FloeExpectations"

Dive 2 was a successful mission to survey the ~1.5 km^2 ice floe "FloeExpectations" proximal to the Jason Peninsula on 24 January 2019 (cf. Table 6.1; Figure 4.1). Correcting for ice-floe drift, an area totalling ~0.56 km^2 was surveyed (Table 6.1) underneath an area of relatively rough surface topography. In addition, a thin (<1.5 m) layer of sea ice and several adjacent floes seaward of Floe #2 were also imaged. The spatial extent of this mission relative to the positioning of on-floe fieldwork is presented in Figure 6.2.

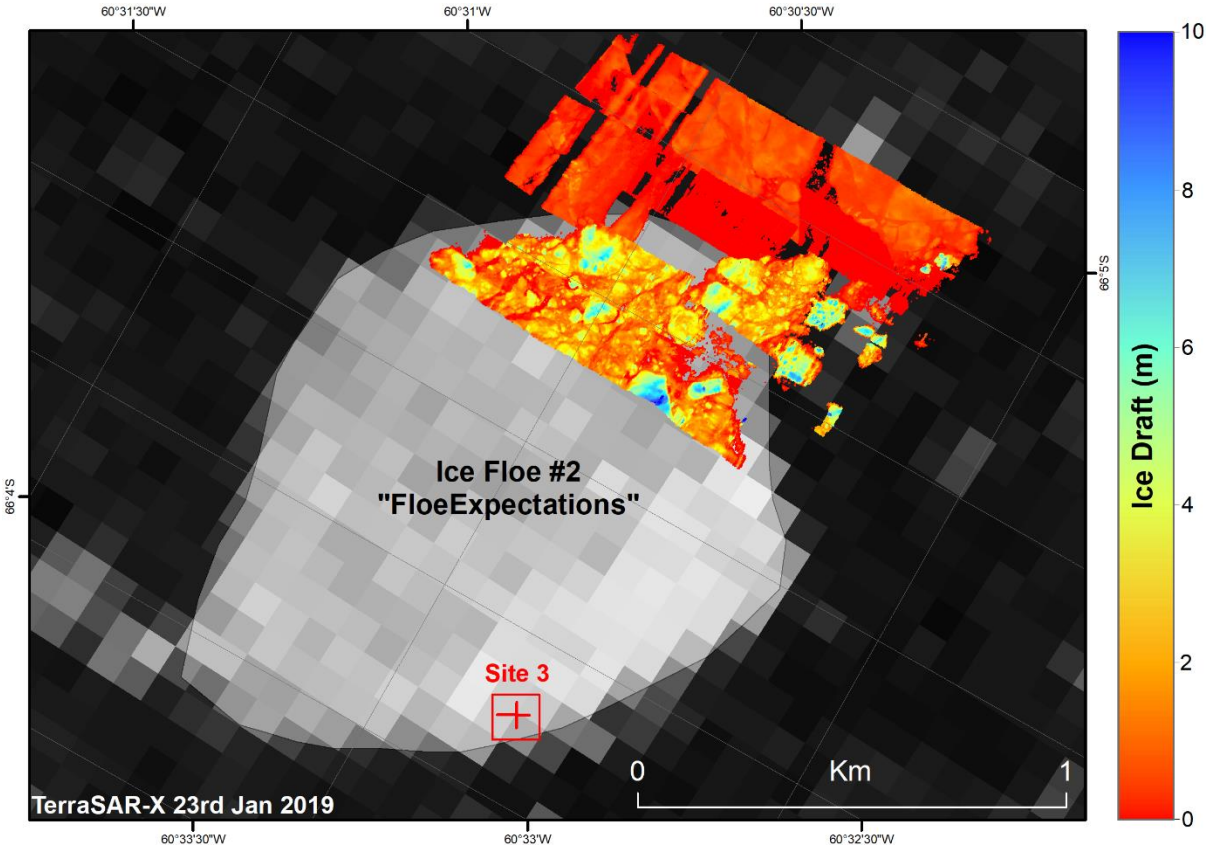

Figure 6.2 *Floe #2 AUV-derived ice draft (1 m posting) with respect to the WGS84 ellipsoid, superimposed on the location of the floe on 23 January 2019 as observed by TerraSAR-X. The on-floe measurement location "Site 3" (cf. Section 6.3) is also shown. Note: AUV and on-floe site locations have been orientated onto a common reference plane (TerraSAR-X image coordinates).*

6.2.3 Dive 3: Upward-looking survey at Floe #3: "FloeRida"

Dive 3 was a successful mission to survey the ~5.0 km^2 ice floe "FloeRida" in the vicinity of Snow Hill Island on 26 January 2019 (cf. Table 6.1; Figure 4.1). Compensation for ice-floe drift prior to the dive meant that minimal post-processing of the data was needed to realign the AUV survey line in time and space, and the dataset was delivered in a pre-mosaicked format.

In total, approximately ~1.07 km^2 of the ice floe was surveyed, over a relatively smooth snow surface in comparison to Floes #1 and 2. The spatial extent of this mission relative to the positioning of on-floe fieldwork is presented in Figure 6.3.

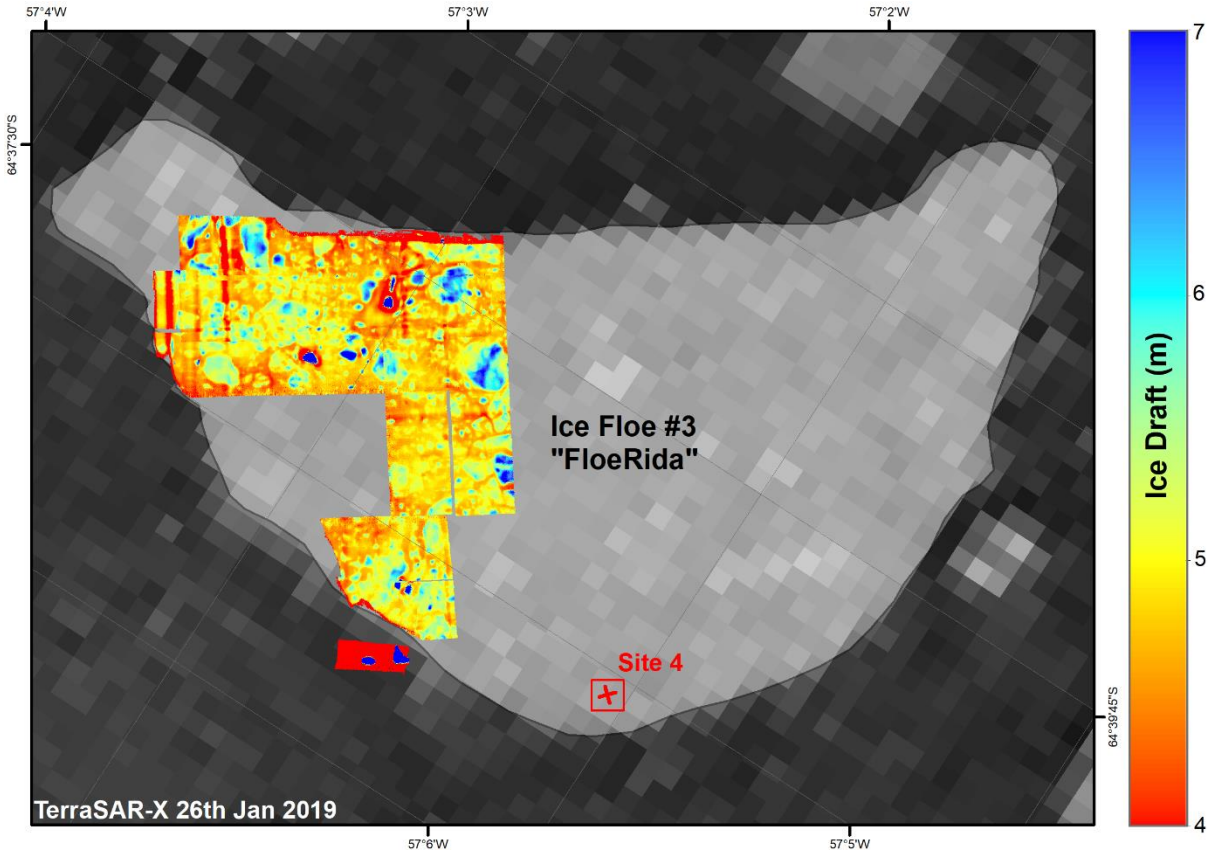

Figure 6.3. *Floe #3 AUV-derived ice draft (1 m posting) with respect to the WGS84 ellipsoid, superimposed on the location of the floe on 26 January 2019 as observed by TerraSAR-X. The on-floe measurement location "Site 4" (cf. Section 6.3) is also shown. Note: AUV and on-floe site locations have been orientated onto a common reference plane (TerraSAR-X image coordinates).*

6.3 Sea-Ice sampling stations and snow profiles

Four sea-ice floe stations were chosen for on-site sea-ice measurements (Fig. 6.4) on the three ice floes shown in Figures 6.1 to 6.3. The floes were selected on the basis of stability and accessibility. The sea ice had to be thick enough to ensure the safety of the personnel working on the floe. In addition, relatively large areas of open water were required to (i) allow AUV deployment and data acquisition (approximately 2 km), and (ii) to enable the ship to remain in contact with or close to the floe.

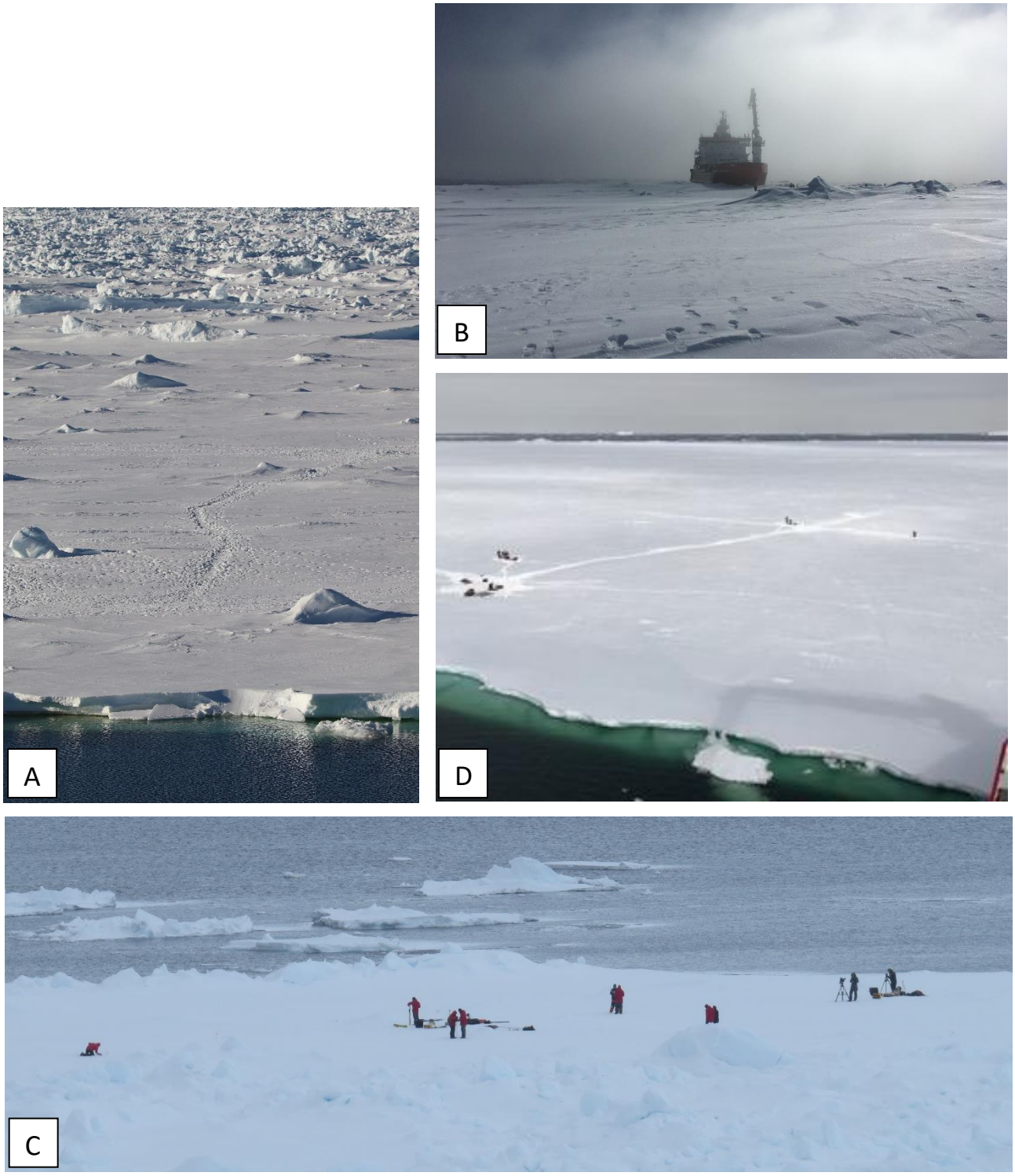

***Figure 6.4**. Four on-ice stations were sampled from three sea-ice floes. A. and B from "FloeTilla" on 16 and 17 January, respectively; C. "FloeExpectations", 24 January; D. "FloeRida", 26 January.*

6.3.1 Methods

Personnel were transported on and off the *S.A. Agulhas II* by rope basket (Figure 6.5b). A maximum of 3 hours was allocated for fieldwork per ice-floe site.

The field procedure on each of the on-ice stations was to mark two perpendicular transects for the snow thickness data (transect visible in Fig. 6.4d), drone radar/photogrammetry lines and sea-ice coring, with one or more centrally located snow pit(s) for snow stratigraphy and density measurements. Equipment used included a Temposonics G-Series Magna Probe (Probe 754; Fig. 6.5c) for snow thickness, a Kovacs hand drill with four one-metre lengths of stainless steel drilling flights, and three drones equipped with optical cameras and a snow radar system (Section 6.4).

Sea-ice floe locations and the types of field measurements carried out on each floe are listed in Table 6.2.

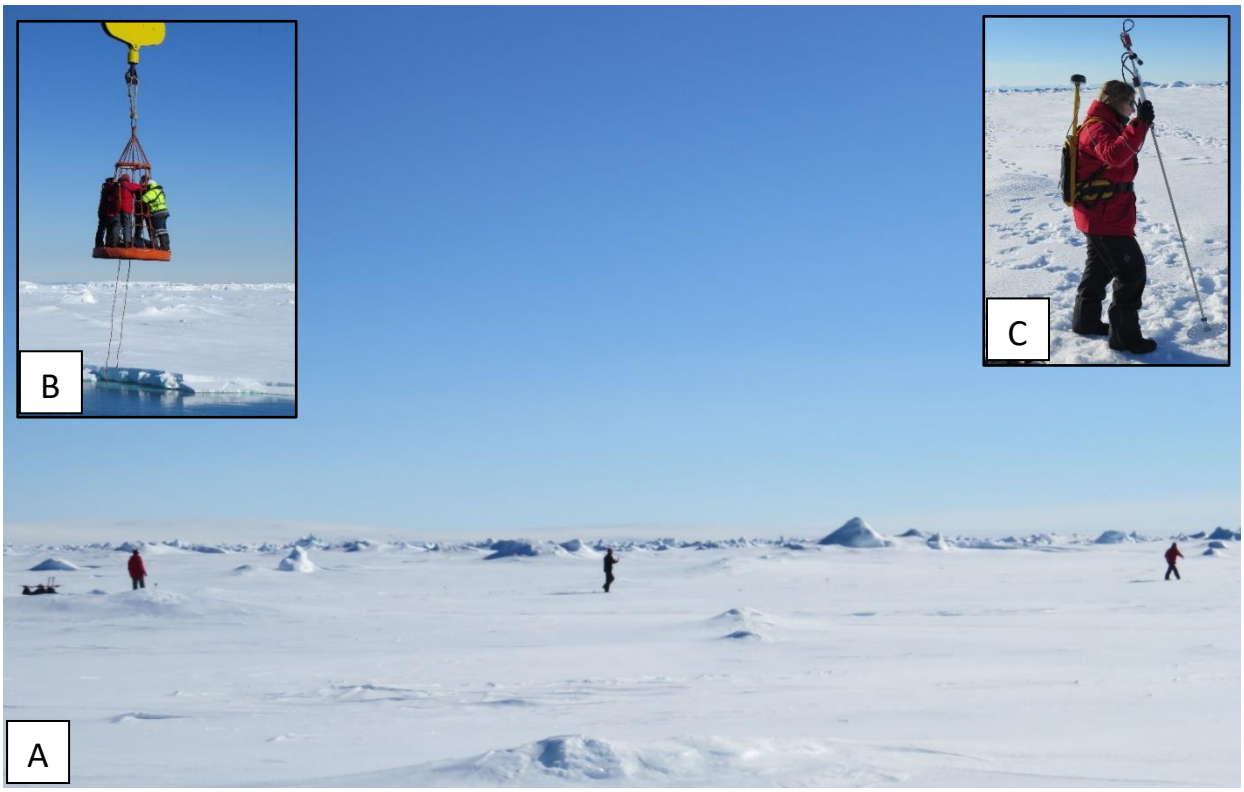

Figure 6.5. *Personnel and equipment were transferred from the S.A. Agulhas II to the ice-floe (A) via rope baskets (B) where field measurements were then carried out (C).*

6.3.2 Results

Surface characteristics

The three sea-ice floes used for the four stations had different surface characteristics. Floe 1 ("FloeTilla"), which was sampled at two separate locations on 16 and 17 January, was a composite floe consisting of a relatively smooth section of multi-year ice with only a few pressure ridges and a rough section of multi-year ice with enclosed fragments of iceberg growlers (Figs. 6.3a, b). The latter had pressure ridges up to approximately 4 m in height. The composite floe may have formed in part, if not wholly, as shorefast ice in an embayment which would have provided lateral constraints to allow the ice to become thicker than expected for smoother first-year sea ice. Floe 2 ("FloeExpectations") was also largely deformed multi-year ice (Fig. 6.3c), partly flooded, whereas Floe 3 ("FloeRida") had a smooth surface giving the appearance of first-year ice (Fig. 6.3d). However, measured ice thicknesses of more than 2.5 m, coupled with an overlying snow thickness similar to other multi-year floes measured in this study, indicate that this floe was also composed of multi-year ice.

Table 6.2. *Sea-Ice Floe Stations*

Station	Date	General Location	Ship's approximate position at start of transect	Operations	Notes
SI01 "FloeTilla"	16/01/ 2019	Northern Larsen C	60° 23.412'W 66° 1.57'S	Magna probe (EKD, JAD), snow pit stratigraphy (WR, SM), drones (PB, CH)	Sunny day; a number of snow depth measurements exceeded magna probe length (>120 cm)
SI02 "FloeTilla"	17/01/ 2019	Northern Larsen C	60° 31.425'W 65° 46.282'S	Magna probe (EKD, SM), snow pit stratigraphy (WR, CLB), drones (PB, CH)	Blizzard was coming in and therefore limited transect to 60 m.
SI03 "Floe-Expectations"	24/01/ 2019	Cape Framnes (Jason Peninsula)	60° 36.514'W 66° 4.948'S	Manual snow thickness transect (SM, EKD); snow pit and four drill holes (WR, FC); drones had technical difficulty (PB, CH).	Cloudy day and snow fall; ship had to move due to encroaching ice. Lots of refrozen surface meltwater on floe.
SI04 "FloeRida"	26/01/ 2019	Snow Hill	57° 7.579'W 64° 38.575'S	Magna probe (EKD); snow pit (WR, FC), snow cores (WR, SM), drones (PB, CH)	Refreezing in drill hole – lost 2 m of drill flights. Ship moved position due to sea-ice.

Snow Thickness

Examples of modal snow thicknesses in the western Weddell Sea have previously been reported to be about 0.2-0.5 m for first-year ice and 0.75 m for second-year ice (Haas et al., 2007). We found snow thickness above the ice layer to be consistently on the upper bound of reported values for all of the sea-ice floes measured. It is important to note that thicknesses measured by the Magna Probe necessarily include the slush layer, which was 25 cm on floe 1 and similar in other locations. This added a complication primarily on Floe 1 in that the magna probe measuring limit of 120 cm was often exceeded. This is an indication that the age of this floe is much older than second-year ice and possibly formed as shorefast ice in an embayment over a long period of time. An additional consideration in the snow thickness data presented below is the presence of ice layers in the snow stratigraphy. Where these were impenetrable with the magna probe, additional neighbouring points were added to the profile.

The distribution of snow thickness measurements taken on 16 January on floe site 1 is shown in Figure 6.6a and b. Note that, due to the high values for snow thickness, many of the points along both profiles record as 120 cm, although they are likely to be higher. Internal layers were hard enough to prevent penetration in at least two instances where values of 11.82 cm and 45.81 cm were recorded. Sea-ice floe site 2 was located on a different part of the ice floe from site 1 (Fig. 6.1) and shows similarly high values of snow thickness (Fig. 6.7a and b).

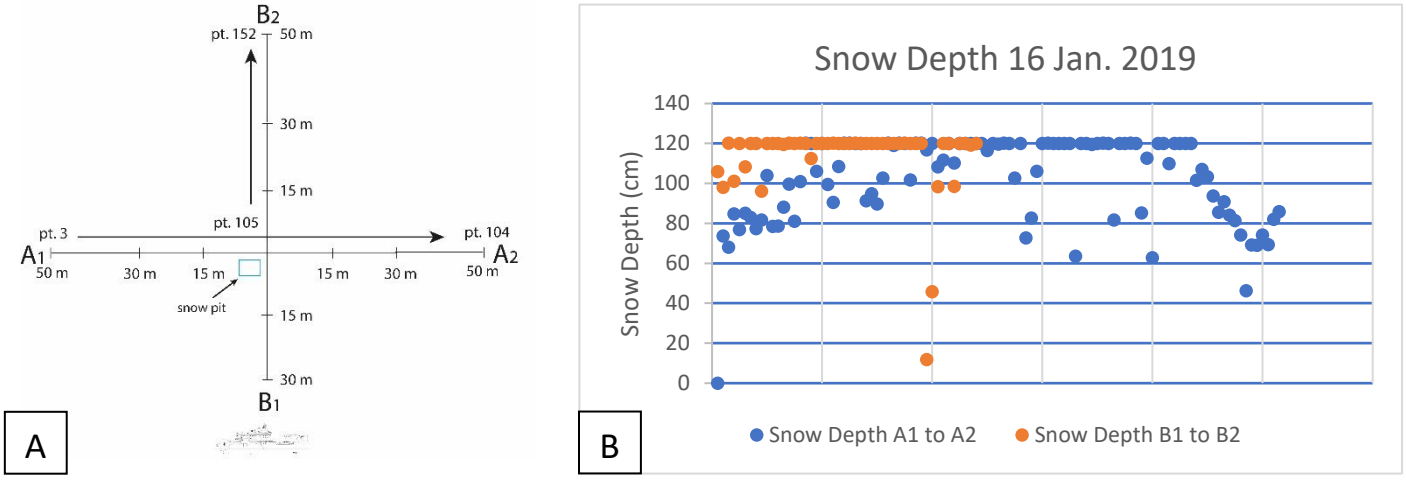

***Figure 6.6**. 16 January, site 1: 100 m transect from A1 to A2, east to west, followed by a 50 m transect from B1 to B2, north to south (ship facing south towards B2). The coordinates of the snow pit are: 65.787°S and 60.549°W.*

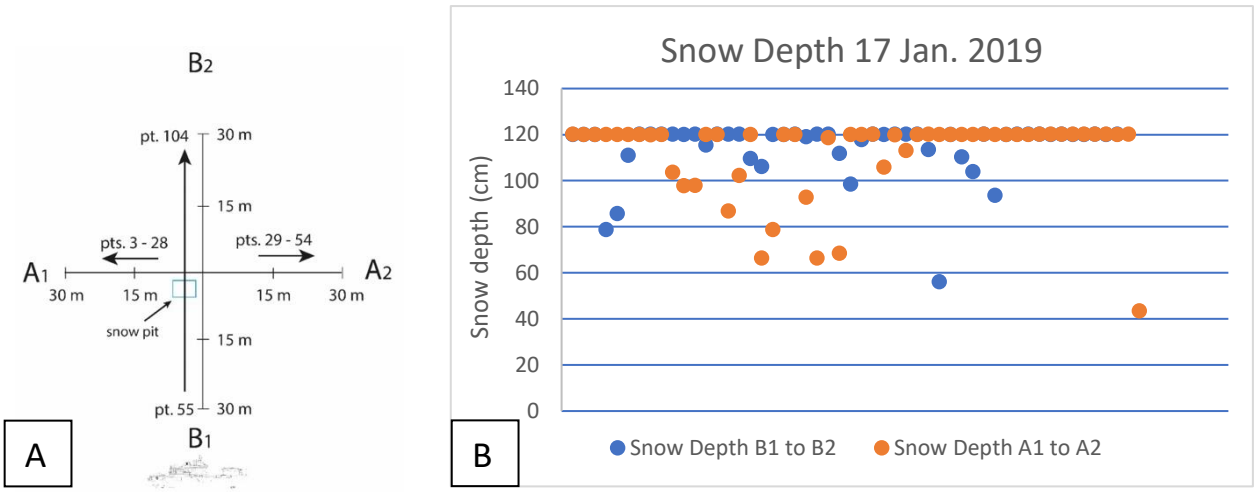

***Figure 6.7**. 17 January. Due to weather closing in, only 30 m transects were carried out. The B1 to B2 transect trends north to south (ship is facing south towards B2). The coordinates of the snow pit are: 65.774°S and 60.523°W.*

Floe 3, sampled on 24 January, was chosen not only for its stability, but also because it was expected to provide an example of first-year sea ice. Its surface expression was relatively smooth, although there were sastrugi and a few pressure ridges present (Figure 6.4c). Snow thickness measurements show an average snow thickness of 66 cm+/- 24 cm (Figure 6.8), considerably lower than the averages for sites 1 and 2 (107+/-20 and 113+/-15, respectively), and almost in agreement with second-year ice found by Haas et al. (2007). Furthermore, sea-ice thickness measurements of between 2.29 and 2.75 m strongly suggest that this floe is composed of multi-year sea ice (Table 6.2).

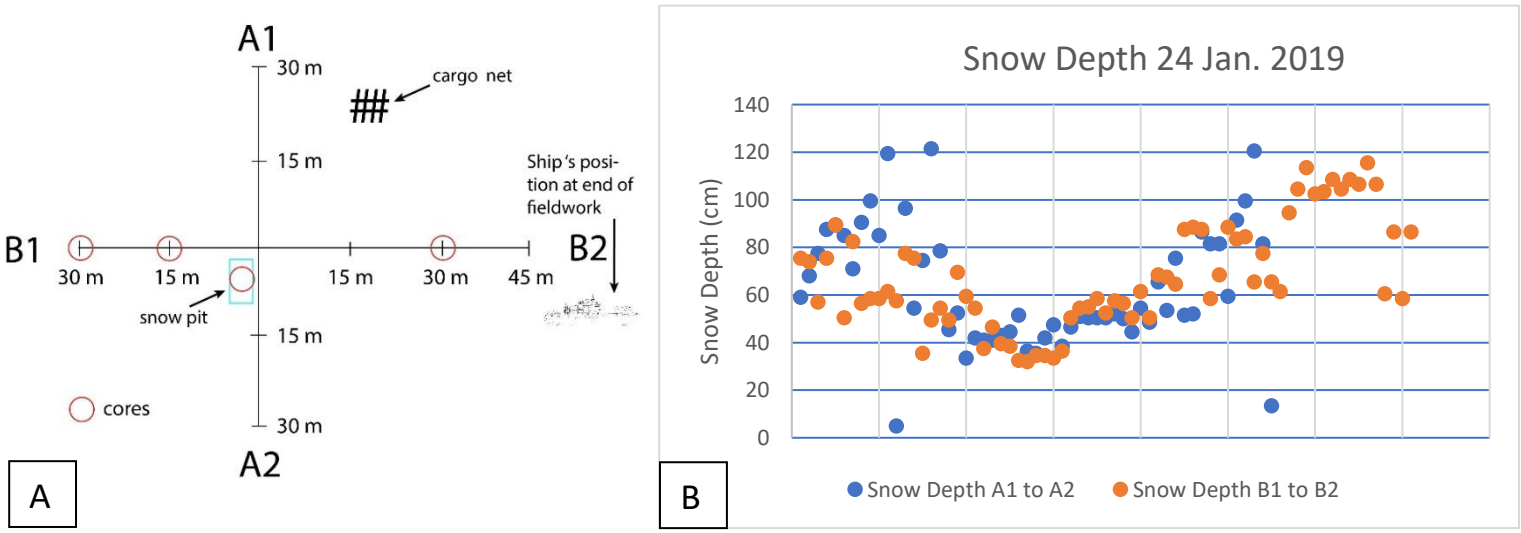

Figure 6.8. *24 January snow-depth measurement transects. The ship relocated during this survey due to sea-ice encroachment. The transects were carried out after the ship moved in a counter-clockwise direction and the ice floe rotated clockwise, hence the location of the ship's position at the end of the field session is shown in A. The positions of the 4 drill holes are shown. The coordinates of the snow pit are: 66.089°S and 60.617°W.*

The sea-ice floe sampled on 26 January, site 4, has similar average snow thickness values to site 3 (67+/-15; Fig. 6.9). However, the thickness of the snow cover is much more consistent, with most values between approximately 60 cm and 80 cm (Fig. 6.9b). A lower layer of snow thickness values corresponds to a hard layer ('pencil'; see below) between approximately 24 cm and 43 cm, which the magna probe was not able to penetrate.

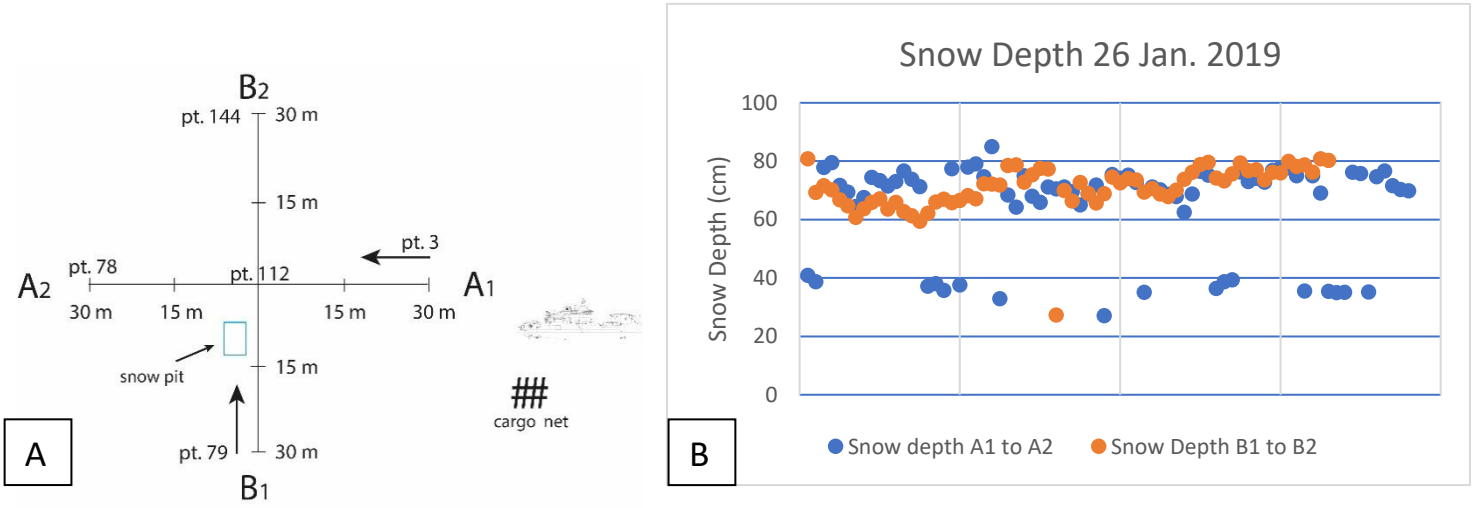

Figure 6.9. 26 January. *Four 30 m transects were measured at Site4 near Snow Hill. Points 3 to 78 represent transect A1 to A2; Points 79 to 144 = transect B1 to B2. Point 112 is the centre mark on Transect B. The ship is facing southeast. Points 1 and 2 are omitted as these were made for calibration purposes only. Coordinates of snow pit are: 64.658°S 57.15°W.*

Snow pit studies and drill hole measurements

A snow pit study was used on every measurement site to retrieve snow density with depth and basic information on snow stratigraphy by visual observation. The average snow density of between 387 and 463 kg/m^3 was variable, but within the expected range for this time of the year. The snow pit was also used as a comparison to drone and Magna Probe measurements in order to identify ice layers which otherwise could have been mistaken as compact ice below snow. The mean values of snow and ice measurements are given in Table 6.3.

Table 6.3. *Main characteristics of snow and ice at the measurement sites*

Site	Mean density [kg m^{-3}]	Snow depth [m]	Ice thickness / Freeboard [m]	Comment
FloeTilla 1	456	0.84# (0.25)	n.a.	too thick to drill
FloeTilla 2	463	0.61	n.a.	too thick to drill
Floe-Expectation	387	0.61	2.63 / 0.02*	*: mean out of 4 measurements; two holes were flooding
FloeRida	424	0.52# (0.22)	n.a.	drill lost in hole by freezing
Penguin Bukta	439	0.60	1.60 / 0.07	5.6 m of sub-ice platelet layer

snow depth above a slush layer (thickness of slush layer given in brackets)

6.4 AWI ice drifter buoys

A total of five ice drifter buoys were provided by the Alfred Wegener Institute (AWI Bremerhaven, Germany) for this expedition. Every buoy is equipped with a GPS sensor which transmits its position via satellite to Germany in hourly intervals after its deployment and while on the ice. The first three buoys were deployed on the 16, 24, and 26 January near the locations of the field surveys on the ice floes (Figs. 6.4a, c, d and 6.10, a-c). The general sea-ice characteristics (thickness, snow, freeboard), as well as ice floe and environmental conditions, were reported back to AWI in a buoy deployment report form. The two remaining ice buoys were deployed at or close to the *Endurance* sinking location. Drift data are made available by AWI via a sea-ice portal.

Figure 6.10*. Ice drift buoys as deployed on ice floes 'FloeTilla' (left; 16 January 2019), 'FloeExpectations' (middle; 24 January 2019), and 'FloeRida' (right; 26 January 2019).*

The drift tracks of all five buoys and their current locations for 6 March (0700 UTC) are shown in Figure 6.11. The ice floes measured on 16 and 24 January (buoy nr. 10 and 16) are now located in the former Larsen-B area, whereas the ice floe with buoy nr. 14 drifted from east of Snow Hill Island around Ross Island into the northern area of Prince Gustav Channel. The drift tracks of buoy 13 and 15 are very similar and about 150 km to the north corresponding to a drift velocity of about 7km per day during the first 20 days since deployment.

***Table 6.4**. Codes of the five AWI drifter buoys with time (UTC), date, and geographic position of deployment. Buoy AWI-UTA-0015 was deployed after leaving the Endurance search site.*

buoy code	location	date / time	position
AWI-UTA-0010	FloeTilla	2019-01-16 / 21.00	*65.78728 S / 60.5492 W*
AWI-UTA-0016	FloeExpectation	2019-01-24 / 14.00	*66.08952 S / 60.6175 W*
AWI-UTA-0014	FloeRida	2019-01-26 / 15.00	*64.65835 S / 57.1502 W*
AWI-UTA-0013	Endurance search site	2019-02-13 / 17.15	*68.75915 S / 52.3265 W*
AWI-UTA-0015	Endurance search site	2019-02-14 / 11.15	*69.04333 S / 50.1750 W*

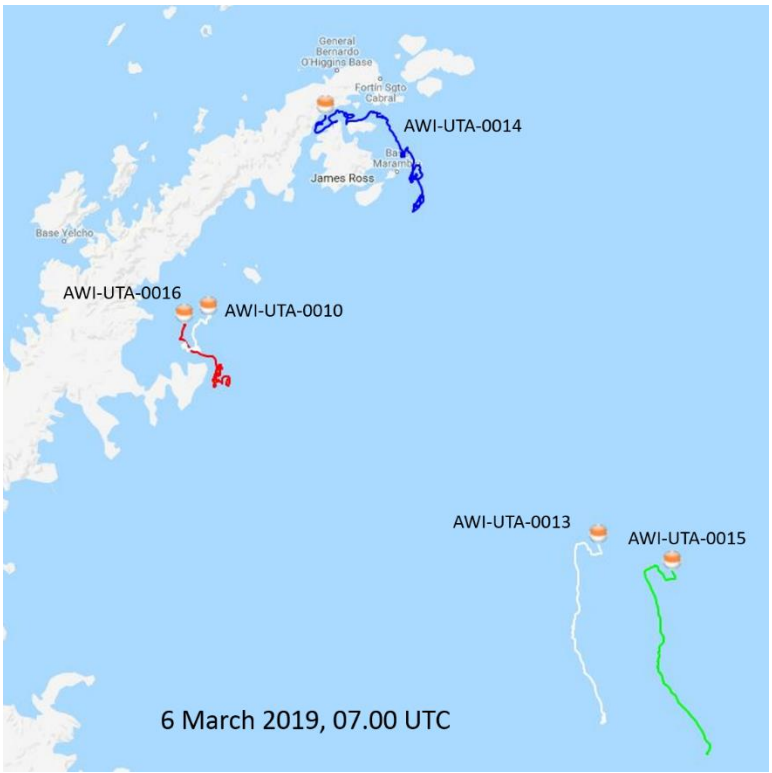

***Figure 6.11**. Location of AWI ice drift buoys and drift tracks since deployment.*

6.5 Drone Work

The goal of the drone project was to obtain representative measurements of (i) snow thickness using a snow radar system and (ii) surface topography using stereo imaging and Structure from Motion (SfM) processing. Preliminary results from both instruments are shown below.

6.5.1 Snow radar

The drone snow radar (1.5 to 4.5 GHz) is a joint development by the University of Canterbury and Lincoln Agritech (both New Zealand) which was successfully tested on sea ice in McMurdo Sound (Ross Sea) in 2017. The snow radar was operated from one of two multirotor drones (octocopter). We used the original snow radar (SR-1) with a ground resolution of 1 m from a 5 m flight level, and a newer lighter version (SR-2; about half the size and weight) with a 2 m radar footprint, also from a 5 m flight level. After initial measurements in Penguin Bukta and FloeTilla it was decided to utilise the newer SR-2, which is easier to fly and operate. The instrument performed according to expectations on shorefast ice in Penguin Bukta (Fig. 6.12).

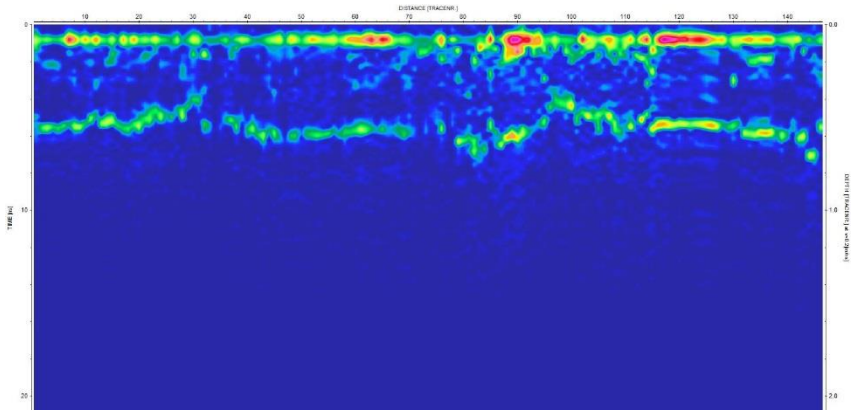

***Figure 6.12**. Radargram showing snow thickness distribution on shorefast ice in Penguin Bukta on 1 January 2019. The length of the profile is about 200 m. The axis on the left shows two-way travel time in ns, the axis on the right is snow thickness assuming a radar wave speed of 0.2 m /ns.*

The snow cover on the other measurement sites was more heterogeneous compared to the first measurement area in Penguin Bukta. The radargrams based on preliminary processing for these sites show reflections of internal layers, and a mostly weak but significant reflection of either the snow/ice or (in most cases) snow/slush interface. Although reflections of the lower boundaries are not particularly strong, they have been validated with the in-situ measurements in the snow pits and by the Magna Probe snow thickness data. In one extreme case (Fig. 6.13b), a very thick ice layer at about 20 cm depth scattered almost all of the transmitted radar energy and prevented penetration of the weakened radar signal to the snow/ice or snow/slush interface.

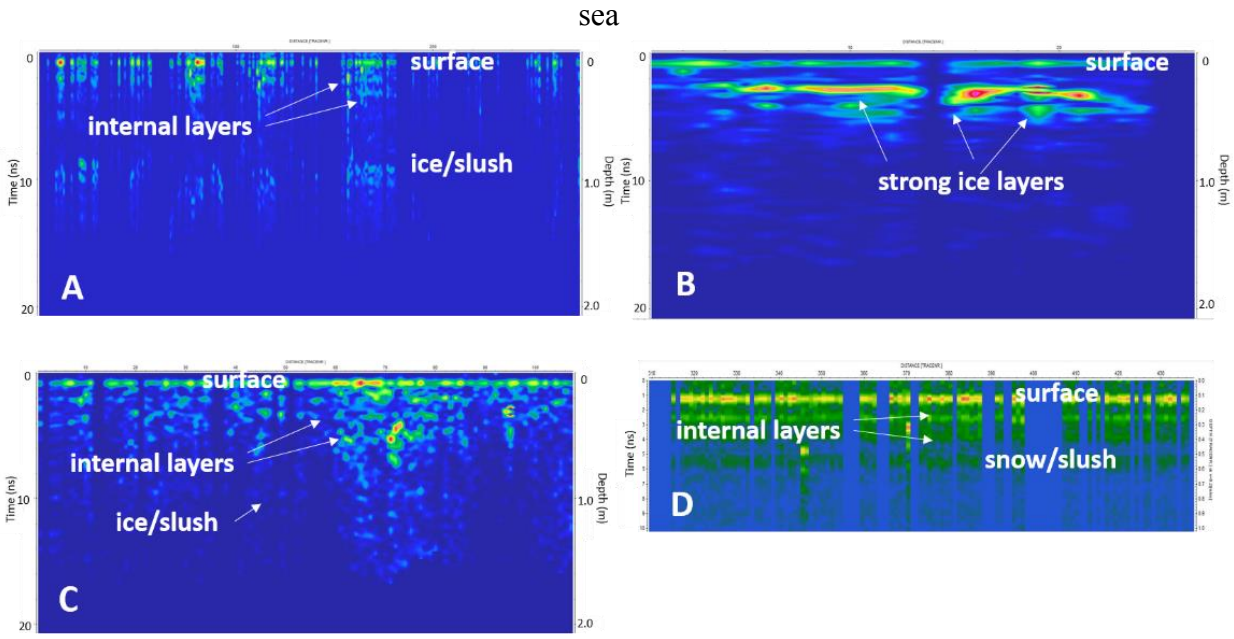

***Figure 6.13**. Examples of radargrams for sites FloeTilla 1 (A), FloeTilla 2 (B), FloeExpectations (C), and FloeRida (D).*

6.5.2 Optical imagery

A drone equipped with optical cameras was used to capture high resolution images and surface topography of the ice floes. The quality of the post-processing depends critically on the overlap between images. The drift and rotation of ice floes during the set-up of the survey and the measurement itself can aggravate the processing. Examples for image products are shown in Figure 6.14 which were acquired on the ice floe FloeTilla on 15 January 2019 (Fig. 6.10).

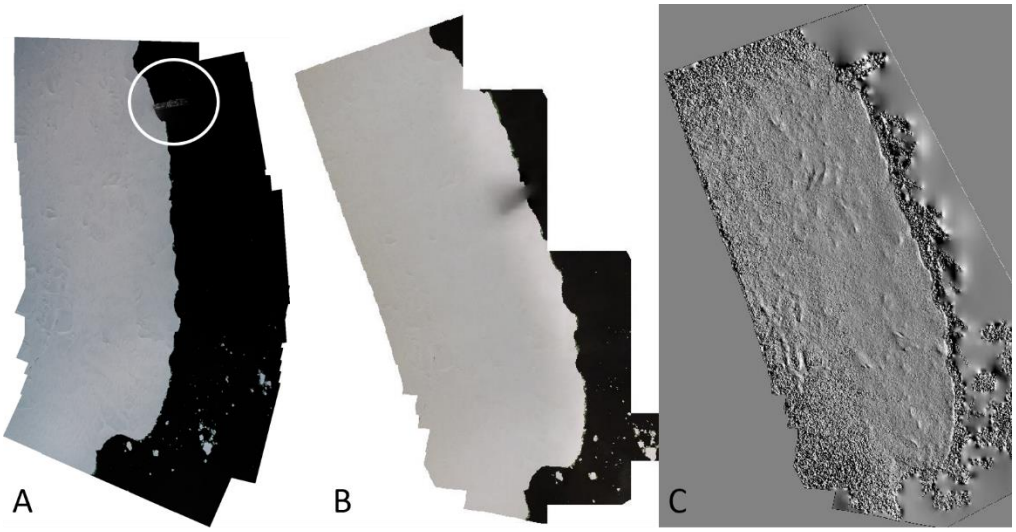

***Figure 6.14.** Image products for ice floe FloeTilla from a drone flight on 16 January 2019. A: raw image mosaic with SA Agulhas II (circle); B: orthorectified image product; C: surface topography derived by Structure from Motion (SfM) technique.*

6.6 Radar pilot study from the front of the ship

As one snow radar system (SR-2) remained in use on the drone, the older and heavier version (SR-1) was mounted on the ship's bow for a pilot study to measure snow depth when breaking sea ice (Fig. 6.15). The height of the radar was about 6.80 m above sea level.

A typical waveform of a reflected radar wave is shown in Figure 6.16 for snow of about 60 cm thickness. The waveform was recorded with the ship standing still and is therefore an ideal example. Radar measurements of snow thickness from the moving ship breaking through sea ice are yet to be processed.

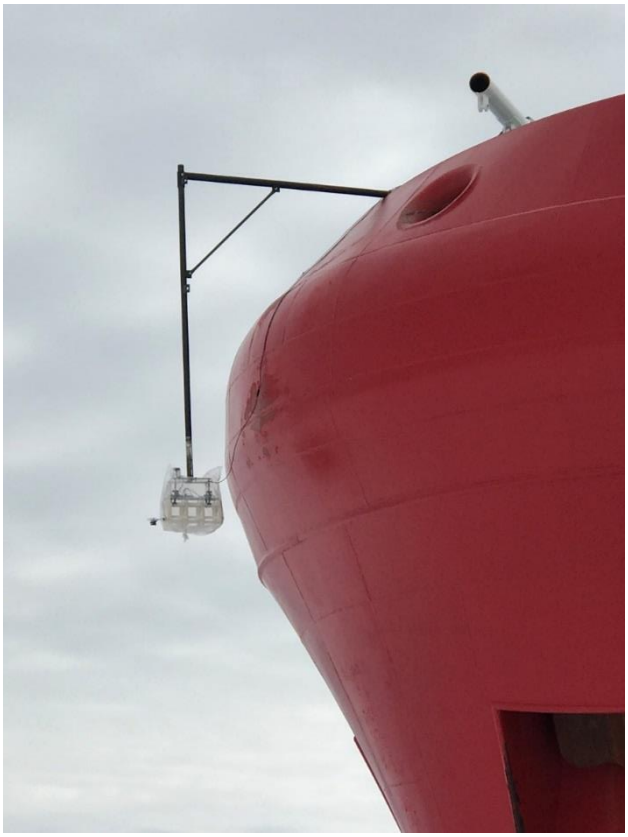

***Figure 6.15**. Drone snow radar mounted on the ship's bow of SA Agulhas II for a pilot study to measure snow thickness over sea ice.*

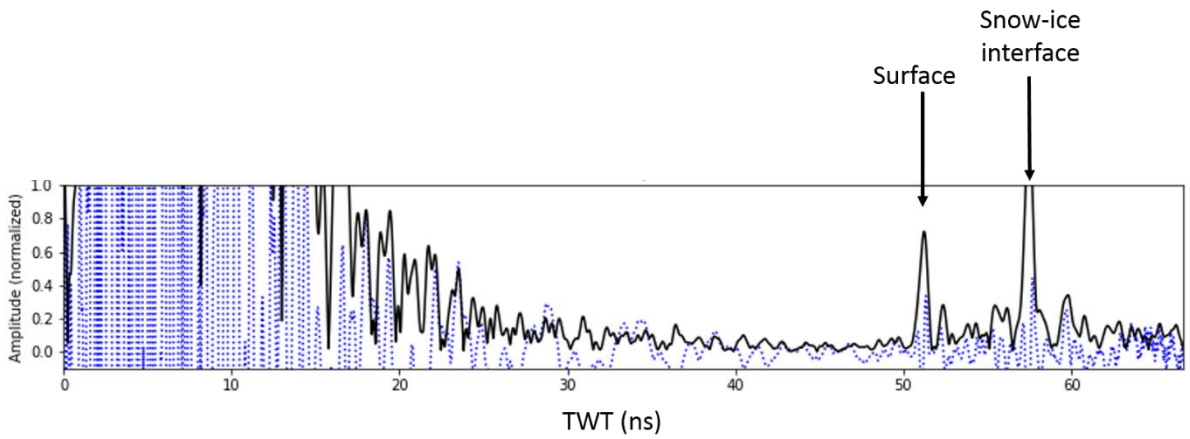

Figure 6.16. *Radar waveform of bow radar measurement from SA Agulhas II when parked against sea ice floe 'FloeRida.' The reflections of the snow surface and the snow-ice interface are shown.*

6.7 References

Gordon, A.L., 1993. Ice Station Weddell Group of Principle Investigators, and Chief Scientists, Weddell Sea exploration from ice station. *EOS Transactions AGU,* 74, 121.

Haas, C., Nicolaus, M., Willmes, S., Worby, A. and Flinspach, D., 2008. Sea ice and snow thickness and physical properties of an ice floe in the western Weddell Sea and their changes during spring warming. *Deep-Sea Research II*, 55, 963-974, doi:10.1016/j.dsr2.2007.12.020

Heil, P., Hutchings, J.IK., Worby, A.P., Johansson, M., Launiainen, J., Haas, C. and Hibler, W.D., 2008. Tidal forcing on sea-ice drift and deformation in the western Weddell Sea in early austral summer, 2004. *Deep-Sea Research II*, 55, 943-962, doi:10.1016/j.dsr2.2007.12.02

Hellmer, H.H., Schroeder, M., Haas, C., Dieckmann, G.S. and Spindler, M., 2008. The ISPOL drift experiment. *Deep-Sea Research II*, 55, 913-917. doi: 10.1016/j.dsr2.2008.01.001

James, R.W., 1924. Some problems relating to Antarctic sea-ice. In: Manchester Memoirs, Vol. LXVIII, No. 7.

Renner, A.H.H. and Lytle, V., 2007. Sea ice thickness in the Weddell Sea, Antarctica: a comparison of model and upward-looking sonar data. *Annals of Glaciology*, 46, 419-427.

7. Oceanography: the characteristics and role of Antarctic shelf and bottom water in CO_2 cycling, nutrient supply and upper ocean productivity

Sarah Fawcett, Thomas Bornman, Katherine Hutchinson, Riesna Audh, Jessica Burger, Raquel Flynn, Tahlia Henry, Hermann Luyt, Shantelle Smith and Kurt Spence

7.1 Broad Motivation

The Southern Ocean is an important driver of Earth's climate as it transports large quantities of heat, salt and dissolved gases, and supplies ~85% of the global ocean's nutrients (Keffer and Holloway 1988; Sarmiento et al. 2004; Lee et al. 2007). However, much remains unknown about the chemistry, biology, and physics of the Southern Ocean, which renders predicting (and subsequently managing) its response to environmental change a challenge. The Weddell Sea represents a point of origin in the Southern Ocean, where water masses form and communicate with the atmosphere (Muench and Gordon 1995; Talley et al. 2011), thereby setting the physical and chemical conditions of the deep global ocean. No picture of Antarctic oceanography would thus be complete without an understanding of the physical processes and biogeochemical cycling ongoing in the Weddell Sea.

7.2 Physical Oceanography: water-mass hydrography

7.2.1 Introduction

The unique environmental conditions on the Weddell Sea continental shelf facilitate complex interactions between the surface of the ocean and the atmosphere, sea ice, and neighbouring ice shelves. The products of these interactions are the formation of the coldest and densest water masses in the world, Weddell Sea Deep and Bottom Water (WSDW and WSBW) which evolve and mix to form Antarctic Bottom Water (AABW) once they are exported from the Weddell Sea (Gordon, 1998; Nicholls et al., 2009; Kerr et al., 2018). AABW is considered a vital component of global thermohaline circulation as it acts as a window between the atmosphere and the deepest 1000 m of the ocean and ventilates these depths with cold, oxygen rich water of Antarctic origin (Orsi et al., 1999; Gordon, 2009; Kerr et al., 2018).

The Weddell Sea is estimated to produce over half of the world's AABW at two main sites: the Filchner Ronne Ice Shelf (FRIS) and the Larsen C Ice Shelf (LCIS) (Gordon et al., 1993; Caspel et al., 2015; Kerr et al., 2018). Circumpolar Deep Water (CDW) flowing within the Antarctic Circumpolar Current (ACC) enters the Weddell Sea at approximately 30^0E and is

incorporated into the Weddell Gyre current (Gordon et al., 1993; Robertson et al., 2002). This water mass cools and mixes with neighbouring waters along its path within the gyre, becoming what is known as Weddell Deep Water or Warm Deep Water (WDW) (Robertson et al., 2002). In the vicinity of FRIS and LCIS this WDW experiences a loss of buoyancy through intense cooling due to interactions with the atmosphere and ice shelves, and a salinification via brine rejection during the formation of marine ice. High Salinity Shelf Water (HSSW) is consequently formed at the ocean surface when the seawater is cooled to its freezing point (-1.9^{0}C) and the salinity is raised to greater than 34.61 (Gordon, 2009). The HSSW circulates underneath the sub ice-shelf cavity where its freezing point is depressed with increasing pressure. One consequence of the depression in freezing point is that the water circulating beneath the ice shelf can cause basal melting, which gives rise to a new water mass variety called Ice Shelf Water (ISW) (Nicholls et al., 2009). This water is fresher and thus more buoyant than the ambient seawater and so it rises to the surface, partially re-freezing to the base of the ice shelf as frazil ice as the pressure decreases and the freezing point once again rises (Holland, 2008; Nicholls et al., 2009). This ocean-ice shelf interaction is thought to play an important role in modulating ice-shelf stability and thus Antarctica's glacial mass balance, however little is known about these processes in the vicinity of LCIS (Gordon, 2009).

The dense deep-water masses, WSDW and WSBW, are formed as the shelf water spills over the continental shelf break, and sinks down the continental slope mixing with neighbouring waters during the descent (Fahrbach et al., 1995; Nicholls et al., 2009). Coriolis deflection acts to direct these water masses north along the western rim of the basin as part of the Weddell Gyre boundary current (Fahrbach et al., 1995; Gordon, 2009). Upon reaching the tip of the Antarctic Peninsula, the slightly lighter and warmer variety of dense water overflows the South Scotia Ridge and continues eastward along the southern Scotia Sea, and the heavier component branches north along the South Sandwich Trench (Orsi et al., 1999). The densest version of bottom water is topographically trapped within the confines of the Weddell Abyssal Plain until it mixes upwards with lighter waters (Fahrbach et al., 1995; Orsi et al., 1999; Absy et al., 2008).

The dense waters that escape the Weddell Sea are re-named AABW. This water mass subsequently circulates eastwards as part of the Antarctic Circumpolar Current (ACC) and penetrates northwards into the Pacific, Atlantic and Indian Ocean basins. As dense waters are exported away from the continental shelf, older water masses are in turn pulled onshore, facilitating both the meridional transfer of heat and salt and the ventilation of the deep ocean through bottom water formation. In total it is thought that between 10 and 20 Sv (10^6 m^3/s) of AABW are exported from the Southern Ocean, representing a significant limb of the global overturning circulation (Fahrbach et al., 1995; Nicholls et al., 2009).

Larsen C Shelf Circulation: The area offshore of LCIS has been of interest to oceanographers and glaciologists for many years due to the complex interplay between the ocean and cryosphere, and the recent ice-shelf changes observed there. The loss of both Larsen A and B ice shelves and the pronounced atmospheric warming identified over the Antarctic Peninsula has raised concern regarding the stability of both Larsen C Ice Shelf and the formation rate of the parent water masses of AABW in the area (Absy et al., 2008; Caspel et al., 2015).

The ocean surface layer in the vicinity of Larsen C Ice Shelf constitutes cold and fresh Antarctic Surface Water (ASW) underlain by WDW, with WSDW and WSBW residing below the WDW layer. Nicholls et al. (2004) argued that the Larsen C continental shelf is flushed not by HSSW from the southern continental shelf, but by Modified Weddell Deep Water (MWDW; a ventilated form of CDW) across the shelf break. The MWDW observed by Nicholls et al. (2004) at two stations along the Larsen C ice front was hypothesised to have tracked west along the north-facing slopes of cross-shelf depressions that reach to the shelf break. Note that no hydrographic data was actually collected in the Jason Trough offshore of Larsen C to verify the circulation proposed by this hypothesis.

An interesting hypothesis proposed by Nicholls et al. (2004) is that MWDW reaching the ice shelf loses heat through preconditioning before being subducted beneath the ice shelf. This is said to imply that changes in temperature taking place in the deep Weddell Sea are not likely have a major impact on melt rates at the base of LCIS (Nicholls et al., 2004; Nicholls et al., 2009). This hypothesis is supported by the findings of Nicholls et al. (2012) where mixing gradients were used to determine that the source waters for the sub ice-shelf circulation need to be at surface freezing point. No investigation was, however, undertaken regarding the transformation of water masses on the slope or shelf prior to subduction into the sub ice-shelf cavity, and thus the role of MWDW in the ocean ice shelf interactions of LCIS remains poorly understood. The Nicholls et al. (2004 and 2009) hypothesis that MWDW is not causing basal melting at Larsen C can be viewed as somewhat controversial given both the observed thinning of LCIS (Shepherd et al., 2004) and the warming of the Southern Ocean since the 1950s (Gille, 2002; Etourneau et al., 2019). The ice shelf could be thinned either mechanically through changes in current velocity, or thermally via an increase in water temperature (Nicholls et al., 2012). In the area of LCIS, a change in the ocean currents would take place only if there was an alteration of the salinity field below the ice shelf – a phenomenon which is highly unlikely (Nicholls et al., 2012). Ocean warming is thus left as a main candidate to explain the observed thinning of LCIS.

In 2010 a giant crack was observed in LCIS, which continued to grow culminating in the breaking off of a massive 6000 km^2 iceberg, named A68, in 2017 (Etourneau et al., 2019). The historic studies in the LCIS have not presented sufficient evidence to rule out the role of the ocean in driving basal and frontal melting, ice shelf thinning, and ice shelf calving in the region of Larsen C. We, therefore, undertook a high resolution hydrographic survey of the ocean conditions along the Larsen C ice front and in Jason Trough leading offshore between the ice shelf and A68 iceberg.

7.2.2 Methods

A Seabird CTDO (Conductivity-temperature-depth-oxygen) sensor package (SBE 911) attached to a 24 x 12 L Niskin bottle rosette with extra PAR sensor was deployed at 21 stations in the Weddell Sea (Figure 7.2) and 3 stations at Penguin Bukta prior to the departure of the vessel (Table 7.1). The CTDO+rosette was deployed from the starboard side of the vessel

through the environmental hanger door. The sensor package records a measurement at a frequency of 1KHz, and conductivity measurements are automatically converted to salinity by the CTDO software (SBE – Seabird Processing).

The hydrographic component of this research project requires that salinity be known to very high accuracy, such that the CTDO must be calibrated to direct salinity measurements. Seawater was collected in the Niskin bottles at 13-18 depths throughout the water column during each CTD cast. ~200 mL of sample water from each depth was transferred into a clean glass bottle. Samples were taken at higher (lower) resolution in shallower (deeper) waters where more (fewer) bottles were closed and where the salinity variability was higher (lower). Samples were measured in triplicate using a Portasal 8410A salinometer and averaged before correlations with the CTD salinities were investigated. The salinometer was located in the underway laboratory and operated at 23°C bath temperature and 21°C ambient laboratory temperature. It was calibrated using IAPSO Seawater Standards, batch P158, manufactured by OSIL every ~100 samples (on 23/12/2018, 10/01/2019 and 21/01/2019). The salinometer was last serviced and aligned in June 2018 with additional service and alignment scheduled for June 2019 and June 2020, respectively. A total of 321 samples were processed and the measured salinities yielded a slope of 1.087 and a correlation coefficient of 0.991 when compared with the CTDO measurements (Figure 7.1). CTD-derived salinity measurements will be corrected using this empirical relationship.

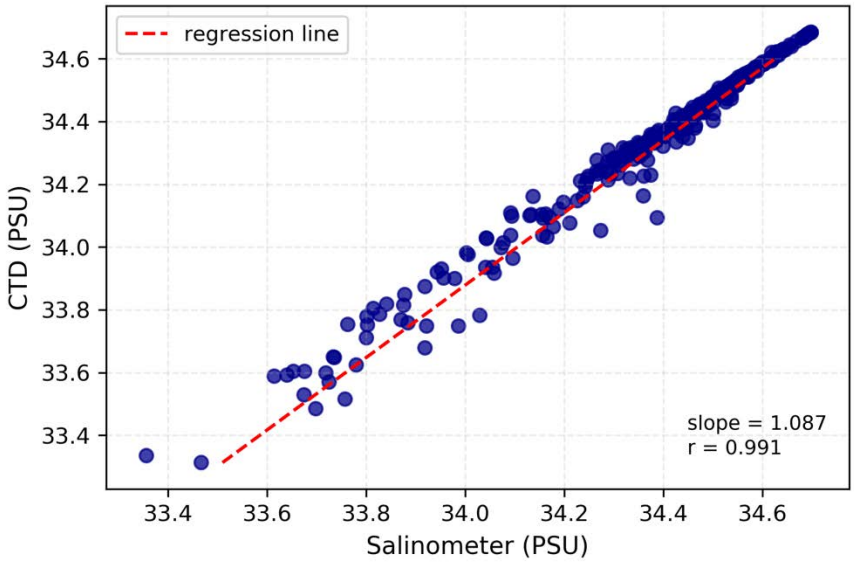

***Figure 7.1**. Correlation of CTD sensor-based and direct salinity measurements*

7.2.3 Results

Three stations were occupied on the continental slope north of Larsen C (CTD stations T1-3; Table 7.1). The water masses sampled at these stations can be considered the advected products of the water transformed on the continental shelf adjacent to Larsen C, as the boundary current that flows along the western rim of the Weddell Gyre facilitates the direct transport of

these waters northwards (Nicholls et al., 2004). Subsequently, 22 CTD stations were undertaken in the area between LCIS and iceberg A68, revealing both the thermohaline conditions along the Larsen C ice front during January 2019 and the hydrography in the Jason Trough. The locations of the CTD stations occupied in the Larsen C area of the Weddell Sea (Table 7.1) can be seen in Figure 7.2. A single deep CTD station was performed during the transit out of the Weddell Sea to capture the final stages of the dense waters as they are exported from the Weddell Gyre (station D1; Table 7.1).

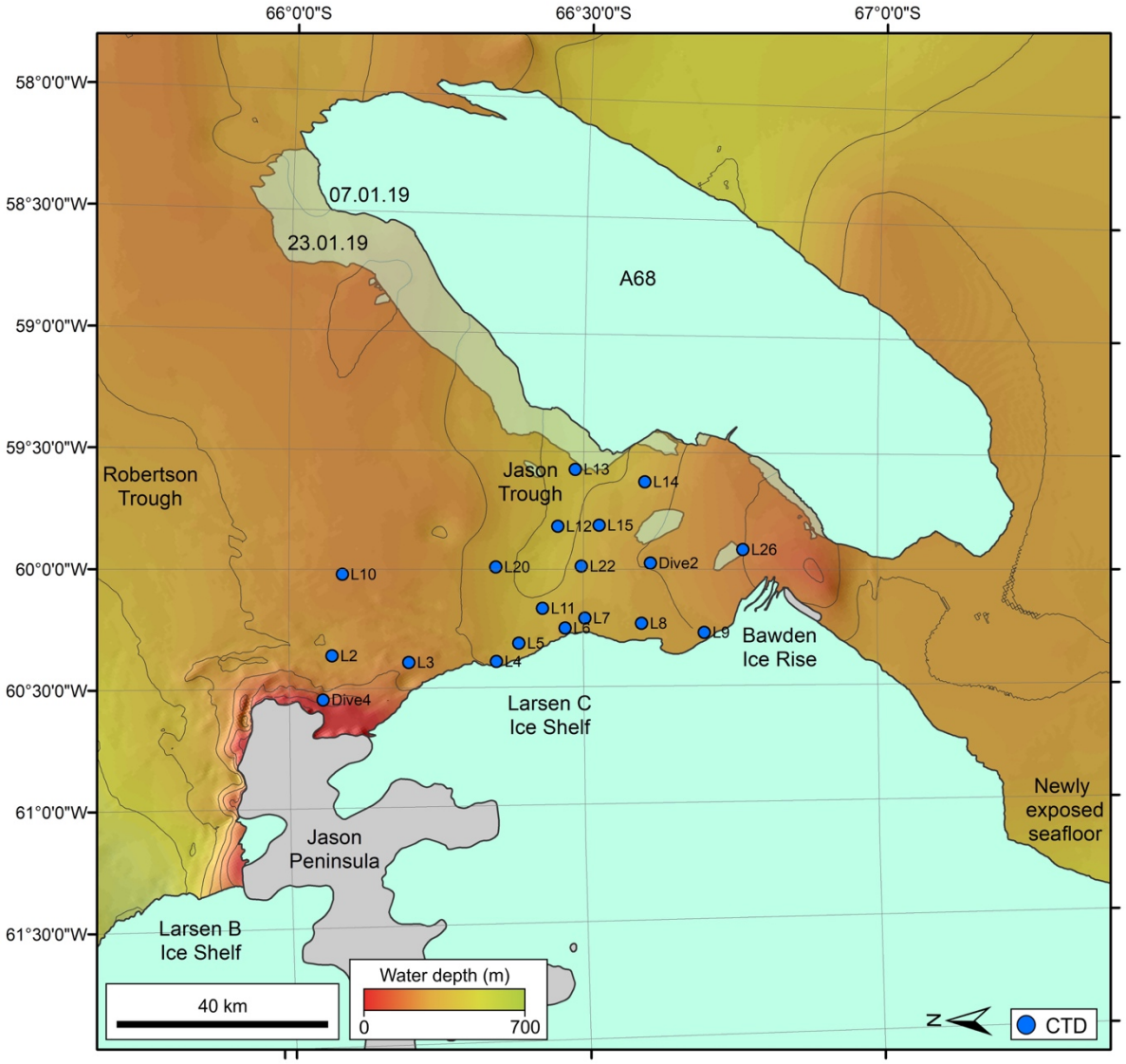

***Figure 7.2**. Map of CTD station in the northern Larsen C area of the western Weddell Sea.*

Thermohaline distributions

Figure 7.3 shows the distribution of the water masses in temperature-salinity space where the shading of the data points represents the pressure (depth) of the measurement. All major Weddell Sea water masses were sampled during this study. A relatively fresh form of HSSW (maximum salinity=34.68) was observed. This is due to the fact that the measurements were obtained during the end of summer when this water mass is relatively scarce. Note that we were not able to sample the densest WSBW variety in the deep sea station as the maximum depth was 4284 m. Instead, this water mass was sampled at an earlier stage in its evolution during the CTD transect along the continental slope north of Larsen C (station T1; maximum depth 2155 m).

The water masses identified during the Larsen C shelf CTD stations will be discussed in the next paragraph; here attention is drawn to the deeper water masses: MWDW, WDW, WSDW and WSBW sampled at stations T1-3 on the continental slope and the deep offshore station D1. The variety of MWDW found on the north-western rim of the Weddell Gyre is a warmer variety of this water mass, closer in properties to its parent water-mass WDW than the variety found close to Larsen C. The water sampled here may have never come into contact with an ice shelf front and thus never undergone cooling and ventilation via mixing with ASW and WW. WDW is the warmest water mass sampled with potential temperatures between 0^{o}C and 1^{o}C. It is found mid-depth in the water column, between 500 m and 1000 m, featuring as a subsurface temperature maximum. Below 1500 m, the parent water mass of AABW (WSDW) is present, and below this WSBW is identifiable by salinities above 34.62 and temperatures below 0.8^{o}C (Robertson et al., 2002). It is worth noting that the coldest and saltiest water mass sampled offshore of the continental shelf, at depths deeper than 600 m, was WSBW at station T1 below 2000 m depth.

The presence of WSBW at shallow depths on the continental slope north of Larsen C indicates that this water mass was likely recently formed and advected northwards as part of the western boundary current. Our CTD station therefore sampled WSBW during its descent down the continental slope to the abyss of the Weddell Sea where it eventually resides beneath the WSDW layer at depths below 5000 m. This bottom water was not captured by CTD station D1 (max depth 4284 m) in the middle of the Weddell Sea, as at this location WSBW has already sunk to reside in the abyssal trenches.

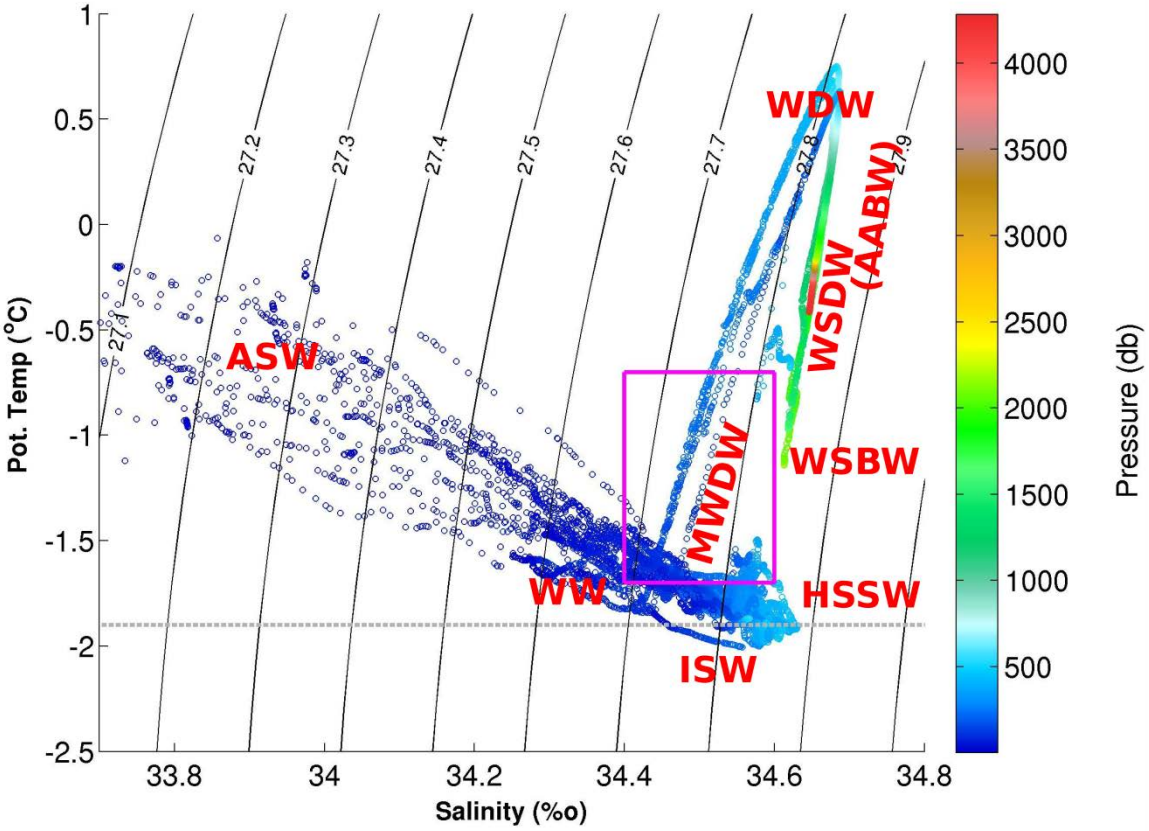

Figure 7.3. *Hydrographic data from the 26 CTD stations undertaken within the Weddell Sea plotted in temperature-salinity space. The background contours show density and the colour shading indicates the pressure corresponding the measurement. The magenta box delimits the potential temperature and salinity range of Modified Weddell Deep Water (MWDW). The grey dotted line indicates the surface freezing point of seawater (-1.9 ºC). The water mass labels correspond to Antarctic Surface Water (ASW), Winter Water (WW), Ice Shelf Water (ISW), High Salinity Shelf Water (HSSW), Warm Deep Water (WDW), Weddell Sea Deep Water (WSDW), Antarctic Bottom Water (AABW) and Weddell Sea Bottom Water (WSBW).*

The second T-S plot (Figure 7.4) shows the variety of water masses sampled on the continental shelf adjacent to Larsen C. The fresh ASW resides in the surface layer (upper 100 m), along with the cooler and slightly saltier Winter Water (WW). The WW layer is an artefact of deep convection during wintertime. Atmospheric warming and sea ice melt during summer heat and freshen the top of this layer, leaving WW identifiable as a subsurface temperature minimum located between 50 and 100 m depth. The subsurface WW cold layer was only identified in a few stations located in the Jason Trough, and was likely overridden by the melt water signal at stations closer to the ice shelf front. With increasing depth, water properties progressively move towards higher salinities on continental shelf (Figure 7.4). Between 300 m and 400 m depth, a ventilated form of MWDW is identifiable at some stations; this will be discussed in greater details in the next section. The data from CTDs located along the ice front of Larsen C show a clear signature of ISW where properties are below freezing point (grey dotted line in Figure 7.4) and occupy a salinity range between 34.45 and 34.66. The fresher variety of HSSW is identified at depths below 400 m and salinities above 34.6. While HSSW

is present all year round, the flushing of this water into the sub-ice cavity is thought to take place in pulses, mostly during wintertime (Nicholls et al., 2009), thus explaining the scarcity of this water mass in our samples.

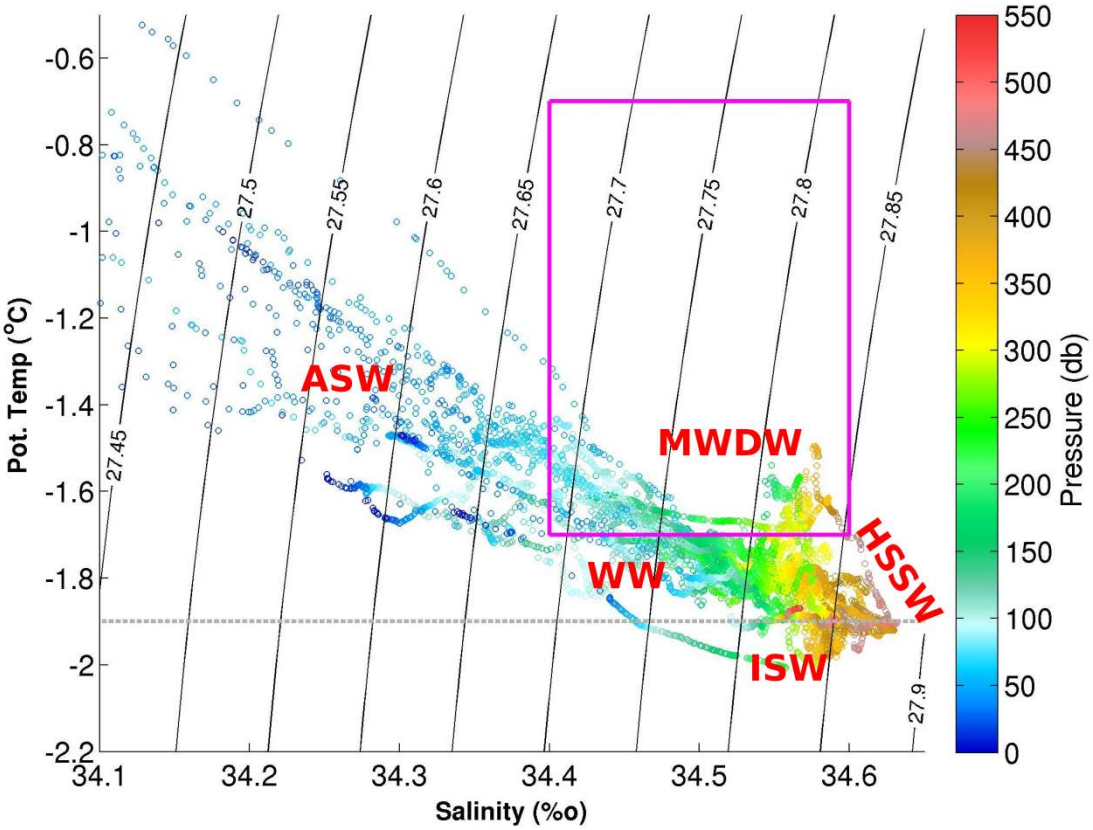

***Figure 7.4**. Hydrographic data from the 22 CTD stations undertaken on the continental shelf of the western Weddell Sea plotted in temperature-salinity space. The background contours show density and the colour shading indicates the pressure corresponding to the measurement. The magenta box delimits the potential temperature and salinity range of Modified Weddell Deep Water (MWDW). The grey dotted line indicates the surface freezing point of seawater (-1.9 °C). The water mass labels correspond to Antarctic Surface Water (ASW), Winter Water (WW), Ice Shelf Water (ISW), and High Salinity Shelf Water (HSSW).*

Modified Weddell Deep Water

The magenta square overlaid on Figures 7.3 and 7.4 shows the thermohaline limits of MWDW properties. The characteristics and distribution of this water mass is of great interest due to the possible role that it could play in driving both basal melting of Larsen C and influencing the production rate of dense water masses.

The *James Clark Ross* undertook 9 CTD stations in the same region adjacent to the northern section of Larsen C ice shelf in February 2002 (Nicholls et al., 2004). Given the similarity in seasons and locations of the hydrographic measurements, some useful comparisons in findings can be made. Nicholls et al. (2004) argued that the Larsen C continental shelf is flushed not by HSSW from the southern continental shelf, but by MWDW across the shelf break. MWDW was observed by Nicholls et al. (2004) at two stations along the ice front and was said to have tracked west along the north facing slopes of depressions that reach to the shelf break. Nicholls

et al. (2004) suggested that ISW near the ice front was not derived from MWDW directly, but instead sourced from an altered version of this water mass that was pre-conditioned by winter cooling and salinification via sea ice production.

As a preliminary exploration into the role of MWDW in influencing the hydrography of the LCIS continental shelf, the stations where this water mass was identified as being clearly detected are circled in red in Figure 7.5. CTD stations where a cooled version of this water mass is identified are circled in yellow in Figure 7.5. Nicholls et al. (2004) proposed that MWDW is advected onshore along the north facing slope of the Jason Trough. While this is consistent with our observations, one would, however, expect to see a ubiquitous signal throughout the depression, whereas this is not observed. The "patchy" presence of the water mass could be due to a number of factors and thus further investigation on this topic is planned. The ADCP data collected at each CTD station has yet to be processed and will shed much light onto the shelf circulation at the time of sampling, exposing the possible advection routes of MWDW. The stations circled in yellow (Figure 7.5) exhibit a spike in temperature at depth associated with the presence of MWDW within the water column, however the temperature signatures of these spikes are too cool to place them clearly within the MWDW category. Mixing with overlying cooler layers of WW and ISW could explain the water mass transformation observed. Once again, an in depth investigation on this topic is planned.

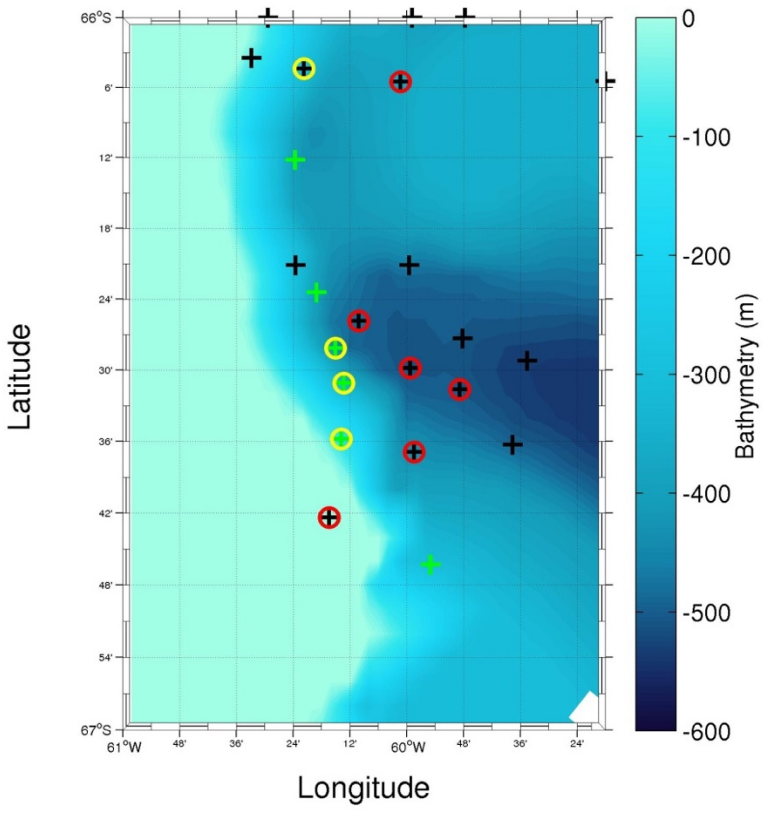

***Figure 7.5**. Map showing locations of CTD stations in the vicinity of Larsen C with the bathymetry (m) of seafloor as background shading. Stations circled in red clearly show the presence of Modified Weddell Deep Water (MWDW), and stations circled in yellow show an altered form of this water mass*

where the T-S signature is similar but slightly colder than the MWDW limits. Green crosses correspond to locations where the CTD profiles suggest the presence of meltwater.

Meltwater Signals

A latitudinal section of the thermohaline and dissolved oxygen concentrations of the upper 100 m of the water column sampled along the ice front of Larsen C is shown in Figure 7.6. Pockets of fresh water occupying the upper 25 m to 50 m of the water column are identified, exposing a clear meltwater signal in some areas. The stations where a meltwater layer is present are indicated by green crosses in Figure 7.5 (stations: L3, L5-L8 and L26 in Figure 7.2). This water is comparatively warm, fresh and has a very high dissolved oxygen concentration. A possible explanation for the high oxygen levels could be that the buoyant meltwater is conducive to productivity, keeping the plankton in the photic zone. Additionally, meltwater may be high in both nutrients and iron from sediment deposition, thereby further promoting productivity. This is to be investigated further once the results from the water samples taken from the Niskin bottles of the CTD rosette become available. Observations made by the naked eye while adjacent to the LCIS revealed no meltwater streams coming off the ice face (W. Rack, pers. comm.). While this is a crude measurement, it suggests that the majority of the meltwater may be from basal melting rather than surface melt. Once the ADCP data are processed, they will provide greater insights into the current speeds and directions adjacent to the ice shelf. There may be a relationship between the MWDW identified on the shelf and the locations of meltwater inflow, this is something planned for further investigation.

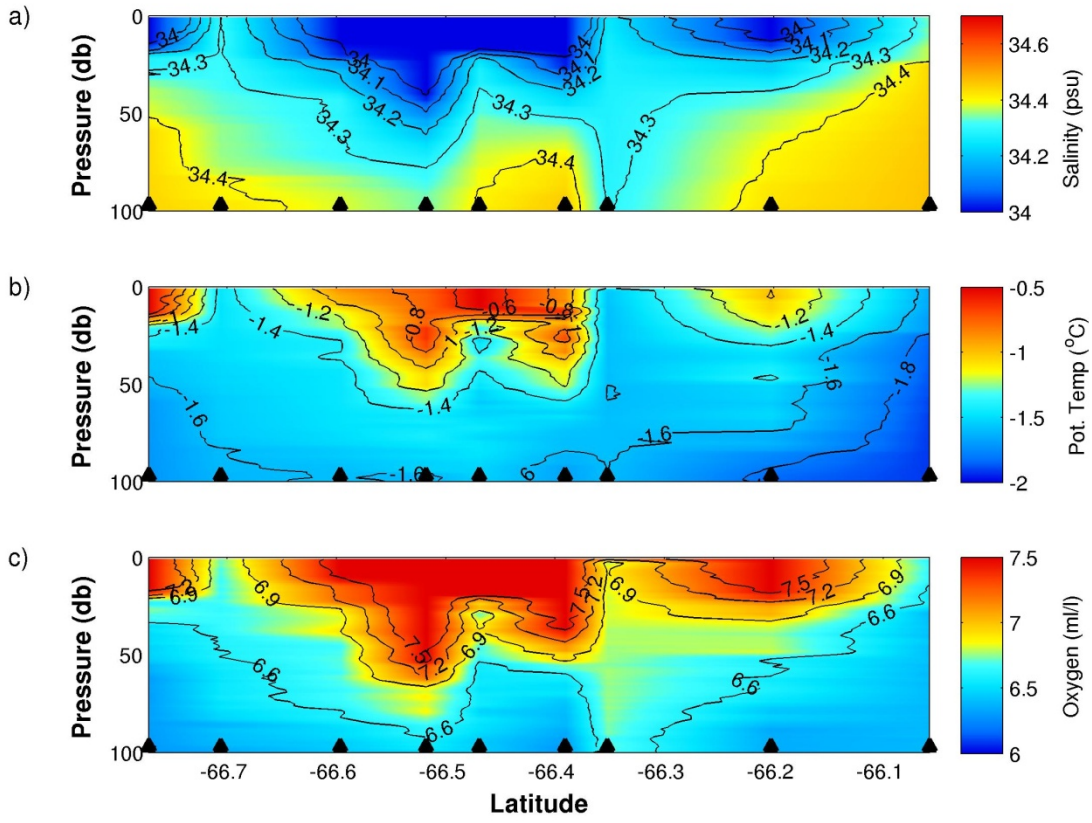

***Figure 7.6**. Along ice-shelf section (stations: AUV dive 4, L3, L4, L5, L6, L7, L8, L9 and L26 in Figure 7.2) of the top 100 m of the water column showing a) salinity, b) potential temperature and c) dissolved oxygen.*

Sections showing the thermohaline and dissolved oxygen properties along the north facing bank of the Jason Trough (CTD stations L4, L5, L11, L15, L22 and L14) are shown in Figure 7.7. Two plumes of meltwater are visible – one emanating from the boundary with A68 iceberg and the other from Larsen C. The melt water plume tapers off towards the western edge of the section, closest to Larsen C. At the westernmost station, the surface salinity is elevated compared to the neighbouring offshore station, yet the salinity at depth is fresher. The temperature at the station adjacent to the ice shelf is cooler than offshore, providing further evidence suggesting an ocean driven basal melting is taking place in place of atmospheric surface melting of the ice shelf. The pool of fresh water adjacent to A68 could be a combination of basal, surface and side melting together with the introduction of freshwater from calving events (some of which were observed by the naked eye). While these sections are preliminary results, they highlight the complexity of process taking place in the vicinity of LCIS.

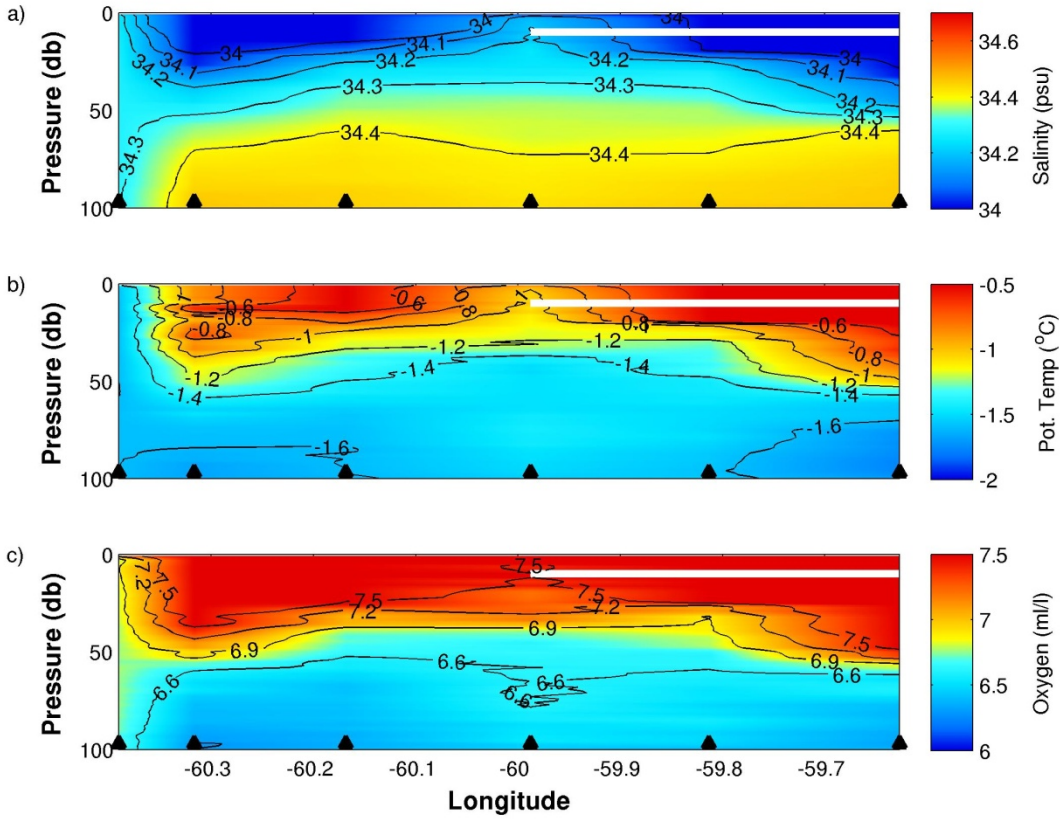

***Figure 7.7**. Along ice shelf section (stations: L4, L5, L11, L22, L15 and L14 in Figure 7.2) of the top 100 m of the water column showing a) salinity, b) potential temperature and c) dissolved oxygen.*

7.2.4 Conclusions

In total 26 full-depth CTD stations were undertaken within the Weddell Sea during January 2019. The preliminary results from these measurements suggest that the role of MWDW in

influencing the hydrography in the vicinity of LCIS, and consequently the thickness and stability of LCIS, cannot be discounted. MWDW is derived from CDW, and thus carries with it climate signals from the ACC and possibly from water mixed in from other ocean basins. Despite the important role that this water mass plays in ocean-cryosphere interactions and dense water formation, our understanding regarding the manner in which this water is circulated onto the continental shelf and underneath LCIS is currently poorly understood and will thus be the focus of a study emanating from the data gathered as part of the Weddell Sea Expedition. Studies such as this highlight the importance of monitoring the ice shelves and the adjacent ocean so that we may improve our understanding regarding the ocean-ice-atmosphere interplay and better constrain these processes in global ocean circulation models that forecast how processes such as the meridional overturning circulation will adjust in various emission scenarios.

7.3 Biogeochemical Oceanography: carbon formation, export, and sequestration in southern Antarctic waters

7.3.1. Introduction

A key uncertainty facing our current understanding of the Earth's climate system is the role played by biology in the Southern Ocean. Observations show that nitrate (an essential macro-nutrient to phytoplankton) is never fully consumed in Antarctic surface waters, likely due to a combination of iron and light limitation of phytoplankton (Martin et al. 1991; Sunda and Huntsman 1997), although the role of planktonic community composition remains poorly understood. On an annual basis, phytoplankton growth in the sunlit upper ocean that is fuelled by nitrate supplied from below (i.e., "new production") is balanced by the export of sinking organic matter into the ocean interior (i.e., "export production"; Dugdale and Goering 1967; Eppley and Peterson 1979), thus driving CO_2 sequestration. Phytoplankton growth can also be supported by nitrogen (N) forms such as ammonium that are recycled in surface waters (i.e., "regenerated production"); in net, regenerated production results in no removal of CO_2 to the deep ocean.

The biologically-driven flux of carbon (C) from surface waters (i.e., the ocean's "biological pump") acts to transfer CO_2 to the isolated waters of the deep ocean, lowering the atmospheric concentration of this greenhouse gas. The high nitrate - low chlorophyll state of the present-day Southern Ocean represents a "leak" in the global ocean's biological pump since by consuming nitrate more completely, Antarctic phytoplankton could lower atmospheric CO_2. Indeed, a more efficient biological pump at high latitudes is a leading hypothesis for the decrease in atmospheric CO_2 that characterized the ice ages (Sigman and Boyle 2000; Sigman et al.., 2010). Understanding the controls on biological nitrate utilization in the modern Antarctic Ocean is thus central to our understanding of its outsized role in setting atmospheric CO_2 today and in the past, and in absorbing CO_2 in the future (Sarmiento and Toggweiler 1984). Given the importance of the Weddell Sea for setting the biogeochemical conditions of the Southern Ocean, our focus is on a series of measurements and experiments designed to

investigate 1) the rate of organic carbon biomass formation (i.e., primary production) in Weddell Sea surface waters, including at night when light levels are low but not zero, 2) the importance of different phytoplankton groups for total, new, regenerated, and export production, as well as for sea ice biogeochemistry, 3) the effects of (overlapping) biogeochemical transformations on the signature of water masses formed in the Weddell Sea, and 4) how well surface-produced biogeochemical signatures are preserved in diatom microfossils on the seafloor.

Experimental overview: Primary production is an indicator of the amount of energy available to an ecosystem, which is centrally important to ecological processes and biogeochemical cycling. To assess the summertime fertility of the Weddell Sea and the relative importance of different phytoplankton groups for driving production, simulated *in situ* experiments (^{13}C and ^{15}N incorporation; Cullen 2001; Dugdale and Goering 1967) were conducted to measure rates of net primary production, and new and regenerated production by both the bulk and size-fractionated phytoplankton community. Rates of nitrification (the regeneration of nitrate from ammonium) were also quantified (Peng et al. 2018; Mdutyana et al. *in prep*). This ensemble of coupled measurements has never previously been generated for the Weddell Sea. The rate data will allow for accurate calculation of the f-ratio (shorthand for "flux ratio"; Eppley and Peterson, 1979), which provides an indication of the strength of the region's biological pump and thus its capacity for biological CO_2 removal.

In addition to the bulk and size-fractionated community N transformation experiments, a series of ^{15}N incubations (urea, NO_3^- and NH_4^+ uptake) were undertaken. The resultant particle samples collected at the end of the incubations will be flow cytometrically-sorted and measured for N isotopes. These data will allow for the quantification of taxon-specific rates of urea, NO_3^- and NH_4^+ uptake (e.g., by *Synechococcus*, eukaryotes, diatoms, heterotrophic bacteria). This will enhance our understanding of the role of different phytoplankton groups in driving the biological pump, with implications for future Southern Ocean biogeochemistry given predictions that phytoplankton community composition is likely to change under conditions of global warming.

The natural abundance N isotopic composition ($\delta^{15}N$) of suspended particles (PN) has been used as a tracer of the dominant N source supporting production (i.e., new vs. regenerated N). For example, the consumption of subsurface nitrate yields high- $\delta^{15}N$ PN whereas ammonium uptake yields low-$\delta^{15}N$ PN (Rau et al. 1990; Treibergs et al. 2014). Inferring N source from bulk PN $\delta^{15}N$ is problematic, however, because this pool includes heterotrophs and detritus in addition to phytoplankton (Fawcett et al. 2011, 2014). This can be overcome by coupling fluorescence activated cell sorting (FACS) and high sensitivity N isotope analysis (Fawcett et al. 2011; 2014; Treibergs et al. 2014). Using this approach, important biological populations can be isolated from mixed environmental samples and population-specific $\delta^{15}N$ can be measured. This yields an integrated (over the organism lifetime) view of the primary N source supporting different phytoplankton groups, revealing their role in new and export production and complementing the rate experiments, which integrate over only a few hours.

7.3.2 Methods

Field collections

Seawater samples: Seawater samples were collected underway for nutrients and nitrate (NO_3^-) isotopes every 4 hours (Figure 7.8) and from hydrocasts at each CTD station. From each cast, water was collected at regular intervals between the surface and bottom in 50 mL HDPE bottles, then frozen at -20°C. Ammonium (NH_4^+), phosphate and nitrite (NO_2^-) were measured onboard (see below), while NO_3^- and silicate will be measured in the Marine Biogeochemistry Laboratory at UCT (MBL-UCT) by flow injection analysis. Seawater samples were also collected from all depths at all stations for the later analysis of water isotopes (i.e., $\delta^{18}O\text{-}H_2O$), and at select depths at most stations for ammonium isotopes (i.e., $\delta^{15}N\text{-}NH_4^+$). $\delta^{18}O\text{-}H_2O$ will be measured using a Picarro L2140-i isotope and gas concentration analyser at UCT and $\delta^{15}N\text{-}NH_4^+$ in the MBL-UCT via the method of Zhang et al. (2007).

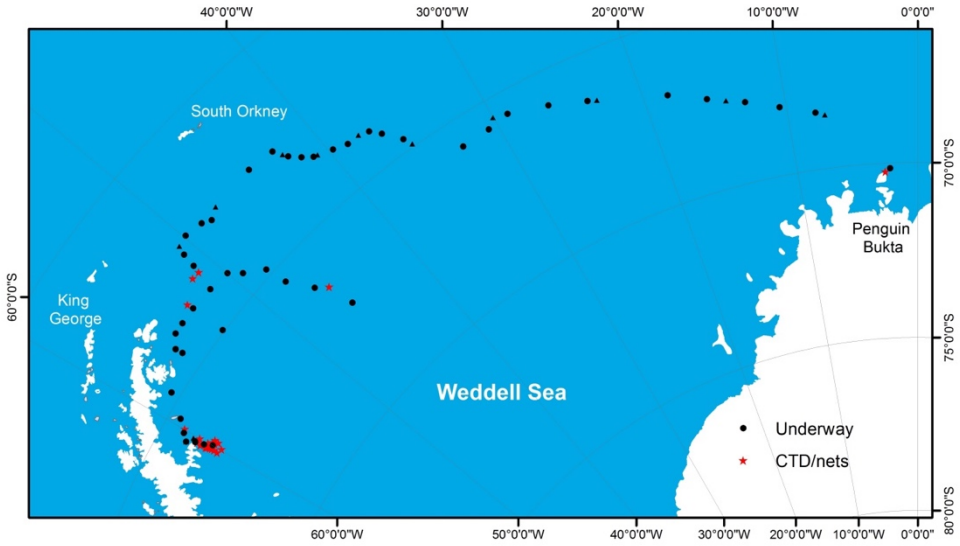

***Figure 7.8**. Location of underway stations (black dots) with CTD/net tow stations overlaid (red stars).*

Chlorophyll: Seawater was collected from each underway station and all CTD casts at five discrete depths over the upper 80-100 m (encompassing the mixed layer and euphotic zone) in opaque HDPE bottles. Prior to filtration, the bottles were gently and repeatedly inverted to homogenize the sample. 1 L of seawater from each sample was filtered through a 22 µm nylon mesh filter, 500 mL through a 2.7 µm glass fibre filter (GF/F) and the remaining 500 mL was filtered through a 0.3 µm GF/F. Filters were immediately transferred to 20 mL glass scintillation vials to which 8 mL of 90% acetone was added before the vials were left in the -20°C freezer for 24 hours to extract.

N isotopes of bulk particles and specific phytoplankton taxa: Water samples for bulk N isotopic analysis of particulate organic nitrogen biomass (PN) were collected at each underway station and from five euphotic zone depths on each hydrocast (the same depths as the chlorophyll samples). At each underway station, three 4 L HDPE bottles were filled with seawater that was then filtered under gentle vacuum through pre-combusted GF/F filters with nominal pore sizes

of 0.3 µm, 2.7 µm and 22 µm. At each CTD station, 4 L of seawater was collected and filtered for the >22 µm size-class, and 1-2 L each for the 0.3-2.7 µm and 2.7-22 µm size-classes. After filtration, the filters were folded in half using ethanol-cleaned forceps and stored in ashed tinfoil envelopes at -80°C pending analysis.

Water samples for taxon-specific nitrogen isotopes were collected at each underway station and from three euphotic zone depths on various hydrocasts (Table 7.1). At each underway station, four 4 L HDPE bottles were filled with seawater, while at CTD stations, two 2 L bottles of seawater were taken from each depth of interest. Seawater was filtered through a polycarbonate (PC) membrane filter with a nominal pore size of 0.4 µm under gentle vacuum. After filtration, the PC filters were placed in 4 mL cryovials to which ~4 mL of filtered seawater and 100 µL of glutaraldehyde were added in order to resuspend the cells from the filters and preserve them. The cryovials were subsequently stored in the fridge for 1-4 hours and thereafter frozen at -80°C pending analysis.

Incubation experiments: Tracer incubation experiments were conducted at multiple stations to directly quantify rates of carbon fixation (i.e., primary production), urea, NO_3^- and NH_4^+ uptake (Table 7.1; "PP"), and NH_4^+ and NO_2^- oxidation (Table 7.1; "NTR"). Water samples were collected in 1 L PC bottles (uptake) and 250 mL black HDPE bottles (nitrification) from three euphotic zone and three to four sub-euphotic zone depths. Seawater was pre-screened through a 200 µm nylon mesh to remove large grazers. Duplicate 1 L bottles from each euphotic zone depth were amended with $^{15}NO_3^-$ or $^{15}NH_4^+$ or ^{15}urea (for N uptake), and duplicate 250 mL bottles from all depths are amended with $^{15}NH_4^+ + ^{14}NO_2^-$ carrier or $^{15}NO_2^-$ (for NH_4^+ and NO_2^- oxidation, respectively). The isotope tracers were added at ~10% of the ambient nutrient concentration. Two of the six 1 L bottles from each depth were also amended with ^{13}C-bicarbonate in order to quantify net carbon fixation.

Prior to incubation, 40 mL subsamples (T_0) were collected from all nitrification bottles and frozen at -20°C. All bottles (for uptake and nitrification) were then placed in a custom-built on-deck incubator equipped with neutral density screens to simulate *in situ* light levels and a supply of circulating seawater to maintain a constant temperature. Uptake experiments were incubated for 4-6 hrs and nitrification experiments for 20-30 hrs. A second 40 mL subsample (T_f) was collected from each nitrification bottle at the end of the incubation. The N uptake and carbon fixation incubations were terminated by size-fractionated filtration (0.3-2.7 µm, 2.7-22 µm, 22-200 µm) onto ashed GF/Fs that were then oven dried at 40°C and pelletized into tin cups for analysis at the Stable Light Isotope Laboratory at UCT.

In addition, a series of ^{15}N incubations (urea, NH_4^+ and NO_3^- uptake; Table 7.1 "FACS N uptake") were terminated via filtration onto PC filters so that the samples can later be sorted using fluorescence activated cell sorting (e.g., for *Synechococcus*, eukaryotes, diatoms, heterotrophic bacteria, etc.). Samples were incubated, filtered, and preserved as described above for *N isotopes of specific phytoplankton taxa*. In the laboratory, these samples will be sorted and measured for ^{15}N enrichment as outlined below. From five surface depths on all casts, samples were also collected for flow cytometric counting of phytoplankton particles,

which aid in the quantification of different phytoplankton groups; this information is critical for ground-truthing the FACS data.

Plankton taxonomy: At all CTD stations, phytoplankton and zooplankton samples were collected using a drift net and bongo net, respectively. The mesh size of the drift net was 50 µm and the bongo net had two cod ends with mesh sizes of 90 µm and 200 µm. Nets were lowered to 100 m and then immediately raised again. The collected samples were preserved in a mixture of seawater + glutaraldehyde in HDPE bottles until later analysis via light and scanning electron microscopy.

WSE Station	Station	Latitude (°S)	Longitude (°W)	Nutrients	NH_4^+	NH_4^+ isotope	NO_3^- isotope	Flow cytometry	POC/PON	Chl-a	FACS NA	O_2	$\delta^{18}O$ water	PP	NTR	FACS N uptake
F1	AM00969	70.172	2.131	x	x		x	x	x	x	x	x				
F2	AM00970	70.164	2.140	x	x		x	x	x			x	x	x		
F3	AM00971	70.246	2.691	x	x		x	x	x	x	x			x	x	
T1	AM00972	63.035	51.084	x	x		x	x	x	x	x	x	x	x	x	
T2	AM00973	63.411	51.610	x	x		x	x	x	x	x	x	x	x	x	
T3	AM00974	63.738	53.111	x	x		x	x	x	x	x	x	x	x	x	
L3	AM00975	66.204	60.393	x	x	x	x	x	x	x	x	x	x			
L4	AM00976	66.352	60.391	x	x	x	x	x	x	x		x	x			
L4	AM00977	66.352	60.391	x	x	x	x	x	x	x	x	x	x	x	x	x
L14	AM00978	66.605	59.627	x	x	x	x	x	x	x	x	x	x	x	x	x
L13	AM00979	66.487	59.576	x	x	x	x	x	x	x	x	x	x	x	x	
L15	AM00980	59.813	66.527	x	x	x	x	x	x	x		x	x			
L22	AM00981	66.497	59.988	x	x	x	x	x	x	x		x	x			
L2	AM00982	66.074	60.363	x	x	x	x	x	x	x	x	x	x	x	x	
L10	AM00983	66.092	60.021	x	x	x	x	x	x	x	x	x	x	x	x	
L5	AM00984	66.391	60.320	x	x	x	x	x	x	x		x	x			
L6	AM00985	66.470	60.251	x	x	x	x	x	x	x	x	x	x	x	x	
L7	AM00986	66.510	60.216	x	x	x	x	x	x	x		x	x			
L8	AM00987	66.596	60.229	x	x	x	x	x	x	x		x	x			
L26	AM00988	66.773	59.911	x	x	x	x	x	x	x		x	x			
L9	AM00989	66.706	60.273	x	x	x	x	x	x	x	x	x	x	x	x	x
L11	AM00990	66.431	60.169	x	x	x	x	x	x	x		x	x			
L12	AM00991	66.456	59.802	x	x	x	x	x	x	x	x	x	x	x	x	x
L20	AM00992	66.352	59.991	x	x	x	x	x	x	x	x	x	x	x	x	
R1	AM00993	59.979	65.590	x	x	x	x	x	x	x	x	x	x	x	x	x

Table 7.1: List and location of CTD deployments with parameters sampled from each cast.

Laboratory methods

Nitrate and silicate analysis: Nitrate and silicate concentrations will be measured on a Lachat QuickChem Flow Analysis platform in MBL-UCT following published auto-analysis protocols (Diamond, 1994; Grasshoff, 1976). The configuration typically used gives the Lachat QuickChem Flow Analysis platform a detection limit of 0.1 µM.

Nitrite analysis: Nitrite concentrations were determined shipboard using the benchtop colorimetric Greiss reaction (Bendschneider and Robinson, 1952; Parsons et al., 1984). Absorbance was measured using a Thermo Scientific Geneysis 30 Visible spectrophotometer at a wavelength of 543 nm. The method has a detection limit of 0.05 µM.

Phosphate analysis: Phosphate concentrations were determined shipboard using the Strickland and Parsons colourimetric method (Strickland and Parsons, 1968). Samples and standards were

measured using a Thermo Scientific Geneysis 30 Visible spectrophotometer at a wavelength of 880 nm. The method has a detection limit of 0.05 μM.

Ammonium analysis: Ammonium concentrations were determined using the Holmes fluorometric method (Holmes et al., 1999). Samples and standards were measured using a Turner Designs Trilogy Fluorometer 7500-000 equipped with a UV module. The method has a detection limit of 0.05 μM. Since NH_x samples are easy to contaminate, precautions were taken to prevent contamination during sample collection and processing. Following the addition of the orthophthaldialdehyde (OPA) working reagent to frozen samples, a water bath was used to defrost the samples. Once at room temperature, the samples and standards were allowed to react for four hours. The matrix effect, from the comparison of seawater samples and standards made with type-1 ultrapure water, was calculated according to the standard addition method (Saxberg & Kowalski, 1979). Final concentrations were corrected for the matrix effect.

Nitrate isotope analysis: The $\delta^{15}N$ of NO_3^- (and its $\delta^{18}O$, which offers additional constraints on NO_3^- cycling) will be measured in the MBL-UCT using the newly-installed "denitrifier-isotope ratio mass spectrometer (IRMS)". Briefly, denitrifying bacteria lacking a terminal nitrous oxide (N_2O) reductase quantitatively convert sample NO_3^- (and NO_2^-) to N_2O (Sigman et al. 2001; Casciotti et al. 2002) that is then measured using a Thermo Delta V Plus IRMS and purpose-built on-line N_2O extraction and purification system. Precision for $\delta^{15}N$ and $\delta^{18}O$ is ≤0.1‰ and ≤0.3‰, respectively, for NO_3^- concentrations ≥0.5 μM. NO_2^- removal, if necessary, will be undertaken via the method of Granger and Sigman (2009) prior to sample analysis.

Chlorophyll-a concentrations: The updated method for chlorophyll-a determination outlined by Rathbun (1997) was used to measure the chlorophyll-a concentrations on board the ship. This method is based on the Welschmeyer method for non-acidified chlorophyll-a determination (Welschmeyer, 1994). Samples and standards were measured using a Turner Designs fluorometer with a chl-a non-acidified module.

FACS-N isotope analysis: Central to this project is the coupled flow cytometry-N isotope protocol (Fawcett et al. 2011; 2014; Treibergs et al. 2014). All sorting will take place at the UCT Flow Cytometry Core Facility. Vials are thawed in the dark and gently vortexed to dislodge cells from filters. Re-suspended cells are filtered through a 35 μm mesh; the >35 μm particles are archived for future analysis. All sorts will be conducted using a BD FACS Jazz Cell Sorter equipped with a 488 nm blue laser. Samples will be sorted for *Synechococccus* and total eukaryotic phytoplankton according to Fawcett et al. (2011), as well as cryptophytes and heterotrophic bacteria (Marie et al., 2997). We also aim to optimize the flowcytometry protocol for sorting diatoms; we will begin with the approach of McNair et al. (2015) and Hansman and Sessions (2015).

Sorted PN will be converted to NO_3^- at MBL-UCT using the persulfate oxidation method of Knapp et al. (2005) as modified by Fawcett et al. (2014). Briefly, sorted particles are filtered onto ashed 0.3 μm GF-75s, then transferred to combusted 4 mL glass Wheaton vials to which 2 mL of persulfate oxidizing reagent (POR) is added. POR is also added to triplicate vials

containing a GF-75 blank plus varying amounts of two L-glutamic acid isotope standards, USGS-40 and USGS-41 (Qi et al. 2003); this allows for quantification of the N content and $\delta^{15}N$ of the blank. POR is made by dissolving 1-2 g of NaOH and 1-2 g of 4-times recrystallized, methanol-rinsed potassium persulfate in 100 mL of DI water. After POR addition, vials are autoclaved at 121°C for 55 mins on a slow-vent setting. Sample pH is lowered to 5-8 and vials are centrifuged at 3000 rpm for 10 mins to separate residual GF-75 from the liquid sample. The concentration of the resultant NO_3^- is measured via chemiluminescent analysis (Garside 1982; Braman and Hendrix 7.3.31989) using a NOx analyzer (Teledyne T200) with custom-built front-end at MBL-UCT. The $\delta^{15}N$ of the oxidized NO_3^- is analysed using the denitrifier method. The precision of the full collection/cytometry/N isotope protocol is ~0.4‰ (Fawcett et al. 2011; 2014).

7.3.3 Preliminary results

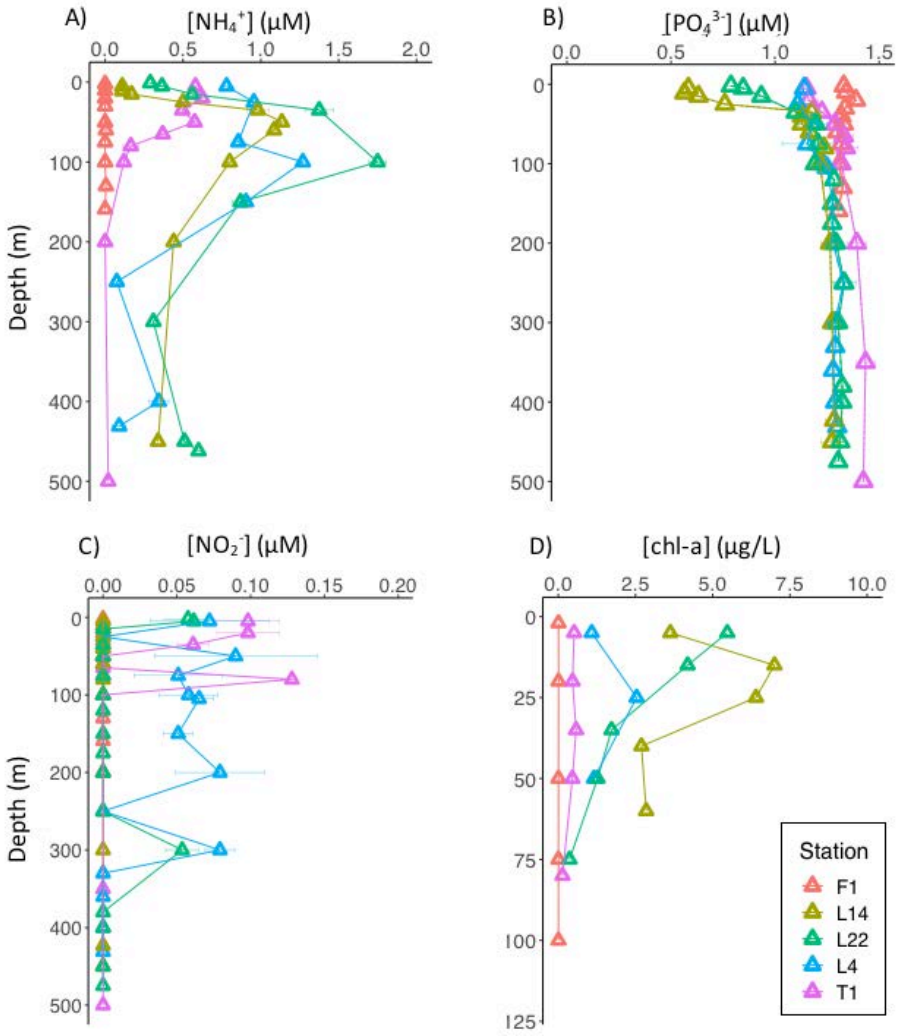

Figure 7.9. *Depth profiles of ammonium (NH_4^+), b) phosphate (PO_4^{3-}), c) nitrite (NO_2^-) and d) bulk chlorophyll concentrations from five example CTD casts. All samples were measured shipboard. See Figure 7.2 for CTD locations.*

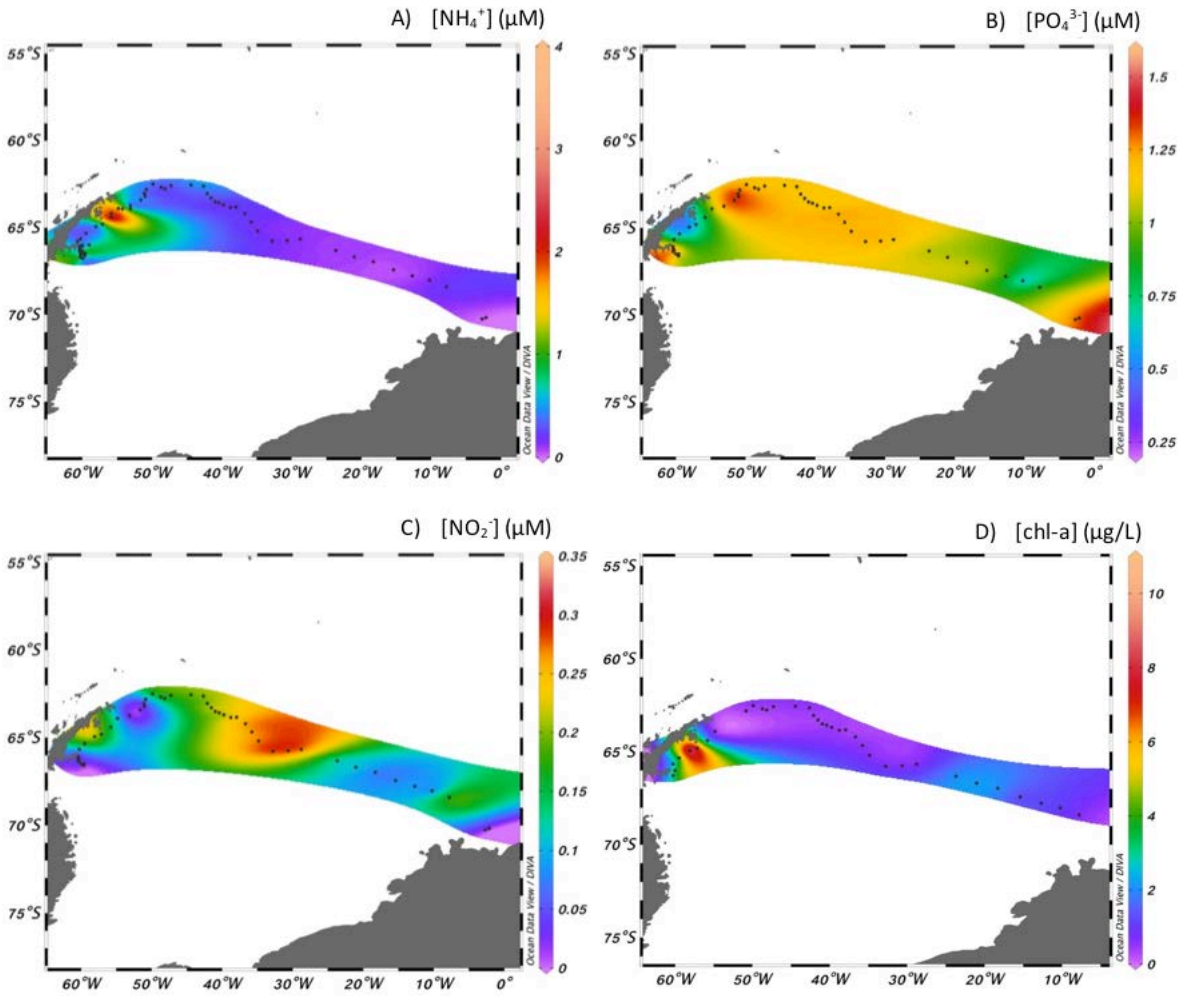

***Figure 7.10**. Surface concentrations of a) ammonium (NH_4^+), b) phosphate (PO_4^{3-}), c) nitrite (NO_2^-) and d) bulk chlorophyll for samples collected on the underway leg from RSA Penguin Bukta to the Larsen C ice shelf. All samples were measured shipboard.*

7.4 Palaeoceanography: microfossil recorders of past ocean nutrient conditions

7.4.1 Introduction

The ultimate fate for carbon biomass that is produced in surface waters and escapes recycling is deposition on the seafloor. This sedimentary layer is thus affected by climatic and environmental changes over Earth's history, and palaeoceanographic reconstructions based on microfossils and isotopes preserved in deep-sea sediments provide clues to regional temperature variations, fluctuations in global amplifiers of regional signals (e.g., CO_2) and the degree of seasonal nitrate drawdown. Deciphering these records is a challenge, however, because they are not based on direct measurements. Instead, they rely on palaeoproxies that have to be constrained through ground-truthing studies, few of which exist, particularly for remote sites such as the Southern Ocean and in particular the Weddell Sea. Here, we focus on diatom microfossils, which we will analyse for community composition and N isotopic

composition. This latter measurement is thought to provide a reliable metric of past nitrate utilization by phytoplankton (e.g., Studer et al. 2012; 2013) because the organic N intrinsic to diatom fossils is protected from diagenetic alteration and contamination by the diatom's resilient silica frustules (Robinson et al. 2012; Meckler et al. 2011). However, still lacking is a direct comparison of modern (i.e., upper ocean phytoplankton and sea-ice diatoms) and recently-deposited organisms with the environmental variables that they are thought to record (e.g., surface nitrate isotopic composition).

7.4.2 Methods

Surface sediment samples: Surface sediment samples were collected from both the gravity core deployments and the multi corer (supplied and operated by NIOZ) at the following stations:

Gravity corer: AM00984; AM0085; AM0086; GC0022; AM00989
Multi corer: AM00978; AM00979; AM00988; AM00990; AM00991; AM00992; AM00993

It was not always possible to determine the exact surface layer of the gravity core samples such that these samples will be used only as back-up material. The multi corer collected a sediment core of 30-40 cm in length with a clear distinguishable surface layer. Microcentrifuge tubes (1.5 mL) were used to take a subsample of the surface layer down to a maximum depth of 0.5 cm. Two samples were collected from each core surface and a minimum of 5 cores (i.e., n = 10) were sampled per station. The microcentrifuge tubes were sealed with parafilm and frozen at -20^{0}C for later analyses of isotopes and diatoms.

Full length multi core samples: Six full length multi core samples were collected (Table 7.2) and sectioned onboard into 1 cm slices. Each section was split into two halves for diatom and isotopic analyses, respectively. Each half section was separately bagged and frozen at -20^{0}C (for 24 hours) and thereafter at -80^{0}C for later analyses of isotopes and diatoms.

Station	Core length (cm)	Sections
AM00978	40	34
AM00979	37	28
AM00988	39	32
AM00990	38	32
AM00992	36	31
AM00993	29	27

***Table 7.2**. List of multi core samples collected and sectioned on board.*

***Figure 7.11**. (a) Multi Corer back on deck (b) Dense phytoplankton floc on the surface of a core*

7.4.3 Preliminary results

The samples from the surface sediment and core sections will be analysed at the UCT for N isotopes and Nelson Mandela University for diatom identification. These data will be compared to surface layer collections of diatoms and nitrate isotopes. A scan of the surface sediment under a Zeiss microscope onboard revealed a very high concentration and diversity of diatoms from both the phytoplankton and the sea-ice habitat (Figure 7.12). A large percentage of the diatoms appeared to still contain cellular matter, which will be useful for isotopic analysis. The dead plankton floc layer on the seafloor was several cm thick at some of the sites, illustrating the importance of phytoplankton (particularly diatoms) for deep-sea carbon sequestration.

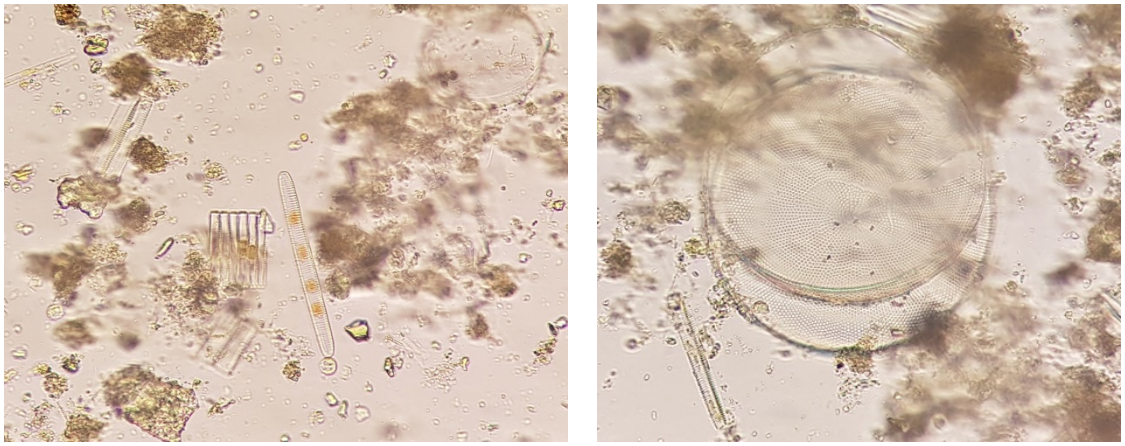

***Figure 7.12.** Two light micrographs of the surface sediment with obvious intact diatom frustules*

7.5 Atmospheric Chemistry

7.5.1 Introduction

The emissions of anthropogenic nitrogen (N) to the atmosphere, and its subsequent deposition, have increased greatly since preindustrial times causing substantial impacts on the global N cycle (Galloway et al., 2004). The effects of this increased anthropogenic N deposition are well documented and have led to a series of consequences for atmospheric chemistry, ecosystems, and human health, referred to as the 'nitrogen cascade' (Erisman et al., 2013; Fowler et al., 2013; Galloway et al., 2003; Vitousek et al., 1997; Elser et al., 2009; Howarth et al., 2000; Peierls and Paerl, 1997). However, the implications of atmospheric deposition of anthropogenic N to the open ocean and the amount of N released to the marine atmosphere from the ocean through natural processes, such as surface ocean photochemistry and biological activity, are still uncertain (Duce et al., 2008). The Southern Ocean and the Weddell Sea are the most remote marine regions on Earth, which allows for the study of marine emissions without interference from anthropogenic signals. The results in the Southern Ocean may also act as a proxy for the preindustrial scenario, which, in the case of ammonia gas (the precursor to particulate ammonium), will also give information about the largest preindustrial ammonia source, with implications for aerosol formation and radiative forcing uncertainty.

The goal of this work is to investigate the surface ocean and lower atmosphere N cycle in the most remote marine region of the global ocean to test the hypothesis that the surface ocean can be a significant source of N to the marine atmosphere. N isotopes can be used to trace marine vs. anthropogenic N sources, augmented by inorganic N concentration measurements and NOAA HYSPLIT model (NOAA Hybrid Single-Particle Lagrangian Integrated Trajectory Model) airmass back trajectories.

7.5.2 Methods

High volume air sampler (HV-AS): Pre-combusted glass fibre filters (GFFs) were used to collect atmospheric samples using a Tisch Environmental high-volume air sampler (HV-AS) fitted with a five-stage cascade impactor, including a sixth filter that acted as a backup sample. The HV-AS, mounted to the port side of deck 8 was functional for the entire duration of the expedition. A Campbell Scientific Africa sector collector was used to restrict the periods when the HV-AS was active, such that the HV-AS would only switch on if the wind direction was <75° and >140° from the bow of the ship for at least ten minutes, so as to avoid contamination from the ship's fume stack. Samples were left until the HV-AS had been switched on for 24 hours. GFFs were mounted and removed from the cascade impactor in an Air Science laminar flow cabinet, and the cascade impactor was cleaned with 99.9% reagent-grade ethanol after filters were removed. Samples were placed in individual zip-sealed plastic bags and stored at -20°C pending analysis at MBL-UCT for inorganic and organic nitrogen concentrations, and ammonium and nitrate N isotopic compositions ($\delta^{15}N$).

Ambient ion monitor-ion chromatography (AIM-IC): An ambient ion monitor and two ion chromatographs were used to measure the concentrations of anions (sulphate, nitrate, nitrite, bromide, fluoride, chloride, and phosphate) and cations (ammonium, calcium, lithium, sodium, magnesium, and potassium) in the gas and particle phase. The AIM-IC was run during the transit leg from RSA Penguin Bukta to the Weddell Sea, from 4 January to 11 January 2019. The inlet to the AIM was mounted at the highest point on the ship to avoid sampling smoke and other ship-related emissions. A check-standard (lithium bromide) was analysed regularly by the system and used to track any drift from the baseline. A calibration sequence of the seven anions and six cations, each containing a range of six standard solutions, was run at the beginning of the expedition. The AIM collected samples over consecutive two-hour periods, which lined up temporally with every second underway station since underway stations were sampled four hourly.

7.6 Ice operations

7.6.1 Introduction

Sea ice is a vital component of the global climate system. The presence of sea ice influences the albedo of the polar regions; deep water formation and the transfer of heat, moisture and momentum between the ocean and the atmosphere. In addition, sea ice has significant implications for the biological and chemical properties of the polar oceans. Sea ice growth leads to the entrapment of nutrients and biological components in the sea ice, which may develop into a sympagic community and eventually bloom. This entrapment allows a Biologically Active Layer (BAL) to develop. Despite its importance, very little is known about the internal vertical structure of sea ice, the distribution of biogeochemical constituents and the biogeochemical cycling that occurs both within the ice and between the ice and underlying ocean. Understanding sea ice cover is essential for the development of physical and biogeochemical models and for improving the accuracy of existing models in the region. More accurate data is required for models to produce optimum results (Smith, 1987).

Tedesco et al. (2010) introduced the novel approach for modelling sea ice biology by defining the BAL as the time varying fraction of sea ice connected to the ocean where microorganisms are able to live and grow. The layer is characterised by a brine volume greater than 5% and is required to be in continuous connection with sea water in order to receive sufficient nutrients and dissolved gasses necessary for growth (Figure 7.13).

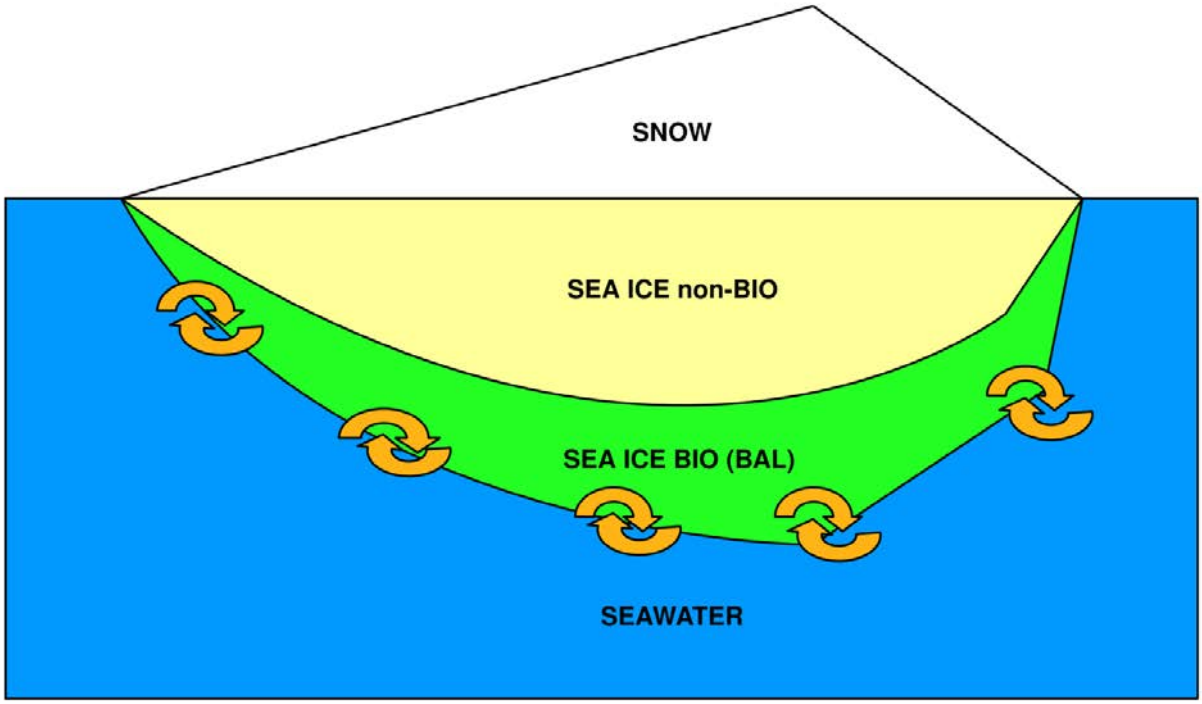

Figure 7.13. *Representation of the Biologically Active Layer in sea ice (Tedesco et al., 2010).*

7.6.2 Methods

Sea ice fieldwork: For the duration of the expedition, sea ice field work was conducted opportunistically by the joint UCT-SUN teams. The aim was to develop a suitable sea ice sampling protocol to investigate the physical and biogeochemical properties of sea ice, including the BAL, using sea ice cores taken from sea ice floes that varied in age and thickness.

Once a suitable floe was identified, it was assessed for health and safety purposes by the expedition leader. The scientists selected locations according to snow thickness and floe topography. The location of each core drilling site is listen in Table 7.3. A snow pit was dug first to measure the snow thickness and to enable the ice cores to be taken as close to the ice surface as possible (Figure 7.14). The first core extracted was measured for length and stored for later biogeochemical analysis at the UCT under strict laboratory conditions to prevent any contamination. The work on the physical properties of the ice cores began immediately after a second core was collected. The temperature was measured every 10 cm by drilling a hole in the core and inserting a temperature probe. Once onboard the vessel, the cores were sectioned and cut into 10 cm segments and melted down. Each melted sample was filtered onto a 25 mm 0.3 µm glass fibre filter (GF/F) for chlorophyll-a determination, and the filtrate was kept for the analysis of salinity and nutrients. This protocol was followed for all the sea ice cores taken during the WSE; for an overview, see Table 7.3.

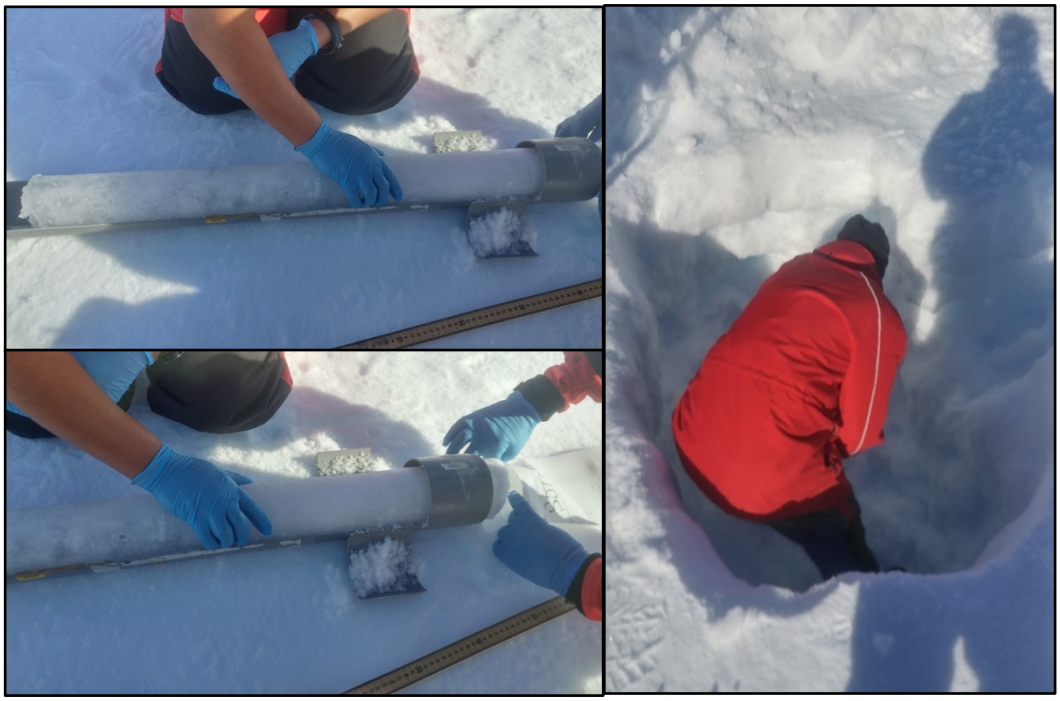

***Figure 7.14**. Anticlockwise from right: Snow pit being dug by one of the scientists involved in sampling; ice core resting in a PVC cradle where both length and temperature were measured; sea ice core being bagged for transport and storage.*

The observational data will be combined with numerical modelling, the main objective of which is to explain the processes leading to the accumulation of chemical and biological components in the marginal ice zone (MIZ) and their evolution as the ice season advances. A model for sea-ice biogeochemistry has been proposed by Tedesco et al. (2009, 2010), and can be expanded to include features that are specific to the Antarctic pancake ice field.

CORE TYPE	NUMBER	DATE CORED	LOCATION	ICE TYPE	SNOW THICKNESS (cm)	NUMBER OF SEGMENTS	TOTAL LENGTH (cm)
Physical	1	1/1/2019	70.173 S; 2.129 W	Bay ice	Unknown	3	157
BGC	1	1/1/2019	70.173 S; 2.129 W	Bay ice	Unknown	3	163
Physical	2	1/1/2019	70.173 S; 2.129 W	Bay ice	48.5	3	159
BGC	2	1/1/2019	70.173 S; 2.129 W	Bay ice	48.5	3	176
Physical	3	2/1/2019	70.173 S; 2.129 W	Bay ice	55.6	3	155
BGC	3	2/1/2019	70.173 S; 2.129 W	Bay ice	55.6	2	142.5
Physical	4	16/01/2019	65.779 S; 60.556 W	Sea ice	80	8	661
BGC	4	16/01/2019	65.779 S; 60.556 W	Sea ice	80	7	480
BGC	5	17/01/2019	65.773 S; 60.5198 W	Sea ice	161.5	10	537.5

***Table 7.3**. List of all sea ice cores taken during the WSE. Number of segments indicate the number of pieces that make up a complete core.*

Sea ice observations: The MIZ is the boundary region between the sea-ice covered ocean and the open ocean. This abrupt change results in intense air-sea interactions. These interactions and their intensity influence the variability of sea-ice cover in the MIZ (Muench, 1989). Understanding how the sea-ice cover evolves as the vessel moves from the open ocean into the sea-ice dominated region is vital for navigational and scientific purposes. General sea ice characteristics can be obtained from passive microwave satellite sensors. Although satellites can provide uninterrupted observations, they are limited in what they can observe. Ship-based observations and data collection enable us to obtain more detailed records of sea ice. By following the Antarctic Sea Ice Processes and Climate (ASPeCt) protocol, which is an internationally accepted method of sea-ice observation, observers are able to assess a broader spectrum of sea-ice characteristics.

The ASPeCt protocol looks at the sea-ice type, thickness, shape, edge properties, snow characteristics, and total concentration compared to open water to assess the sea-ice cover in the Polar region. Sea-ice features like leads, weathered ridges and types of rafting are also identified (Table 7.4). Included in the ASPeCt protocol are meteorological observations of the conditions that would influence the sea-ice cover in the area e.g., cloud cover, current weather conditions, wind speed and air temperature (Table 7.5).

Ice observations for the WSE leg started on the 3 January 2019 and continued through the search for the Endurance and transit back to Penguin Bukta. The observations are conducted from the bridge of the *SA Agulhas II* whenever the vessel is sailing through ice-covered waters. These observations are supplemented by video recordings of the ice conditions from wide-angle action cameras mounted on the port side of monkey island.

***Table 7.4**. Ice observations log sheet following the ASPeCt Protocol*

Date (Z): *NOTE: Primary sea ice is of greatest concentration. Hence c1 > c2 > c3

SEA ICE OBSERVATIONS

POSITION			PRIMARY							SECONDARY							TERTIARY								
hr (Z)	Lat (°S)	Lon (°E)	Conc. (tenths)	c	ty	z (cm)	f	t	s	sz (cm)	c	ty	z (cm)	f	t	s	sz (cm)	c	ty	z	f	t	s	sz (cm)	O/W	hr (Z)

Key	
Hr (z)	Hour
Total Conc.	Total concentration of the observed sea ice environment
c	Concentration of type of sea ice observed
ty	Type of ice observed
z	Sea ice thickness
f	Floe size
Twater	Water Temperature
Tair	Air temperature
Wind	Wind speed
Cloud	Cloud cover
Visib	Visibility
Weather	Current weather conditions
s	Type of snow observed
sz	Snow thickness

Table 7.5. *Meteorological observations log sheet following the ASPeCt Protocol*

METEOROLOGICAL OBSERVATIONS

hr (Z)	Twater (°C)	Tair (°C)	Wind (Knots)	Cloud (oktas)	Visib (v)	Weather (ww)	COMMENTS	OBSERVER	hr (Z)

7.7 References

Absy, J. M., Schröder, M., Muench, R., and Hellmer, H., 2008. Early summer thermohaline characteristics and mixing in the western Weddell Sea. *Deep Sea Research Part II*: Topical Studies in Oceanography, 55, 1117-1131.

Bendschneider, K. and Robinson, R.J., 1952. A new spectrophotometric method for the determination of nitrite in sea water. *Technical Report No. 8*. University of Washington.

Casciotti, K.L., Sigman, D.M., Hastings, M.G., Böhlke, J.K. and Hilkert, A., 2002. Measurement of the oxygen isotopic composition of nitrate in seawater and freshwater using the denitrifier method. *Analytical Chemistry*, 74, 4905–4912. doi:10.1021/ac020113

Cullen, J.J., 2001. Plankton: Primary Production Methods. *In* Steele, J., Thorpe, S., Turekian, K. (eds) *Encyclopedia of Ocean Sciences*. Academic Press, San Diego, 2277–2284.

Dentener, F. et al., 2008. Impacts of Atmospheric Anthropogenic Nitrogen on the Open Ocean. *Science,* 320, 893-897.

Diamond, D., 1994. QuikChem Method 10-114-21-1-B: Silicate by flow injection analysis. Lachat Instruments.

Dugdale, R.C., and Goering, J.J., 1967. Uptake of new and regenerated forms of nitrogen in primary productivity. *Limnology and Oceanography*, 12, 196–206.

Duce, R.A., LaRoche, J., Altieri, K.E., Arrigo, K.R., Baker, A.R., Capone, D.G., Cornell, S., itousek, P., Aber, J., Howarth, R., Likens, G., Matson, P., Schindler, D., Schlesinger, W. and

Eppley, R.W. and Peterson, B.J., 1979. Particulate organic matter flux and planktonic new production in the deep ocean. *Nature*, 282, 677-680.

Erisman, J., Galloway, J., Seitzinger, S., Bleeker, A., Dise, N., Petrescu, A., Leach, A., and de Vries, W., 2013. Consequences of human modification of the global nitrogen cycle. *Philosophical Transactions of the Royal Society B: Biological Sciences*, 368.

Etourneau, J., Sgubin, G., Crosta, X., Swingedouw, D., Willmott, V., Barbara, L. and Goosse, H., 2019. Ocean temperature impact on ice shelf extent in the eastern Antarctic Peninsula. *Nature Communications*, 10, 304.

Fahrbach, E., Rohardt, G., Scheele, N., Schröder, M., Strass, V. and Wisotzki, A., 1995. Formation and discharge of deep and bottom water in the northwestern Weddell Sea. *Journal of Marine Research*, 53, 515-538.

Fawcett, S.E., Lomas, M.W., Ward, B.B. and Sigman, D.M., 2014, The counterintuitive effect of summer-to-fall mixed layer deepening on eukaryotic new production in the Sargasso Sea. *Global Biogeochemical Cycles,* 28, 86-102.

Fawcett, S.E., Lomas, M.W., Casey, J.R., Ward, B.B. and Sigman, D.M., 2011. Assimilation of upwelled nitrate by small eukaryotes in the Sargasso Sea. *Nature Geoscience,* 4, 717-722.

Galloway, J.N., Aber, J.D., Erisman, J.W., Seitzinger, S.P., Howarth, R.W., Cowling, E.B., and Cosby, B.J., 2003. The Nitrogen Cascade. *BioScience*, 53, 341–356.

Galloway, J.N., Dentener, F.J., Capone, D.G. et al., 2004. *Biogeochemistry*, 70, 153.

Gille, S.T., 2002. Warming of the Southern Ocean since the 1950s. *Science,* 29, 1275-1277.

Gordon, A., 2009. *Bottom Water Formation.* Associated Press.

Gordon, A.L., Huber, B.A., Hellmer, H.H. and Ffield, A., 1993. Deep and Bottom Water of the Weddell Sea's Western Rim. *Science*, 262, 95-97.

Granger, J. and Sigman, D.M., 2009. Removal of nitrite with sulfamic acid for nitrate N and O isotope analysis with the denitrifier method. *Rapid communication in mass spectrometry*, 23, 3753-3762.

Grasshoff, K., 1976. Methods of seawater analysis. Verlag Chemie, Weinheim and New York.

Holland, P.R., Jenkins, A. and Holland, D.M., 2008. The response of ice shelf basal melting to variations in ocean temperature. *Journal of Climate*, 21, 2558-2572.

Holmes, R., Aminot, I., Kërouel, R., Hooker, B. and Peterson, B., 1999. A simple and precise method for measuring ammonium in marine and freshwater ecosystems. *Canadian Journal of Fisheries and Aquatic Sciences*, 56, 1801-1808.

Howarth, R., 2000. *Nutrient pollution of coastal rivers, bays, and seas*. Washington, DC: Ecological Society of America.

Kerr, R., Dotto, T.S., Mata, M.M. and Hellmer, H.H., 2018. Three decades of deep water mass investigation in the Weddell Sea (1984–2014): temporal variability and changes. *Deep Sea Research Part II*: Topical Studies in Oceanography, 149, 70-83.

Martin, J.H., Gordon, R.M. and Fitzwater, S.E., 1991. The case for iron. *Limnology and Oceanography,* 36, 1793-1802.

Meckler, A.N., Ren, H.A., Sigman, D.M., Gruber, N., Plessen, B., Schubert, C.J. and Haug, G.H., 2011. Deglacial nitrogen isotope changes in the Gulf of Mexico: Evidence from bulk sedimentary and foraminifera-bound nitrogen in Orca Basin sediments. *Paleoceanography* 26, PA4216.

Muench, R., 1989. The sea ice margins: A summary of physical phenomena. *NOAA Tech. Memo* ERL PMEL-88, 51.

Nicholls, K.W., Makinson, K. and Venables, E.J., 2012. Ocean circulation beneath Larsen C Ice Shelf, Antarctica from in situ observations. Geophysical Research Letters, 39.

Nicholls, K.W., Østerhus, S., Makinson, K., Gammelsrød, T. and Fahrbach, E., 2009. Ice-ocean processes over the continental shelf of the southern Weddell Sea, Antarctica: A review. *Reviews of Geophysics*, 47.

Nicholls, K., Pudsey, C. and Morris, P., 2004. Summertime water masses off the northern Larsen C Ice Shelf, Antarctica. *Geophysical Research Letters*, 31.

Orsi, A., Johnson, G. and Bullister, J., 1999. Circulation, mixing, and production of Antarctic Bottom Water. *Progress in Oceanography*, 43, 55-109.

Parsons, T.R., Maita, Y. and Lalli, M., 1984. A Manual of Chemical and Biological Methods for Seawater Analysis.

Peierls, B.L. and Pearl, H.W., 1997. Bioavailability of atmospheric organic nitrogen deposition to coastal phytoplankton. *Limnology and Oceanography*, 42, 1819–1823.

Peng, X., Fawcett, S.E., van Oostende, N., Wolf, M.J., Marconi, D., Sigman, D.M. and Ward, B.B., 2018. Nitrogen uptake and nitrification in the subarctic North Atlantic Ocean. *Limnology and Oceanography*.

Post, A.L., Galton-Fenzi, B.K., Riddle, M.J., Herraiz-Borreguero, L., O'Brien, P.E., Hemer, M.A., McMinn, A., Rasch, D. and Craven, M., 2014. Modern sedimentation, circulation and life beneath the Amery Ice Shelf, East Antarctica. *Continental Shelf Research*, 74, 77-87.

Rathbun, C., 1997. Measurement of Chlorophyll a and Phaeopigments by Fluorometric Analysis. *In* Bermuda Atlantic Time-series Study Methods.

Robertson, R., Visbeck, M., Gordon, A.L. and Fahrbach, E., 2002. Long-term temperature trends in the deep waters of the Weddell Sea. *Deep Sea Research Part II*: Topical Studies in Oceanography, 49(21), 4791-4806.

Robinson, R.S., M. Kienast, A.L. Albuquerque, M. Altabet, S. Contreras, R. De Pol Holz, N. Dubois, R. François, E. Galbraith, T.-C. Hsu, T. Ivanochko, S. Jaccard, S.-J. Kao, T. Kiefer, S. Kienast, M. Lehmann, P. Martinez, M. McCarthy, J. Möbius, T. Pedersen, T.M. Quan, E. Ryabenko, A. Schmittner, R. Schneider, A. Schneider-Mor, M. Shigemitsu, D. Sinclair, C. Somes, A. Studer, R. Thunell, J.-Y. Yang. A review of nitrogen isotopic alteration in marine sediments (2012) *Paleoceanography* 27, PA4203.

Sarmiento, J.L. and Toggweiler, J.R., 1984. A new model for the role of the oceans in determining atmospheric pCO_2. *Nature,* 308, 621-624.

Saxberg, B. and Kowalski, W., 1979. Generalised standard edition method. *Analytical Chemistry*, 51, 1031-1038.

Shepherd, A., Wingham, D. and Rignot, E., 2004. Warm ocean is eroding West Antarctic ice sheet. *Geophysical Research Letters*, 31.

Sigman, D.M. and Boyle, E.A., 2000. Glacial/interglacial variations in atmospheric carbon dioxide. *Nature,* 407, 859-869.

Sigman, D., Casciotti, K.L., Andreani, M., Barford, C., Galanter, M. and Böhlke, J.K., 2001. A Bacterial Method for the Nitrogen Isotopic Analysis of Nitrate in Seawater and Freshwater. *Analytical Chemistry*, 73, 4145–4153.

Sigman, D.M., Hain, M.P. and Haug, G.H, 2010. The polar ocean and glacial cycles in atmospheric CO_2 concentration. *Natur,e* 466, 47-55.

Smith Jr, W.O., 1987. Phytoplankton dynamics in marginal ice zones. Oceanography. *Marine Biology*, 25, 11-38.

Strickland, J.D. and Parsons, T.R., 1968. A practical handbook of seawater analysis. *Bull. Fish. Res. Bd. Can*., 167.

Studer, A.S., Ellis, K.K., Oleynik, S., Sigman, D.M. and Haug, G.H., 2013. Size-specific opal-bound nitrogen isotope measurements in North Pacific sediments *Geochmica et Cosmochimica Acta,* 120, 179-194.

Studer, A.S., Martínez-García, A., Jaccard, S.L., Girault, F.E., Sigman, D.M. and Haug, G.H., 2012. Enhanced stratification and seasonality in the Subarctic Pacific upon Northern Hemisphere glaciation new evidence from diatom-bound nitrogen isotopes, alkenones and archaeal tetraethers. *Earth and Planetary Science Letters,* 351, 84-94.

Sunda, W.G. and Huntsman, S.A., 1997 Interrelated influence of iron, light and cell size on marine phytoplankton growth. *Nature,* 390, 389-392.

Tedesco, L., Vichi, M., Haapala, J. and Stipa, T., 2009. An enhanced sea-ice thermodynamic model applied to the Baltic Sea. *Boreal Environmental Research*, 14, 68–80.

Tedesco, L., Vichi, M., Haapala, J. and Stipa, T., 2010. A dynamic biologically-active layer for numerical studies of the sea ice ecosystem. *Ocean Modelling*, 35, 89–104.

Treibergs, L.A. and Granger, J., 2011. Enzyme level N and O isotope effects of assimilatory and dissimilatory nitrate reduction. *Limnology and Oceanography*, 62, 272-288.

van Caspel, M., Schröder, M., Huhn, O. and Hellmer, H., 2015. Precursors of Antarctic Bottom Water formed on the continental shelf off Larsen Ice Shelf. *Deep Sea Research Part I*: Oceanographic Research Papers, 99, 1-9.

Welschmeyer, N., 1994. Fluorometric analysis of chlorophyll a in the presence of chlorophyll b and phaeopigments. *Limnology and Oceanography*, 39,1985-1992.

8. Marine Biology

L. Woodall, M. Taylor and B. Frinault

8.1 Introduction

8.1.1 Background

There have been just ten major ice-shelf calving events from the Larsen C Ice Shelf in the last few decades. These events have widespread impacts on glaciology, local and regional biogeochemistry (Peck et al., 2010), physical oceanography (Arrigo et al., 2002), and the structure and function of local and regional ecosystems, and their biology. Against this background there has been hardly any research of under-ice environments, prior to ice calving. The first study to reveal life below an ice sheet was at two highly crevassed region of the Ross Ice Shelf in 1962, they documented amphipods, polychaetes, hydroids, coral, sponges, pycnogonids and gastropods amongst others (Littlepage and Pearse, 1962). In the late 1970s (Clough and Hansen, 1979) at the Ross Ice Shelf found amphipods, some isopods (through baited traps), and *Trematomus* fish species, confirming life beneath this ice shelf. About 100 km away from the open-ocean, beneath the Amery Ice Shelf, benthic organisms similar to other deep-sea Antarctic fauna were found including at least seven phyla (Riddle et al., 2007). Later Post et al. (2014) found fewer suspension feeders and more deposit feeders deeper under the ice shelf than towards the ice-shelf edges. This minimal background of data leaves a mixed picture of what life to expect under ice shelves and how this could change in regime-shift conditions such as ice-shelf collapse and retreat.

The above research is hampered by access to under ice-shelf areas. Iceberg calving events provide an opportunity, albeit a short-term one, to study life "under the ice" in an easier manner. However, post-ice calving studies tend to be delayed due to issues with access, funding and ship availability, amongst other logistical challenges. This makes them few and far between (Gutt et al., 2011, 2013; Fillinger et al., 2013).

8.1.2 Research Questions

Our research questions were initially focused on understanding the differences in biological communities before and after they are covered by shelf ice following a calving event such as that of the huge iceberg A68 from the Larsen C Ice Shelf in July 2017. In addition, we were interested in comparing community composition at distances of 10, 50, 100 and 500 m under the ice shelf. We planned to conduct research into mega benthic fauna, pelagic bacteria and macro infauna communities. Following the realisation that we were unable to get to the A68 calving site, because of unnavigable sea ice, questions were amended to:

- Are megabenthic communities from sites of most recent ice-shelf collapse more depauperate than those from sites from which ice was been gone for a longer period? Video data.
- How do macro infaunal communities vary over a gradient of disturbance (iceberg ploughing intensity)? Sediment (multicore) data.
- How do microorganism communities change from ice shelf areas to the open sea? Water filtration samples.

8.2 Megafauna benthic communities

8.2.1 Methods

- Locations that had been clear of shelf ice for different periods were identified (Cook et al., 2016). Sites that were clear for 5, 20 and 50 years were chosen along with a control that appeared not to have been covered in recent history. All sites chosen were expected to be in approximately 400 m depth, with flat to gently sloping terrain and be dominated by soft sediment. It should be noted that although ice-shelf extent was known, the percentage of time covered by sea ice was unmapped. It is known that this was extensive for most of the last twenty years; however, this is yet to be elucidated in detail.
- The remotely operated vehicle (ROV) ran three video transects of approximately 750 m. This was later demonstrated to be of sufficient length to capture the biodiversity of the sites.
- When possible, a biological collection was made at the end of each dive using the ROV manipulator arm in order to assign correct identification to morphotypes seen on the video of the seafloor. However, it was only possible to undertake extensive collections at site A.

8.2.2 Dive narratives

Five ROV dives were dedicated to biological research (Fig. 8.1). The dive narratives follow.

Site B: Inside the 1963 line - Exposed for about 50 years

Ice prevented the deployed at the start of transect 1 so we transited to the start of transect 2 to start the dive. The dive with ROV *Lassie* was conducted with no biobox as this was not tested during the trials dives and there was too much ice in the area to consider leaving a box on the seabed. The vehicle performed very well, with one camera fault that required returning to the surface. The cause of which was subsequently determined by the Eclipse team, and was fixed. Transect 2 was followed as the first transect, however the start location and heading for the second and third transects were made on the fly, according to ice conditions and limited time available.

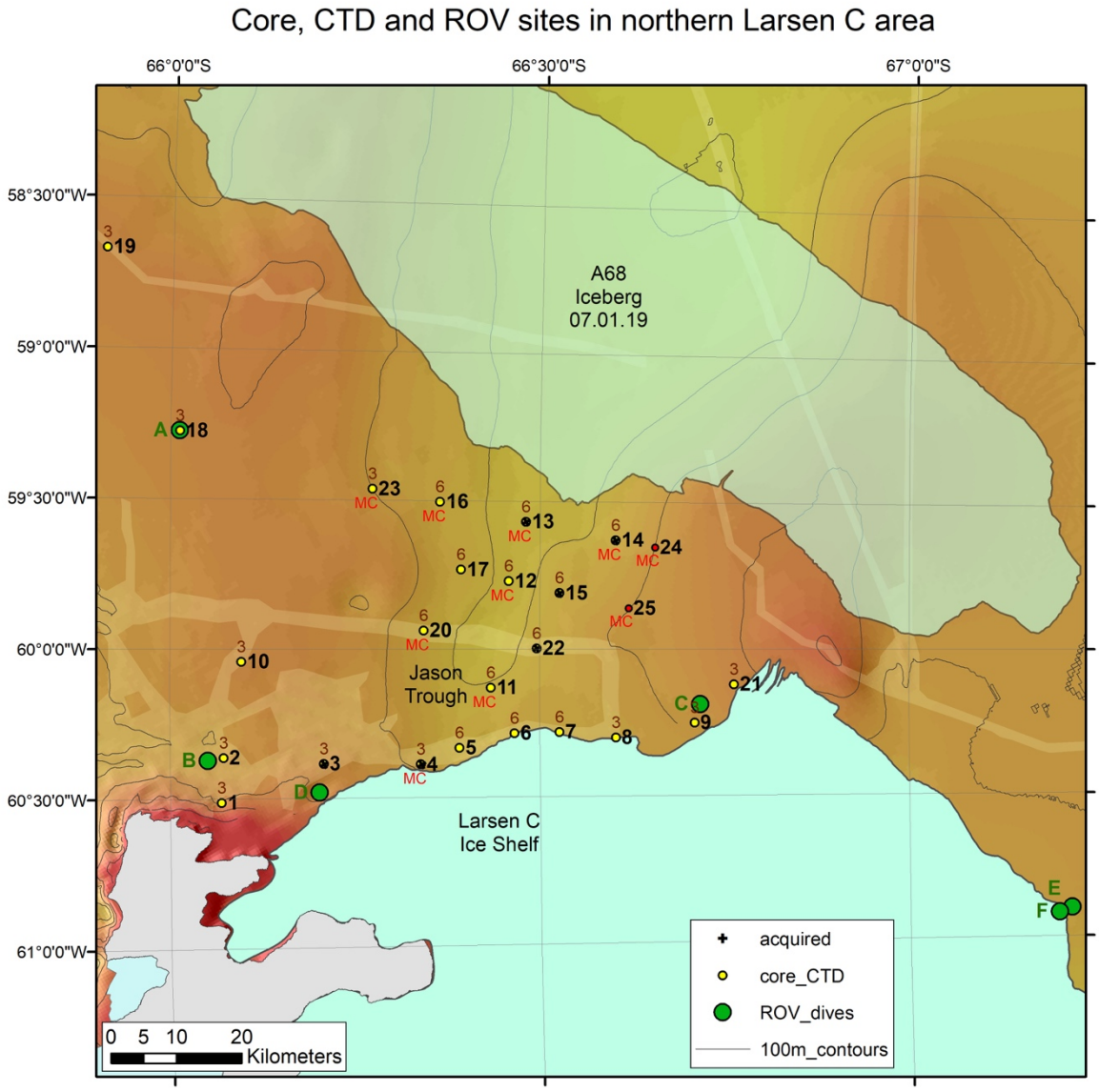

***Figure 8.1**. Map to show successful deployments of the sediment corer, CTD and ROV.*

The seabed was initially flat with patchy and high accumulations of drop stones and other rocks. At the end of the final transect the ground undulated gradually but the maximum and minimum depths did not differ by more than 10 m in total across the entire dive, with an average depth of 400m. There was evidence of a recent planktonic bloom on the seabed and in the water column, which was previously identified by net and CTD operations. This meant the entire seafloor and much of the fauna was covered in green flocculent, making identification of organisms more challenging.

Most of the fauna encountered were Echinoderms. Brittle stars making up most of the visible biomass. In addition, feather and cushion stars were frequently seen. Crinoids, urchins and sea cucumbers (Holothuroidea) were seen, each with 10, 4 and 6 morphotypes respectively. Cnidaria were also present, although in lower numbers. Coral and anemones had 11 morphotypes each and were seen in higher numbers in transect 3. Cnidaria included a number of octocorals, Stolonifera, solitary (*Flabellum*), the seapen *Umbellula,* and dead whip corals. Furthermore pycnogonids (sea spiders), tunicates (sea squirts), worms (seen as worm mounds

and assumed to be polychaetes) and porifera (sponges) were seen. Carnivorous sponges were the most numerous types of sponge, but barrel, stalked and encrusting morphotypes were also seen. Notably two stalked jellyfish (Staurozoa) were observed just a few meters from each other attached to small rocks. Fish fauna was limited to three morphotypes including black fin icefish (*Chaenocephalus aceratus*). In addition, krill were numerous during the entire dive. Species accumulation curves demonstrated sufficient transect length (Fig. 8.2).

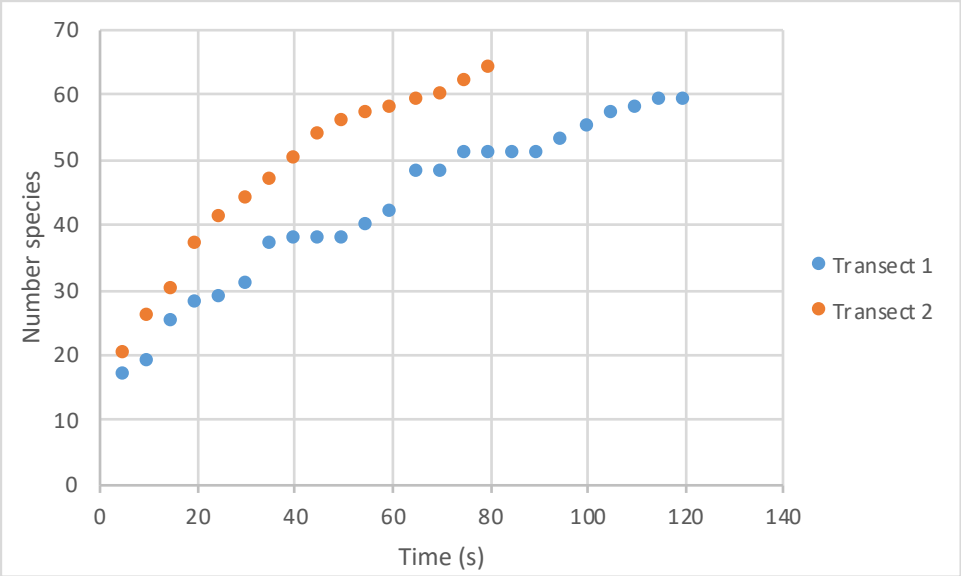

***Figure 8.2**. Species accumulation curve for two transects of site B: The levelling off of the lines demonstrates appropriate sampling.*

Site D: 2001 to 2004 – 15 to 18 years since ice shelf coverage

This site was surprisingly shallow (270 m). From extrapolated bathymetric data it was thought to be about 400m. The seafloor had regular depressions of about 2-3 m depth and 5-8 m width, and these are assumed to be scars from ice. Large boulders were sometimes observed at the top of these scars in addition to the small rocks and sediment that were present throughout. An indented impact zone was visible around some of the larger boulders.

Less marine snow was seen here compared with other sites, this correlated with a decrease of plankton at the surface, observed by pelagic sampling methods. This was the most depauperate site, with only 90 morphotypes seen. Again, Echinodermata dominated this location across all transects. Of note, on transect 1 a siphonophore (Fig. 8.3a) were first observed, transect. The icefish *Hapagifer* sp. was also seen for the first time at this site.

a b c

Figure 8.3. *Typical organism of Antarctica as seen at site D transect 2. (a) Siphonophore at 260 m (Rhodaliidae). (b) Sea pig. (c) Nemertina worm.*

Site C: 2009 to 2014 - Exposed for 5 to 10 years

The location, heading and total length of transects at site C were completely determined by ice conditions. The ship's crew understood the transect requirements and conducted transects as requested when possible, however transects had to be stopped, moved and direction changed as safety of the vessel dictated. The transects were conducted on different dives but were only a few km apart. It was not possible to complete the entire third transect due to sea-ice influx.

The transects differed in their bottom type. Transect 1 had gently shelving terrain with occasional scar-like features. Larger rocks were more frequently seen that at other sites. Transect 2 and 3 had fewer rocks especially large ones. Strong tidal currents were encountered and this site also had the most marine snow.

Site C was the most speciose site, with a high diversity of coral (bottlebrush, fan and whip) (13), brittle stars (14) and holothurians (6). Abundance was high for most taxa, but some such as crinoids, stalked ascidians and sponges appeared less frequently. Notably in transect 1 two burrowing octopus were seen, and the later transects had a higher diversity and abundance of whip corals. Furthermore, clams related to chemosynthetic environments, in this case thought to be cold seeps, and likely to be *Calyptogena* sp., were seen in large dead aggregations in transects (Fig. 8.4).

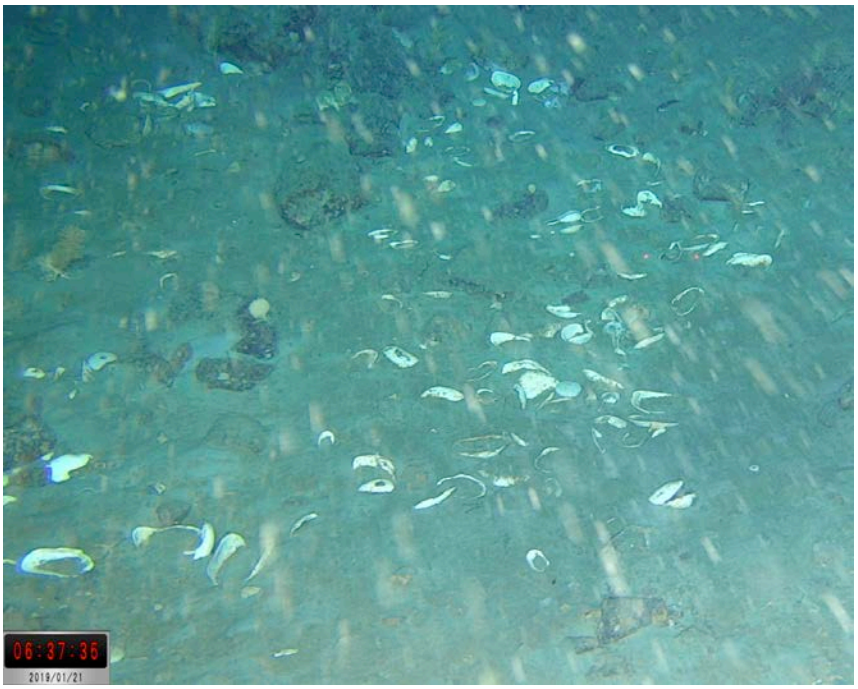

***Figure 8.4**. Clam Calyptogena sp. in a large aggregation.*

Site A (10): Pre-1963 - Not covered by ice shelf in recent history according to records

The seafloor was initially very flat with small rocks then some larger rocks appears at the tops of the banks later in the dive. Fauna were similar to site C, with a total of 182 morphotypes. However, there were a number of specimens and observations of note. These included octopus, sea pens and nudibranch (Fig. 8.5). There was greater diversity and abundance in anemones (9) and well as holothurians (6). Finally, juvenile icefish were observed in some nests.

***Figure 8.5**. Notable fauna from site A: octopus (transect 1), sea pen (transect 2) and nudibranch (transect 3).*

8.3 Faunal Collections

Collections were made from sites B, C and 10. All but the collection at site 10 was just one main specimen. At site 10 multiple collections were made into a bio-box. All were preserved in ethanol with subsamples taken when deemed necessary for DNA preservation or in the case of glass sponges dried for silicate analysis. A total of 38 separate specimens were documented (Fig. 8.6). Additional collections were made at Erebus and Terror Gulf, and resulted in an additional 211 specimens, but 70% were small arthropoda (Fig. 8.6b).

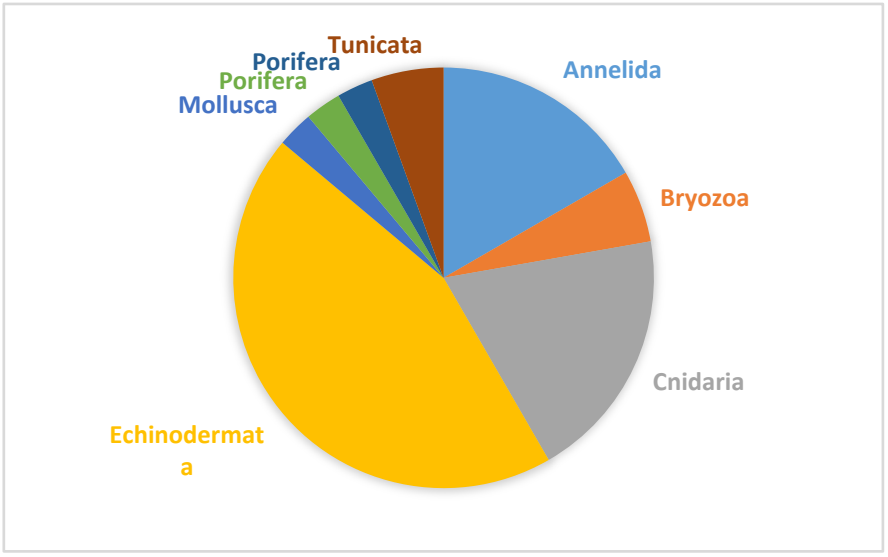

a

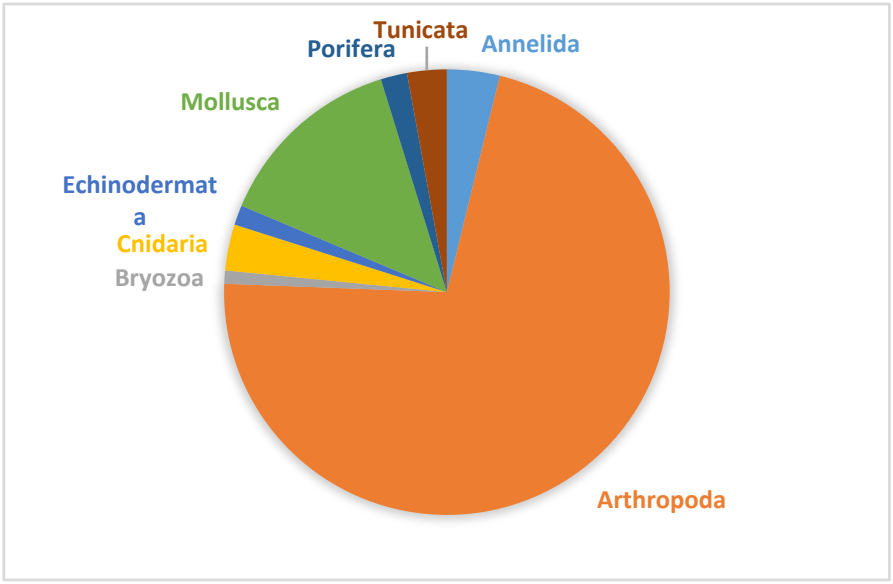

b

***Figure 8.6**. Proportion of specimens collected from five dives at Larsen C sites (a) and one at Erebus and Terror Gulf (b).*

8.4 Multi-core sampling for macrofaunal and sediment

Disturbance is a major driver of diversity in many ecosystems. Icebergs scour is an important disturbance event in benthic Antarctic areas. Benthic macrofauna are food for a range of Antarctic organisms and play a crucial role in benthic and pelagic foodwebs. As iceberg scouring is predicted to increase in scale in future warmer climate scenarios it is therefore important to understand the impact such events have on macrofaunal communities.

When all multicore tubes were successful deployed, six small cores (67 mm diameter) and two large cores (100 mm diameter) were sliced at eight different horizons (0-1, 1-2, 2-3, 3-4, 4-5, 5-10, 10-15 and 15-20 cm). The same depth horizons were combined from the small and large cores separately and material sieve through a 300 um sieve. Retained parts were preserved in 95% ethanol and stored in the fridge. Successful deployments are given as Table 8.1.

Area	*Replicate 1*	*Replicate 2*	*Replicate 3*	*Alternative locations*
Undisturbed	Site 11 - AM000990, 512m	Site 12 - AM000991, 521m	Site 13 – AM00978, 512m	R1 – AM000993, 529m
Medium disturbance	Site 20 - AM000992, 476m	Site 14- AM00978, 446m	Site 16	Site 17
Disturbed	East of trough 24, 25	West of trough – 23	26 - AM000988, 323m	28 – no MC done

***Table 8.1**. Planned and completed (in grey) sediment sampling for macrofaunal. Note - Site 3 was a failed multi-core (MC) where the seafloor was all rubble with no sediment.*

As disturbed-area sites were not collected we shall use this dataset to compare communities against known multicore data sets from Larsen A and B. These data will be worked up be an undergraduate.

8.5 Water sampling for micro-organisms

Microorganisms are, by some estimations, more than 90% of biomass in marine environments (Suttle, 2005). They have many roles in marine ecosystems; perhaps the most important is in nutrient cycling and decomposition. By combining data from water nutrients, oxygen, POC etc. with metagenomics we can investigate how microorganisms change from a

gradient of ice-covered to open ocean environments. As ice-shelves are melting, these changes at the base of marine foodwebs, may have large cascading impacts and are therefore important to understand.

Water was filtered, using a setrivac filter, from three different depths at CTD casts against the ice shelf, away from the ice shelf and in an open ocean environment. The three depths chosen were based on the florescent maximum (Fmax), bottom water, and a middle depth of mixed water layer (Table 8.2). When additional water masses were present additional water samples were obtained (* marks where four filter depths were taken, $ marks where six filter depths were taken). One litre of water was filtered through a sterivac filter per sample.

Area	*Replicate 1*	*Replicate 2*	*Replicate 3*	*Alternative locations*
Water coming off ice shelf	Site 4/AM00976, 445m	Site 6/ AM000985, 457m	Site 8/ AM000987, 427m	
Away from ice shelf	Site 13 /AM00979, 512m	Site 14/AM00978, 446m	Site 16	Site A
Open ocean	CTD9/T1/ AM00973, 2155m*	CTD10/ T2/AM00973, 1680m	CTD11/T3/ AM00974, 576m	??/AM00994, 4200m$

***Table 8.2**. Planned and completed (in grey) water sampling for microorganisms*

8.6 References

Arrigo, K.R., van Dijken, G.L., Ainley, D.G., Fahnestock, M.A. and Markus, T., 2002. Ecological impact of a large Antarctic iceberg. *Geophysical Research Letters*, 29, doi:10.1029/2001GL014160.

Clough, J.W. and Hansen, L.B., 1979. The Ross Ice Shelf Project. *Science*, 203, 433-434.

Cook, A.J., Holland, P.R., Meredith, M.P., Murray, T., Luckman, A. and Vaughan, D.G., 2016. Ocean forcing of glacier retreat in the western Antarctic Peninsula. *Science*, 353, 283-286.

Fillinger, L., Janussen, D., Lundälv, T. and Richter, C., 2013. Rapid glass sponge expansion after climate-induced Antarctic Ice Shelf collapse. *Current Biology*, 23, 1330-1334.

Gutt, J., Barratt, I., Domack, E., d'Udekem d'Acoz, C., Dimmler, W., Grémare, A., Heilmayer, O., Isla, E., Janussen, D., Jorgensen, E., Kock, K.-H., Sophia Lehnert, L., López-Gonzáles, P., Langner, S., Linse, K., Eugenia Manjón-Cabeza, M., Meißner, M., Montiel, A., Raes, M., Robert, H., Rose, A., Sañé Schepisi, E., Saucède, T., Scheidat, M., Schenke, H.-W., Seiler, J. and Smith, C., 2011. Biodiversity change after climate-induced ice-shelf collapse in the Antarctic. *Deep-Sea Research, Part II: Topical Studies in Oceanography*, 58, 74-83.

Gutt, J., Cape, M., Dimmler, W., Fillinger, L., Isla, E., Lieb, V., Lundälv, T. and Pulcher, C., 2013. Shifts in Antarctic megabenthic structure after ice-shelf disintegration in the Larsen area east of the Antarctic Peninsula. *Polar Biology*, 36, 895-906.

Littlepage, J.L. and Pearse, J.S., 1967. Biological and oceanographic observations under an Antarctic ice shelf. *Science,* 137, 679-681.

Peck, L.S., Barnes, D.K.A., Cook, A.J., Fleming, A.H. and Clarke, A., 2010. Negative feedback in the cold: ice retreat produces new carbon sinks in Antarctica. *Global Change Biology*, 16, 2614-2623.

Post, A.L., Galton-Fenzi, B.K., Riddle, M.J., Herraiz-Borreguero, L., O'Brien, P.E., Hemer, M.A., McMinn, A., Rasch, D. and Craven, M., 2014. Modern sedimentation, circulation and life beneath the Amery Ice Shelf, East Antarctica. *Continental Shelf Research*, 74, 77-87.

Riddle, M.J., Craven, M., Goldsworthy, P.M. and Carsey, F., 2007. A diverse benthic assemblage 100 km from open water under the Amery Ice Shelf, Antarctica. *Paleoceanography and Paleoclimatology*, 22, PA1204.

Suttle, C.A., 2005 Viruses in the sea. *Nature*, 437, 356–61.

9. Full-scale engineering measurements of ship responses to sea ice

Anriëtte Bekker, Liangliang Lu, Christof van Zijl and James-John Matthee

9. Introduction

Polar supply and research vessels operate in some of the harshest dynamic environments on earth. Knowledge of sea ice, its properties and resultant loading on vessels is far from complete and as such the safety of ships operating in these environments is based on the extrapolation of engineering data with reasonable assumptions from scale model tests in ice tanks and simulation models. Paramount to this, understanding of operational ice and wave loading on ships in the Southern hemisphere is particularly sparse. The SA *Agulhas II* (SAA II) is a polar supply and research vessel owned by the South African Department of Environmental Affairs, Figure 9.1. She was manufactured by STX Finland in Rauma shipyard and measures 121.3 m between perpendiculars and is 21.7 m wide. She is propelled by four Wärtsilä 3 MW diesel generators that power two Conver Team electric motors, which are each connected to a shaft with a variable pitch propeller. Accommodations are available for 44 crew and 100 passengers on annual research and re-supply voyages to Antarctica, Gough Island and Marion Island.

Vessel passengers are scientists who are not regularly sea-borne and work in laboratories on-board during oceanographic research expeditions. The SAA II is the first vessel in her class to be built to the SOLAS 2009 Passenger Ship Rules and as such, her design provides valuable operational experience towards the commissioning of other polar supply and research vessels by several countries. Globally, future trends towards the reduced cost and increased availability of satellite connections indicate that the increased ability to handle and process data will affect the maritime industry. A position paper by DNV-GL, Lœvoll and Kadal, (2014), predicts that this new data reality will affect the shipping industry in the spheres of technical operation and maintenance, energy efficiency, safety performance, risk management and monitoring, commercial operations and the automation of ship operations. Such endeavours require the acquisition, processing and utilization of large volumes of continuously measured data on an increasingly real-time basis. The full-scale measurement project on the SA Agulhas II is the most comprehensive open operational data set of such a vessel to date, which positions this ship as an ideal mule to prototype digital services and automated ship operations (Bekker *et al.*, 2018).

Figure 9.1. *SAA II vessel during offloading operations at Penguin Bukta, December 2018, Antarctica (Photo Credit: James-John Matthee).*

An international research consortium comprising the University Stellenbosch, Aalto University, Aker Arctic, DNV GL, Rolls-Royce, STX Finland, University of Oulu, Wärtsilä and the Department of Environmental Affairs South Africa initiated a full-scale measurement program on the SAA II for her ice-trails in the Baltic Sea in March 2012, Suominen et al. (2013). Subsequently, Stellenbosch University and Aalto University have expanded on this effort, resulting in a one-of-a-kind full-scale measurement campaign which, to date, includes six Antarctic relief voyages and two voyages to Marion Island. The measurements on the Weddell Sea Expedition 2019 includes: ice loads on the ship hull and propulsion system, ice-induced structural vibrations and noise, whole-body vibration comfort, ship dynamics in ice, global ice loads, underwater noise and mechanical and physical sea-ice properties.

9.2 Ship-based underway measurements

Table 9.1. *Full-scale ship-based measurement instrumentation on the SA Agulhas II.*

Measurement	Variables	Equipment	Number of channels	Sample rate
Ship context	Camera footage	Bosch underway camera system	~40	1 Hz
Wave	Height, direction	Visual observations	1	4 hours
Sea Ice	Thickness, ice cover, floe size	GPS	2	1 Hz
		Underway top camera - floe size, ice concentration	2	0.5 Hz
		Underway stereo camera – ice thickness	2	3 Hz
		Visual observations (Concentration, floe size, thickness)	3	10 Min
Ship vibration response (hull and super-structure)	Acceleration (Rigid body motion and flexure)	DC accelerometers,	10	2048 Hz
		ICP accelerometers	20	2048 Hz
Ship - shaft-line torsional and thrust vibration	Thrust, Torque,	Strain gauges, V-links and Quantum data acquisition units	2	600 Hz
	Bearing acceleration	Accelerometers to Quantum data acquisition units	6	2048 Hz
Ship - hull ice loading	Bow, bow shoulder and stern shoulder loads	Strain gauges, Central measurement unit	56 (+ 9)	200 Hz
Ship – AIS data	Various sensors and ship central measurement unit	Time, latitude, longitude, SOG, COG, HDT, relative wind direction, wind speed, depth	9	1 Hz
Ship machine control		Propeller motor current, speed and voltage for starboard propeller. Rudder order, position and pitch for port- and starboard shaft, rpm.	26	0.5 Hz
Ship rigid body motion	Inertial measurement units (IMU)	yaw, pitch, roll, heave, surge, sway	2	1 Hz

Full-scale measurements on the SAA II include almost 200 data channels as presented in Table 9.1. These comprise measurements of hull-loading, global vibration responses, indirect measurements of torque and thrust (portside shaft), operational ship parameters and context and finally, subjective observations of ice conditions and wave height. These

measurements have evolved in maturity since the ice trails of the SAA II in the Baltic Sea in 2012 (Bekker *et al.*, 2014), over six Antarctic relief voyages and two voyages to Marion Island.

9.2.1 Hull-ice loading

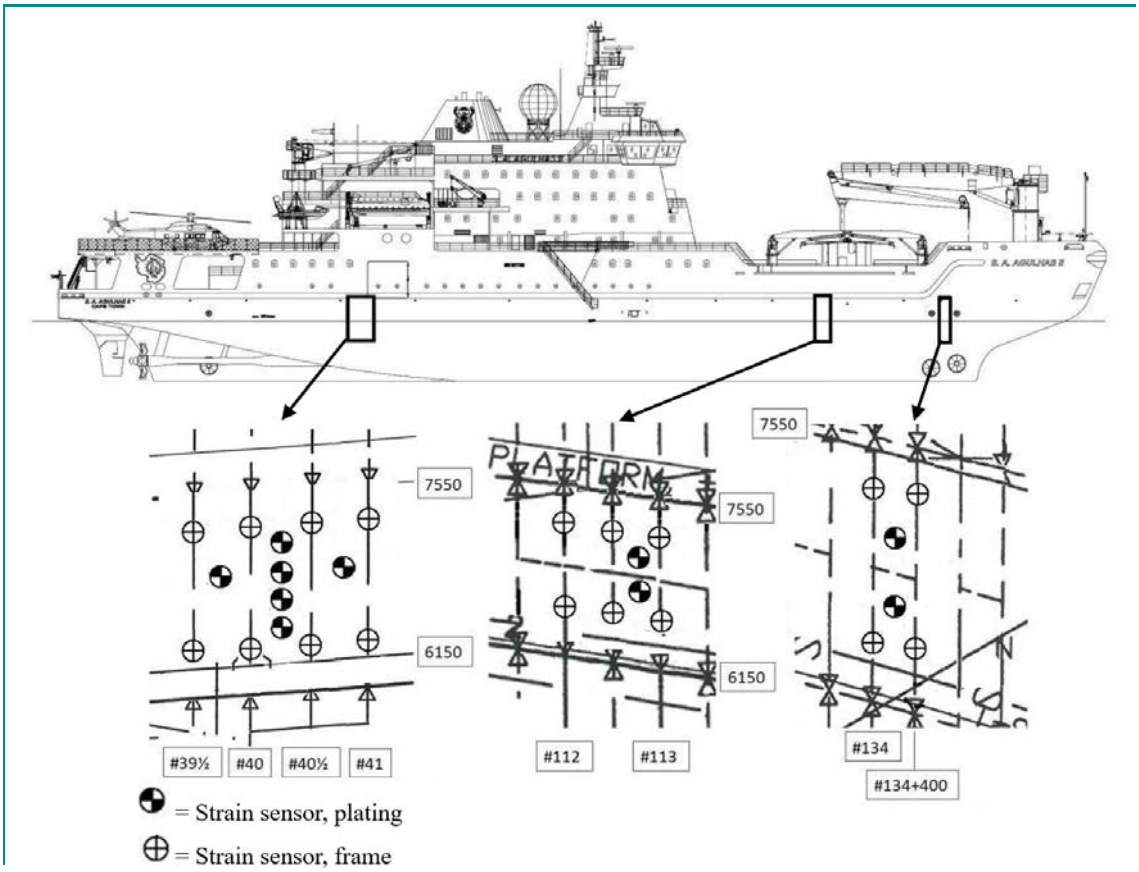

Figure 9.2. *Strain gauge instrumentation on the ship hull at bow, bow shoulder and aft shoulder (Suominen* et al.*, 2013).*

The starboard side of the vessel hull is permanently instrumented with strain sensors in three areas to measure ice loads, as shown in Figure 9.2. The strain gauges measure the shear strain on the upper and lower part of the frame and the ice load (shear force) is determined through an algorithm as outlined by Kotilainen et al. (2017) and Bekker et al. (2014). Strain measurements are sampled at a rate of 200 Hz. The SA Agulhas II is rated as a PC-5 vessel. However, her hull was maximally enforced to a hull classification of DNV ICE 10. For reference the design limit values for ice class PC-5 and DNV ICE 10 are listed in Table 9.2. Hull measurements therefore provide insight as to operational loading of an ice-going ship in the Antarctic environment.

Table 9.2. *Design limits for ice loading on SA Agulhas II hull.*

	PC-5	**DNV ICE 10**
Stern	700 kN	790 kN
Bow	1150 kN	1650 kN

Strain measurements are organized in five-minute sample records and referenced to UTC time. Ice loads are determined through a statistical process called Raleigh separation (Kotilainen *et al.*, 2017). As an example, five minute maximum ice loads were calculated for measurements from 1 to 10 January when the ship navigated as rapidly as was safely possible from Penguin Bukta to the Larsen-C ice shelf in the western Weddell Sea as shown in Figure 9.3. The navigational strategy avoided ice whenever possible and opted for open water leads in floe fields. Ship speed was reduced as required for safe ship navigation.

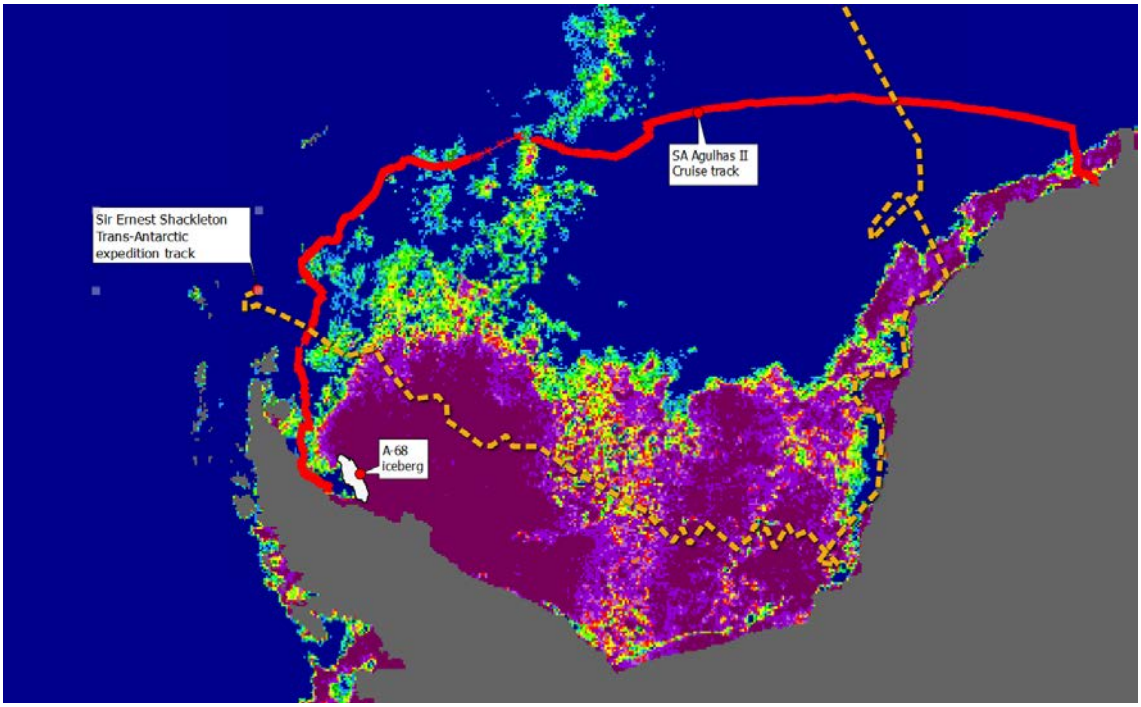

Figure 9.3. *The SA Agulhas II cruise track from 3 to 10 January between Penguin Bukta and the Larsen C Ice Shelf.*

Figures 9.4 to 9.6 represent ice load data at the bow, bow shoulder and stern shoulder from 1 to 10 January. The bow is mostly loaded by ice with significantly less loading at the bow shoulder and stern shoulder. When considering the design limits (in Table 9.2) it is clear that the transit between Penguin Bukta and the Western Weddell Sea did not challenge the structural design of the vessel.

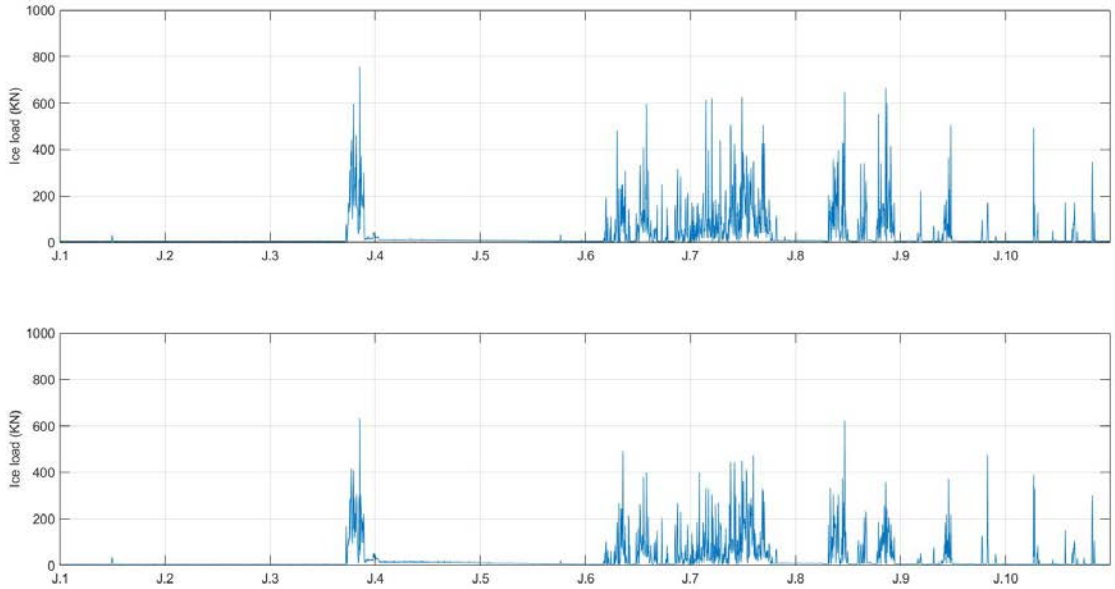

Figure 9.4. *Ice loads measured on two structural frames on the starboard side of the bow for 1 to 10 January.*

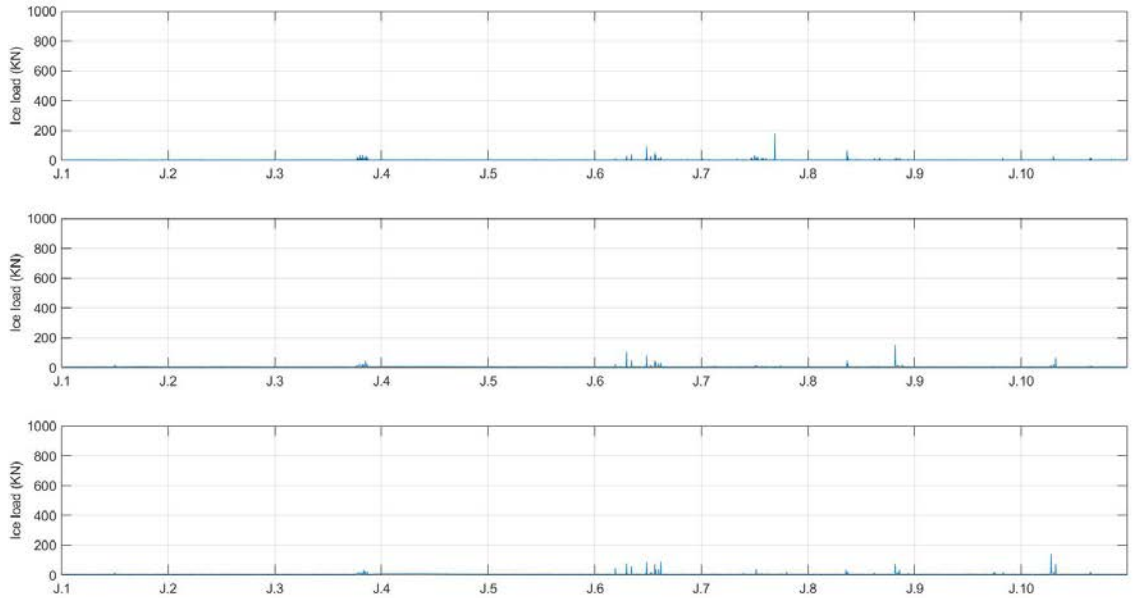

Figure 9.5. *Ice loads measured on three structural frames on the starboard side of the bow shoulder for 1 to 10 January.*

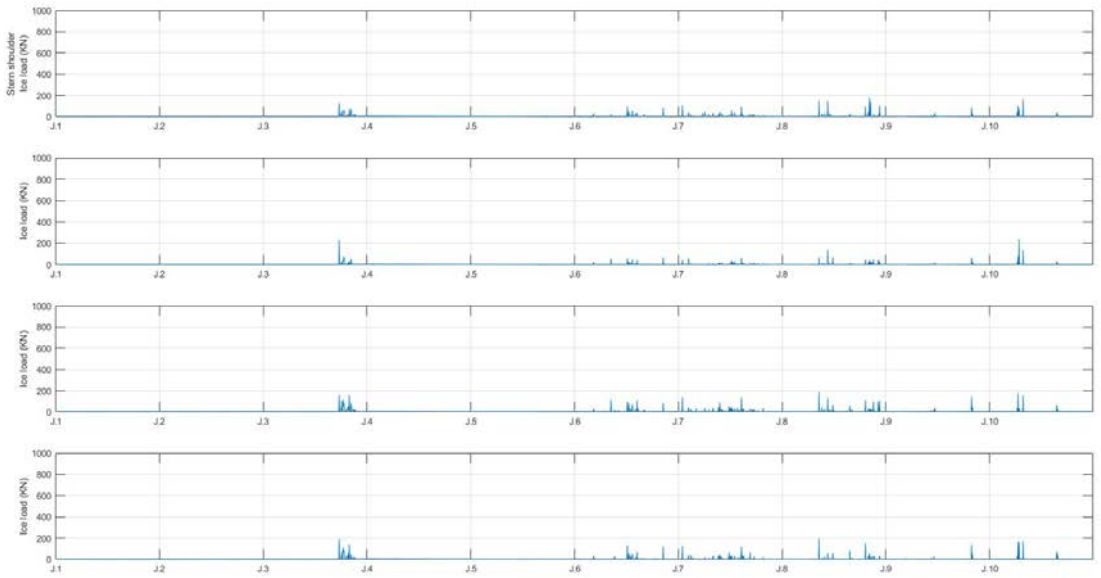

Figure 9.6. *Ice loads measured on four structural frames on the starboard side of the stern shoulder for 1 to 10 January.*

9.2.2 Structural vibration

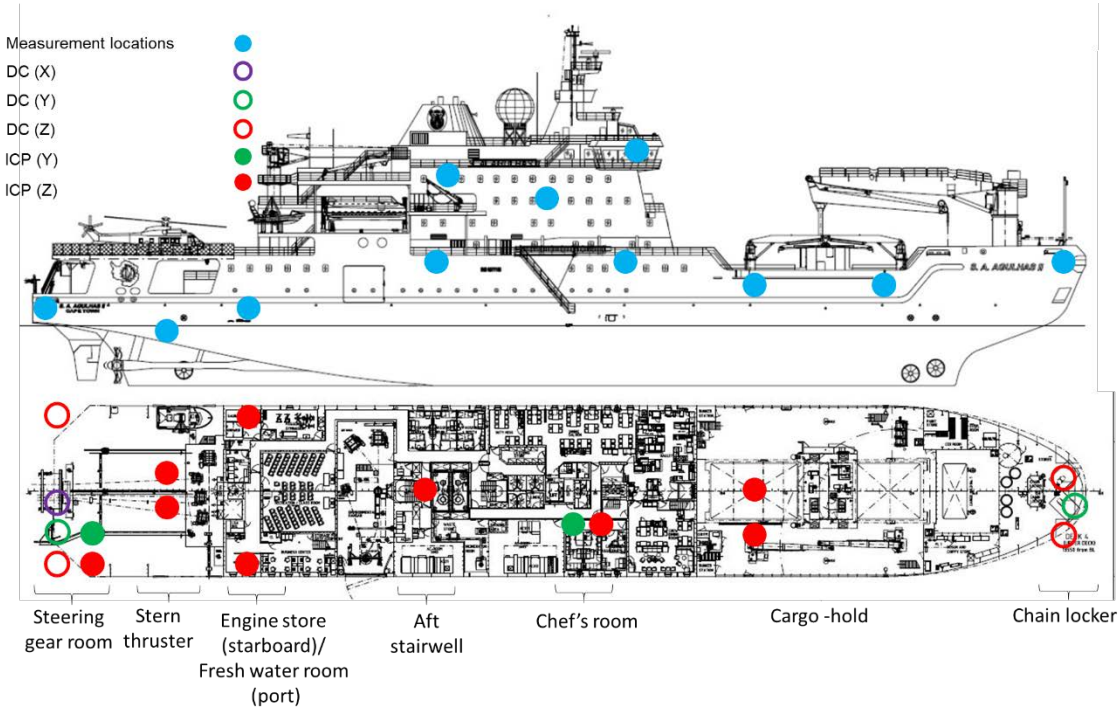

Figure 9.7. *Diagram of the accelerometer network used for full-scale measurements on the SA Agulhas II.*

For the Weddell Sea Expedition, an accelerometer network of 30 accelerometers was utilized and referenced to a vessel-centric coordinate system, where the respective axes,

xyz refer to fore-aft, lateral and vertical acceleration. All measurements were sampled at 2048 Hz by this accelerometer network which is suitable to capture rigid body and flexural motion. Measurement locations are presented in Figure 9.7. The global response of the ship hull is captured by six pairs of accelerometers on the port- and starboard sides of the vessel hull. Lateral motion is measured by two sensors, one on the starboard side at the stern and one on the vessel centre line in the bow chain locker. The remaining sensors monitored accelerations in the super-structure, closer to accommodation areas, recreational spaces and the bridge. The sensor network includes both DC and ICP accelerometers as summarized in Table 9.3.

Table 9.3. *A list of sensor locations, sensors and measurement specifics for full-scale acceleration measurements.*

Channel	Location	Side	Point ID	Deck	Axis	Type	Sensitivity $[mV/m/s^2]$
1	Bridge	Starboard	B01_S_X	9	X	DC	20.19
2	Bridge	Starboard	B01_S_Y	9	Y	DC	20.22
3	Bridge	Starboard	B01_S_Z	9	Z	DC	20.13
4	Bridge	Port	B02_P_Z	9	Z	ICP	10.18
5	Deck 8	Port	D801_P_Y	8	Y	ICP	10.2
6	Deck 8	Port	D801_P_Z	8	Z	ICP	10.06
7	Deck 7	Starboard	D701_S_Y	7	Y	ICP	10.03
8	Deck 7	Starboard	D701_S_Z	7	Z	ICP	10.13
9	Bow	Starboard	CL01_S_Z	4	Z	DC	20.24
10	Bow	Centre	CL02_0_Y	4	Y	DC	20.29
11	Bow	Port	CL03_P_Z	4	Z	DC	20.46
12	Chef's room	Starboard	CR01_S_Y	4	Y	ICP	10.13
13	Chef's room	Starboard	CR01_S_Z	4	Z	ICP	9.96
14	Aft stairwell	Centre	AS01_0_Z	4	Z	ICP	10.05
17	Cargo-hold	Starboard	CH01_S_Z	3	Z	ICP	9.7
18	Cargo-hold	Port	CH02_P_Z	3	Z	ICP	10.25
19	Cargo-hold	Starboard	CH03_S_Z	3	Z	ICP	10.23
20	Cargo-hold	Port	CH04_P_Z	3	Z	ICP	10.44
21	Engine store	Starboard	ES01_S_Z	2	Z	ICP	10.43
22	Fresh water	Port	FW01_P_Z	2	Z	ICP	10.42
23	Stern thruster	Starboard	ST01_S_Z	2	Z	ICP	10.34
24	Stern thruster	Port	ST02_P_Z	2	Z	ICP	10.36
25	Steering gear	Starboard	SG01_S_X	2	X	DC	20.23
26	Steering gear	Starboard	SG01_S_Y	2	Y	DC	20.23
27	Steering gear	Starboard	SG01_S_Z	2	Z	DC	20.29
28	Steering gear	Starboard	SG02_S_Y	2	Y	ICP	10.39
29	Steering gear	Starboard	SG02_S_Z	2	-Z	ICP	10.45
30	Steering gear	Port	SG03_P_Z	2	Z	DC	20.31

Data were acquired using an LMS SCADAS master-slave system, connected with fibre-optic cables and LMS. Turbine testing data acquisition software enables truly continuous data recording.

Vibration analysis and data veracity

An important first step in handling large amounts of data is to verify the "veracity" of the data (Løvoll and Kadal, 2014). "Veracity" refers to the quality of measured data and provides an indication of how representative the data is of the physical phenomena that is being measured. In the present context, checking veracity of full-scale measurements is important to decide whether measurements from different measurement channels are useful for building a modal model and predicting the global vibration response of the vessel. To this end, vibration measurements obtained during the Weddell Sea Expedition were checked daily.

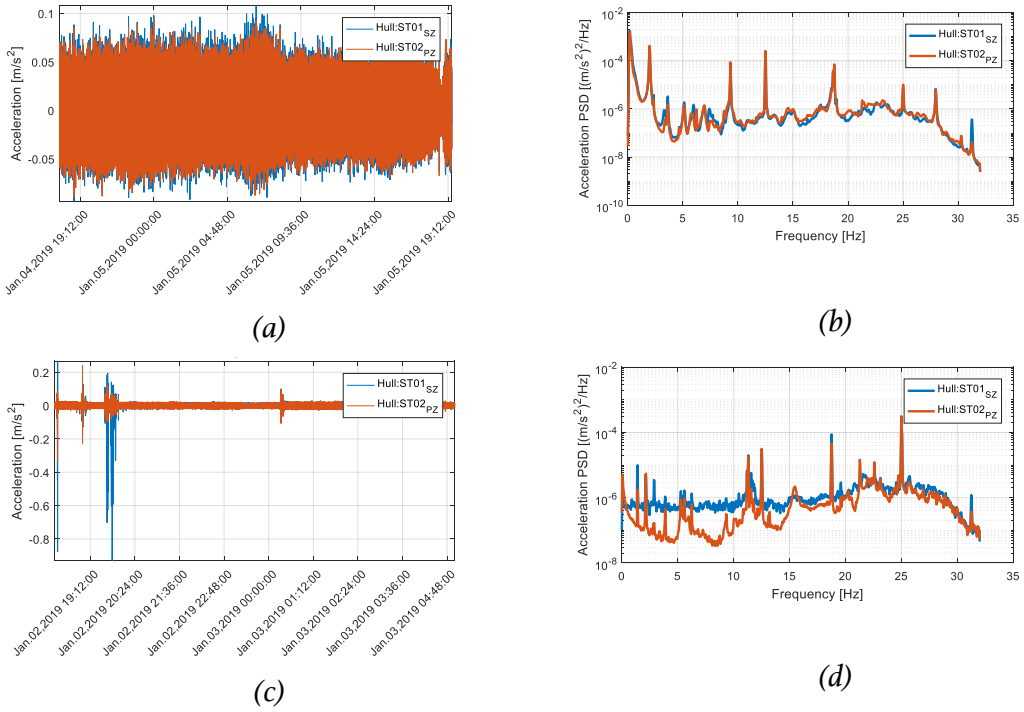

Figure 9.8. *Examples of data veracity checks where (a) the time signal and (b) frequency domain signals on mirrored hull acceleration measurements predict similar results. Possible anomalous results are shown for (c) time and ((d) frequency domain signals which indicate contradicting responses.*

Firstly, acceleration signals from different sensor locations on the vessel were analysed in the time- and frequency-domain. This involved studying the signals and their characteristics. As an example, consider a set of measurements obtained from sensors mounted on the starboard and port side of the vessel in the stern thruster room. Figure

9.(a) and (b) shows "healthy" time- and frequency-domain signals from these two sensor locations measured between 4 and 5 January 2019. The signals from the two sensors are similar in both domains. This is important since the sensors are located approximately symmetrically about the centreline of the ship at the same location along the length. It is thus expected that a similar global vibration response would be measured at both locations. An example of potentially anomalous measurements obtained between 2 and 3 January 2019 from the same location is presented in Figure 9.8 (c) and (d). In this case, both sensors measure impulsive events but the sensor mounted on the starboard side further measures local events that are not associated with the global vibration response of the structure at that location. In the frequency-domain this results in a higher noise floor in the measured signal that disguises significant modal peaks.

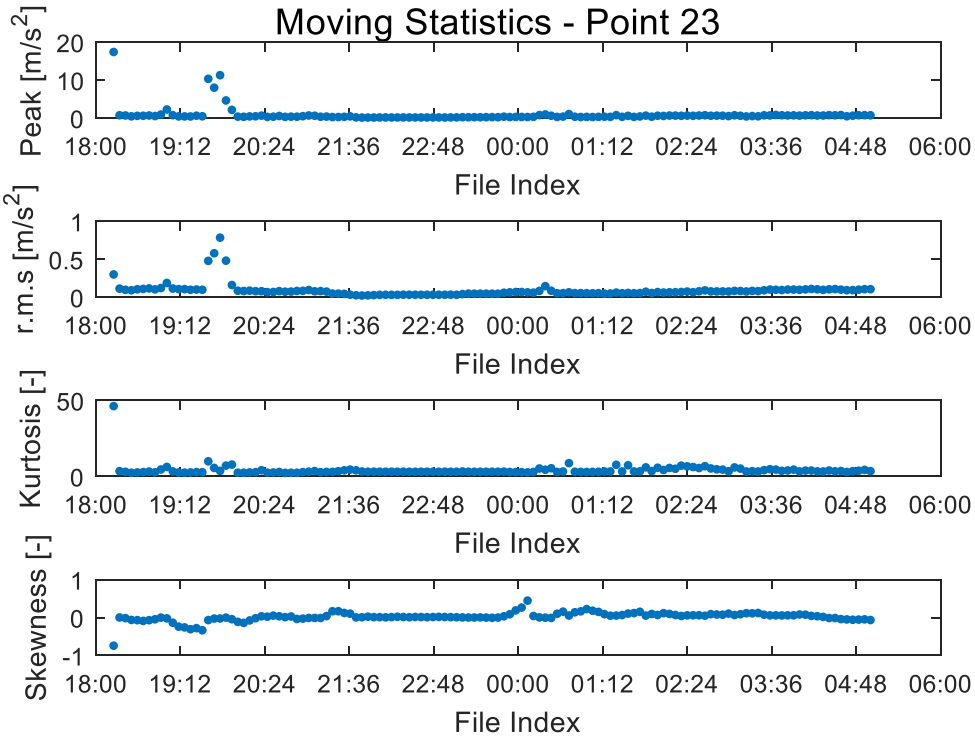

Figure 9.9. *Statistical moments and tracking of time domain acceleration values.*

Anomalies in signals are easily detected by studying the characteristics of the time-domain signal. The characteristics of the signal are described by metrics such as the peak value, root-mean-square (r.m.s) value, kurtosis and skewness. Figure 9.9 presents vibration metrics of the signal from the starboard sensor in the stern thruster room measured between 2 and 3 January 2019. Each point represents a vibration metric calculated from five-minutes of data. Abnormal deviations in the peak, kurtosis and skewness are normally indicators of anomalous events or case studies of interest. As an example statistics from Figure 9. indicate a potentially interesting event around 20:00 for

the analysis in question. Overview statistics such as these are used along with prior knowledge from historical data to efficiently identify data for deeper analysis.

Operational Modal Analysis

Global structural responses of the SAA II were investigated through Operational Modal Analysis, Soal et al. (2015b). The normal bounds of modal migration can be identified from real-time monitoring data and used to devise operational strategies to extend the useful lifecycle of the SAA II. A combination of in-house and published algorithms were used to determine the structural dynamic characteristics of the operational vessel from response-only measurements.

Operational modal analysis (OMA) was performed on the processed full-scale measurement set. In the present study the Frequency Domain Decomposition (FDD) technique and data-driven Stochastic Subspace Identification (SSI) techniques are used to perform operational modal analysis (OMA) on the SA Agulhas II. In-house MATLAB algorithms were developed from the companion code of an OMA textbook (Brincker and Ventura, 2015), the Abravibe signal processing and modal analysis toolbox (Brandt, 2013) and an open source SSI toolbox available on Github called openSID (Soal, 2018).

Frequency domain decomposition

In FDD a singular value decomposition (SVD) is calculated from the spectral density matrix of output-only response measurements at discrete frequency lines. The singular values at discrete frequencies contain information about the response of the structure at that frequency as well as measurement noise. If a mode is present near certain frequency lines there will be a peak in the singular values at these frequency lines. In a simple peak-picking version of FDD, natural frequencies may be determined by locating peaks in singular values and using the first singular vector that that frequency as an estimate of the mode shape. The singular vector corresponding to the singular value at this frequency is an estimate of the mode shape. Modifications of the FDD algorithm such as enhanced FDD (EFDD) (Ventura, Brincker and Andersen, 2001) further makes it possible to estimate damping ratios.

Stochastic subspace identification

The reference-based SSI-data algorithm may be summarised by seven steps as illustrated in Figure 9.10. Much more detailed explanations are presented in (Van Overschee, P; De Moor, 1996) and(Peeters and de Roeck, 1999). First a data matrix is constructed directly from time-series acceleration measurements. At this stage the user must decide how many measurement samples to include in the data matrix (i.e. how long the measurement run must be). This is also referred to the block length of the data. The data matrix $Y \epsilon \mathbb{R}^{n_c \times n_s}$ consists of n_s data samples (columns) from n_c channels (rows):

$$[Y] = \begin{bmatrix} \boldsymbol{y}_{\boldsymbol{1:ns}}^{\boldsymbol{1}} \\ \boldsymbol{y}_{\boldsymbol{1:ns}}^{\boldsymbol{2}} \\ \vdots \\ \boldsymbol{y}_{\boldsymbol{1:ns}}^{\boldsymbol{nc}} \end{bmatrix}$$

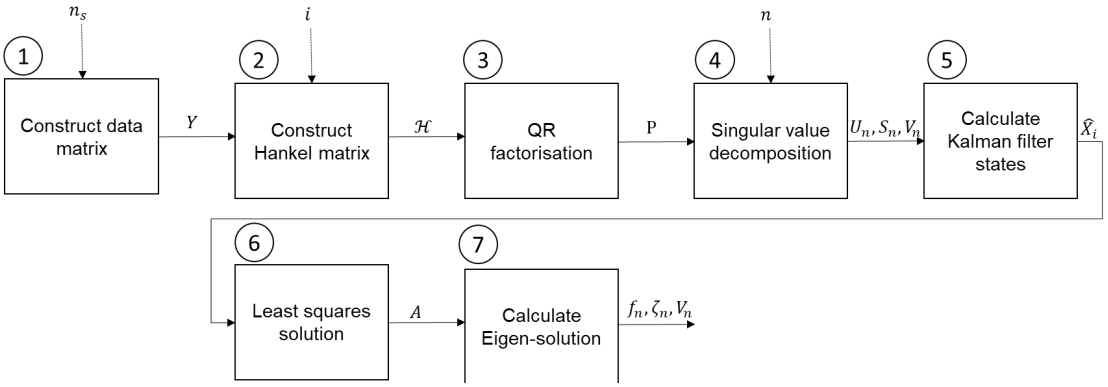

Figure 9.10. *Data-driven stochastic subspace identification algorithm.*

The second step is to build a Hankel matrix. In order to construct the Hankel matrix, the user must decide on a parameter referred to as the block size, i. Once the block length and block size are set, the Hankel matrix with $2i$ block rows is constructed by placing $j = n_s - 2i + 1$ samples in each block row. Each consecutive block row in the Hankel matrix is shifted by one measurement sample. The Hankel matrix may further be divided into two parts, a "past" and "future" part each having i block rows. In the reference-based version of SSI-data only a subset of reference channels are included in the "past" part of the Hankel matrix. The construction of the Hankel matrix is presented in Equation 2:

$$H = \frac{1}{\sqrt{j}} \left(\begin{array}{cccc} y_1^{ref} & y_2^{ref} & \cdots & y_j^{ref} \\ y_2^{ref} & y_3^{ref} & \cdots & y_{j+1}^{ref} \\ \vdots & \vdots & \ddots & \vdots \\ y_i^{ref} & y_{i+1}^{ref} & \cdots & y_{i+j-1}^{ref} \\ \hline y_{i+1} & y_{i+2} & \cdots & y_{i+j} \\ y_{i+2} & y_{i+3} & \cdots & y_{i+j+1} \\ \vdots & \vdots & \ddots & \vdots \\ y_{2i} & y_{2i+1} & \cdots & y_{2i+j-1} \end{array} \right) = \begin{pmatrix} H_p \\ H_f \end{pmatrix}$$

Third in the SSI-data algorithm is a QR factorisation of the block Hankel matrix. A part of the R factor from the QR factorisation is used to define a projection matrix that projects the "past" part of the Hankel matrix onto the "future" part. This projection matrix contains information for predicting future responses from past responses. The fourth step is to calculate singular value decomposition (SVD) of the projection matrix. A subspace of the factors of SVD matrices is then used to compute an observability matrix and Kalman filter state sequence in the fifth step of the algorithm.

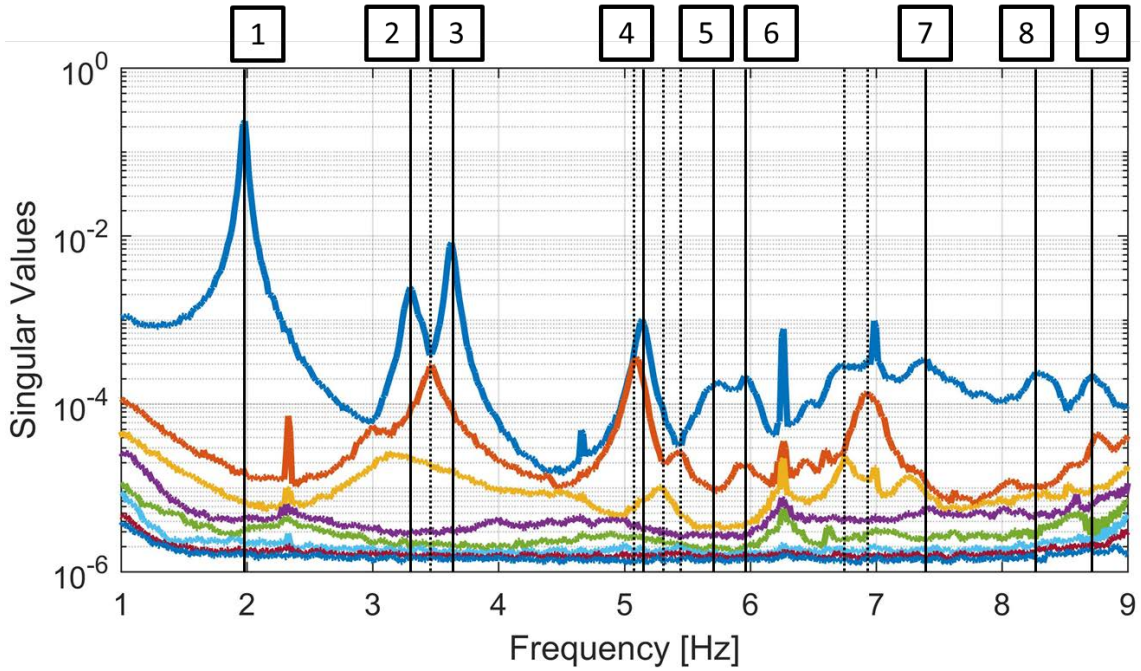

Figure 9.11. *Singular value decomposition of spectral density matrix.*

It is important to note that the dimensions of the subspace that is used to compute the observability matrix and Kalman filter states is another user defined parameter referred to as the model order. The observability matrix and Kalman filter states are well-defined in control engineering theory and for more details the reader is referred to (Van Overschee, P; De Moor, 1996), (Peeters and de Roeck, 1999) and (Peeters and de Roeck, 2001). The relevance of the observability matrix and Kalman filter states in the present context is that the system matrix A can be obtained through solving a least squares problem, step six of the SSI-data algorithm. The system matrix is important as its Eigen-solution contain all the information necessary to characterise the dynamic behaviour of a physical structure. Therefore, step seven of the algorithm calculates the natural frequencies, damping ratios and mode shapes through an eigenvalue decomposition of the system matrix. The number of modes in the identified modal model is directly related to the model order selected by the user in Step 4.

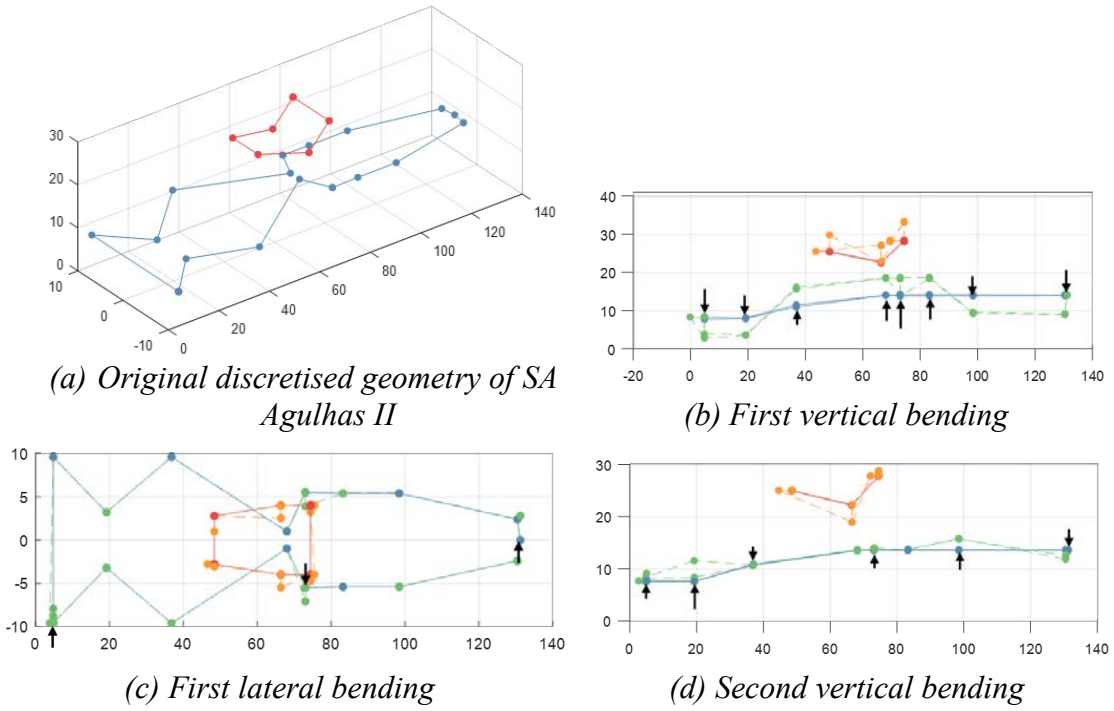

(a) Original discretised geometry of SA Agulhas II

(b) First vertical bending

(c) First lateral bending

(d) Second vertical bending

Figure 9.12. *Operational modes identified using FDD on measurements of the SA Agulhas II.*

A simple peak-picking version of the Frequency Domain Decomposition (FDD) technique was used to conduct a preliminary OMA analysis to determine estimates of the natural frequencies of the structure. Figure 9.11 presents the first eight singular values of the spectral density matrix of the processed signal. Most of the information relating to the physical structure are contained in the first three sets of singular values. This includes both peaks that represent modes of the structure and harmonics of rotating machinery. Harmonics are different from modal peaks in that they are sharper and narrower than modal peaks. The remaining singular values contain mostly information relating to measurement noise. Nine modal peaks may be identified from the first set of singular values as indicated in Figure 9.11. Additional peaks in the second and third set of singular values are identified in Figure 9.11 with dotted lines and may represent local modes of structural components on the ship.

In the present study, only the first three modes identified in Figure 9.11 are explored in further detail. The reasoning behind selecting these modes is that they appear to be well-excited and are the dominating modes in a modal model of the ship and that a more in-depth study can be performed if fewer modes are considered. The natural frequencies of these modes are 1.97 Hz, 3.28 Hz and 3.63 Hz. Figure 9.12 (a) presents a simple discretised geometry of the hull (blue) and superstructure (red) of the SA Agulhas II. Figure 9.12 (b), (c) and (d) presents the mode shapes of the first three modes. Deformations of the hull are in green and the superstructure in orange. By inspection these modes appear to be the first vertical hull bending mode, the first lateral hull bending

mode and second vertical hull bending mode. This agrees reasonably well with the modes determined using a finite element (FE) model of the ship (STX, 2010) and previous studies by Soal (2015).

9.2.3 Shaft-line torque and thrust

Shaft-line measurements (Figure 9.13) entailed the installation of strain gauges on the port side shaft line of the SAA II to determine the shear and axial strain as described in De Waal et al. (2017). This enables the determination of the instantaneous torque and thrust at the measurement locations on the shaft line. Measurements on the shaft-line have a three-fold purpose: firstly, to obtain an indication of the transient torque and thrust in the shaft and secondly, to provide a means through which propeller loads can be estimated by inverse methods, Ikonen et al. (2014). Finally, the potential exists to provide estimates of global resistance forces through concurrent analysis of the shaft thrust and ship speed, Su et al. (2011).

The analysis of shaft-line data provides potentials such as the rainflow counting of the transient torque and thrust cycles in order to gain insight into the respective demands of different operational environments. Through such an investigation the operational loading of the SAA II shaft line could be evaluated against the Maximum Continuous Rating specified in the ICE Class Rules, *De Waal (2017)*. The measurements comprise two measurements each of torque, thrust and bearing support accelerations on the port-side shaft line as shown in Figures 9.13 and 9.14.

The torque and thrust on the shaft from 1 to 10 January 2019 has been investigated. At this time, ice up to 2 metres thick was broken, the ship reached speeds up to 18 knots.

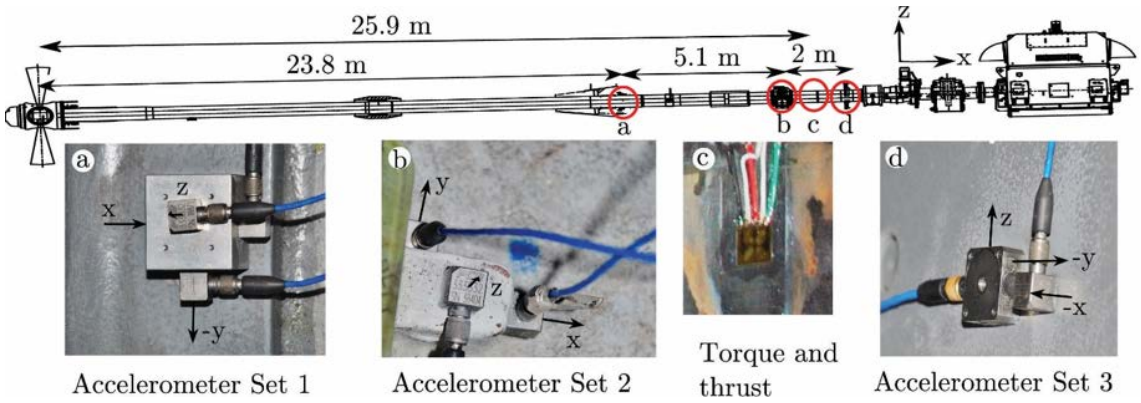

Figure 9.13. *Accelerometers and strain gauges are mounted along the port-side shaft line for the SAA II (Adapted from technical ship drawings, source: STX Finland).*

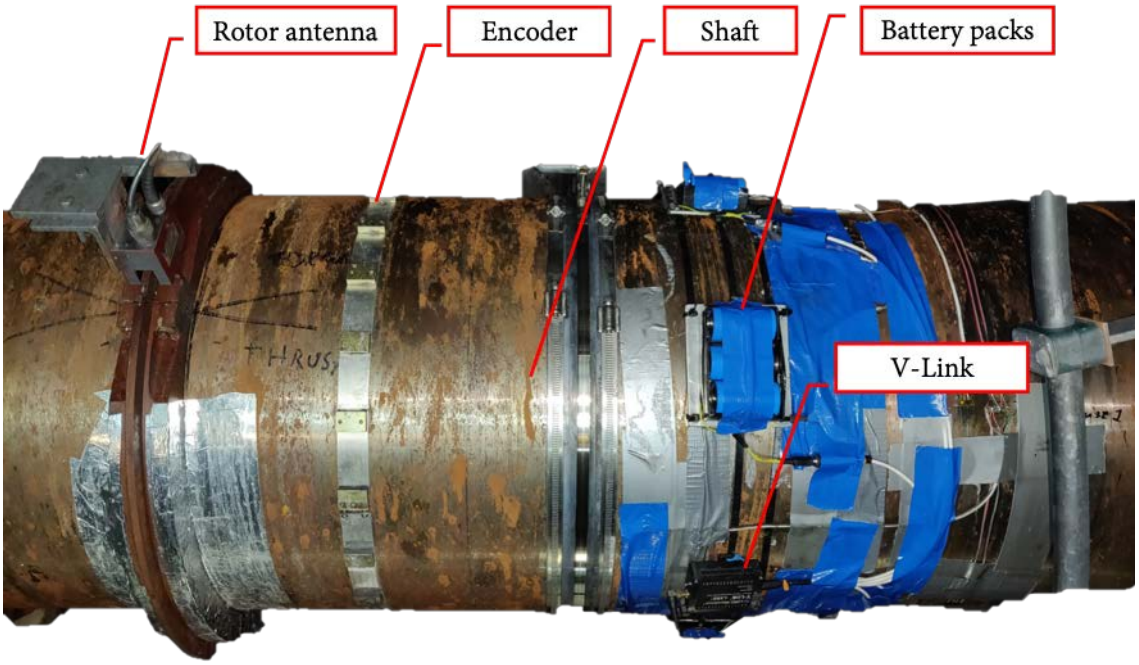

Figure 9.14. *A photographic diagram of the full-scale shaft line rig with telemetric strain measurements via a V-link and multiple battery packs for extended measurement life.*

Cavitation influences the torque and thrust amplitude, as well as increase shaft vibrations, especially in the x-direction (fore-aft). The pitch of the propeller and shaft speed have a direct effect on the torque and thrust measurements and contributes to possible cavitation when the pitch and shaft speed reach specific operational levels, De Waal (2017).

Shaft line torque and thrust were measured since the vessel started to navigate through ice on the 15 December 2018. The system was stopped while cargo offloading took place at Penguin Bukta. The Weddell Sea Expedition started on 3 January 2019. The shaft line torque was measured, as the ship sailed through ice and open water. An algorithm was written during the voyage to separate the open water and ice navigation periods by investigating the Crest Factor of the time-signal. The Crest Factor (CF) measures the relationship between the peak value of the time signal and the RMS value. A higher CF indicates a more sporadic signal, more common in ice navigation than in open water, due to impulsive forces induced by the ice. Problems arose with the synchronization of the CATman software and the computer time. This resulted in the system malfunctioning and some data losses between daily instrumentation checks. This problem was corrected by synchronizing the respective system clocks.

The Torque in *kN.m* for the transit leg of the WSE are plotted in Figure 9.15. Higher overall torque values are observed during open water transit from the 4 to 6 January. This is attributed to increased hydrodynamic torque levels at higher shaft speeds and a larger pitch angles of the propeller blades for open water navigation at speeds up to 18 knots.

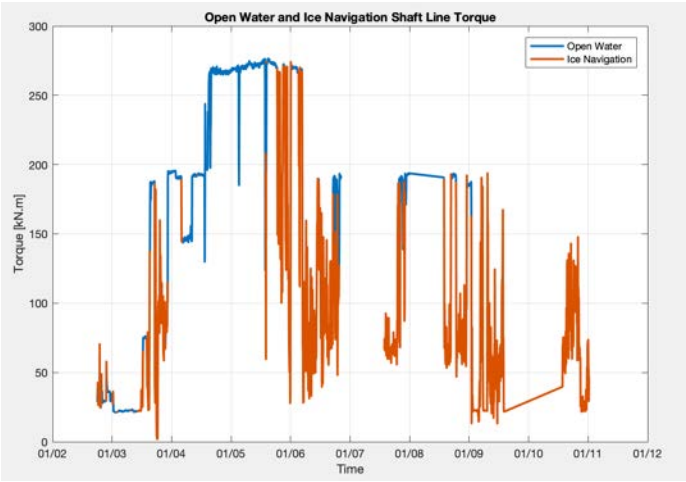

Figure 9.15. *Open water and ice navigation torques for the port side shaft line between 2 to 10 January 2019.*

The histograms for ice passage and open water torque are presented in Figure 9.16. The distribution is widely spread for open water navigation with peaks at 23 kN.m, 148 kN.m, 190 kN.m and 276 kN.m. Stationary and open water torques are not separated. This could be done by extracting times from the CMU data where the vessel's SOG were zero. The torque peaks are skewed to the right for ice navigation. The lower overall torque values during ice navigation are a result of lower ship speed, shaft speed and propeller pitch. It is expected that the deviation from the hydrodynamic torque would increase in amplitude for ice navigation.

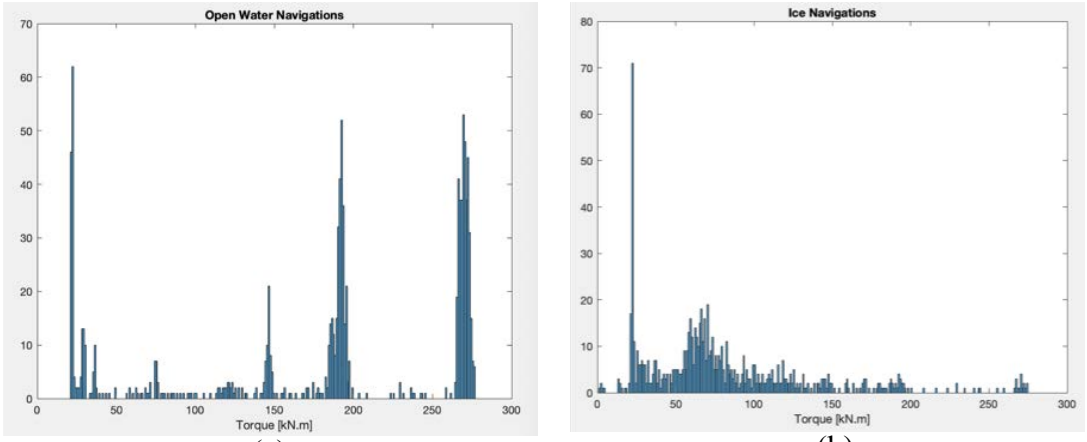

(a) (b)

Figure 9.16. *Torque peak rainflow cycles for the SAAII in (a) open water and (b) ice for transit between Penguin Bukta and the Larsen C Ice Shelf, 2 to 10 January 2019.*

The absolute peak amplitudes for torque and thrust are summarized in Table 9.4, along with the time of incidence. During further analysis, statistically prudent measures will be applied to determine appropriate distributions and quantification metrics to quantify shaft

loading for the full voyage. The maximum absolute peak torque and maximum amplitude torque occurred when the ship was navigating through ice with a thickness between 20 and 40 cm. Underway footage from the top camera and stereo cameras and vessel operational information could be interrogated to gain more insight into the operational conditions of the vessel at this point.

At 20:08 on 7 January the ship entered open water after ice navigation. The maximum peak and maximum amplitude shaft torque occurred simultaneously. Similarly, the peak thrust amplitude and peak measurements occurred concurrently on 7 January 20:09. This indicates potentially impulsive, transient events which are not regular, steady operating states of the ship. The maximum rated torque, Q_{MCR}, is the torque at which the propulsion system can safely operate continuously, (Det Norske Veritas, 2011b). The maximum rated torque for the SAAII is 307 kN.m. This value was exceeded several times during the first transit leg of the expedition as presented in Figure 9.17(a) for the transit to Larsen C ice shelf. Quantitatively, the number of five- minute peaks exceeding the maximum continuous rating, $Q_{MCR,}$ occurred less than 1% of the total time of the transit.

Table 9.4*. Summary of torque and thrust measurements from 2 to 10 January 2019.*

	Torque [kN.m]	Date, Time	Thrust [kN]	Date, Time
Max abs. peak	336.6	10-Jan-2019 15:13:40	972.8	07-Jan-2019 20:09:38
Max amp.	239.7	10-Jan-2019 15:13:40	573.0	07-Jan-2019 20:09:38

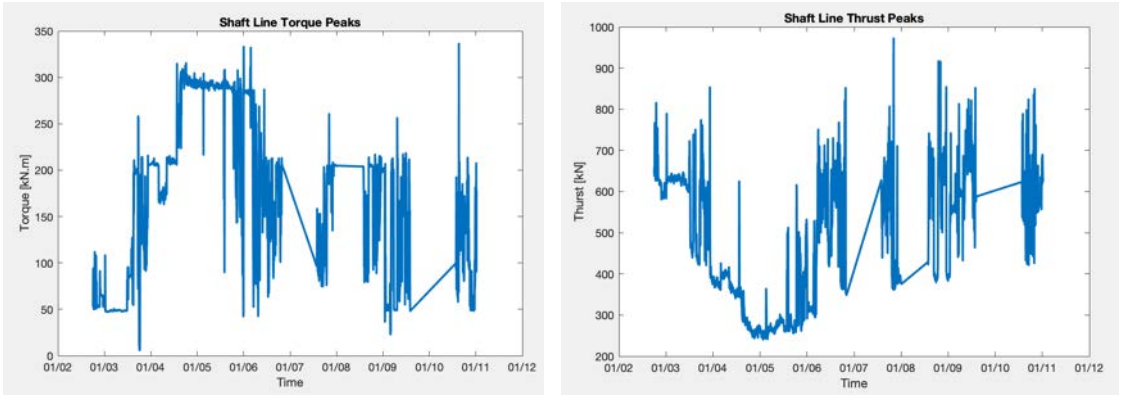

(a) (b)

Figure 9.17. *(a) Thrust and (b) torque peaks of the SAAII port side shaft line from the 2 to 10 January 2019.*

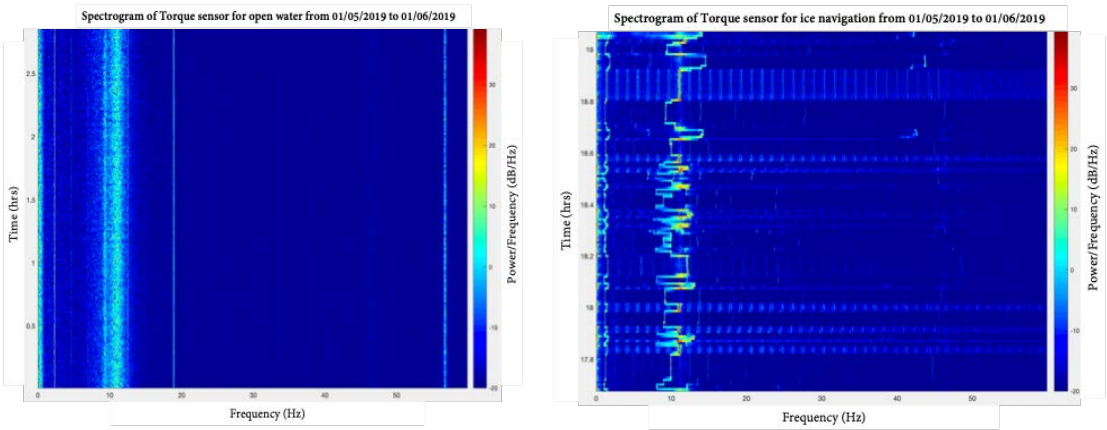

(a) (b)

Figure 9.18. *Spectrograms for two hours of transit of SAAII from Penguin Bukta to Larsen C for (a) open water- and (b) ice navigation.*

The torque and thrust data in the time domain could be transformed to the frequency domain by using a short-time Fourier Transform. The spectrograms indicate the power/frequency magnitude over time. Two cases were investigated: an open water navigation case and an ice navigation case. The Fourier transforms in the spectrograms were calculated using the sample rate of 600 Hz, 38400 NFFT points and a Hanning window with 50% overlap.

The vertical lines in Figure 9.18 indicate steady frequency excitation over time, while horizontal lines indicate excitation of the shaft line over the broad frequency band on a specific time (which is typical of impulsive events). For open water navigation in Figure 9.18(a) it is clear that the vessel propulsion system operates in a stationary state. The first shaft rotational harmonic is apparent around 2.3 Hz (for 140 rpm) along with the blade-pass frequency for four propeller blades (2.3 Hz x 4 = 9.2 Hz). A natural frequency band is visible above 10 Hz along with the constant excitation from diesel generators at 12 Hz (generator speed of 750 rpm).

In contrast, the shaft is subject to significantly more excitation during ice navigation. As evident from Figure 9.18(b), the shaft response shows a more sporadic frequency excitation spectrogram attributed to ice impacts on the propeller and frequent shaft speed changes. Closely spaced, vertical ripples in Figure 9.18(b) are harmonics of the shaft rotational speed. These harmonics are more dominant at specific shaft speeds which could be attributed to the inverter switching strategy when the captain selects propulsion parameters for navigation in “ice mode”. This mode allows for rapid control changes which are affected via the inverter to change the frequency and shape of the current supplies of the propulsion motor or propeller pitch. The harmonic of this current would be evident in the torsional shaft vibration response.

In order to estimate the forces exerted on ship propellers during ice navigation, the rotational dynamics of the propulsion system need to be accurately modelled. Direct measurement of ship propeller loads during ice navigation is challenged by the harsh

operating environment. Indirect measurements are thus performed on the dynamic model of the shaft line of such ships to estimate propeller loads through an inverse problem.

The CMU data were compared with certain torque and thrust characteristics to investigate contributions to certain physical behaviours on the shaft line or vice versa. The propeller pitch could be adjusted separately from the shaft's rotational speed. A good balance between the two settings could improve shaft line efficiencies. The propeller pitch and shaft speed are presented in Figure 9.18 for the port side shaft line during the transit leg of the WSE. There are two linear trends in propeller pitch versus shaft speed. The propeller pitch increases from 0 to a 97% (limited) as the shaft speed increases from 50 to 80 rpm. Another line runs parallel to the previously described one with the propeller pitch linearly increasing with the increasing shaft speed. Vertical lines at 84 rpm and 120 rpm suggest that the ship operated at these conditions for longer times and that the pitch of the propeller changed while maintaining the shaft speed. These trends are artefacts of the enforced propulsion profiles dictated by Rolls Royce propulsion design. These profiles dictate (and control) the relationship between propeller pitch and shaft speed for ship operational profiles as selected by the ship captain during navigation.

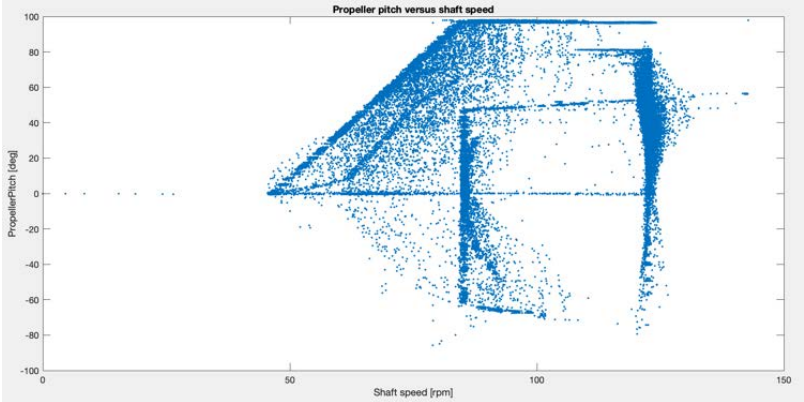

Figure 9.19. *Propeller pitch [%] versus shaft speed [rpm] during the transit.*

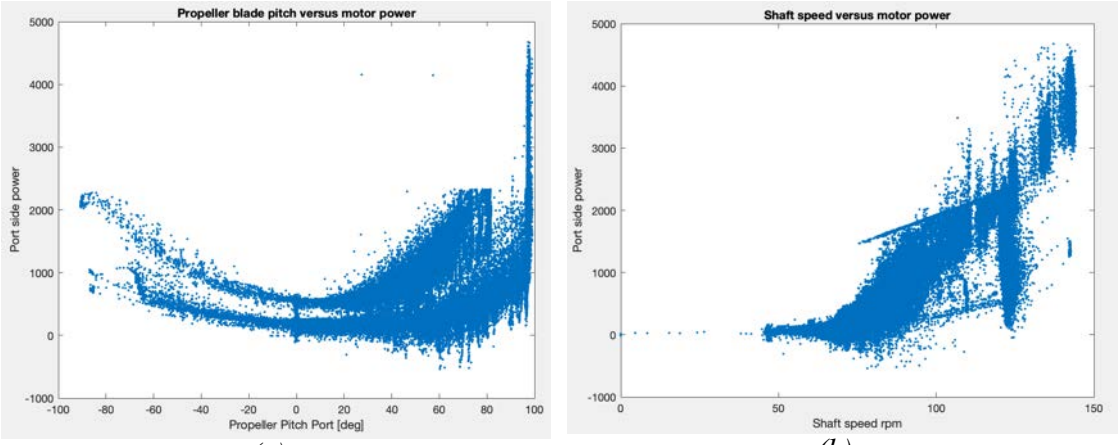

(a) *(b)*

Figure 9.20. *(a) Propeller blade pitch versus motor power (b) and shaft speed versus motor power.*

The angle of the controllable-pitch propeller blades drives propulsion power according to a parabolic trend as presented in Figure 9.(a). The angle of the local slope is dependent on the shaft speed. Increased shaft speeds are generally correlated with positive power consumption as shown in Figure 9.(b). The underlying trend lines are again artefacts of the ship propulsion settings where the Rolls Royce design dictates the appropriate shaft speed and propeller pitch combinations for ice and open water navigational profiles.

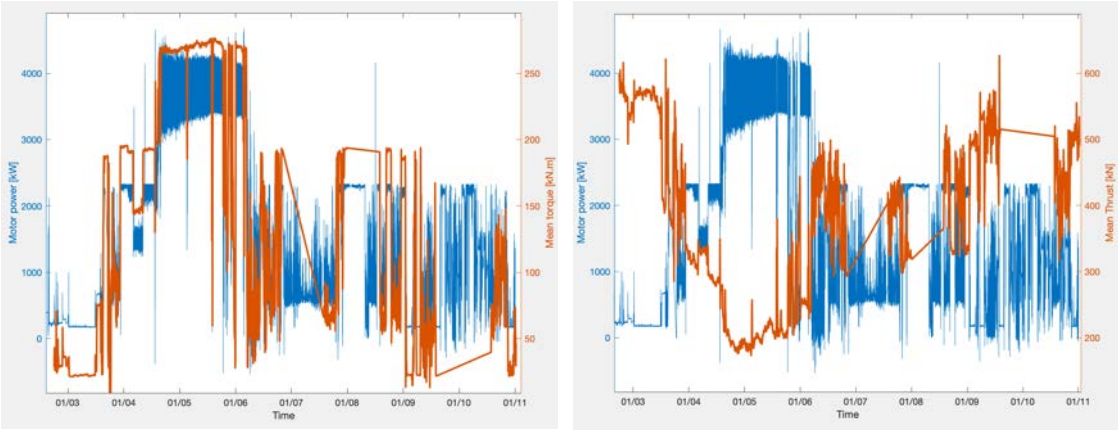

(a) *(b)*

Figure 9.21. *The power consumption of the port side motor over mean torque (a) and power consumption of port side motor versus mean thrust (b).*

The maximum power usage by the motor, is associated with a shaft speed of 140 rpm and a propeller pitch of 97%. The power consumption at this stage was 4660 kW, instantaneously exceeding the power specified for the nominal rated torque, which is 4500 kW.

The power consumption versus instantaneous mean torque and thrust are presented in Figure 9.21(a) and (b), respectively. The torque and power consumption follow a correlated trend, whereas the thrust and power consumption trend is inverted as expected.

9.2.4 Underway measurements of sea ice

A primary aim of the full-scale measurement effort was to deepen current understanding of sea ice and ship responses. Ice investigations on the Weddell Sea Expedition include:

- Visual observations performed by observers on the bridge and
- Under-way measurements with ice cameras.

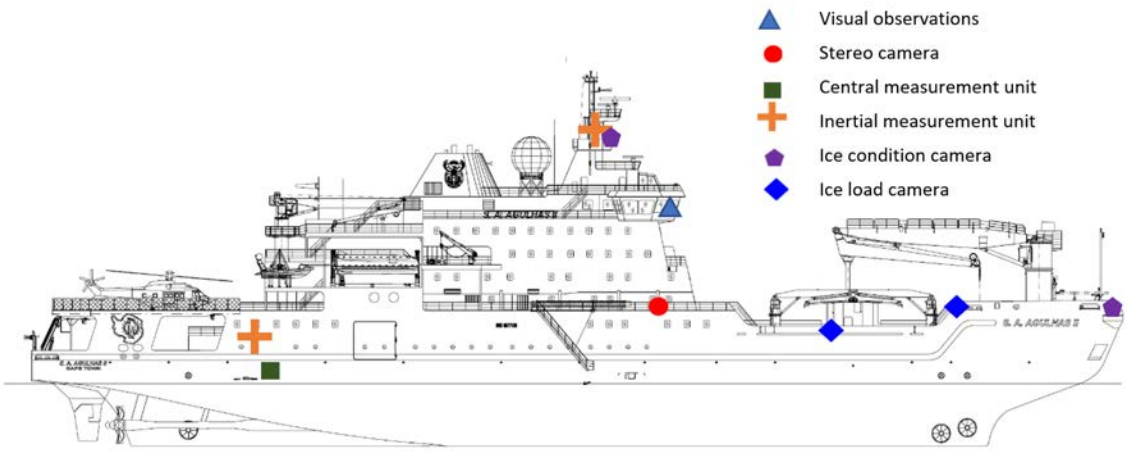

Figure 9.22. *A summary of underway ice measurements on the SA Agulhas II*

Visual Observations

Ice thickness is also determined from visual observations on the Bridge in round-the-clock surveillance shifts when the vessel engages in ice-passage as shown in Figure 9.23. A yardstick with 10 cm long black and white markings is suspended over the edge of the ship. As the ice rotates upwards alongside the hull the observer is tasked to judge for how many minutes in a 10 minute interval a certain ice thickness was experienced, *Bekker et al. (2017), Suominen et al. (2013,2017)*. Furthermore, the observations include 10-minute estimates of floe size and ice concentration, a rating (1 to 10) for the amount of brash ice and the amount of vibration experienced (rating 0 to 3). The observations included comments (describing the event and time) in instances which resulted in significant vibration. These events included ice impacts on the hull or propeller or cavitation.

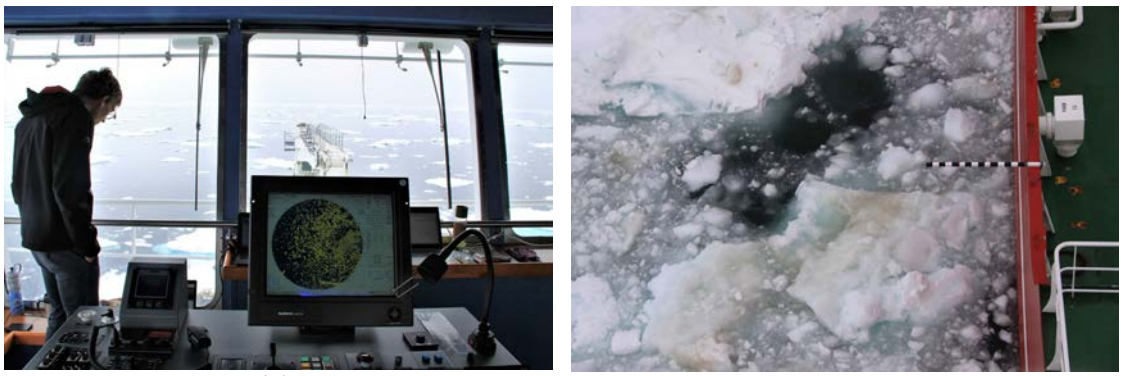

(a) *(b)*

Figure 9.23. *(a) An observer on the bridge uses a (b) yardstick, suspended from the port side of the ship to estimate the thickness of over-turning ice as the vessel navigates through ice.*

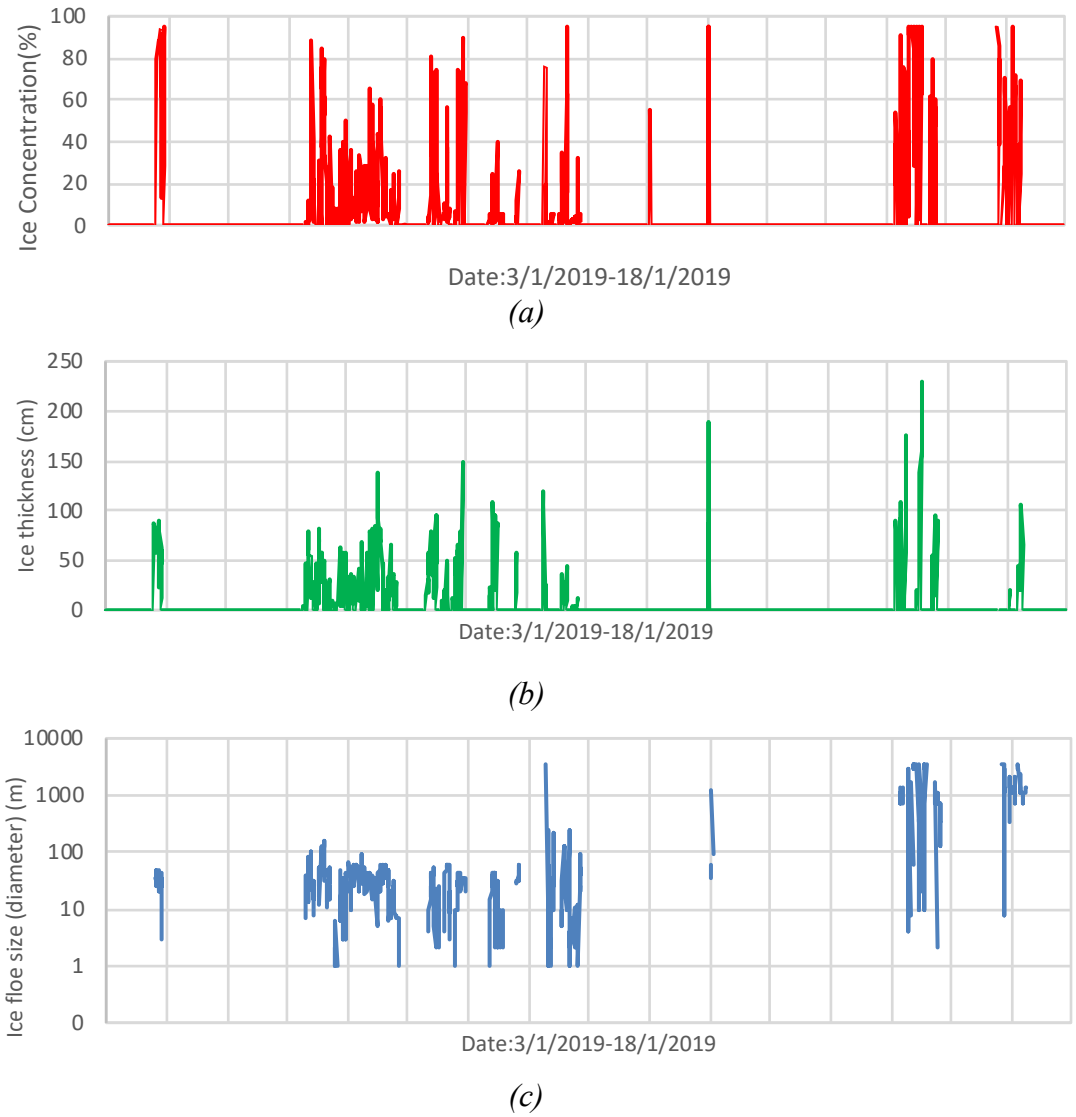

Figure 9.24. *Visual observations for (a) ice thickness, (b) ice concentration and (c) floe size.*

Preliminary conclusions (not all shown in sample analysis) include that the most challenging conditions included a maximum ice thickness of 6.5 m. Experiences on the SAA II have typically shown that the onset of ice navigation is around 60 degrees latitude when the ship voyages to Antarctica down the Greenwich meridian in December (Suominen et al., 2017). In general, ice thickness increases towards the south and the most challenging conditions are encountered close the ice shelf when the ship performs logistics at Penguin Bukta. In ice concentrations <100% the ship was commonly able to navigate through even multi-year ice by navigating between the floes or pushing floes aside. This typically results in increased lateral excitation of the vessel structure.
Difficulties with ice navigation were mostly encountered where ice concentration and ice thickness increased. Ships are able to push smaller floes aside and navigate between the

floe. However, in a case of large floes, the ship is forced to break through the ice, if the floe cannot be circumnavigated (Suominen et al., 2017).

9.2.5 Ice cameras

The most promising automated ice property estimators involve carefully trained image processing algorithms whereby footage from stereographic ice cameras is to be analysed, *Kulovesi and Lehtiranta (2014)*. The vessel was equipped with two camera systems which respectively determine the floe size and ice concentration and ice thickness.

- The top camera system for the determination of ice concentration and floe size
- Stereo camera system for the determination of ice thickness.

Top camera system (ice concentration and floe size)

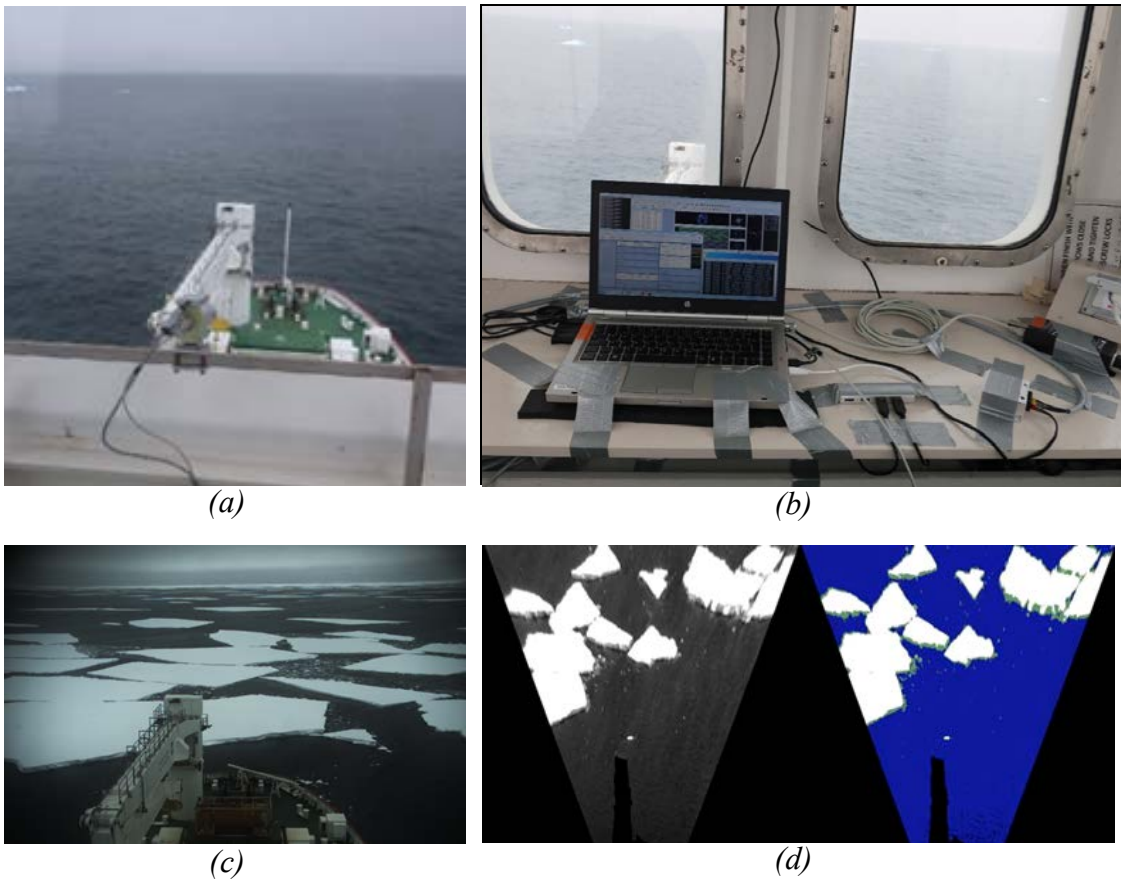

(a) *(b)*

(c) *(d)*

Figure 9.25. *(a) Camera position, (b) measurement computer, (c) sample image and (d) image processing to determine ice concentration and floe size using the top camera.*

The top camera is new this year to monitor the general ice conditions, as shown in Figure 9.25. The installed system contains one industrial camera connected to a laptop inside the crow's nest via an Ethernet link. The camera is installed on the frame with a

closed kit and heating plate. The position of the camera is listed in Table 9.1. Each photo is 18 Mb and will be processed to get the ice floe size and concentration by a machine vision algorithm. In addition, the top camera records the ice condition the ship encountered and is very useful to link the ice condition to the relevant ice loads.

Stereo camera system

The cameras were fixed to the ship railing on the starboard side of the ship at the 6th vertical support as shown in Figure 9.26. The installation comprises two industrial cameras connected to a measurement computer in the Wet Geology Laboratory (via ethernet links). The two cameras form a rigid stereo baseline which is approximately one meter wide. The baseline direction is perpendicular to the ship bow-aft line and the vertical axis. In other words, the stereo camera baseline points roughly towards the ship beam for the downward-looking cameras.

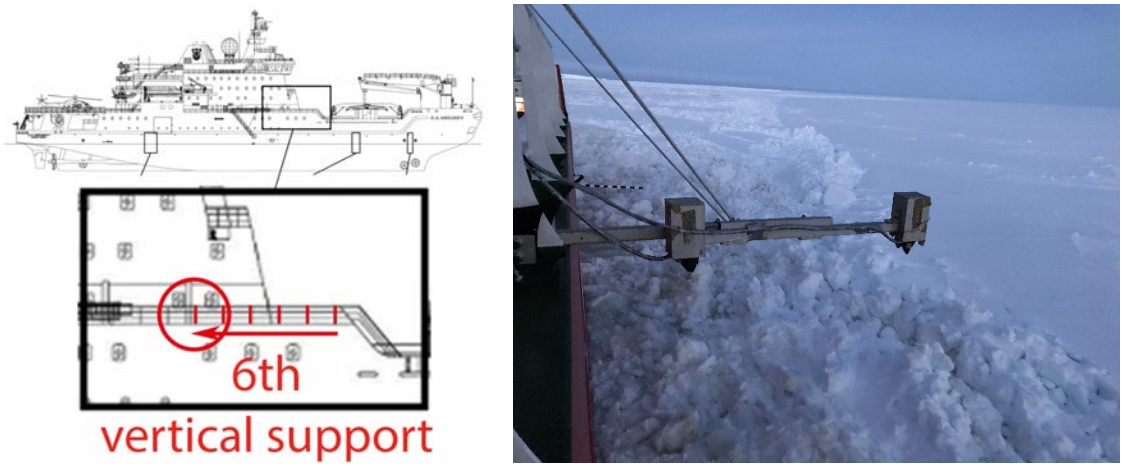

Figure 9.26. *Stereo camera placement on the ship starboard side on the sixth railing vertical support.*

The fixed and calibrated stereo baseline allows the cameras to perform 3D measurements. Measurements target sea ice, which overturns alongside the vessel. In idealized cases the ice reveals its cross-section, such that the snow depth and ice thickness can be measured as the vessel progresses through the ice. The processing of this data is semi-automated. A human operator is required to identify suitable over-turned floes for further processing by computer vision algorithms. Human processing is still required to obtain maximum reliability and precision.

9.3 Sea ice field work

Sea ice field work was performed on an opportunistic basis in collaboration with researchers from the University of Cape Town. Descriptions of the investigated sites,

along with associated activities, are presented in Table 9.4. The date and time refer to UTC time and locations refer to the positions recorded at the time of field work, bearing in mind that floes are subject to drift. For reference the associated vessel operations are added to document future case studies for combined analysis. Satellite images of the investigated floes are presented in Figure 9.27.

Table 9.5. *General information of ice property investigation work.*

#	Description	Date and time	Location	Activity
A	Bay ice at Penguin Bukta	2019.1.1 14:36	70°10' S, 02°07' W	i) Ice coring
B	Multi-year rafted ice floe (Figure 9.5(a) - Site 1), "FloeTilla"	2019.1.16 22:00	65°48' S 60°30' W	i) Ice coring.
C	Multi-year rafted ice floe (Figure 9.5(b) - AUV site), "FloeTilla"	2019.1.19 13:00	65°48' S 60°42' W	i.) Ice fishing, bending tests . ii) Ice coring in the fished yellow ice block. iii) Ramming with the vessel to free AUV9.
D	Multi-year rafted ice floe (Figure 9.5(c) - site 3) "FloeExpectations"	2019.1.24 15:00	66°00' S 60°30' W	i.) Full power ice breaking through ice with multi-year occlusions.
E	Multi-year level ice floe (Figure 9.5(d) - site 4) "FloeRida"	2019.1.26 18:00	64°39' S 57°08' W	i.) Ice coring (partially – corer stuck). ii) Ice fishing. iii) Bending and compression tests. iv) Light impact with vessel to dislodge "ice fish.

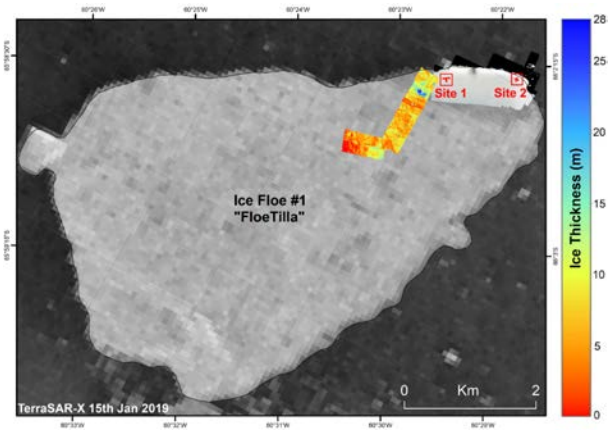

(a) Case B.

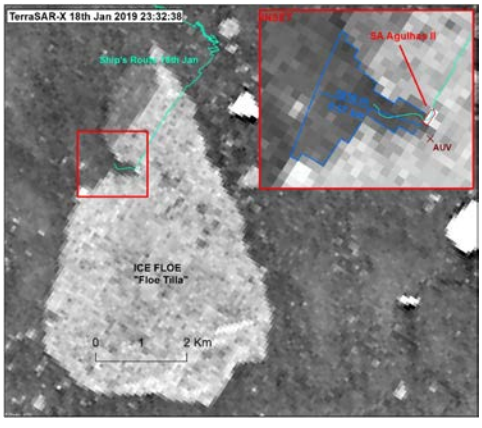

(b) Case C.

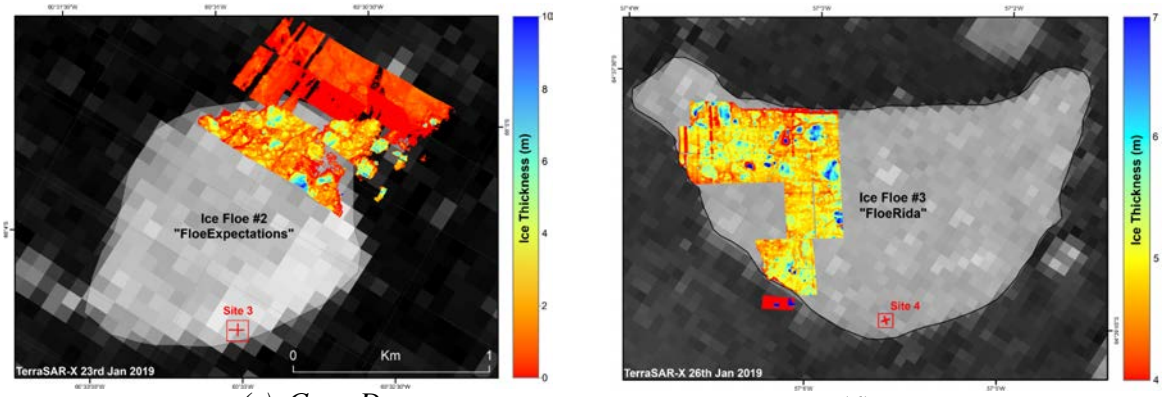

(c) Case D. *(d) Case E.*

Figure 9.5. *TerraSAR-X satellite images detailing the geometry and site locations of ice floes which were subjected to field work investigations during the Weddell Sea Expedition 2019 (Images by Scott Polar Research Institute).*

9.3.1 Ice fishing

Samples of floe ice were collected by ramming into the floes with the vessel. This dislodged debris which floated in the vessel proximity post impact. Sea ice samples were fished from the ocean using a cargo net and spreader beams, which were suspended from the starboard crane as shown in Figure 9.28. The net was submerged by adding four heavy shackles for weight. The net was dipped under a hand-picked fragment of ice-debris and hoisted on board. Here it was hacked into sample beams of about 100 x 20 x 20 cm for immediate testing on board. These tests involved bending and compression tests which aimed to determine the flexural and compressive strength of the ice associated with ramming loads.

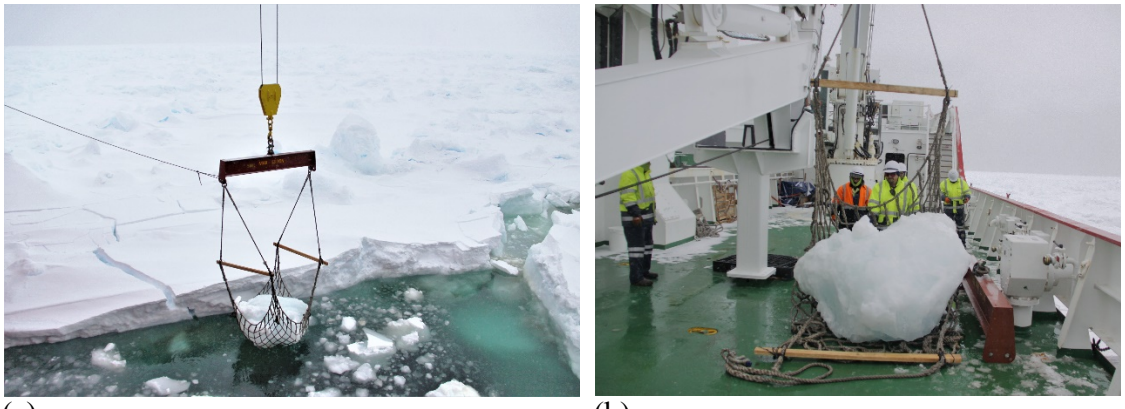

(a) (b)

Figure 9.28. *(a) After ramming a sample of freshly broken ice debris is collected with a cargo net. (b) The sample is lifted onto the deck where it is sawed into bending test samples.*

9.3.2 Bending tests

Bending samples were collected at two sites. Four samples (S1 to S4) were cut with a hand saw from an ice sample which was fished from the ocean, shortly after ramming with the vessel at the recovery site of AUV9 (Figure 9.27(b)). From observation the floe was thick, ridged and comprised multi-year ice occlusions and a non-homogeneous structure, with possible sections of bay ice. The floe size in this location was 2 to 5 km. The ice concentration of the floe was 100% and very little brash ice (<1/10) was present in the surrounding water. Ice thickness was estimated at 1.5 to 3 m through subjective observations aided with a yardstick. According to visual observations the ice was covered by 80 to 100 cm of snow.

Three further samples were collected from a level multi-year ice floe, "Floerida" (Figure 9.27(d)). In this case the vessel approached the 2 to 5 km floe in open water and knocked it gently at a speed of 2 kn. Very little fragmentation was observed in the breaking ice, with significant snow cover of about 60 cm. It is thought that this ice is land fast ice with several phases of re-freezing. The ice thickness was estimated more than 3 m. Two large samples of the top 50 cm of the ice floe were recovered using a cargo net, suspended from the starboard side crane.

The ice samples were subjected to bending tests on a custom-designed rig (Figure 9.29), which is equipped with a load cell and LVDT. The ultimate bending strength σ_{ut} [MPa] for a rectangular beam with a beam height, h [mm], and width, w [mm], simply supported on a span, D [mm], is:

$$\sigma_{ut} = \frac{3FD}{2wh^2}$$

This estimate excludes self-weight of the beam which will be calculated in more detail when all density tests are completed.

A sample calculation is provided for beam samples from Case C, the recovery site of AUV9 on "Floetilla" Figure 9.27 (b). The approximate beam dimensions are provided in Table 9.5. The density, ρ, of ice samples was also determined from the average of six smaller samples from the fractured beam. The averages of these density measurements are reported in Table 9.6.

Table 9.6. *Beam dimensions for samples extracted from the AUV9 recovery site on "Floetilla".*

Sample #	*w* [mm]	*h* [mm]	*D* [mm]	*P [kg/m^3]*	*F* [N]	σ_{ut} [kPa]
s1	167	177	767	833.0	516	113.5
s2	207	208	1010	826.4	1343	227.1
s3	197	195	1100	796.4	1092	240.6
s4	165	150	767	814.1	607	196.7

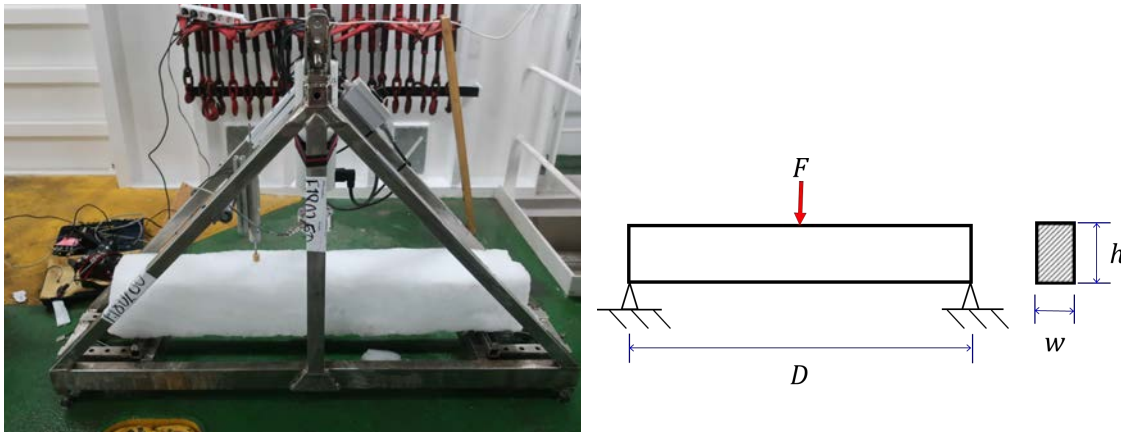

(a) (b)

Figure 9.29. *(a) A photograph of an ice sample in the three-point bending rig. (b) A diagram showing the beam dimensions and bending force which governs the beam equations.*

9.3.3 Ice compression tests

Compression tests were performed on seven ice samples (c1 to c7), which were extracted from ice fishing at "FloeRida" on 26 January 2019 (Table 9.7). Wooden supports were used in a sub-optimal configuration to compress ice blocks with approximate dimensions of 100 mm x 100 mm using the force applied by the bending rig. This data is likely to be inconclusive. However, it is expected that the ice samples should be double and quadruple the flexural strength in transverse and through-thickness compression, respectively.

Table 9.7. *The dimensions of compression samples from "FloeRida".*

Sample #	w [mm]	L [mm]	h [mm]	Direction of test	Note on fracture
c1	114	131	149	Trough thickness	--
c2	90	129	94	Trough thickness	--
c3	96	103	99	Transverse	Broke in layer
c4	97	88	114	Transverse	Broke 90˚ with layer
c5	98	104	70	Through thickness	Broke in the middle
c6	78	90	53	Transverse	Broke into 3 pieces
c7	81	127	113	Through thickness	Chipped off

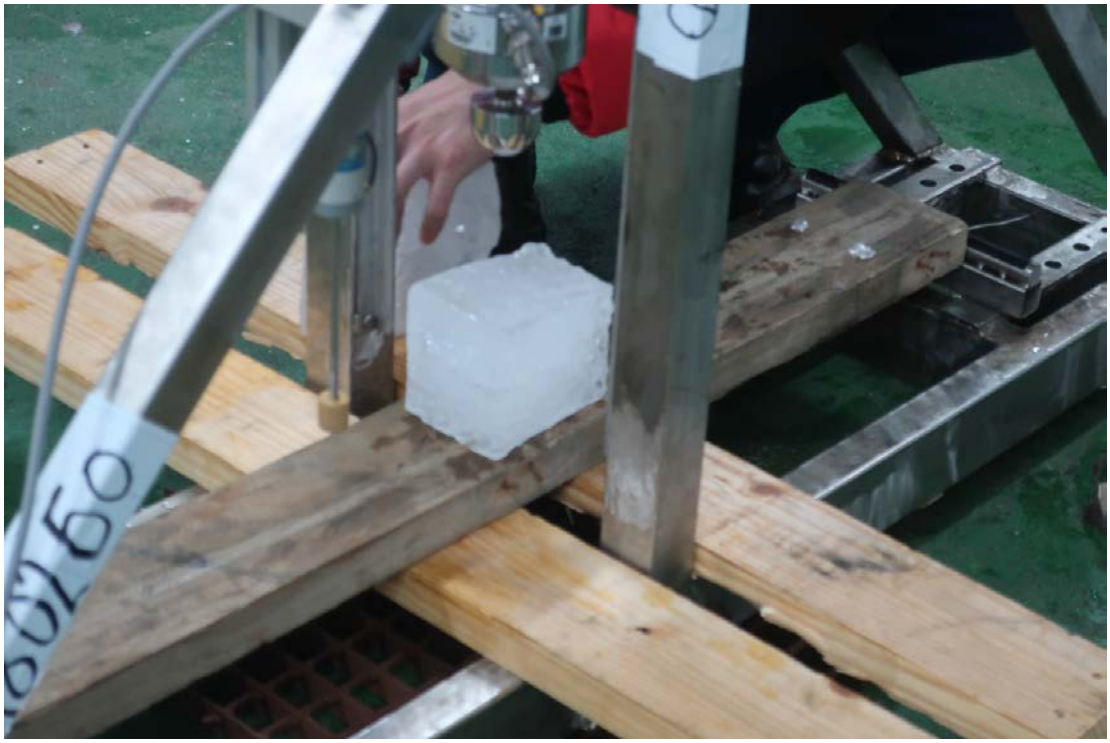

Figure 9.30. *A photograph showing a compression test on extracted sea ice.*

9.3.4 Ice coring

Cores were extracted on three occasions on the Weddell Sea Expedition on an opportunistic basis. The aim of ice coring was to investigate temperature, salinity, density, crystal structure. The temperature is measured on the ice after ice coring. Investigation of salinity, density and crystal structure are conducted onboard.

Once in the field, a suitable selection of level-looking floe was selected. In Figure 9.31 a series of photographs describe the process. Two team members dig a snow pit to remove excess snow from the ice below. Two team members operated a corer to ensure that cores are drilled vertically (Figure 9.(a)). When the core was drilled to depth the motor was removed, whilst a second operator held the core pole and inserted the T-bar handle.

(a) *(b)*

(c) *(d)*

Figure 9.31. *(a) Ice is cored using a motorized drill after clearing snow from the ice. (b) Temperature is measured and samples are (c) bagged and carried away from the body. (d) An extension pole is added and one person maintains contact with the corer.*

This handle is turned anti-clockwise to dislodge the core blades and cut the internal ice core from the under-lying sea ice. The corer removed from the drill hole and core sample is placed on a measurement tray. Two team members note and measure the length and temperature, which was determined by inserting an electronic temperature probe as shown in Figure 9.31(b). A temperature reading was recorded as soon as the temperature reading stabilized (after about 30 seconds). Samples are placed into marked bags, which

are closed with cable ties. In order to retain samples in their frozen state they are carried far away from the body (Figure 9.31(c)), stored under shoveled snow in the field and taken on board for storage in a freezer (-20 ˚C) as soon as possible. In the meantime, the drill team add extension poles (Figure 9.31(d)) to the corer if required for extraction of the next sample.

Ice cores (Case A - 2019.1.1)

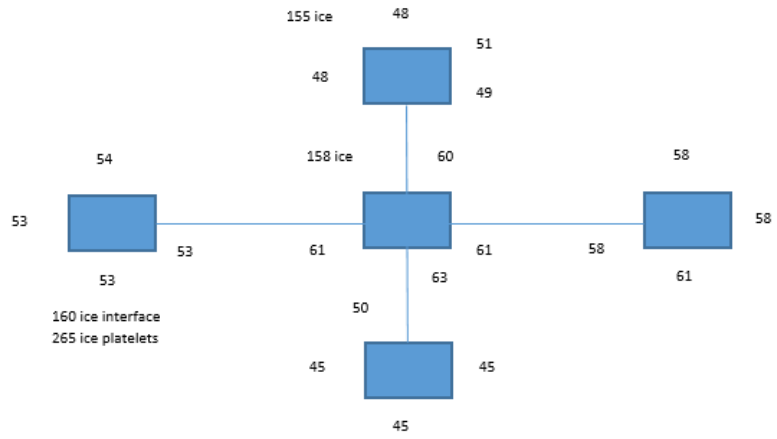

Figure 9.32. *A diagram showing the layout of the ice fieldwork site at Penguin Bukta. Five snow pits were dug. The ice thickness and depth of ice platelets are indicated in cm.*

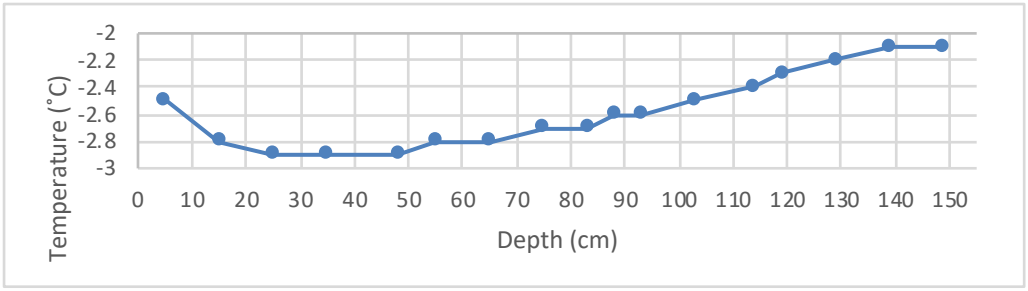

(a) Case A- Ice core 1: temperature (155 cm ice, 60 cm snow, center sample location)

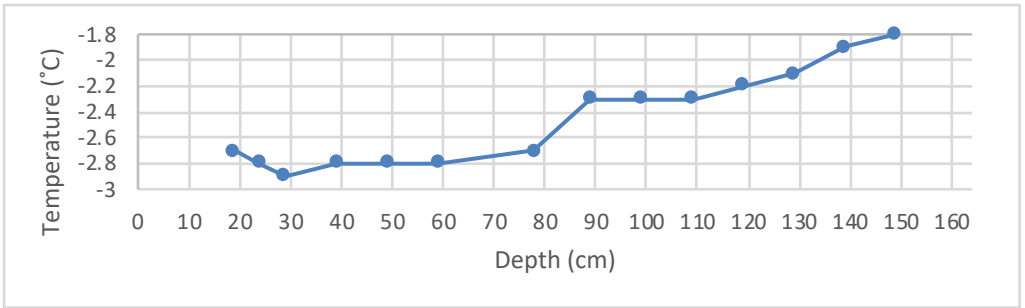

(b) Case A - Ice core 2: temperature profile

Figure 9.33. *Case A - Temperature profiles for 2 cores on the bay ice at Penguin Bukta.*

(a) Case A - Ice core 3 in the - 20˚C freezer laboratory: Thin sectioning, 156 cm ice, 60 cm snow, centre sample location.

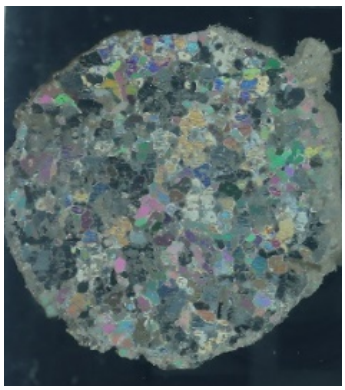

(b) Depth ~3cm

(c) Depth ~11cm

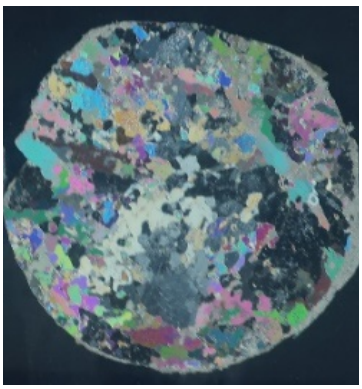

(d) Depth ~22 cm

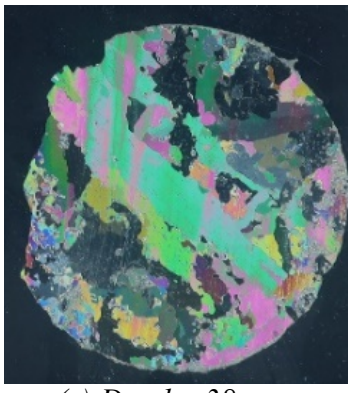

(e) Depth ~38 cm

(f) Depth ~51 cm

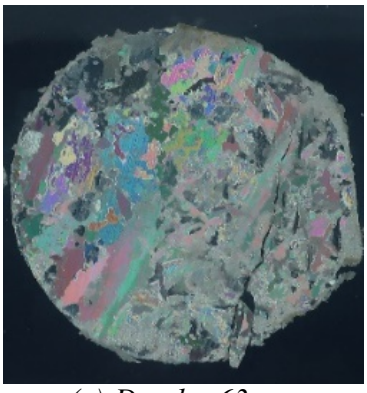

(g) Depth ~63 cm

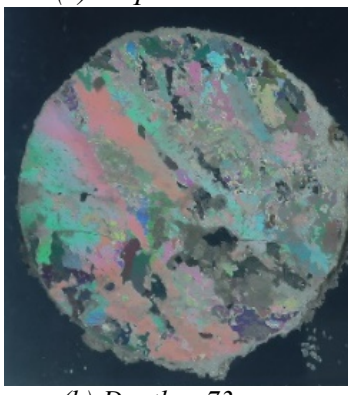

(h) Depth ~ 73 cm

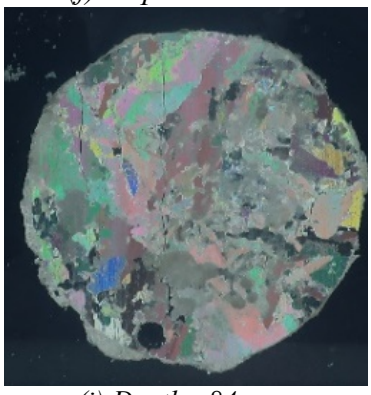

(i) Depth ~84 cm

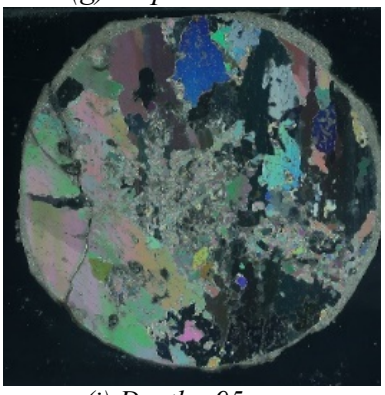

(j) Depth ~95 cm

Figure 9.34. *Preliminary results from transverse sectioning of an ice core extracted from bay ice at Penguin Bukta.*

Three ice cores were extracted from the bay ice at Penguin Bukta for analysis by the Stellenbosch / Aalto University team. It was found that the bay ice was covered by about 60 cm of snow and that the thickness of this ice was approximately 1.5 m. Platelets were found upon closer investigation of the sample site. This is indicative of re-freezing processes.

The third core was taken on board and stored in a -20 ˚C freezer. This core was covered by 60 cm of snow and comprised a length of 156 cm. Preliminary results are presented as found from transverse thin sectioning which was performed in the planes of stratification of the ice core. It can be seen that the grain size of the ice increases in size with increasing depth.

Case B - Ice core (2019.1.16)

Ice fieldwork for Case B involved the extraction of two cores from floe “Floetilla”. All ten available extension poles were used to drill to sufficient depth with the ice corer. A total length of 5.2 m of ice was extracted. A photograph of this core is presented along with the temperature profile in Figure 9.35. It is noted that the temperature of the core is colder than surrounding core temperatures at depths of 140 cm and 220 cm.

(a)

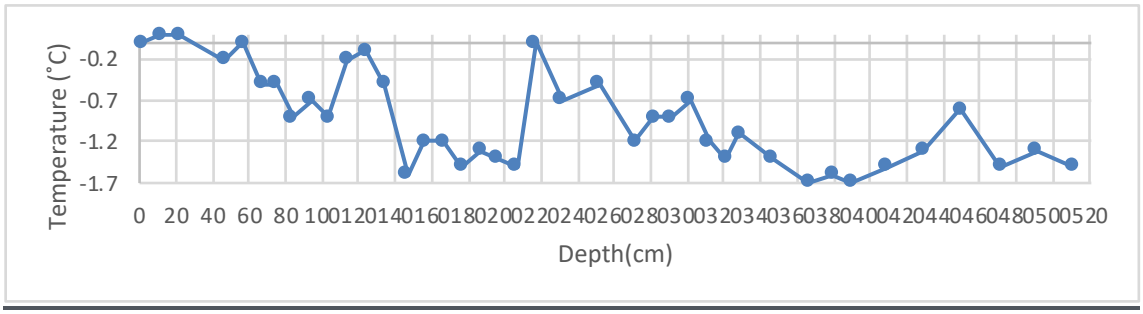

(b)

Figure 9.35. *(a) A core exceeding 5 m length was extracted from Site 1 on "FloeTilla" with a temperature variation as shown in (b).*

9.4 References

Bekker, A. *et al.*, 2014. Full-scale measurements on a polar supply and research vessel during maneuver tests in an ice field in the Baltic Sea. In *Proceedings of the International Conference on Offshore Mechanics and Arctic Engineering - OMAE*. doi: 10.1115/OMAE2014-24128.

Bekker, A. *et al.*, 2018. From data to insight for a polar supply and research vessel. *Ship Technology Research*, pp. 1–34.

Bekker, A., Soal, K.I. and McMahon, K.J., 2017. Whole-body vibration exposure on board a Polar Supply and Research Vessel in open water and in ice. *Cold Regions Science and Technology*. doi: 10.1016/j.coldregions.2017.06.008.

Brandt, A., 2013. The ABRAVIBE Toolbox for Teaching Vibration Analysis and Structural Dynamics. In *Conference Proceedings of the Society for Experimental Mechanics Series*, pp. 131–141.

Brincker, R. and Ventura, C., 2015. *Introduction to Operational Modal Analysis*.

Ikonen, T., Peltokorpi, O. and Karhunen, J., 2014. Inverse ice-induced moment determination on the propeller of an ice-going vessel. *Cold Regions Science and Technology*, 112, 1–13. doi: 10.1016/j.coldregions.2014.12.010.

Kotilainen, M. *et al.*, 2017. Predicting ice-induced load amplitudes on ship bow conditional on ice thickness and ship speed in the Baltic Sea. *Cold Regions Science and Technology,* 135, 116–126.

Løvoll, G. and Kadal, J.C., 2014. *Big data - the new data reality and industry impact*. Hovik, Norway.

Van Overschee, P. and De Moor, B., 1996. *Subspace Identification for Linear Systems: Theory - Implementation - Applications*. Dordrecht: Kluwer Academic Publishers.

Peeters, B. and de Roeck, G., 1999. Reference-based Stochastic Subspace Identification for Output-only Modal Analysis. *Mechanical Systems & Signal Processing*, 13, 855–878.

Peeters, B. and de Roeck, G., 2001. Stochastic system identification for operational modal analysis: a review. *Journal of Dynamic Systems, Measurement and Control*, 123. doi: 10.1115/1.1410370.

Soal, K., 2018. *System identification and modal tracking of ship structures*. Stellenbosch University.

Soal, K., Bienert, J. and Bekker, A., 2015. Operational modal analysis on the polar supply and research vessel the S.A. Agulhas II. In *6th International Operational Modal Analysis Conference*.

Soal, K.I., 2015. *Vibration response of the polar supply and research vessel the S. A. Agulhas II in Antarctica and the Southern Ocean*. Stellenbosch :

Stellenbosch University.

STX, 2010. *FINNSAP finite element analysis of the PSRV NB1368*. Rauma, Finland.

Su, B., Riska, K. and Moan, T., 2011. Numerical study of ice-induced loads on ship hulls. *Marine Structures*, 24, 132–152.

Suominen, M. *et al.*, 2013. Full-scale measurements on board PSRV S.A. Agulhas II in the Baltic Sea. In *Proceedings of the International Conference on Port and Ocean Engineering under Arctic Conditions, POAC*.

Suominen, M. *et al.*, 2017. Visual Antarctic Sea Ice Condition Observations during Austral Summers 2012-2016. In *Port and Ocean Egineering under Arctic Conditions*. Busan, Korea.

Ventura, C.E., Brincker, R. and Andersen, P., 2001. Damping Estimation by Frequency Domain Decomposition. In *Proceedings of the International Modal Analysis Conference XIX*, 698–703.

De Waal, R.J.O., 2017. *An investigation of shaft line torsional vibration during ice impacts on PSRVs*. Stellenbosch University.

10. Meteorology

Mmathapelo Makgabutlane

10.1 Introduction

The South African Weather Service participated in the Weddell Sea Voyage with the purpose of gathering observational weather data as well as providing weather forecasts for ship operations. The observations were done through surface synop observations, releasing weather balloons to gather upper air observations, as well as deploying drifting weather buoys to collect ocean surface data. All of these data were sent to the Global Telecommunication System (GTS) for use by the meteorological community worldwide. The observational weather data gathered would be useful for numerical weather models, which are essential for forecasters around the world.

Surface meteorological observations are conducted internationally at the same time following Greenwich Meridian Time (GMT) at synoptic hours. The main synoptic hours are 00:00, 06:00, 12:00 and 18:00, and the intermediate hours are 03:00, 09:00, 15:00 and 21:00. Measuring instruments record air temperature, humidity, barometric pressure, sea surface temperature, and wind speed and direction. Visual observations by a human observer include weather, visibility, cloud (amount, type and height), sea state, as well as sea ice conditions. In addition to being used in numerical weather models, these observations are used for synoptic analyses by meteorological offices mapping weather patterns.

Upper air observations of the atmospheric profile are done by attaching a radiosonde to a weather balloon and releasing the balloon into the atmosphere. The radiosonde has sensors that measure temperature, humidity and pressure. The sonde also has global positioning system (GPS) capabilities from which the wind speed and direction can be derived. The information gathered through upper ascents is extremely useful for understanding what is happening in the upper portions of the atmosphere. This understanding is important as the atmosphere is three-dimensional and pressure systems in the upper levels affect weather at the surface.

Drifting weather buoys are periodically deployed to gather weather information over the ocean surface. The buoys measure parameters such as air temperature, sea surface temperature and air pressure and the data are transmitted via the iridium communication systems. A buoy typically lasts for anything from six months to two years. Deploying weather buoys into the southern ocean is vital for collecting weather information over this area as there is no land where most of the weather systems that affect the southern hemisphere continents are formed between the mid-latitudes and the Antarctic continent. This is, therefore, one of the few ways for weather information that goes into weather models and surface analyses can be obtained. This is the first time the South African Weather Service has deployed drifting weather buoys into the Weddell Sea.

10.2 Methods

10.2.1 Surface synoptic data

Synoptic information was gathered every three hours from 06:00 to 21:00 every day from the start of the Weddell Sea cruise on 3 January 2019. On some days when the meteorologist was involved in other work that required later hours, the 00:00 observation was also conducted. All of the synops were immediately sent to the South African Weather Service communications server, where after they were disseminated to the GTS for use in the numerical weather models and by other users of meteorological information.

10.2.2 Upper air observations

Three weather balloons were released during the transit to the Larsen C Ice Shelf. The details of each ascent are shown below:

Ascent 1 65°47.697'S 032°40.090'W

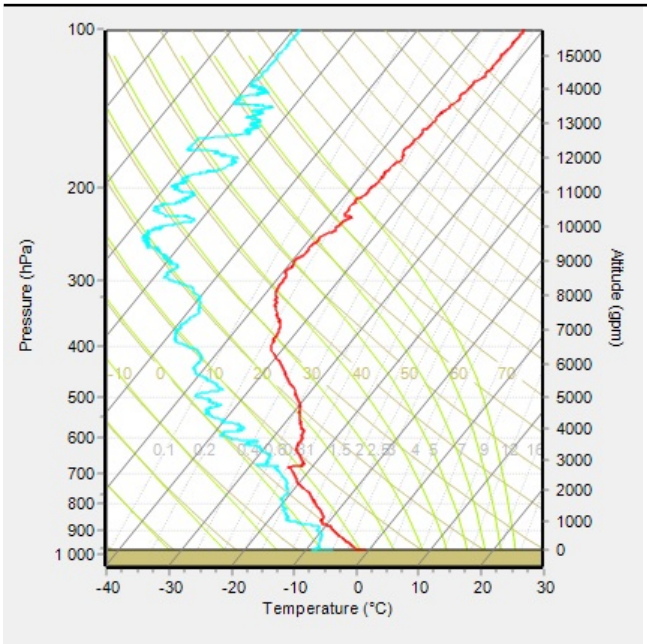

Item	Detail
Date	6 January 2019
Time	00:00 GMT
Burst height	20 136m
Minimum pressure	52.58hPa
Minimum temperature	-49.9°C

***Figure 10.1**. Skew-t gram showing data from upper air ascent on 6 January 2019.*

Ascent 2 63°06.549'S 050°58.356'W

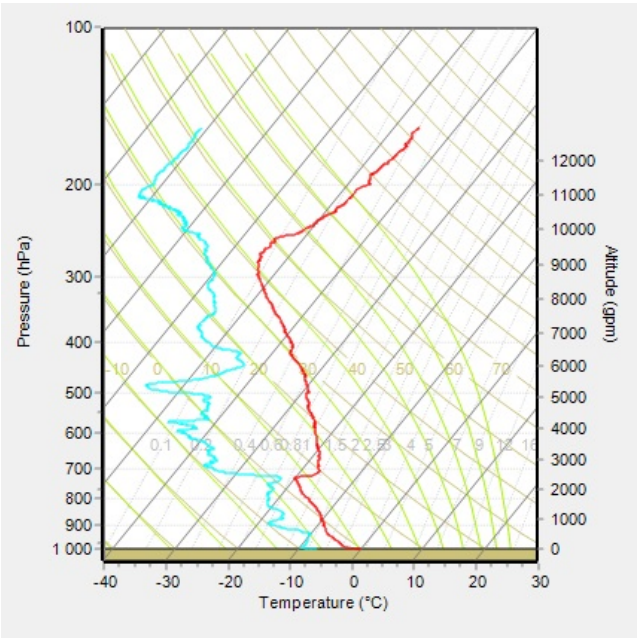

Item	Detail
Date	9 January 2019
Time	00:00 GMT
Burst height	12 938m
Minimum pressure	156.00hPa
Minimum temperature	-55.2°C

***Figure 10.2**. Skew-t gram showing data from upper air ascent on 9 January 2019.*

Ascent 3 66°21.059'S 60°18.199'W

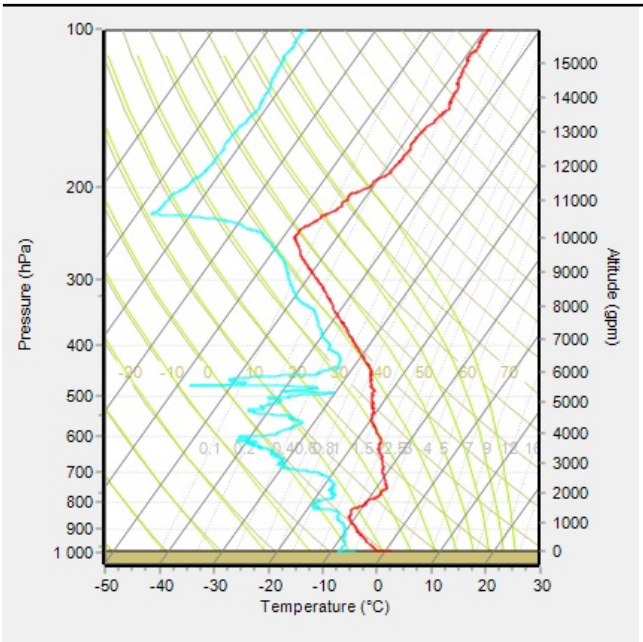

Item	Detail
Date	12 January 2019
Time	00:00 GMT
Burst height	22 692m
Minimum pressure	36.85hPa
Minimum temperature	-58.1°C

***Figure 10.3**. Skew-t gram showing data from upper air ascent on 12 January 2019.*

10.2.3 Weather buoys

Two drifting weather buoys were deployed. The positions are shown in Figure 10.4.

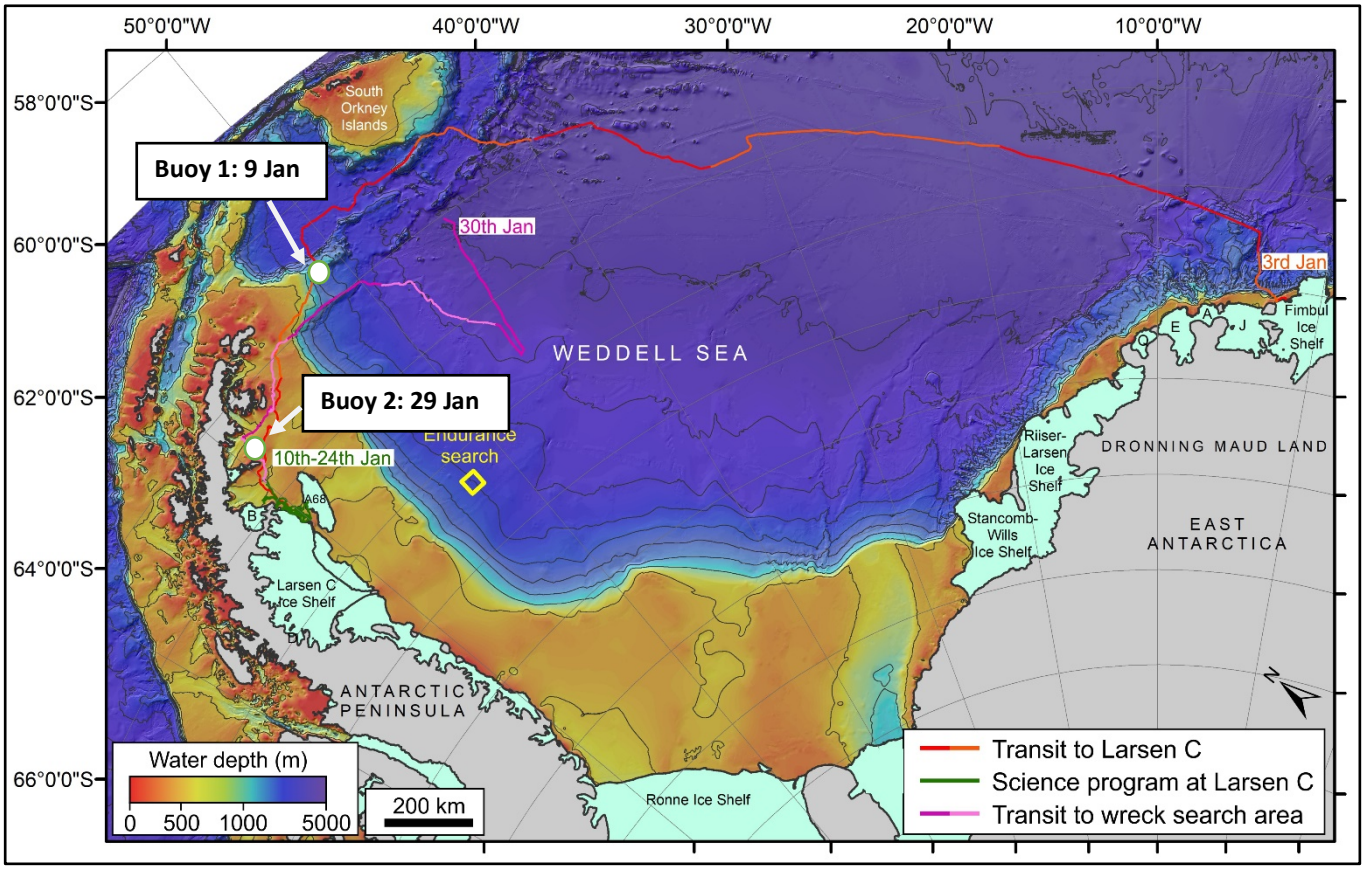

***Figure 10.4**. Positions of the two weather buoys deployed during the Weddell Sea Expedition*

The latitudes and longitudes of the deployments were:

Buoy deployment 1: 63°25.708'S 051°41.958'W

Buoy deployment 2: 64°43.616'S 058°36.593'W.

10.2.4 Forecasts

Two types of forecasts were compiled daily by the on board meteorologist. The first was a forecasts for the purposes of the general user as well as for the navigational officers and the master. This forecast covered the entire day as a whole and included information such as expected weather, cloud cover, temperatures, wind speeds and direction, sea state, as well as a synopsis of the general circulation in the area. The second type of forecast was a specialised

forecast compiled for the purposes of the operation of the underwater vehicles. This forecast detailed wind speed and direction at 3 hour intervals, as this was the most important weather-related operational factor affecting the use of the underwater vehicles. It also include a general weather outlook for the day, as well as expected minimum and maximum temperatures.

10.3 Conclusions

The Weddell Sea is a rarely charted area of the world. In order for weather forecasts to improve in accuracy, one of the essential steps is for an increase in the density of meteorological observations, particularly over the Southern Ocean. The weather data gathered during the Weddell Sea Expedition of 2019 will provide additional data for weather forecasting purposes.

11. Concluding remarks

11.1 The scientific work of the expedition

The datasets reported on in the earlier sections of this report show that the scientific investigations of the WSE produced many new observations from a part of the Weddell Sea that has been little studied previously; the area east of the Larsen C Ice Shelf (Figures 2.2 to 2.5). This area was selected for study given the recent changes that have been observed on the Larsen ice shelves in the past two decades (Section 1.1). It was the use of the SA *Agulhas II* that enabled so much scientific work to carried out successfully in the ice-infested waters of this part of Antarctica.

The samples of ice, water, sediment and micro-organisms that we have collected, along with much geophysical data on the morphology of ice floes and the seafloor, will be analysed in the laboratories of the scientists who took part in the expedition (Section 2.3.1). Significant parts of this analytical work, and the scientific papers that result from it, will be collaborative between institutions and disciplines.

We look forward to working up these novel and varied datasets and preparing papers for publication in the international scientific literature.

11.2 Acknowledgements

We thank the Flotilla Foundation for their generous support of the entire expedition.

The technical teams on the ship, from Ocean Infinity, Deep Ocean Search and Eclipse, worked tirelessly to achieve the maximum amount of scientific work, often in difficult circumstances. Captain Knowledge Bengu and Captain Freddie Ligthelm and the Officers and Crew of the SA *Agulhas II* were outstandingly helpful and also masterful in working through the sea ice of the Weddell Sea. We are also grateful for the support of AMSOL and the South African Antarctic Programme and for White Desert for transport between Cape Town and the ship.

12. Cumulated References

Absy, J. M., Schröder, M., Muench, R., and Hellmer, H., 2008. Early summer thermohaline characteristics and mixing in the western Weddell Sea. *Deep Sea Research Part II*: Topical Studies in Oceanography, 55, 1117-1131.

Arndt, J.E. and 15 others, 2013. The International Bathymetric Chart of the Southern Ocean (IBCSO) Version 1.0 – A new bathymetric compilation covering circum-Antarctic waters. *Geophysical Research Letters*, 40, 3111-3117.

Arrigo, K.R., van Dijken, G.L., Ainley, D.G., Fahnestock, M.A. and Markus, T., 2002. Ecological impact of a large Antarctic iceberg. *Geophysical Research Letters*, 29, doi:10.1029/2001GL014160.

Balco, G. A., Schaefer, J. M., and LARISSA Group., 2013. Terrestrial exposure-age record of Holocene ice sheet and ice-shelf change in the northeast Antarctic Peninsula. *Quaternary Science Reviews*, 59, 101-111.

Bekker, A. *et al.*, 2014. Full-scale measurements on a polar supply and research vessel during maneuver tests in an ice field in the Baltic Sea. In *Proceedings of the International Conference on Offshore Mechanics and Arctic Engineering - OMAE*. doi: 10.1115/OMAE2014-24128.

Bekker, A. *et al.*, 2018. From data to insight for a polar supply and research vessel. *Ship Technology Research*, pp. 1–34.

Bekker, A., Soal, K.I. and McMahon, K.J., 2017. Whole-body vibration exposure on board a Polar Supply and Research Vessel in open water and in ice. *Cold Regions Science and Technology*. doi: 10.1016/j.coldregions.2017.06.008.

Bendschneider, K. and Robinson, R.J., 1952. A new spectrophotometric method for the determination of nitrite in sea water. *Technical Report No. 8*. University of Washington.

Bentley, M.J., Hodgson, D.A., Smith, J.A., Ó Cofaigh, C., Domack, E.W., Larter, R.D., Roberts, S.J., Brachfeld, S., Leventer, A., Hjort, C., Hillenbrand, C.-D., Evans, J., 2009. Mechanisms of Holocene palaeoenvironmental change in the Antarctic Peninsula region. *The Holocene*, 19, 51-69.

Brachfeld, S., Domack, E.W., Kissel, C., Laj, C., Leventer, A., Ishman, S. Gilbert, R., Camerlenghi, A., Eglinton, L.B., 2003. Holocene history of the Larsen-A Ice Shelf constrained by geomagnetic paleointensity dating. *Geology*, 31, 749-752.

Brandt, A., 2013. The ABRAVIBE Toolbox for Teaching Vibration Analysis and Structural Dynamics. In *Conference Proceedings of the Society for Experimental Mechanics Series*, pp. 131–141.

Brincker, R. and Ventura, C., 2015. *Introduction to Operational Modal Analysis*.

Camerlenghi, A., Domack, E., Rebesco, M., Gilbert, R., Ishman, S., Leventer, A., Brachfeld, S. and Drake, A., 2001. Glacial morphology and post-glacial contourites in northern Prince Gustav Channel (NW Weddell Sea, Antarctica). *Marine Geophysical Research*, 22, 417-443.

Casciotti, K.L., Sigman, D.M., Hastings, M.G., Böhlke, J.K. and Hilkert, A., 2002. Measurement of the oxygen isotopic composition of nitrate in seawater and freshwater using the denitrifier method. *Analytical Chemistry*, 74, 4905–4912. doi:10.1021/ac020113

Cullen, J.J., 2001. Plankton: Primary Production Methods. *In* Steele, J., Thorpe, S., Turekian, K. (eds) *Encyclopedia of Ocean Sciences*. Academic Press, San Diego, 2277–2284.

Clough, J.W. and Hansen, L.B., 1979. The Ross Ice Shelf Project. *Science*, 203, 433-434.

Cook, A.J., Holland, P.R., Meredith, M.P., Murray, T., Luckman, A. and Vaughan, D.G., 2016. Ocean forcing of glacier retreat in the western Antarctic Peninsula. *Science*, 353, 283-286.

Davies, B.J., Hambrey, M.J., Smellie, J.L., Carrivick, J.L. and Glasser, N.F., 2012. Antarctic Peninsula Ice Sheet evolution during the Cenozoic Era. *Quaternary Science Reviews*, 31, 30-66.

Dentener, F. et al., 2008. Impacts of Atmospheric Anthropogenic Nitrogen on the Open Ocean. *Science,* 320, 893-897.

Depoorter, M.A., Bamber, J.L., Griggs, J.A., Lenaerts, J.T.M., Ligtenberg, S.R.M., van den Broeke, M.R. and Moholdt, G., 2013. Calving fluxes and basal melt rates of Antarctic ice shelves. *Nature*, 502, 89-92, doi:10.1038/nature12567.

De Waal, R.J.O., 2017. *An investigation of shaft line torsional vibration during ice impacts on PSRVs*. Stellenbosch University.

Diamond, D., 1994. QuikChem Method 10-114-21-1-B: Silicate by flow injection analysis. Lachat Instruments.

Domack, E., Duran, D., Leventer, A., Ishman, S., Doane, S., McCallum, S., Amblas, D., Ring, J., Gilbert, R., Prentice, M., 2005. Stability of the Larsen B ice shelf on the Antarctic Peninsula during the Holocene epoch. *Nature*, 436, 681-685.

Dowdeswell, J.A., Evans, J., Mugford, R., Griffiths, G., McPhail, S., Millard, N., Stevenson, P., Brandon, M.A., Banks, C., Heywood, K.J., Price, M.R., Dodd, P.A., Jenkins, A., Nicholls, K.W., Hayes, D., Abrahamsen, E.P., Tyler, P., Bett, B., Jones, D., Wadhams, P., Wilkinson, J.P., Stansfield, K. and Ackley, S., 2008. Autonomous underwater vehicles (AUVs) and investigations of the ice-ocean interface in Antarctic and Arctic waters. *Journal of Glaciology*, 54, 661-672.

Dowdeswell, J.A., Canals, M., Jakobsson, M., Todd, B.J., Dowdeswell, E.K. and Hogan K.A., (eds), 2016. Atlas of Submarine Glacial Landforms: Modern, Quaternary and Ancient. *Geological Society, London, Memoirs*, 46, 618 pp.

Dugdale, R.C., and Goering, J.J., 1967. Uptake of new and regenerated forms of nitrogen in primary productivity. *Limnology and Oceanography*, 12, 196–206.

Duce, R.A., LaRoche, J., Altieri, K.E., Arrigo, K.R., Baker, A.R., Capone, D.G., Cornell, P., Aber, J., Howarth, R., Likens, G., Matson, P., Schindler, D., Schlesinger, W. and Janussen, D., Lundälv, T. and Richter, C., 2013. Rapid glass sponge expansion after climate-induced Antarctic Ice Shelf collapse. *Current Biology*, 23, 1330-1334.

Eppley, R.W. and Peterson, B.J., 1979. Particulate organic matter flux and planktonic new production in the deep ocean. *Nature*, 282, 677-680.

Erisman, J., Galloway, J., Seitzinger, S., Bleeker, A., Dise, N., Petrescu, A., Leach, A., and de Vries, W., 2013. Consequences of human modification of the global nitrogen cycle. *Philosophical Transactions of the Royal Society B: Biological Sciences*, 368.

Etourneau, J., Sgubin, G., Crosta, X., Swingedouw, D., Willmott, V., Barbara, L. and Goosse, H., 2019. Ocean temperature impact on ice shelf extent in the eastern Antarctic Peninsula. *Nature Communications*, 10, doi:10.1038/s41467-018-08195-6.

Evans, J. and Pudsey, C.J., 2002. Sedimentation associated with Antarctic Peninsula ice shelves: implications for palaeoenvironmental reconstructions of glacimarine sediments. *Journal of the Geological Society, London,* 159, 233–238.

Evans, J., Pudsey, C.J., Ó Cofaigh, C., Morris, P.W. and Domack, E.W., 2005. Late Quaternary glacial history, dynamics and sedimentation of the eastern margin of the Antarctic Peninsula Ice Sheet. *Quaternary Science Reviews*, 24, 741-774.

Evans, J. and Hogan, K.A., 2016. Grounding-zone wedges on the northern Larsen shelf, Antarctic Peninsula. *In* Dowdeswell, J.A., Canals, M., Jakobsson, M., Todd, B.J., Dowdeswell, E.K. and Hogan K.A., (eds), *Atlas of Submarine Glacial Landforms: Modern, Quaternary and Ancient. Geological Society, London, Memoirs*, 46, 237-238.

Fahrbach, E., Rohardt, G., Scheele, N., Schröder, M., Strass, V. and Wisotzki, A., 1995. Formation and discharge of deep and bottom water in the northwestern Weddell Sea. *Journal of Marine Research*, 53, 515-538.

Fawcett, S.E., Lomas, M.W., Ward, B.B. and Sigman, D.M., 2014, The counterintuitive effect of summer-to-fall mixed layer deepening on eukaryotic new production in the Sargasso Sea. *Global Biogeochemical Cycles,* 28, 86-102.

Fawcett, S.E., Lomas, M.W., Casey, J.R., Ward, B.B. and Sigman, D.M., 2011. Assimilation of upwelled nitrate by small eukaryotes in the Sargasso Sea. *Nature Geoscience,* 4, 717-722.

Galloway, J.N., Aber, J.D., Erisman, J.W., Seitzinger, S.P., Howarth, R.W., Cowling, E.B., and Cosby, B.J., 2003. The Nitrogen Cascade. *BioScience*, 53, 341–356.

Galloway, J.N., Dentener, F.J., Capone, D.G. et al., 2004. *Biogeochemistry*, 70, 153.

Gilbert, R. and Domack, E.W., 2003. Sedimentary record of disintegrating ice shelves in a warming climate, Antarctic Peninsula. *Geochemistry Geophysics Geosystems*, 4, doi:10.1029/2002GC000441.

Gilbert, R., Domack, E.W. and Camerlenghi, A., 2003. Deglacial history of the Greenpeace Trough: ice sheet to ice shelf transition in the northern Weddell Sea. *In* Domack, E., Leventer, A., Burnett, A., Bindschadler, R., Convey, P. and Kirby, M., (eds.), *Antarctic Peninsula Climate Variability: Historical and Palaeoenvironmental Perspectives*, 79. Antarctic Research Series, AGU, Washington, DC, 195–204.

Gille, S.T., 2002. Warming of the Southern Ocean since the 1950s. *Science,* 29, 1275-1277.

Gordon, A., 2009. *Bottom Water Formation.* Associated Press.

Gordon, A.L., 1993. Ice Station Weddell Group of Principle Investigators, and Chief Scientists, Weddell Sea exploration from ice station. *EOS Transactions AGU,* 74, 121.

Gordon, A.L., Huber, B.A., Hellmer, H.H. and Ffield, A., 1993. Deep and Bottom Water of the Weddell Sea's Western Rim. *Science*, 262, 95-97.

Graham, A.G.C., Dutrieux, P., Vaughan, D.G., Nitsche, F.O., Gyllencreutz, R., Greenwood, S.L., Larter, R.D. and Jenkins, A., 2013. Seabed corrugations beneath an Antarctic ice shelf revealed by autonomous underwater vehicle survey: origin and implications for the history of Pine Island Glacier. *Journal of Geophysical Research*, 118, 1356-1366.

Granger, J. and Sigman, D.M., 2009. Removal of nitrite with sulfamic acid for nitrate N and O isotope analysis with the denitrifier method. *Rapid communication in mass spectrometry*, 23, 3753-3762.

Grasshoff, K., 1976. Methods of seawater analysis. Verlag Chemie, Weinheim and New York.

Gutt, J., Barratt, I., Domack, E., d'Udekem d'Acoz, C., Dimmler, W., Grémare, A., Heilmayer, O., Isla, E., Janussen, D., Jorgensen, E., Kock, K.-H., Sophia Lehnert, L., López-Gonzáles, P., Langner, S., Linse, K., Eugenia Manjón-Cabeza, M., Meißner, M., Montiel, A., Raes, M., Robert, H., Rose, A., Sañé Schepisi, E., Saucède, T., Scheidat, M., Schenke, H.-W., Seiler, J. and Smith, C., 2011. Biodiversity change after climate-induced ice-shelf collapse in the Antarctic. *Deep-Sea Research, Part II: Topical Studies in Oceanography*, 58, 74-83.

Gutt, J., Cape, M., Dimmler, W., Fillinger, L., Isla, E., Lieb, V., Lundälv, T. and Pulcher, C., 2013. Shifts in Antarctic megabenthic structure after ice-shelf disintegration in the Larsen area east of the Antarctic Peninsula. *Polar Biology*, 36, 895-906.

Haas, C., Nicolaus, M., Willmes, S., Worby, A. and Flinspach, D., 2008. Sea ice and snow thickness and physical properties of an ice floe in the western Weddell Sea and their changes during spring warming, *Deep-Sea Research II*, 55, 963-974.

Heil, P., Hutchings, J.IK., Worby, A.P., Johansson, M., Launiainen, J., Haas, C. and Hibler, W.D., 2008. Tidal forcing on sea-ice drift and deformation in the western Weddell Sea in early austral summer, 2004. *Deep-Sea Research II*, 55, 943-962.

Hellmer, H.H., Schroeder, M., Haas, C., Dieckmann, G.S. and Spindler, M., 2008. The ISPOL drift experiment. *Deep-Sea Research II*, 55, 913-917.

Hemer, M.A. and Harris, P.T., 2003. Sediment core from beneath the Amery Ice Shelf, East Antarctica, suggests mid-Holocene ice-shelf retreat. *Geology*, 31, 127-130.

Heroy, D.C., and Anderson, J.B., 2005. Ice-sheet extent of the Antarctic Peninsula region during the Last Glacial Maximum (LGM) – Insights from glacial geomorphology. *Geological Society of America Bulletin*, 117, 1497-1512.

Heroy, D.C. and Anderson, J.B., 2007. Radiocarbon constraints on Antarctic Peninsula Ice Sheet retreat following the Last Glacial Maximum (LGM). *Quaternary Science Reviews*, 26, 3286-3297.

Hogg, A.E. and Gunmundsson, H., 2017. Impacts of the Larsen-C Ice Shelf calving event. *Nature Climate Change*, **7**, 540-542.

Holland, P.R., Jenkins, A. and Holland, D.M., 2008. The response of ice shelf basal melting to variations in ocean temperature. *Journal of Climate*, 21, 2558-2572.

Holmes, R., Aminot, I., Kërouel, R., Hooker, B. and Peterson, B., 1999. A simple and precise method for measuring ammonium in marine and freshwater ecosystems. *Canadian Journal of Fisheries and Aquatic Sciences*, 56, 1801-1808.

Howarth, R., 2000. *Nutrient pollution of coastal rivers, bays, and seas*. Washington, DC: Ecological Society of America.

Ikonen, T., Peltokorpi, O. and Karhunen, J., 2014. Inverse ice-induced moment determination on the propeller of an ice-going vessel. *Cold Regions Science and Technology*, 112, 1–13. doi: 10.1016/j.coldregions.2014.12.010.

Intergovernmental Panel on Climate Change (IPCC), 2013. The IPCC Fifth Assessment Report, *Climate Change 2013.*

James, R.W., 1924. Some problems relating to Antarctic sea-ice. In: *Manchester Memoirs*, LXVIII, No. 7.

Kerr, R., Dotto, T.S., Mata, M.M. and Hellmer, H.H., 2018. Three decades of deep water mass investigation in the Weddell Sea (1984–2014): temporal variability and changes. *Deep Sea Research Part II*: Topical Studies in Oceanography, 149, 70-83.

Kotilainen, M. *et al.*, 2017. Predicting ice-induced load amplitudes on ship bow conditional on ice thickness and ship speed in the Baltic Sea. *Cold Regions Science and Technology,* 135, 116–126.

Littlepage, J.L. and Pearse, J.S., 1967. Biological and oceanographic observations under an Antarctic ice shelf. *Science,* 137, 679-681.

Løvoll, G. and Kadal, J.C., 2014. *Big data - the new data reality and industry impact*. Hovik, Norway.

Martin, J.H., Gordon, R.M. and Fitzwater, S.E., 1991. The case for iron. *Limnology and Oceanography,* 36, 1793-1802.

Meckler, A.N., Ren, H.A., Sigman, D.M., Gruber, N., Plessen, B., Schubert, C.J. and Haug, G.H., 2011. Deglacial nitrogen isotope changes in the Gulf of Mexico: Evidence from bulk sedimentary and foraminifera-bound nitrogen in Orca Basin sediments. *Paleoceanography* 26, PA4216.

Mouginot, J., Rignot, E. and Scheuchl, B., 2017. *MEaSURES Antarctic Boundaries for IPY 2007-2009 from Satellite Radar, Version 1*, digital media, NASA National Snow and Ice Data Center Distributed Active Archive Center, Boulder, Colorado, USA, doi:10.5067/AXE4121732AD.

Muench, R., 1989. The sea ice margins: A summary of physical phenomena. *NOAA Tech. Memo* ERL PMEL-88, 51.

Nicholls, K.W., Makinson, K. and Venables, E.J., 2012. Ocean circulation beneath Larsen C Ice Shelf, Antarctica from in situ observations. Geophysical Research Letters, 39.

Nicholls, K.W., Østerhus, S., Makinson, K., Gammelsrød, T. and Fahrbach, E., 2009. Ice-ocean processes over the continental shelf of the southern Weddell Sea, Antarctica: A review. *Reviews of Geophysics*, 47.

Nicholls, K., Pudsey, C. and Morris, P., 2004. Summertime water masses off the northern Larsen C Ice Shelf, Antarctica. *Geophysical Research Letters*, 31.

Ó Cofaigh, C., Davies, B., Livingstone, S., Smith, J., Johnson, J., Hocking, E., Hodgson, D., Anderson, J., Bentley, M., Canals, M., Domack, E., Dowdeswell, J.A., Evans, J., Glasser, N., Hillenbrand, C.-D., Larter, R., Roberts, S. and Simms, A., 2014. Reconstruction of ice-sheet changes in the Antarctic Peninsula since the Last Glacial Maximum. *Quaternary Science Reviews*, 100, 87-110.

Orsi, A., Johnson, G. and Bullister, J., 1999. Circulation, mixing, and production of Antarctic Bottom Water. *Progress in Oceanography*, 43, 55-109.

Parsons, T.R., Maita, Y. and Lalli, M., 1984. A Manual of Chemical and Biological Methods for Seawater Analysis.

Peck, L.S., Barnes, D.K.A., Cook, A.J., Fleming, A.H. and Clarke, A., 2010. Negative feedback in the cold: ice retreat produces new carbon sinks in Antarctica. *Global Change Biology*, 16, 2614-2623.

Peeters, B. and de Roeck, G., 1999. Reference-based Stochastic Subspace Identification for Output-only Modal Analysis. *Mechanical Systems & Signal Processing*, 13, 855–878.

Peeters, B. and de Roeck, G., 2001. Stochastic system identification for operational modal analysis: a review. *Journal of Dynamic Systems, Measurement and Control*, 123. doi: 10.1115/1.1410370.

Peng, X., Fawcett, S.E., van Oostende, N., Wolf, M.J., Marconi, D., Sigman, D.M. and Ward, B.B., 2018. Nitrogen uptake and nitrification in the subarctic North Atlantic Ocean. *Limnology and Oceanography*.

Post, A.L., Galton-Fenzi, B.K., Riddle, M.J., Herraiz-Borreguero, L., O'Brien, P.E., Hemer, M.A., McMinn, A., Rasch, D. and Craven, M., 2014. Modern sedimentation, circulation and life beneath the Amery Ice Shelf, East Antarctica. *Continental Shelf Research*, 74, 77-87.

Pudsey, C.J and Evans, J., 2001. First survey of Antarctic sub-ice shelf sediments reveals Mid-Holocene ice shelf retreat. *Geology*, 29, 787-790.

Pudsey, C.J., Murray, J.W., Appleby, P., Evans, J., 2006. Ice shelf history from petrographic and foraminiferal evidence, northeast Antarctic Peninsula. *Quaternary Science Reviews*, 25, 2357-2379.

Rack, W. and Rott, H., 2004. Pattern of retreat and disintegration of the Larsen B ice shelf., Antarctic Peninsula. *Annals of Glaciology*, **39**, 505-510.

Rathbun, C., 1997. Measurement of Chlorophyll a and Phaeopigments by Fluorometric Analysis. *In* Bermuda Atlantic Time-series Study Methods.

Reinardy, B.T.I., Pudsey, C.J., Hillenbrand, C.-D., Murray, T. and Evans, J., 2009. Contrasting sources for glacial and interglacial shelf sediments used to interpret changing ice flow directions in the Larsen Basin, Northern Antarctic Peninsula. *Marine Geology*, 266, 156-171.

Reinardy, B.T.I., Hiemstra, J., Murray, T., Hillenbrand, C-D. and Larter, R., 2011. Till genesis at the bed of an Antarctic Peninsula palaeo-ice stream as indicated by micromorphological analysis. *Boreas*, 40, 498-517.

Renner, A.H.H. and Lytle, V., 2007. Sea ice thickness in the Weddell Sea, Antarctica: a comparison of model and upward-looking sonar data. *Annals of Glaciology*, 46, 419-427.

Riddle, M.J., Craven, M., Goldsworthy, P.M. and Carsey, F., 2007. A diverse benthic assemblage 100 km from open water under the Amery Ice Shelf, Antarctica. *Paleoceanography and Paleoclimatology*, 22, PA1204.

Robertson, R., Visbeck, M., Gordon, A.L. and Fahrbach, E., 2002. Long-term temperature trends in the deep waters of the Weddell Sea. *Deep Sea Research Part II*: Topical Studies in Oceanography, 49(21), 4791-4806.

Robinson, R.S., M. Kienast, A.L. Albuquerque, M. Altabet, S. Contreras, R. De Pol Holz, N. Dubois, R. François, E. Galbraith, T.-C. Hsu, T. Ivanochko, S. Jaccard, S.-J. Kao, T. Kiefer, S. Kienast, M. Lehmann, P. Martinez, M. McCarthy, J. Möbius, T. Pedersen, T.M. Quan, E. Ryabenko, A. Schmittner, R. Schneider, A. Schneider-Mor, M. Shigemitsu, D. Sinclair, C. Somes, A. Studer, R. Thunell, J.-Y. Yang. A review of nitrogen isotopic alteration in marine sediments (2012) *Paleoceanography* 27, PA4203.

Rott, H., Skvarca, P. and Nagler, T., 1996. Rapid collapse of Northern Larsen Ice Shelf, Antarctica. *Science,* **271**, 788-792.

Sañé, E., Isla, E., Grémare, A., Gutt, J., Vétion, G. and DeMaster, D., 2011. Pigments in sediments beneath recently collapsed ice shelves: the case of Larsen A and B shelves, Antarctic Peninsula. *Journal of Sea Research*, 65, 94-102.

Sarmiento, J.L. and Toggweiler, J.R., 1984. A new model for the role of the oceans in determining atmospheric pCO_2. *Nature,* 308, 621-624.

Saxberg, B. and Kowalski, W., 1979. Generalised standard edition method. *Analytical Chemistry*, 51, 1031-1038.

Shepherd, A., Wingham, D. and Rignot, E., 2004. Warm ocean is eroding West Antarctic ice sheet. *Geophysical Research Letters*, 31.

Shipp, S.S., Anderson, J.B. and Domack, E.W., 1999, Late Pleistocene-Holocene retreat of the West Antarctic Ice-Sheet system in the Ross Sea: Part 1 – Geophysical results. *Geological Society of America Bulletin*, 111, 1486-1516.

Sigman, D.M. and Boyle, E.A., 2000. Glacial/interglacial variations in atmospheric carbon dioxide. *Nature,* 407, 859-869.

Sigman, D., Casciotti, K.L., Andreani, M., Barford, C., Galanter, M. and Böhlke, J.K., 2001. A Bacterial Method for the Nitrogen Isotopic Analysis of Nitrate in Seawater and Freshwater. *Analytical Chemistry*, 73, 4145–4153.

Sigman, D.M., Hain, M.P. and Haug, G.H, 2010. The polar ocean and glacial cycles in atmospheric CO_2 concentration. *Natur,e* 466, 47-55.

Smith Jr, W.O., 1987. Phytoplankton dynamics in marginal ice zones. Oceanography. *Marine Biology*, 25, 11-38.

Soal, K., 2018. *System identification and modal tracking of ship structures*. Stellenbosch University.

Soal, K., Bienert, J. and Bekker, A., 2015. Operational modal analysis on the polar supply and research vessel the S.A. Agulhas II. In *6th International Operational Modal Analysis Conference*.

Soal, K.I., 2015. *Vibration response of the polar supply and research vessel the S. A. Agulhas II in Antarctica and the Southern Ocean*. Stellenbosch : Stellenbosch University.

Sterken, M., Roberts, S. J., Hodgson, D. A., Vyverman, W., Balbo, A. L., Sabbe, K., Moreton, S.G. and Verleyen, E., 2012. Holocene glacial and climate history of Prince Gustav Channel, northeastern Antarctic Peninsula. *Quaternary Science Reviews*, 31, 93-111.

Strickland, J.D. and Parsons, T.R., 1968. A practical handbook of seawater analysis. *Bull. Fish. Res. Bd. Can.*, 167.

Studer, A.S., Ellis, K.K., Oleynik, S., Sigman, D.M. and Haug, G.H., 2013. Size-specific opal-bound nitrogen isotope measurements in North Pacific sediments *Geochmica et Cosmochimica Acta,* 120, 179-194.

Studer, A.S., Martínez-García, A., Jaccard, S.L., Girault, F.E., Sigman, D.M. and Haug, G.H., 2012. Enhanced stratification and seasonality in the Subarctic Pacific upon Northern Hemisphere glaciation new evidence from diatom-bound nitrogen isotopes, alkenones and archaeal tetraethers. *Earth and Planetary Science Letters,* 351, 84-94.

STX, 2010. *FINNSAP finite element analysis of the PSRV NB1368*. Rauma, Finland.

Su, B., Riska, K. and Moan, T., 2011. Numerical study of ice-induced loads on ship hulls. *Marine Structures*, 24, 132–152.

Suominen, M. *et al.*, 2013. Full-scale measurements on board PSRV S.A. *Agulhas II* in the Baltic Sea. In *Proceedings of the International Conference on Port and Ocean Engineering under Arctic Conditions, POAC*.

Suominen, M. *et al.*, 2017. Visual Antarctic Sea Ice Condition Observations during Austral Summers 2012-2016. In *Port and Ocean Egineering under Arctic Conditions*. Busan, Korea.

Sunda, W.G. and Huntsman, S.A., 1997 Interrelated influence of iron, light and cell size on marine phytoplankton growth. *Nature,* 390, 389-392.

Suttle, C.A., 2005 Viruses in the sea. *Nature*, 437, 356–61.

Tedesco, L., Vichi, M., Haapala, J. and Stipa, T., 2009. An enhanced sea-ice thermodynamic model applied to the Baltic Sea. *Boreal Environmental Research*, 14, 68–80.

Tedesco, L., Vichi, M., Haapala, J. and Stipa, T., 2010. A dynamic biologically-active layer for numerical studies of the sea ice ecosystem. *Ocean Modelling*, 35, 89–104.

Treibergs, L.A. and Granger, J., 2011. Enzyme level N and O isotope effects of assimilatory and dissimilatory nitrate reduction. *Limnology and Oceanography*, 62, 272-288.

van Caspel, M., Schröder, M., Huhn, O. and Hellmer, H., 2015. Precursors of Antarctic Bottom Water formed on the continental shelf off Larsen Ice Shelf. *Deep Sea Research Part I*: Oceanographic Research Papers, 99, 1-9.

van Overschee, P. and De Moor, B., 1996. *Subspace Identification for Linear Systems: Theory - Implementation - Applications*. Dordrecht: Kluwer Academic Publishers.

Ventura, C.E., Brincker, R. and Andersen, P., 2001. Damping Estimation by Frequency Domain Decomposition. In *Proceedings of the International Modal Analysis Conference XIX*, 698–703.

Welschmeyer, N., 1994. Fluorometric analysis of chlorophyll a in the presence of chlorophyll b and phaeopigments. *Limnology and Oceanography*, 39,1985-1992.

Williams, G., Maksym, T., Wilkinson, J., Kunz, C., Murphy, C., Kimball, P. and Singh, H., 2014. Thick and deformed Antarctic sea ice mapped with autonomous underwater vehicles. *Nature Geoscience*, 8, 61-67.